ISSN 0911-5730
UVSOR-41
July 2014

UVSOR ACTIVITY REPORT 2013

UVSOR Facility
Institute for Molecular Science
National Institutes of Natural Sciences

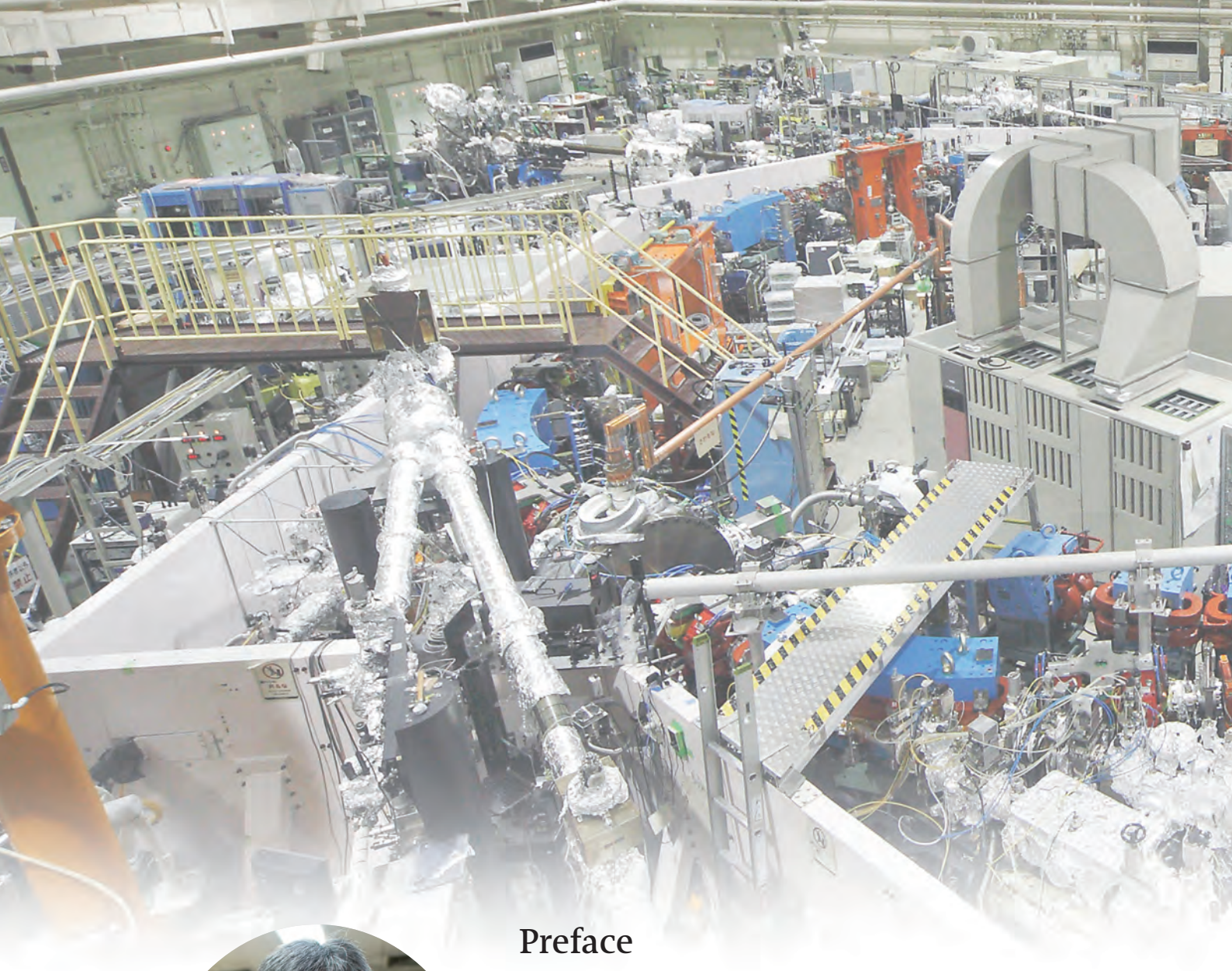

Preface

Last year marked the 30th anniversary of first light at UVSOR facility of the Institute for Molecular Science. We are deeply grateful to all at the Ministry of Education, Culture, Sports, and Science and Technology, the National Institutes of Natural Sciences, the Institute for Molecular Science, and the many others who have guided and supported the UVSOR effort throughout these years, and to all who have utilized this facility in their achievement of discoveries and advances reported at home and abroad.

Given the rapidly advancing world of science and technology, it may seem surprising that our synchrotron radiation system, conceived and constructed some 30 years ago, remains at the forefront of scientific experiment and investigation. This is the result of the construction stage, which involved installation of rock-solid hardware with a basic design marked by foresight; the first stage, during which design performance was reliably achieved with continuing progress in installation of many experimental systems responding to the needs of a broad range of users; and the second

stage, which was marked by progress in heightening the light-source brilliance and installation of beamline undulators. At present, in following these stages, all at the UVSOR facility stand united in their dedication to further heightening and stabilizing the light-source brilliance together with the installation of a scanning transmission x-ray microscope utilizing these characteristics. During the past fiscal year , we have enhanced the BL5U photoelectron spectroscopy beamline and completed construction for imminent start-up of an advanced photoelectric system providing spin- and spatial-resolved as well as angle-resolved operation.

In the time ahead, the UVSOR facility will continue to contribute to the advancement of basic and applied science and technology as an international hub for utilization of low-energy synchrotron light. For all of us at the UVSOR facility, the approach of its 30th anniversary is a time of renewal in spirit and dedication to fulfilling the expectations of all who use the facility and systems, and we hope and trust in your continuing support of this effort.

March 31, 2014
Masahiro Katoh
Director of UVSOR

News 2013

The JSSRR Scientific Award Given to Dr. Masanari NAGASAKA

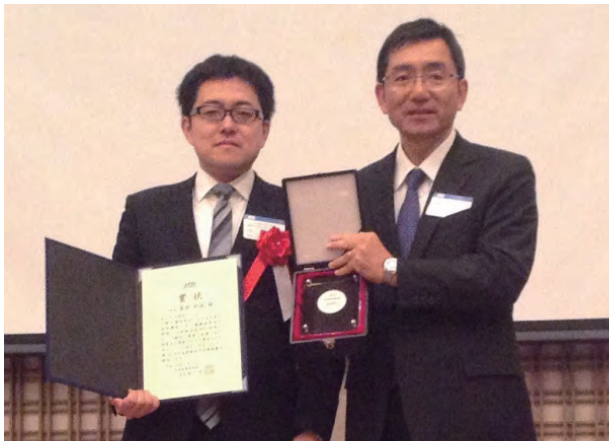

In 2014, Dr. Masanari NAGASAKA, Assistant Professor working with Professor Nobuhiro Kosugi, won the “Scientific Award” from the Japanese Society for Synchrotron Radiation Research (JSSRR) for his outstanding achievements on the "Local Structural Analyses of Molecular Systems and Development of In-situ Observation Methods by Soft X-ray Spectroscopy ". Congratulations!

2013 Annual Meeting Award of the Particle Accelerator Society of Japan Given to Mr. Youhei KAJIURA

Mr. Youhei KAJIURA received the 2013 Annual Meeting Award of the Particle Accelerator Society of Japan for his poster presentation on "Transmission-type Polarized Electron Source for Inverse Photoemission Spectroscopy". He was from Nagoya University and worked in the accelerator group of UVSOR as research assistants. Congratulations!

The JSR14 Scientific Award for Students Given to Mr. Toshiki INAGAKI

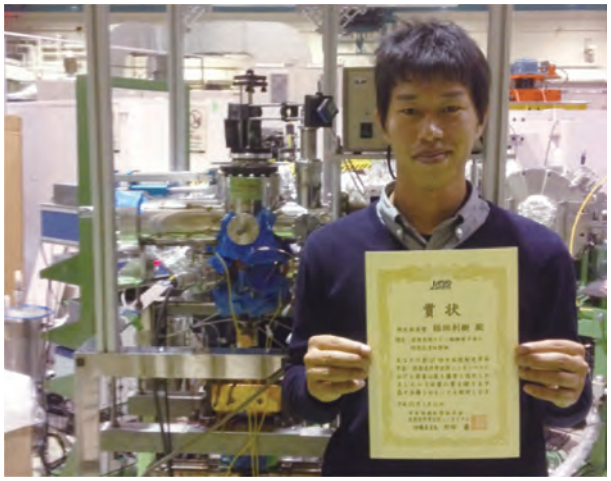

Mr. Toshiki INAGAKI received the JSR14 Scientific Award for Students for his poster presentation on "Measurements of Temporal Response of Transmission-type Spin-Polarized Photocathodes". He was from Nagoya University and worked in the accelerator group of UVSOR as research assistants. Congratulations!

I

Organaizaition and Staff List

UVSOR Organization

April 2014

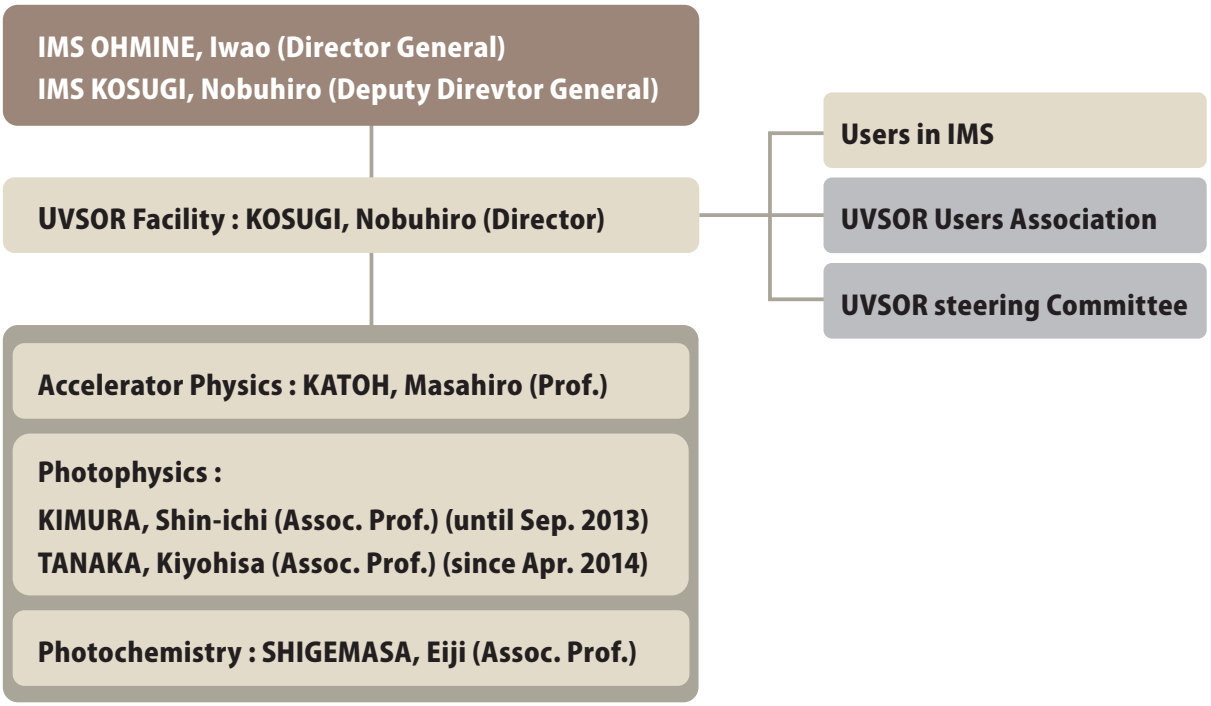

Staff List

UVSOR Staff

Director

KATOH, Masahiro	Professor	mkatoh@ims.ac.jp	(until Mar. 2014)
KOSUGI, Nobuhiro	Professor	kosugi@ims.ac.jp	(since Apr. 2014)

Light Source Division (Accelerator Physics)

KATOH, Masahiro	Professor	mkatoh@ims.ac.jp
OHIGASHI, Takuji	Assistant Professor	ohigashi@ims.ac.jp
KONOMI, Taro	Assistant Professor	konomi@ims.ac.jp
ITO, Atsushi	Visiting Professor	
YAMAZAKI, Jun-ichiro	Unit Chief Engineer	yamazaki@ims.ac.jp
HAYASHI, Kenji	Engineer	h-kenji@ims.ac.jp
TOKUSHI, Tetsuzyo	Supporting Engineer	tetsuzyo@ims.ac.jp
INAGAKI, Yuichi	Supporting Engineer	yinagaki@ims.ac.jp
HAYASHI, Kenichi	Supporting Engineer	khayasi@ims.ac.jp
MINAKUCHI, Aki	Supporting Engineer	minakuchi@ims.ac.jp

Beamline Division (Photophysics)

KIMURA, Shin-ichi	Associate Professor	kimura@ims.ac.jp	(until Jun. 2013)
TANAKA, Kiyohisa	Associate Professor	k-tanaka@ims.ac.jp	(since Apr. 2014)
MATSUNAMI, Masaharu	Assistant Professor	matunami@ims.ac.jp	
HASUMOTO, Masami	Unit Chief Engineer	hasumoto@ims.ac.jp	
SAKAI, Masahiro	Engineer	sakai@ims.ac.jp	
KOSWATTAGE, Kaveenga Rasika	Visiting Researcher	rasika@ims.ac.jp	
HAJIRI, Tetsuya	Visiting Researcher	hajiri@ims.ac.jp	(since Apr. 2014)

Beamline Division (Photochemistry)

SHIGEMASA, Eiji	Associate Professor	sigemasa@ims.ac.jp	
IWAYAMA, Hiroshi	Assistant Professor	iwayama@ims.ac.jp	
HORIGOME, Toshio	Facility Chief Engineer	horigome@ims.ac.jp	
KONDO, Naonori	Engineer	nkondo@ims.ac.jp	
TESHIMA, Fumitsuna	Engineer	tetsu@ims.ac.jp	

Secretary

HAGIWARA, Hisayo	hagiwara@ims.ac.jp	
KAWAI, Shigeko	kawai@ims.ac.jp	(until Mar. 2014)
MASUDA, Michiko	masuda@ims.ac.jp	(since Apr. 2014)

UVSOR Steering Committee

KATOH, Masahiro	UVSOR, IMS	Chair	(until Mar. 2013)
KOSUGi, Nobuhiro	UVSOR, IMS	Chair	(since Apr. 2014)
SHIGEMASA, Eiji	UVSOR, IMS		
KIMURA, Shin-ichi	UVSOR, IMS		(until Mar. 2014)
TANAKA, Kiyohisa	UVSOR, IMS		(since Apr. 2014)
ITO, Atsushi	Tokai Univ. (Visiting Prof., IMS)		
YOKOYAMA, Toshihiko	IMS		
OHSHIMA,Yasuhiro	IMS		(until Mar. 2014)
KERA, Satoshi	IMS		(since Apr. 2014)
FUJI, Takao	IMS		
AKIYAMA, Syuji	IMS		
HARADA, Yoshihisa	Univ. of Tokyo		
NAKAGAWA, Kazumichi	Kobe Univ.		
SODA, Kazuo	Nagoya Univ.		
ADACHI, Shinichi	KEK-PF		(since Apr. 2014)
DAIMON, Hiroshi	NAIST		(since Apr. 2014)

OHASHI, Haruhiko	JASRI	(since Apr. 2014)
SASAKI, Shigemi	Hiroshima Univ.	(since Apr. 2014)
KINOSHITA, Toyohiko	JASRI	(until Mar. 2014)
KOBAYASHI, Yukinori	KEK-PF	(until Mar. 2014)
KONDOH, Hiroshi	Keio Univ.	(until Mar. 2014)
SHIMADA, Kenya	Hiroshima Univ.	(until Mar. 2014)

UVSOR Users Association

HIKOSAKA, Yasumasa	Niigata Univ.	(since Apr. 2014)
HIAHARA, Toru	Tokyo Institute of Technology	(since Apr. 2014)
KIMURA, Shin-ichi	Osaka Univ.	(since Apr. 2014)
KITAURA, Mamoru	Yamagata Univ.	(since Apr. 2014)
YOSHIDA, Tomoko	Nagoya Univ.	(since Apr. 2014)
SODA, Kazuo	Chair, Nagoya Univ.	(until Mar. 2014)
URISU, Tsuneo	Nagoya Univ.	(until Mar. 2014)
TANAKA, Shin-ichiro	Osaka Univ.	(until Mar. 2014)
KERA, Satoshi	Chiba Univ.	(until Mar. 2014)
ITO, Takahiro	Nagoya Univ.	(until Mar. 2014)

Graduate Students

INAGAKI, Ryo	Nagoya Univ.	(since Nov. 2013)
INAGAKI, Toshiki	Nagoya Univ.	(since Nov. 2013)
MITAMURA, Masaki	Nagoya Univ.	(since Nov. 2013)
TSUIKI, Emiri	Nagoya Univ.	(since Nov. 2013)
KAJIURA, Yohei	Nagoya Univ.	(until Sep. 2013)
KATO, Masaki	Nagoya Univ.	(until Sep. 2013)
KANEKO, Masaki	Nagoya Univ.	(until Sep. 2013)
KAWAKAMI, Ryo	Nagoya Univ.	(until Sep. 2013)
MOMIYAMA, Haruya	Nagoya Univ.	(until Sep. 2013)
SEKITA, Sou	Nagoya Univ.	(until Sep. 2013)

Visiting Scientists

WANG, Yu-Fu	Tamkang University	Jun. 2013, Aug. 2013
HITCHCOCK, Adam	McMaster University	Jul. 2013, Jan. 2014
CHO, Soohyun	Yonsei University	Jul. 2013
KIM, Beomyoung	Yonsei University	Jul. 2013
SEO, Jungjin	Yonsei University	Jul. 2013

QIN, Zhisheng	McMaster University	Jul. 2013, Sep. 2013, Dec. 2013
SICHELSCHMIDT, Jorg	Max Planck Institute Chemical Physics of Solids	Jul. 2013
SCHEFFLER, Marc	1 Physikalisches Institut, Universität Stuttgart	Jul. 2013
HAN, Garam	Yonsei University	Aug. 2013
KIM, Namdong	Pohang Acceletarot Laboratory	Aug. 2013
DIAO, Caozheng	National University of Singapore	Aug. 2013, Jan. 2014
TEGUH, Citra Asmara	National University of Singapore	Aug. 2013, Jan. 2014
PONG, Way-Faung	Tamkang University	Aug. 2013, Nov. 2013
CHIOU, Jan-Wern	National University of Kaohsiung	Aug. 2013, Nov. 2013
WANG, Bo-Yao	Tamkang University	Aug. 2013
LIN, Ming-Wei	National Synchrotron Radiation Research Center	Sep. 2013, Dec. 2013
HSU, Yao-Chen	National Synchrotron Radiation Research Center	Sep. 2013
SHIU, Hung-Wei	National Synchrotron Radiation Research Center	Sep. 2013, Dec. 2013
LAI, Yu-Ling	National Synchrotron Radiation Research Center	Sep. 2013, Dec. 2013
FHESCH, Roman	Freie Universität Berlin	Sep. 2013, Feb. 2014
RUEHL, Eckart	Freie Universität Berlin	Sep. 2013, Feb. 2014
KUECHLER, Sarah	Freie Universität Berlin	Sep. 2013, Feb. 2014
SALEH, Muhammad	Univ Gadjah Mada	Oct. 2013
ARRUA, Ruben Dario	University of Tasmania	Oct. 2013
JUNG, Sung Won	Pohang University of Science and Technology	Oct. 2013
SON, Yeong Seop	Pohang University of Science and Technology	Oct. 2013
KIM, Hyo Sung	Pohang University of Science and Technology	Oct. 2013
XIA, Miao	Fudan University	Oct. 2013
XU, Difei	Fudan University	Oct. 2013
NGUYEN, Thi Mua	Hanoi Univ. of technology	Oct. 2013
SHIN, Woojong	Pohang University of Science and Technology	Nov. 2013
HAN, Sang Wook	Pohang University of Science and Technology	Nov. 2013
WANG, Hsaui-tsu	National Tsinghua University	Nov. 2013
ZHANG, Guobin	University of Science and Technology of China	Nov. 2013
SUN, Zhe	University of Science and Technology of China	Nov. 2013
CUI, Shengtao	University of Science and Technology of China	Nov. 2013
KONG, Shuai	University of Science and Technology of China	Nov. 2013
CHANG, Chiao-Kai	National Synchrotron Radiation Research Center	Dec. 2013
CHIOU, Guan-Chiun	National Synchrotron Radiation Research Center	Dec. 2013
ROSENDAHL, Scott	McMaster University	Jan. 2014
ZHU, Xiaohui	McMaster University	Jan. 2014
LINDLE, Dennis	University of Nevada	Feb. 2014
PIANCASTELLI, Maria-Novella	Uppsala universitet	Feb. 2014
LABLANQUIE, Pascal	LCPMR, Universite Pierre-et-Marie-Curie	Feb. 2014
YAMAMOTO, Kenji	Freie Universität Berlin	Feb. 2014

II

Current Status of Light Sources and Beamlines

Light Source in 2013

1. Status of UVSOR Accelerators

In the fiscal year 2013, we operated UVSOR-III from June to February, for 35 weeks for users, which is one week shorter than usual. This shorter operation period was due to the shutdown in April and May 2013 and in March 2014. The former was for an inspection of the main RF cavity and the latter was for a upgrade program on the beam-line BL5U, which included a upgrade on the undulator U5, both of which will be described later.

We operated the machine for 33 weeks in the multi-bunch top-up mode, in which the beam current was kept at 300 mA with the top-up injection, and 2 weeks in the single-bunch/multi-bunch hybrid mode, in which the machine is operated in single-bunch top-up mode during daytime and in the multi-bunch top-up mode during nighttime. The beam current in the single bunch mode is also kept constant at 50 mA with the top-up injection. The monthly statistics of the operation time and the integrated beam current are shown in Fig. 1.

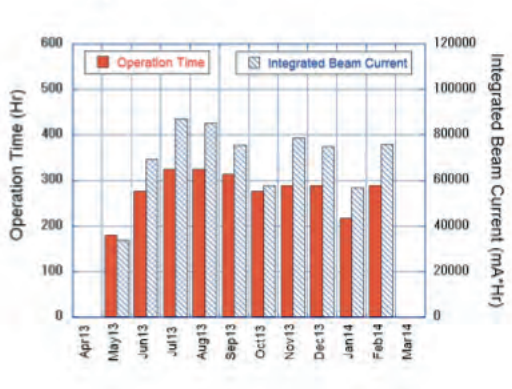

Fig. 1. Monthly statistics in FY2013.

The weekly operation schedule is as follows. On Monday, from 9 am to 9 pm, the machine is operated for machine studies. On Tuesday and Wednesday, from 9am to 9pm, the machine is operated for users. From Thursday 9am to Friday 9pm, the machine is operated for 36 hours continuously for users. Thus, the beam time for users in a week is 60 hours. Usually, we have a few weeks dedicated for machine study, however, in 2013, we did not have them to keep the beam time for users against the rather long shutdowns.

In this fiscal year, we had a few machine troubles on the injector, on the control system and on the reference signal generator. The last one caused sudden beam losses a few times a day. However, fortunately, in all cases the beam time for users could be secured by extending the operation time in the same weeks.

2. Improvements and Developments

Vacuum Pressure Rise in the Main RF Cavity

In 2012, we observed pressure rises in the RF accelerating cavity during the operation, to 10^{-6} Pa level, which was much higher than the normal value around 10^{-7} Pa. Soon, we found that the rises could be avoided by increasing the RF voltage to a certain level. However, month by month, the level was getting higher and higher. Therefore, we decided to open the cavity and to inspect its inside. In April 2013, the cavity was removed from the ring and the big flange was opened as shown in Fig. 2. We found some contamination inside. It was oil-like material and its origin is still unknown. We wiped out them and reconstructed the cavity. After setting it to the ring, we baked the cavity at around 200 degree C, which was higher than before. After this work, we found that the pressure rise was almost completely suppressed. After one year operation, we found no problem anymore.

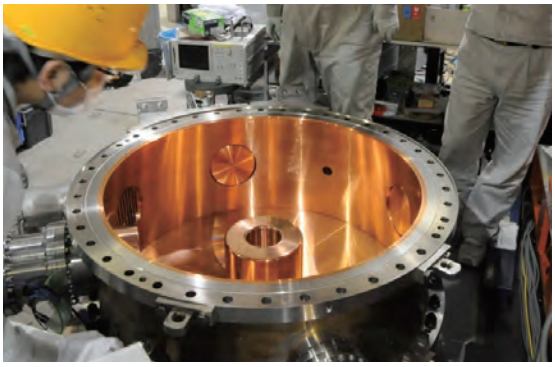

Fig. 2. Main RF Cavity under inspection

Reconstruction of BL5U Polarization Variable Undulator

The undulator for BL5U was designed and constructed in 1996 to provides polarization variable synchrotron radiation to the BL5U beam-line and also to work for the resonator free electron laser as an optical klystron. Since a new optical klystron has been constructed and installed last year at the straight section #1, we decided to remodel this undulator to a normal undulator with higher brightness. The old undulator had three magnet arrays on each pole to produce helical and horizontal linear polarized light. In March 2014, we have changed this magnetic configuration to the APPLE-II one with a shorter period length, 60 mm, as utlizing the present mechanical frame (Fig. 3). The magnetic field measurement was also carried out in the storage ring. The new undulator will be commissioned in May, 2014.

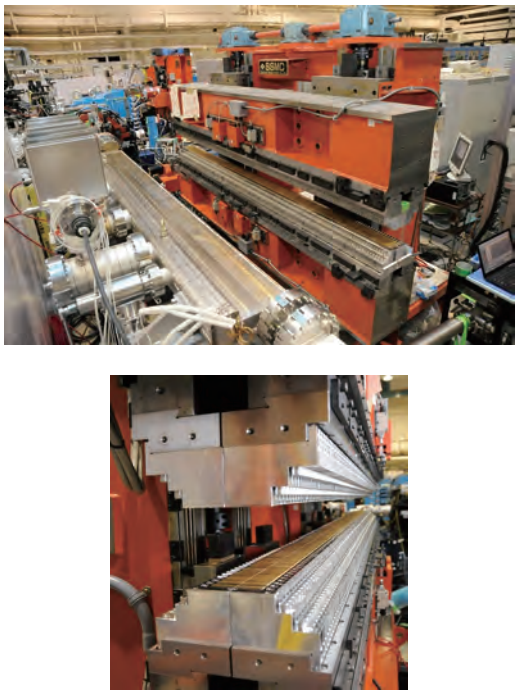

Fig. 3. New U5 undulator and beam duct just before installation (upper) and new magnet configuration (lower).

Electron gun developments towards future quantum beam sources

Electron guns of two types are being developed. One is a spin polarized electron gun. This is being developed towards inverse photo-electron spectroscopy in collaboration with Nagoya University. In FY2013, we have developed a measurement system for temporal response of the gun [1] and a Wien filter to transport the polarized beam [2].

Another electron gun is a superconducting photocathode one towards future high repetition rate free electron laser. At UVSOR, the photocathode part is mainly being developed, in collaboration with KEK [3].

References

[1] T. Inagaki *et al*., in these reports
[2] Y. Kajiura *et al*., in these reports
[3] R. Inagaki *et al*., in these reports

Masahiro KATOH (UVSOR Facility)

UVSOR Accelerator Complex

Injection Linear Accelerator

Energy	15 MeV
Length	2.5 m
Frequency	2856 MHz
Accelerating RF Field	2π/3 Traveling Wave
Klystron Power	1.8 MW
Energy Spread	~1.6 MeV
Repetition Rate	2.6 Hz

UVSOR-III Storage-Ring

Energy	750 MeV
Injection Energy	750 MeV
Maximum Storage Current	500 mA (multi bunch) 100 mA (single bunch)
Normal operation current (Top-up mode)	300 mA (multi bunch) 50 mA (single bunch)
Natural Emittance	17.5 nm-rad
Circumference	53.2 m
RF Frequency	90.1 MHz
Harmonic Number	16
Bending Radius	2.2 m
Lattice	Extended DBA×4
Straight Section	(4 m×4)+(1.5 m×4)
RF Voltage	120 kV
Betatron Tune	
Horizontal	3.75
Vertical	3.20
Momentum Compaction	0.030
Natural Chromaticity	
Horizontal	-8.1
Vertical	-7.3
Energy Spread	5.26×10^{-4}
Coupling Ratio	1%
Natural Bunch Length	128 ps

Booster Synchrotron

Energy	750 MeV
Injection	15 MeV
Beam Current	32 mA (uniform filling)
Circumference	26.6 m
RF Frequency	90.1 MHz
Harmonic Number	8
Bending Radius	1.8m
Lattice	FODO×8
Betatron Tune	
Horizontal	2.25
Vertical	1.25
Momentum Compaction	0.138
Repetition Rate	1 Hz (750 MeV)

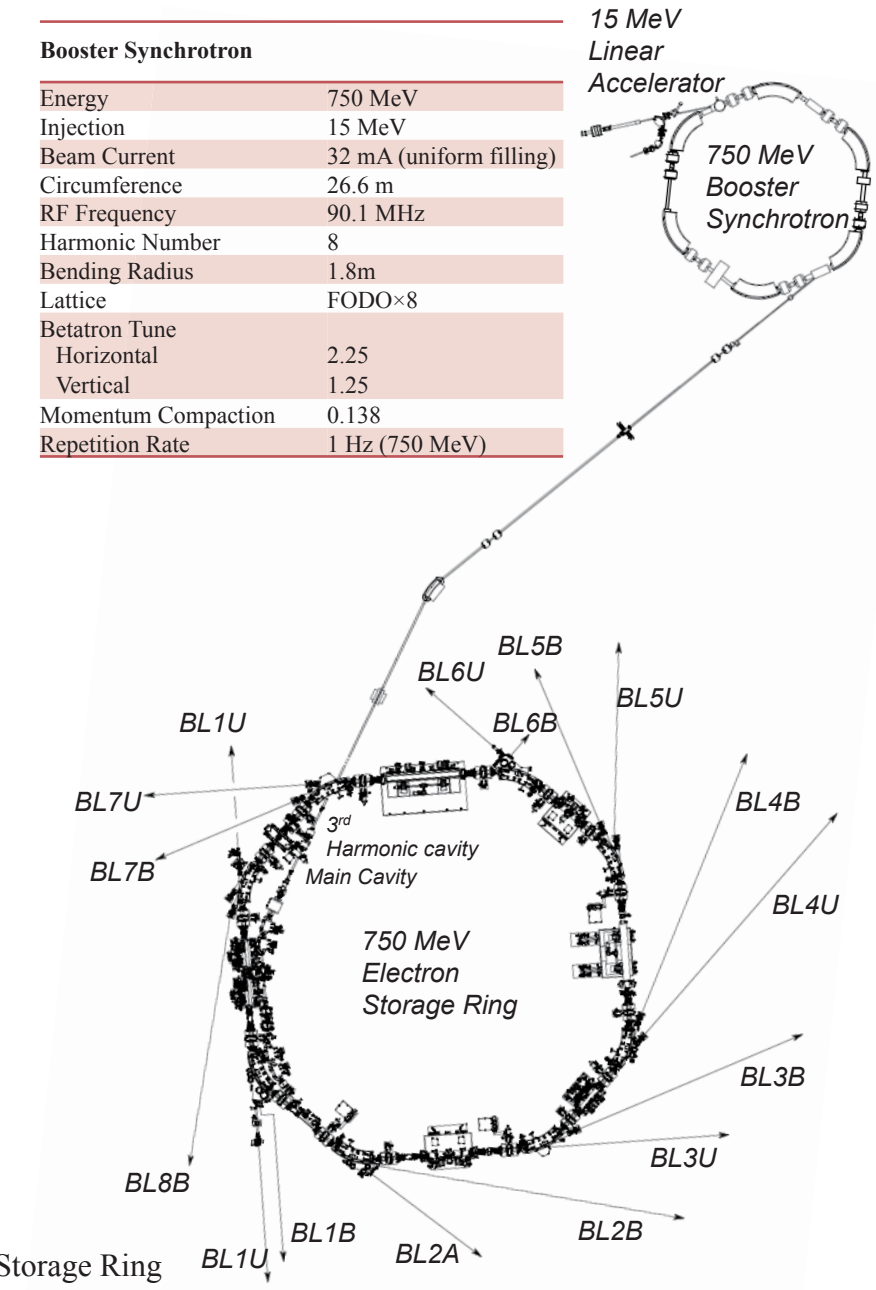

Electron Beam Optics of UVSOR-III Storage Ring

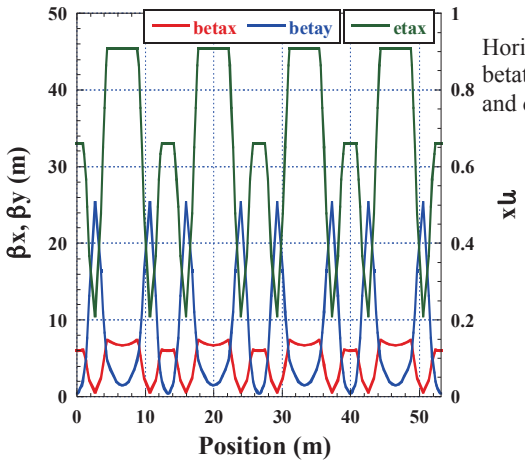

Horizontal/vertical betatron functions and dispersion function

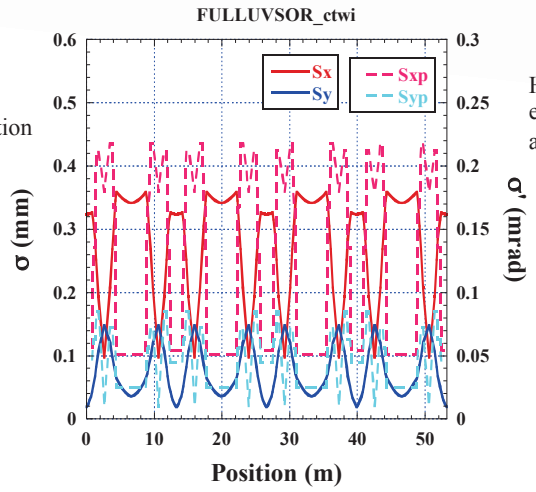

Horizontal/vertical electron beam size and beam divergences

Insertion Device

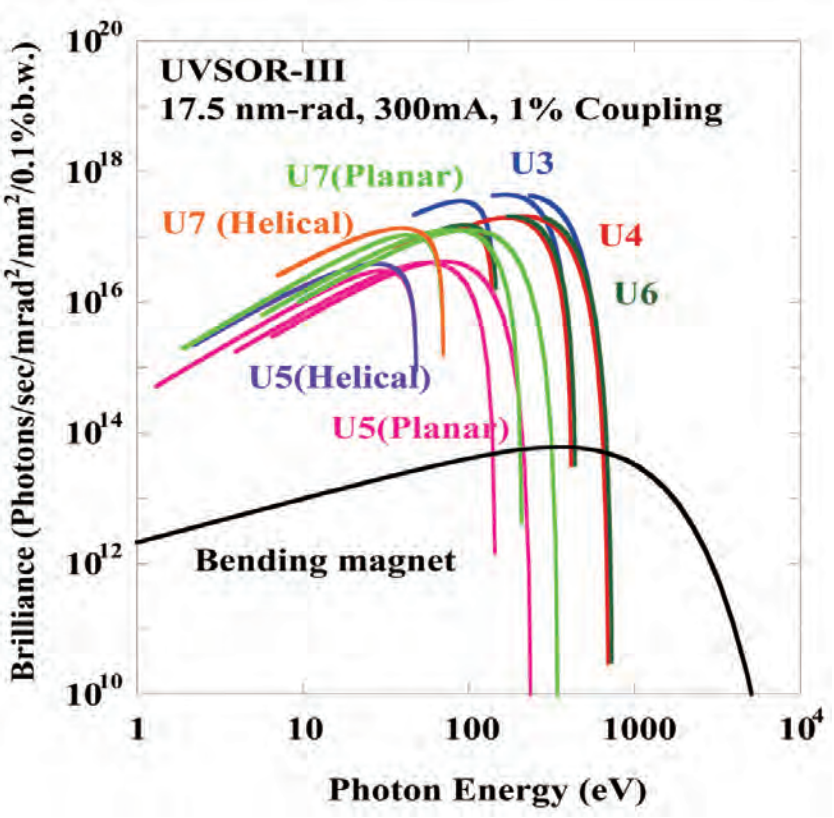

Brilliance of radiation from the insertion devices (U3, U4, U5, U6 and U7) and a bending magnet of UVSOR-III

U1 Apple-II Undulator /

Optical Klystron

Number of Periods	10 + 10
Period length	88 mm
Pole Length	0.968 m + 0.968 m
Pole Gap	24-200 mm
Deflection Parameter	7.36 (Max. Horizontal) 4.93 (Max. Vertical) 4.06 (Max. Helical)

U3 In-vacuum Undulator

Number of Periods	50
Period length	38 mm
Pole Length	1.9 m
Pole Gap	15-40 mm
Deflection Parameter	2.0-0.24

U4 In-vacuum Undulator

Number of Periods	26
Period length	38 mm
Pole Length	0.99 m
Pole Gap	13-40 mm
Deflection Parameter	2.4-0.19

U5 Helical Undulator/ Optical Klystron

Number of Periods	21 / 9+9 (Opt. Kly.)
Period length	110 mm
Pole Length	2.35 m
Pole Gap	30-150 mm
Deflection Parameter	4.6-0.07 (Helical) 8.5-0.15 (Linear)

U6 In-vacuum Undulator

Number of Periods	26
Period length	36 mm
Pole Length	0.94 m
Pole Gap	13-40 mm
Deflection Parameter	1.78 - 0.19

U7 Apple-II

Variable Polarization Undulator

Number of Periods	40
Period length	76 mm
Pole Length	3.04 m
Pole Gap	24-200 mm
Deflection Parameter	5.4 (Max. Horizontal) 3.6 (Max. Vertical) 3.0 (Max. Helical)

Bending Magnets

Bending Radius	2.2 m
Critical Energy	425 eV

Beamlines in 2013

Eiji SHIGEMASA
UVSOR Facility, Institute for Molecular Science

The UVSOR facility is one of the highest brilliance light sources in the extreme-ultraviolet region among synchrotron radiation facilities with electron energy less than 1 GeV, thanks to the successful accomplishment of the upgrade project on the storage ring (UVSOR-III project). The natural emittance of the UVSOR-III storage ring reaches to 17.5 nm-rad.

Eight bending magnets and five insertion devices are available as synchrotron light sources at UVSOR. There has been a total of fourteen operational beamlines in 2013, which are classified into two categories. Twelve of them are the so-called "Open beamlines", which are open to scientists of universities and research institutes belonging to the government, public organizations, private enterprises and those of foreign countries. The rest of the two beamlines are the "In-house beamlines", and are dedicated to the use of research groups within IMS.

There is one soft X-ray station equipped with a double-crystal monochromator, and eight extreme ultraviolet and soft X-ray stations with a grazing incidence monochromator, three vacuum ultraviolet stations with a normal incidence monochromator and two infrared (IR) stations equipped with a Fourier-Transform interferometer, as shown in the appended table (next page) for all available beamlines at UVSOR in 2013.

BL4U, which is equipped with a scanning transmission soft X-ray microscope (STXM), has been newly constructed in 2012. BL4U has been open to users since June 2013, immediately after the shutdown term. Many new results have already emerged from BL4U. The performance of BL4U is close to the theoretically expected one, except in the photon energy region near the C K-shell ionization threshold, due to the so-called "carbon contamination" for the optical elements. In order to improve this situation, the first mirror was recoated by gold and the inner wall of the vacuum chamber as well as all the parts of the mirror holder were washed by hot water to remove the carbon containing elements from the surfaces. As a result, the photon intensity in the C-K edge region has been improved, but has gradually decreased with time. The same cleaning treatment to the grating chamber is planned to be performed during the shutdown term in the spring of 2014.

BL2B, which has long been utilized as an in-house beamline, has been reorganized as an open beamline in 2013. This has been conducted as one of the long-term project proposals. The experimental setup of the angle-resolved photoelectron spectroscopy (ARPES) for inorganic thin films has been brought from Chiba University. The mirror exchanging mechanism in the grating chamber of the BL2B monochromator has been repaired, and the inter-lock system and monochromator control software have been prepared. The commissioning and performance tests will be started from May 2014.

The reconstruction of BL5U has been initiated in 2013. The previous system at BL5U, the SGM-TRAIN monochromator and the APRES end-station, has been stopped its operation in December 2013. The constructions of a new soft X-ray beamline and a spin-resolved photoemission experimental setup have been started since January 2014. As a new undulator for BL5U, an Apple-II type with the period length of 60 mm, whose total length is about 2.5 m, is chosen. The spectral region from 20 eV to 200 eV will be covered with the first and higher harmonic radiation. A variable included angle Monk-Gillieson mounting with an entrance slit-less configuration, which is the same as those installed at BL4U and BL6U, has been selected. The spin-resolved photoemission setup will be equipped with a high-resolution hemispherical electron energy analyzer (MBS A-1) with a highly efficient Mott detector. In pursuit of realizing photoemission experiments with very high spatial resolution, a specially designed post-focusing mirror system is planned to be introduced, where a small beam spot at the sample position (less than 10 μm in diameter) is expected to be achieved. The beamline commissioning of BL5U will be started from May 2014. BL5U will be open to users in the spring of 2015.

In order to promote beamline upgrades and developments of new experimental techniques by users, a new research proposal category named, the "long-term project proposal", has been introduced in 2012. The available period of this proposal category is three years. One proposal on BL1U has been accepted in 2013. Further discussion toward formulating a basic plan on the beamline construction with users, will be continued.

All users are required to refer to the beamline manuals and the UVSOR guidebook (the latest revision in PDF format uploaded on the UVSOR web site in June 2010), on the occasion of conducting the actual experimental procedures. Those wishing to use the open and in-house beamlines are recommended to contact the beamline master (see next page), respectively. For updated information of UVSOR, http://www.uvsor.ims.ac.jp.

Beamlines at UVSOR

Beamline	Monochromator / Spectrometer	Energy Range	Targets	Techniques	Contact
BL1U	Free electron laser	1.6 - 13.9 eV			M. Katoh mkatoh@ims.ac.jp
BL1B	Martin-Puplett FT-FIR	0.5 - 30 meV	Solid	Reflection Absorption	F. Teshima tetsu@ims.ac.jp
BL2A	Double crystal	585 eV - 4 keV	Solid	Reflection Absorption	N. Kondo nkondo@ims.ac.jp
BL2B	18-m spherical grating (Dragon)	24 - 205 eV	Gas	Photoionization Photodissociation	S. Kera kera@ims.ac.jp
BL3U*	Varied-line-spacing plane grating (Monk-Gillieson)	60 - 800 eV	Gas Liquid Solid	Absorption Photoemission Photon-emission	N. Kosugi kosugi@ims.ac.jp
BL3B	2.5-m off-plane Eagle	1.7 - 30 eV	Solid	Reflection Absorption	M. Hasumoto hasumoto@ims.ac.jp
BL4U	Varied-line-spacing plane grating (Monk-Gillieson)	130 - 700 eV	Gas Liquid Solid	Absorption (Microscopy)	T. Ohigashi ohigashi@ims.ac.jp
BL4B	Varied-line-spacing plane grating (Monk-Gillieson)	25 eV - 1 keV	Gas Solid	Photoionization Photodissociation Photoemission	E. Shigemasa sigemasa@ims.ac.jp
BL5U	Spherical grating (SGM-TRAIN†)	5 - 250 eV	Solid	Photoemission	M. Sakai sakai@ims.ac.jp
BL5B	Plane grating	6 - 600 eV	Solid	Calibration Absorption	M. Hasumoto hasumoto@ims.ac.jp
BL6U*	Variable-included-angle varied-line-spacing plane grating	30 - 500 eV	Gas Solid	Photoionization Photodissociation Photoemission	E. Shigemasa sigemasa@ims.ac.jp
BL6B	Michelson FT-IR	3 meV - 2.5 eV	Solid	Reflection Absorption	F. Teshima tetsu@ims.ac.jp
BL7U	10-m normal incidence (modified Wadsworth)	6 - 40 eV	Solid	Photoemission	M. Matsunami matunami@ims.ac.jp
BL7B	3-m normal incidence	1.2 - 25 eV	Solid	Reflection Absorption	M. Hasumoto hasumoto@ims.ac.jp
BL8B	Plane grating	1.9 - 150 eV	Solid	Photoemission	S. Kera kera@ims.ac.jp

Yellow columns represent undulator beamlines.
* In-house beamline.
†Spherical grating monochromator with translating and rotating assembly including normal incidence mount.

BL1U

Free Electron Laser

▼Description

The free electron laser (FEL) at UVSOR-II is being moved to a dedicated long straight section (S1). The FEL is equipped with a variably polarized optical klystron of 3 m in length and an optical cavity of 13.3 m in length. By using various multilayer mirrors for the cavity, the FEL can provide coherent light in a wide wavelength range from 800 nm to 199 nm. The pulse duration is typically several tens of picoseconds. The repetition rate is approximately 11 MHz. The average output power depends on the wavelength but its typical value is several hundred milliwatts. Output power higher than 1 W was recorded at 230 nm and 570 nm. The FEL can be operated in top-up injection mode. Users can use the FEL for several hours with quasi-constant output power. The laser pulses are naturally synchronized with the synchrotron radiation pulses that are provided at other synchrotron radiation beamlines. The laser beam can be transported to the beamlines using a mirror system for pump and probe experiments if requested.

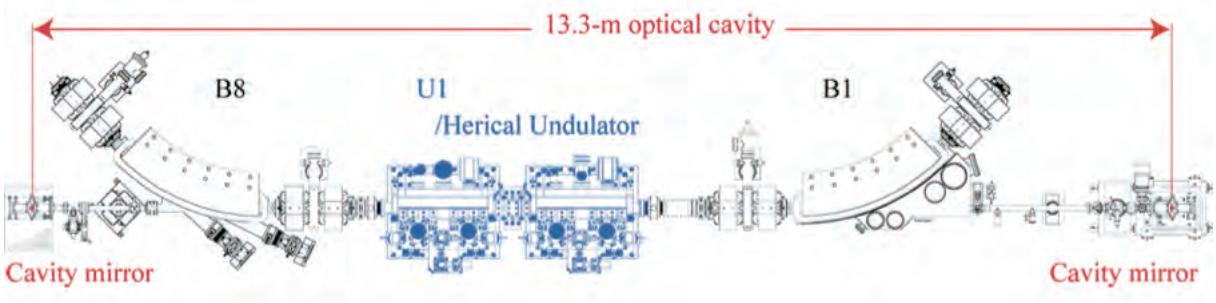

Fig. 1. Schematic of the 13.3 m-long optical cavity.

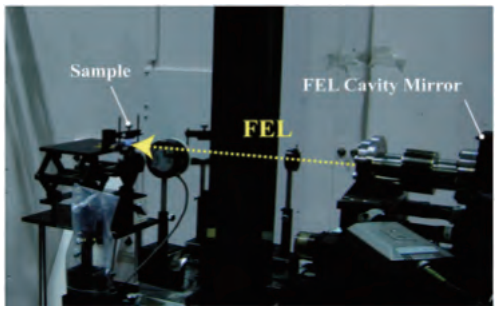

Fig. 2. Left and right circularly polarized FEL being delivered to B4 for an application experiment.

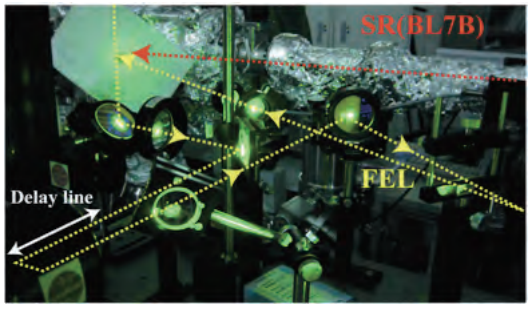

Fig. 3. The FEL is delivered to BL7B. The FEL is irradiated on a target simultaneously with the SR .

▼Technical Data

Wavelength	199-800 nm
Spectral band width	~10^{-4}
Polarization	Circular/linear
Pulse rate	11.26 MHz
Max. average power	~1 W
Cavity type	Fabry-Perot
Cavity length	13.3 m
Cavity mirror	HfO_2, Ta_2O_5, Al_2O_3 multilayer

BL1B

Terahertz Spectroscopy Using Coherent Synchrotron Radiation

▼Description

Coherent synchrotron radiation (CSR) is a powerful light source in the terahertz (THz) region. This beamline has been constructed for basic studies on the properties of THz-CSR. However, it can be also used for measurements of reflectivity and transmission spectra of solids using conventional synchrotron radiation.

The emitted THz light is collected by a three-dimensional magic mirror (3D-MM, M0) of the same type as those already successfully installed at BL43IR in SPring-8 and BL6B in UVSOR-II. The 3D-MM was installed in bending-magnet chamber #1 and is controlled by a 5-axis pulse motor stage (x, z translation; θ_x, θ_y, θ_z rotation). The acceptance angle was set at 17.5-34 degrees (total 288 mrad) in the horizontal direction. The vertical angle was set at ±40 mrad to collect the widely expanded THz-CSR.

The beamline is equipped with a Martin-Puplett type interferometer (JASCO FARIS-1) to cover the THz spectral region from 4 to 240 cm^{-1} ($h\nu$ = 500 μeV-30 meV). There is a reflection/absorption spectroscopy (RAS) end-station for large samples (~ several mm). At the RAS end-station, a liquid-helium-flow type cryostat with a minimum temperature of 4 K is installed.

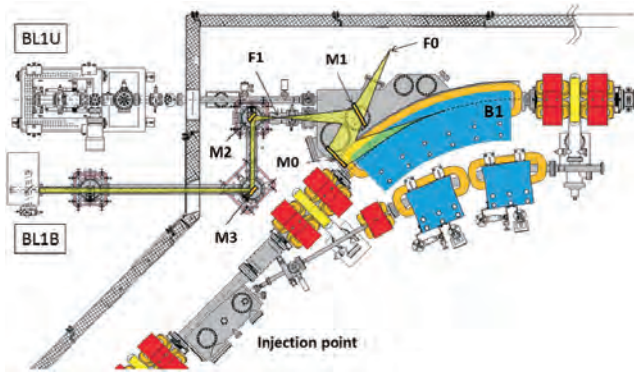

Fig. 1. Schematic top view of the beam extraction part of the THz-CSR beamline, BL1B. The three-dimensional magic mirror (3D-MM, M0) and a plane mirror (M1) are located in the bending-magnet chamber. A parabolic mirror (M2) is installed to form a parallel beam. The straight section (BL1U) is used for coherent harmonic generation (CHG) in the VUV region.

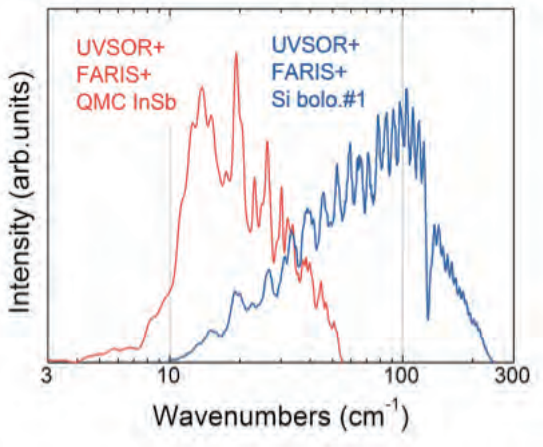

Fig. 2. Obtained intensity spectra with the combination of a light source (UVSOR), interferometer (FARIS-1), and detectors (Si bolometer and InSb hot-electron bolometer).

▼Technical Data

Interferometer	Martin-Puplett (JASCO FARIS-1)
Wavenumber range (Energy range)	4-240 cm^{-1} (500 μeV-30 meV)
Resolution in cm^{-1}	0.25 cm^{-1}
Experiments	Reflection/transmission spectroscopy
Miscellaneous	Users can use their experimental system in this beamline.

BL2A

Soft X-Ray Beamline for Photoabsorption Spectroscopy

▼Description

BL2A, which was moved its previous location as BL1A in 2011, is a soft X-ray beamline for photoabsorption spectroscopy. The beamline is equipped with a focusing premirror and a double-crystal monochromator [1]. The monochromator serves soft X-rays in the energy region from 585 to 4000 eV using several types of single crystals, such as β-Al_2O_3, beryl, KTP ($KTiOPO_4$), quartz, InSb, and Ge. The throughput spectra measured using a Si photodiode (AXUV-100, IRD Inc.) are shown in Fig. 1. The typical energy resolution (E / ΔE) of the monochromator is approximately 1500 for beryl and InSb. There are no experimental setups that are specific to this beamline, except for a small vacuum chamber equipped with an electron multiplier (EM) detector. Photoabsorption spectra for powdery samples are usually measured in total electron yield mode, with the use of the EM detector.

[1] Hiraya *et al.*, Rev. Sci. Instrum. **63** (1992) 1264.

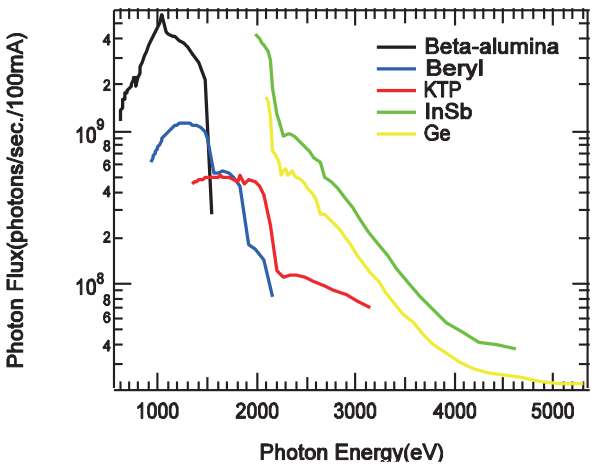

Fig. 1. Throughput spectra of the double-crystal monochromator at BL2A.

Fig. 2. Side view of BL2A.

▼Technical Data

Monochromator	Double crystal monochromator
Monochromator crystals: (2d value, energy range)	β-Al_2O_3 (22.53 Å, 585–1609 eV), beryl (15.965 Å, 826–2271 eV), KTP (10.95 Å, 1205–3310 eV), quartz (8.512 Å, 1550–4000 eV), InSb (7.481 Å, 1764–4000 eV), Ge (6.532 Å, 2094–4000 eV)
Resolution	E/ΔE = 1500 for beryl and InSb
Experiments	Photoabsorption spectroscopy

BL2B
Photoelectron spectroscopy of molecular solids

▼Description

This beamline previously dedicated for experiments in the field of gas phase photoionization and reaction dynamics. Then, the beamline has been reconstructed for photoelectron spectroscopy of molecular solids with a new end station, and experiments can be performed from May 2014. The monochromator is a spherical grating Dragon type with 18-m focal length. High throughput (1×10^{10} photons s^{-1}) and high resolution ($E/\Delta E$ = 2000 - 8000) are achieved simultaneously under the condition of the ring current of 100 mA [1]. The optical system consists of two pre-focusing mirrors, an entrance slit, three spherical gratings (G1 - G3), two folding mirrors, a movable exit slit, and a refocusing mirror [2]. The monochromator is designed to cover the energy range of 23–205 eV with the three gratings: G1 (2400 lines mm^{-1}, R = 18 m) at 80–205 eV; G2 (1200 lines mm^{-1}, R = 18 m) at 40–100 eV; G3 (2400 lines mm^{-1}, R = 9.25 m) at 23–50 eV. The percentage of the second-order light contamination at $h\nu$ = 45.6 eV is 23% for G2 or 7% for G3.

A UHV chamber is placed downstream of the refocusing mirror chamber and equipped silicon photodiode, sapphire plate Au mesh and filters for absolute photon flux measurement, monitor the photon-beam position, relative photon flux measurements and attenuate higher order light, respectively.

The new end station consists of a main chamber with a hemispherical analyzer (SCIENTA R3000) and a liquid-He-cooled cryostat (temperature range of 15-400 K) with 5-axis stage, a sample preparation chamber with a fast-entry load-lock chamber and a cleaning chamber with LEED, ion gun for sputtering and IR heating unit.

[1] M. Ono, H. Yoshida, H. Hattori and K. Mitsuke, Nucl. Instrum. Meth. Phys. Res. A **467-468** (2001) 577.
[2] H. Yoshida and K. Mitsuke, J. Synchrotron Radiation **5** (1998) 774.

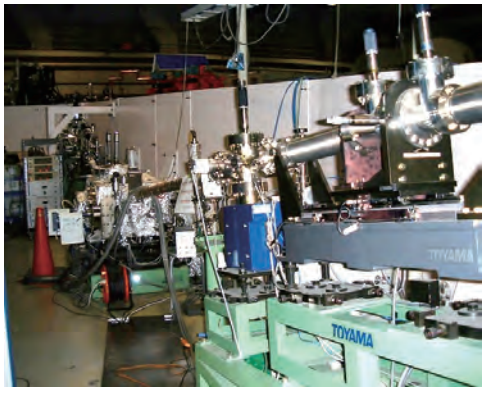

Fig. 1. 18 m spherical grating monochromator at BL2B.

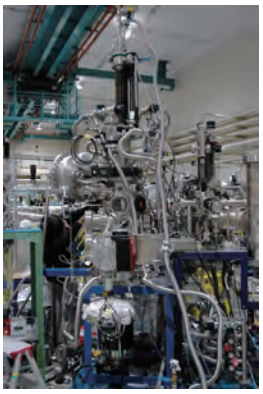

Fig. 2. End station of BL2B for photoelectron spectroscopy of molecular solids.

▼Technical Data

Monochromator	18 m spherical grating Dragon-type
Wavelength Range	23-205 eV
Resolution	2000–8000 depending on the gratings
Experiments	Angle-resolved ultraviolet photoemission spectroscopy

BL3U

Varied-Line-Spacing Plane Grating Monochromator for Molecular Soft X-Ray Spectroscopy

▼Description

The beamline BL3U is equipped with an in-vacuum undulator composed of 50 periods of 3.8 cm period length. The emitted photons are monochromatized by the varied-line-spacing plane grating monochromator (VLS-PGM) designed for various spectroscopic investigations in the soft X-ray range including soft X-ray emission studies. Three holographically ruled laminar profile plane gratings are designed to cover the photon energy range from 60 to 800 eV. The beamline has two endstations, namely, XES setup and multi-purpose setup. The XES setup is used for soft X-ray emission spectroscopy. The beam is horizontally focused onto the sample position by a plane-elliptical mirror, M2X. In the multi-purpose setup, the beam is focused by the toroidal mirror M2. Between the sample position and M2, the differential pumping is placed.

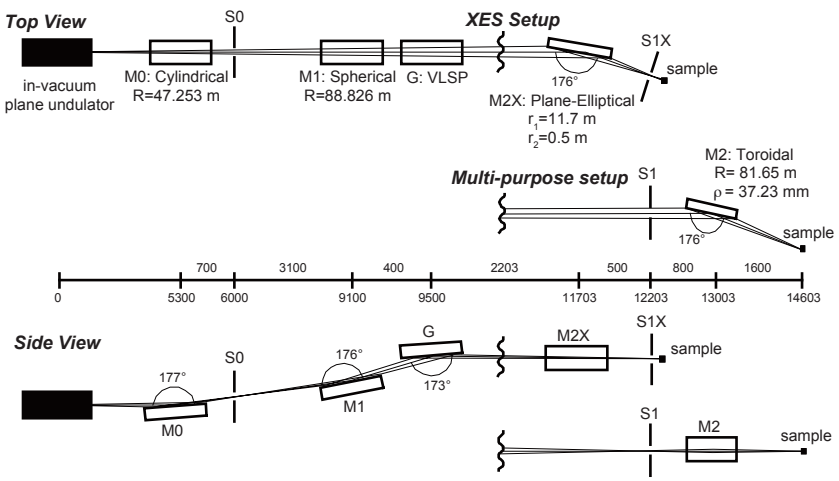

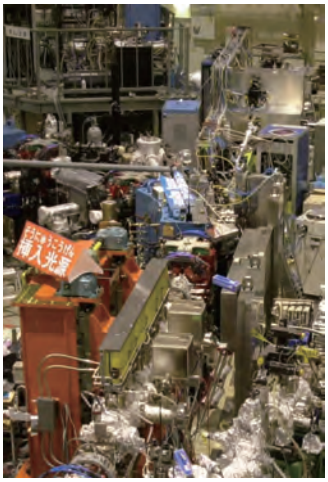

Fig. 1. Schematic layout (left) and the photography (right) of the BL3U. The distances along the beam from the center of the in-vacuum plane undulator are shown in millimeters. S1X and M2X can be replaced with the other exit slit S1 so that experiments can be carried out at either the XES or the multipurpose endstation. In the XES setup, the sample is placed 5–10 mm downstream of S1X.

▼Technical Data

Monochromator	Varied-line-spacing plane grating monochromator
Energy Range	60-800 eV
Resolution	$E / \Delta E > 10\,000$
Experiments	Soft X-ray spectroscopy (XPS, XES, XAS)
Beam Size (XES Endstation)	Gaussian shape Vertical 5-20 μm; Horizontal 41 μm (FWHM)

BL3B (HOTRLU)

VIS-VUV Photoluminescence and Reflection/Absorption Spectroscopy

▼Description

BL3B has been constructed to study photoluminescence (PL) in the visible (VIS) to vacuum ultraviolet (VUV) region. This beamline consists of a 2.5 m off-plane Eagle type normal-incidence monochromator, which covers the VUV, UV, and VIS regions, i.e., the energy (wavelength) region of 1.7-31 eV (40-730 nm), with three spherical gratings having constant grooving densities of 1200, 600, and 300 l/mm optimized at the photon energies of ~20, ~16, and ~6 eV, respectively. The schematic side view and top view layouts are shown in Figs. 1(a) and 1(b), respectively. The FWHM of the beam spot at the sample position is 0.25 mm (V) × 0.75 mm (H). Low energy pass filters (LiF, quartz, WG32, OG53) can be inserted automatically to maintain the optical purity in the G3 (300 l/mm) grating region (1.7~11.8 eV). Figure 2 shows the throughput spectra (photon numbers at a beam current of 300 mA) for each grating with entrance and exit slit openings of 0.1 mm (resolving power E / ΔE of ~2000 (G3, ~6.8 eV)). Since both slits can be opened up to 0.5 mm, a monochromatized photon flux of 10^{10} photons/s or higher is available for PL measurements in the whole energy region.

The end station is equipped with a liquid-helium-flow type cryostat for sample cooling and two detectors; one of which is a photomultiplier with sodium salicylate and the other a Si photodiode for reflection/absorption measurement. For the PL measurements in the wide energy region from VIS to VUV, two PL monochromators, comprising not only a conventional VIS monochromator but also a VUV monochromator with a CCD detector, are installed at the end station.

[1] K. Fukui, R. Ikematsu, Y. Imoto, M. Kitaura, K. Nakagawa, T. Ejima, E. Nakamura, M. Sakai, M. Hasumoto snd S. Kimura, J. Sync. Rad. **21** (2014) 452.

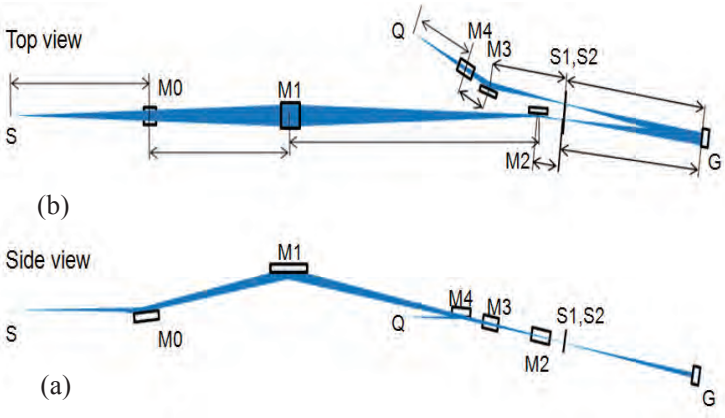

Fig. 1. Schematic layout of the BL3B (a) side view and (b) top view.

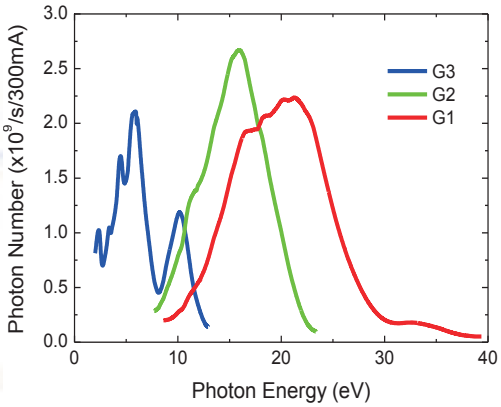

Fig. 2. Throughput spectra for each grating (G1:1200 l/mm, G2:600 l/mm and G3:300 l/mm) with S1 = S2 = 0.1 mm.

▼Technical Data

Monochromator	-2.5 m normal-incidence monochromator
Energy range	1.7-31 eV (40~730 nm)
Resolution (Δhν/ hν)	≥ 12000 (at ~ 6.9 eV, 0.02 mm slits, G1 (1200 l/mm)
Experiments	Photoluminescence, reflection, and absorption spectroscopy, mainly for solids

BL4U

Scanning Transmission X-ray Microscopy in the Soft X-ray Region

▼Description

In the soft x-ray region, there are several absorption edges of light elements and transition metals. The near edge X-ray absorption fine structure (NEXAFS) brings detailed information about the chemical state of target elements. A scanning transmission X-ray microscope (STXM) in the soft X-ray region is a kind of extended technique of the NEXAFS with high spatial resolution. The STXM has a capability of several additional options, for example, in-situ observations, 3-dimensional observation by computed tomography and ptychography, by utilizing the characteristics of the X-rays. The STXM can be applied to several sciences, such as polymer science, material science, cell biology, environmental science, and so on.

This beamline equips an in-vacuum undulator, a varied-line-spacing plane grating monochromator and a fixed exit slit. The soft X-ray energy range from 130 to 770 eV with the resolving power (E/ΔE) of 6,000 is available. The aperture size of the fixed exit slit determines not only the resolving power but also the size of a microprobe. A Fresnel zone plate is used as a focusing optical device through an order select aperture and its focal spot size of ~30 nm is available at minimum. An image is acquired by detecting intensities of the transmitted X-rays by a photomultiplier tube with scintillator with scanning a sample 2-dimensionally. By changing the energy of the incident beam, each 2-dimensional NEXAFS image is stacked. A main chamber of STXM is separated from the beamline optics by a silicon nitride membrane of 100-nm thickness; therefore, sample folders can be handled in vacuum or in helium.

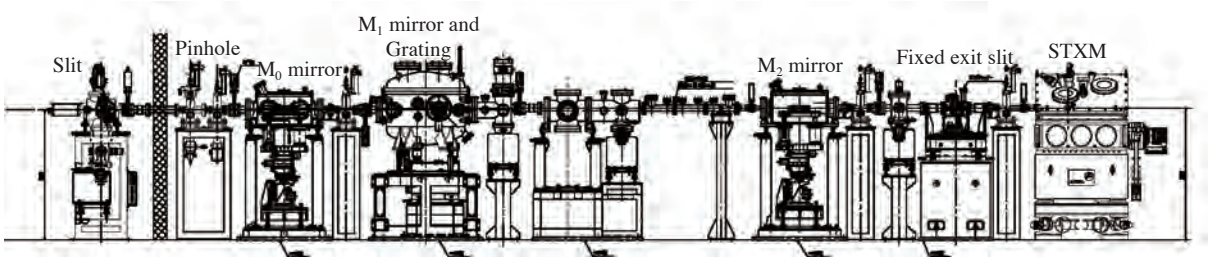

Fig. 1. Schematic image of BL4U

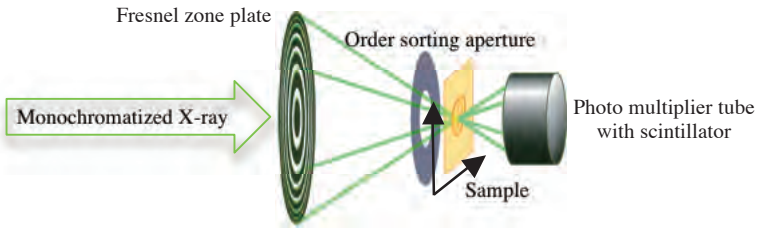

Fig. 2. Schematic image of the STXM

▼Technical Data

Energy range (E)	150 -770 eV
Resolving power (E/ΔE)	~6000
Focusing optical element	Fresnel zone plate
Spatial resolution	~30 nm
Experiments	2-dimensinal absorption spectroscopy
Measurement environment	standard sample folder in vacuum or in helium, specially designed sample cell in ambient condition

BL4B

Varied-Line-Spacing Plane Grating Monochromator for Molecular Soft X-Ray Spectroscopy

▼Description

The beamline BL4B equipped with a varied-line-spacing plane grating monochromator (VLS-PGM) was constructed for various spectroscopic investigations in a gas phase and/or on solids in the soft X-ray range. Three holographically ruled laminar profile plane gratings with SiO_2 substrates are designed to cover the photon energy range from 25 to 800 eV. The gratings with groove densities of 100, 267, and 800 l/mm cover the spectral ranges of 25–100, 60–300, and 200-1000 eV, respectively, and are interchangeable without breaking the vacuum. Figure 1 shows the absolute photon flux for each grating measured using a Si photodiode (IRD Inc.), with the entrance- and exit-slit openings set at 50 and 50 μm, respectively. The maximum resolving power ($E/\Delta E$) achieved for each grating exceeds 5000.

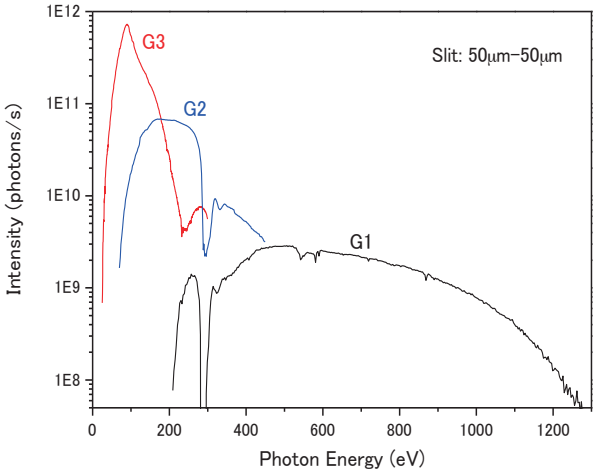

Fig. 1. Throughput from the VLS-PGM monochromator on BL4B.

Fig. 2. Photo of BL4B.

▼Technical Data

Monochromator	Varied-line-spacing Plane Grating Monochromator
Energy range	25-1000 eV
Resolution	E / ΔE > 5000 (at maximum)
Experiments	Soft X-ray spectroscopy (mainly, angle-resolved photoion spectroscopy for gaseous targets and photoelectron spectroscopy for gaseous and solid targets)

BL5U

Photoemission Spectroscopy of Solids and Surfaces

▼Description

This beamline is designed for high-resolution angle-resolved photoemission study of solids and surfaces with horizontal-linearly and circularly (CW, CCW) polarized synchrotron radiation from a helical undulator. The beamline consists of a Spherical Grating Monochromator with a Translational and Rotational Assembly Including a Normal incidence mount (SGM-TRAIN) and a high-resolution angle-resolved photoemission spectrometer.

The SGM-TRAIN is an improved version of a constant-length SGM that aims at realizing the following points: (1) covering the wide energy range of 5–250 eV, (2) high energy resolving power, (3) use of linearly and circularly polarized undulator light, (4) reduction of higher-order light, and (5) two driving modes (rotation and translation of gratings) by computer control. The second-order light is well suppressed using laminar profile gratings and combinations of mirrors and gratings. This beamline will be totally upgraded after Jan 2014.

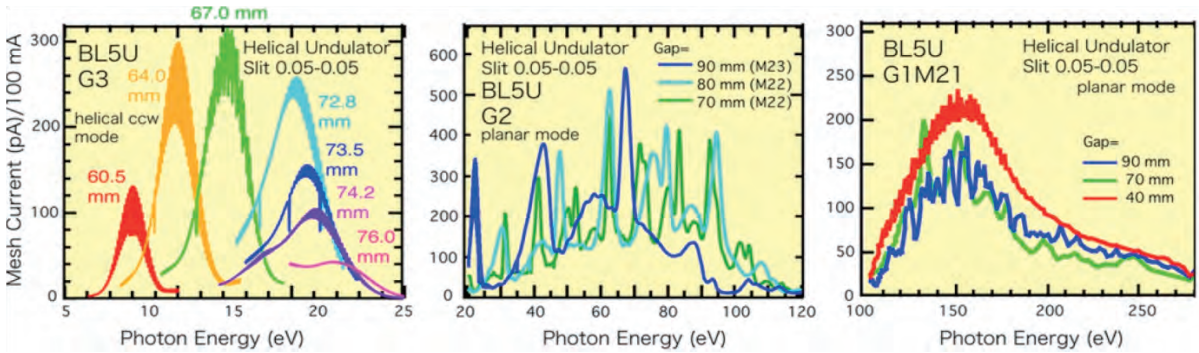

Fig. 1. Throughput spectra from the SGM-TRAIN monochromator at BL5U.

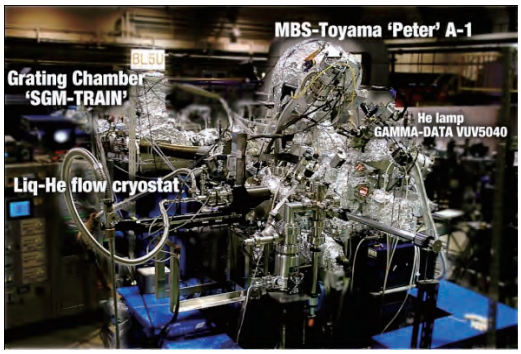

Fig. 2. High-resolution angle-resolved photoemission apparatus at BL5U.

▼Technical Data

Monochromator	SGM-TRAIN
Energy Range	5-250 eV
Resolution	$h\nu$ / ΔE > 2,000 for < 40 μm slits
Experiment	ARPES, AIPES, XAS
Flux	$<10^{11}$ photons/s for <40 μm slits (in the sample position)
Main Instruments	Hemispherical photoelectron analyzer (MBS-Toyama 'Peter' A-1), LEED of reverse type (OMICRON), Liq-He flow cryostat (5-400 K)

BL5B

Calibration Apparatus for Optical Elements and Detectors

▼Description

BL5B has been constructed to perform calibration measurements for optical elements and detectors. This beamline is composed of a plane grating monochromator (PGM) and three endstations in tandem. The most upstream station is used for the calibration measurements of optical elements, the middle one for optical measurements for solids, and the last for photo-stimulated desorption experiments. The experimental chamber at the most downstream station is sometimes changed to a chamber for photoemission spectroscopy. The calibration chamber shown in Fig. 2 is equipped with a goniometer for the characterization of optical elements, which has six degrees of freedom, X-Y translation of a sample, and interchanging of samples and filters. These are driven by pulse motors in vacuum. Because the polarization of synchrotron radiation is essential for such measurements, the rotation axis can be made in either the horizontal or vertical direction (s- or p-polarization).

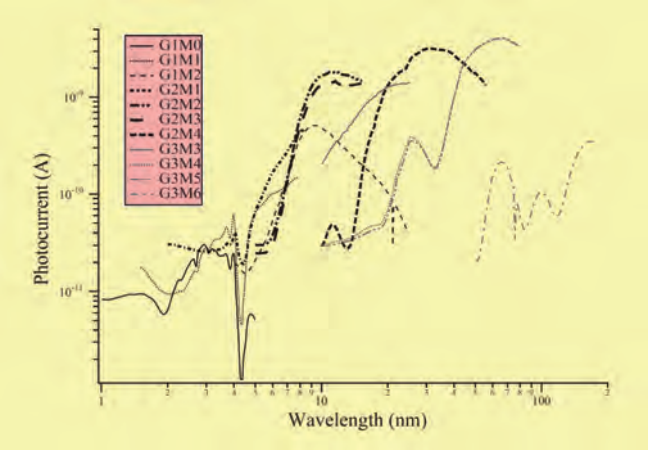

Fig. 1. Throughput spectra for possible combinations of gratings and mirrors at BL5B measured by a gold mesh.

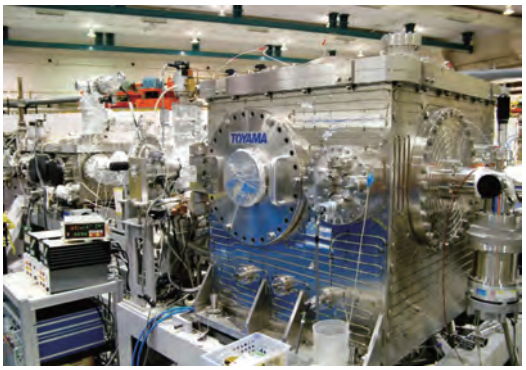

Fig. 2. A side view of the experimental chamber for calibration measurements.

▼Technical Data

Monochromator	Plane Grating Monochromator
Energy range	6-600 eV (2-200 nm)
Resolution	E / ΔE~500
Experiments	Calibration of optical elements, absorption of solids, photo-stimulated desorption from rare-gas solids

BL6U

Variable-Included-Angle VLS-PGM for Molecular Soft X-Ray Spectroscopy

▼Description

The beamline BL6U equipped with a variable-included-angle Monk-Gillieson mounting monochromator with a varied-line-spacing plane grating was constructed for various spectroscopic investigations requiring high-brilliance soft X-rays in a gas phase and/or on solids. Through a combination of undulator radiation and sophisticated monochromator design (entrance slit-less configuration and variable-included-angle mechanism), using a single grating, the monochromator can cover the photon energy ranging from 30 to 500 eV, with resolving power of greater than 10000 and photon flux of more than 10^{10} photons/s. Figure 1 shows an example of the monochromator throughput spectra measured using a Si photodiode, with the exit-slit opening set at 30 μm, which corresponds to the theoretical resolving power of 10000 at 80 eV.

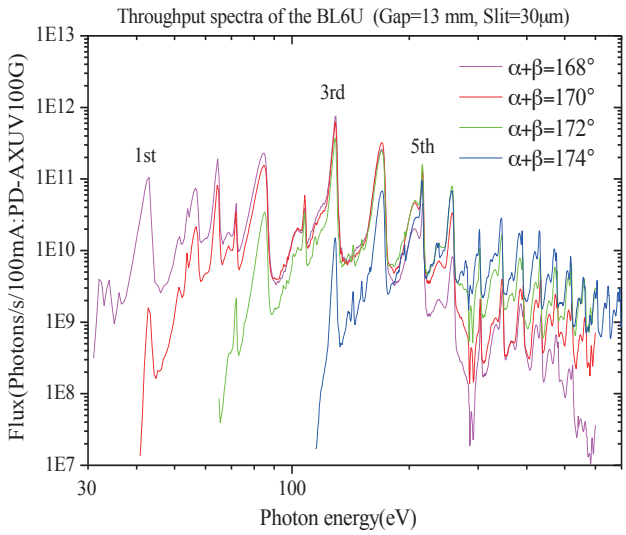

Fig. 1. Throughput spectra of the BL6U monochromator at various included angles.

Fig. 2. Photo of BL6U

▼Technical Data

Monochromator	Variable-included-angle Varied-line-spacing Plane Grating Monochromator
Energy range	40-500 eV
Resolution	$E / \Delta E > 10000$ (at maximum)
Experiments	High-resolution soft X-ray spectroscopy (mainly photoelectron spectroscopy for gaseous and solid targets)

BL6B

Infrared and Terahertz Spectroscopy of Solids

▼Description

Synchrotron radiation (SR) has good performance (high brilliance and high flux) not only in the VUV and soft X-ray (SX) regions but also in the infrared (IR) and THz regions. BL6B covers the IR and THz regions. The previous beamline, BL6A1, which was constructed in 1985, was the pioneer in IRSR research. The beamline was deactivated at the end of FY2003 and a new IR/THz beamline, BL6B (IR), was constructed in FY2004. The front-end part including bending duct #6 was replaced with a new part having a higher acceptance angle (215 (H) × 80 (V) mrad^2) using a magic mirror, as shown in Fig. 1 [1].

The beamline is equipped with a Michelson type (Bruker Vertex70v) interferometer to cover a wide spectral region from 30 to 20,000 cm^{-1} ($h\nu$ = 4 meV-2.5 eV), as shown in Fig. 2. There are two end-stations; one for reflection/absorption spectroscopy (RAS) of large samples (up to several mm) and the other for IR/THz microscopy (transmission microscopy: TM) of tiny samples (up to several tens of m). At the RAS end-station, a liquid-helium-flow type cryostat with a minimum temperature of 10 K is installed. At the TM end-station, pressure- and temperature-dependent THz spectroscopy can be performed. A superconducting magnet with a maximum field of 6 T can be installed by the exchange with the TM end-station.

[1] S. Kimura, E. Nakamura, T. Nishi, Y. Sakurai, K. Hayashi, J. Yamazaki, M. Katoh, "Infrared and terahertz spectromicroscopy beam line BL6B(IR) at UVSOR-II," Infrared Phys. Tech. **49** (2006) 147.

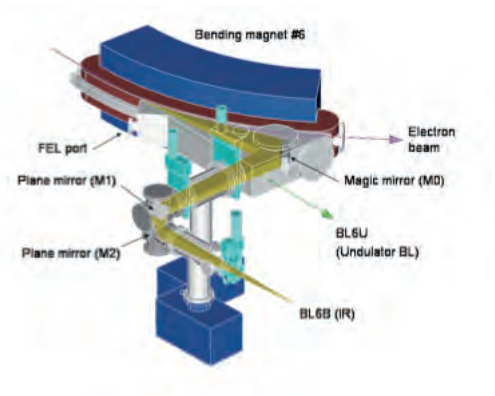

Fig. 1. Design of the optics and front end of BL6B.

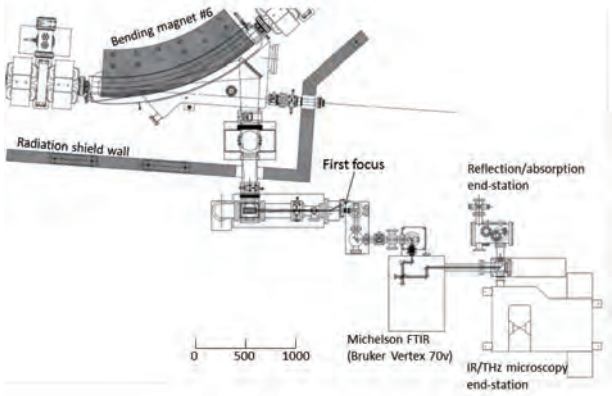

Fig. 2. Schematic top view of BL6B.

▼Technical Data

Interferometer	Michelson (Bruker Vertex70v)
Wavenumber Range (Energy range)	30-20,000 cm^{-1} (4 meV-2.5 eV)
Resolution in cm^{-1}	0.1cm^{-1}
Experiments	Reflectivity and transmission Microspectroscopy Magneto-optics
Miscellaneous	Users can use their experimental system in this beamline.

BL7U (SAMRAI)

Angle-Resolved Photoemission of Solids in the VUV Region

▼Description

Beamline 7U, named the Symmetry- And Momentum-Resolved electronic structure Analysis Instrument (SAMRAI) for functional materials, was constructed to provide a photon flux with high energy resolution and high flux mainly for high-resolution angle-resolved photoemission spectroscopy of solids [1]. An APPLE-II-type variable-polarization undulator is installed as the light source. The undulator can produce intense VUV light with horizontal/vertical linear and right/left circular polarization. The undulator light is monochromatized by a modified Wadsworth type monochromator with three gratings (10 m radius; 1200, 2400, and 3600 lines/mm optimized at $h\nu$ = 10, 20, and 33 eV). The energy resolution of the light ($h\nu$ / $\Delta h\nu$) is more than 10^4 with a photon flux of 10^{11}-10^{12} ph/s or higher on samples in the entire energy region.

The beamline has a photoemission end-station equipped with a 200 mm-radius hemispherical photoelectron analyzer (MB Scientific AB, A-l analyzer) with a wide-angle electron lens and a liquid-helium-cooled cryostat with 6-axis pulse motor control (AVC Co., Ltd., i-GONIO). The main function of the beamline is to determine the three-dimensional Fermi surface and electronic structure of solids at low temperatures and their temperature dependence in order to reveal the origin of their physical properties.

[1] S. Kimura, T. Ito, M. Sakai, E. Nakamura, N. Kondo, K. Hayashi, T. Horigome, M. Hosaka, M. Katoh, T. Goto, T. Ejima, K. Soda, "SAMRAI: A variably polarized angle-resolved photoemission beamline in the VUV region at UVSOR-II," Rev. Sci. Instrum. **81** (2010) 053104.

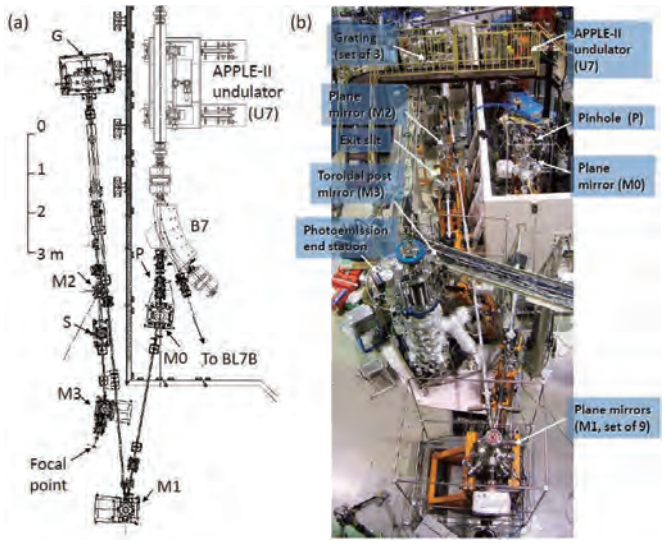

Fig. 1. Layout (a) and photograph (b) of the SAMRAI beamline consisting of an APPLE-II type undulator (U7), a modified Wadsworth type monochromator (M0-S), and a high-resolution photoemission analyzer at the focal point. The monochromator has five major optical components: two plane mirrors (M0 and M1) with water cooling, one set of three spherical gratings (G), an exit slit (S), and one toroidal refocusing mirror (M3). The spherical gratings have a radius of 10 m and are located 22 m from the center of the undulator. There is no entrance slit. S is located 6.47 m from G. A second branch for a VUV microscope end-station is planned to be constructed after the plane mirror (M2) located between G and S.

▼Technical Data

Light source	APPLE-II type undulator (λ_u = 76 mm, N = 36) vertical/horizontal linear, right/left circular
Monochromator	10 m normal-incidence monochromator (modified Wadsworth type)
Photon energy range	6~40 eV (λ = 30~200 nm)
Resolution ($h\nu/\Delta h\nu$)	1×10^4-5×10^4
Photon flux on sample	≥ 10^{12}-10^{11} ph/s (depending on $h\nu$)
Beam size on sample	200 (H) × 50 (V) μm^2
Experiments	Angle-resolved photoemission of solids (MB Scientific A-1 analyzer, acceptance angle: ± 18 deg)

BL7B

3 m Normal-Incidence Monochromator for Solid-State Spectroscopy

▼Description

BL7B has been constructed to provide sufficiently high resolution for conventional solid-state spectroscopy, sufficient intensity for luminescence measurements, wide wavelength coverage for Kramers–Kronig analyses, and minimum deformation to the polarization characteristic of incident synchrotron radiation. This beamline consists of a 3-m normal incidence monochromator, which covers the vacuum ultraviolet, ultraviolet, visible, and infrared, i.e., the wavelength region of 40–1000 nm, with three gratings (1200, 600, and 300 l/mm). Two interchangeable refocusing mirrors provide two different focusing positions. For the mirror with the longer focal length, an LiF or a MgF_2 window valve can be installed between the end valve of the beamline and the focusing position. Figure 1 shows the absolute photon intensity for each grating with the entrance and exit slit openings of 0.5 mm. A silicon photodiode (AXUV-100, IRD Inc.) was utilized to measure the photon intensity and the absolute photon flux was estimated, taking the quantum efficiency of the photodiode into account.

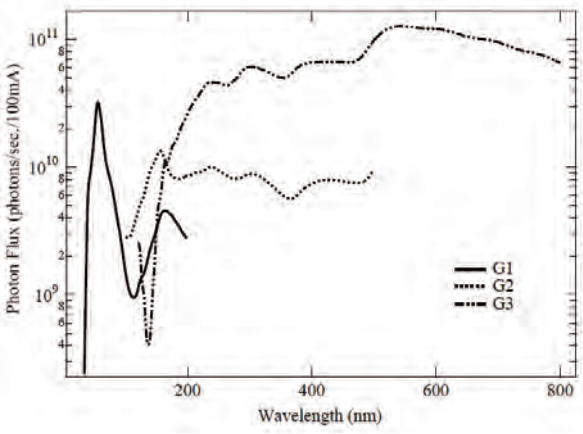

Fig. 1. Throughput spectra of BL7B measured using a silicon photodiode.

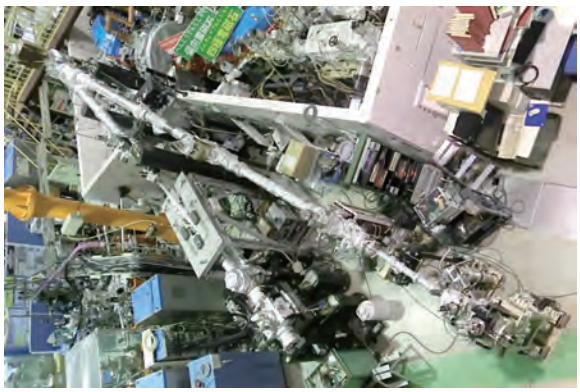

Fig. 2. Photo of BL7B.

▼Technical Data

Monochromator	3 m Normal-Incidence Monochromator
Wavelength Range	50-1000 nm (1.2-25 eV)
Resolution	$E / \Delta E$ = 4000-8000 for 0.01 mm slits
Experiments	Absorption, reflection, and fluorescence spectroscopy, mainly for solids

BL8B

Angle-Resolved Ultraviolet Photoelectron Spectrometer for Solids

▼Description

BL8B is a beamline for the angle-resolved ultraviolet photoemission spectroscopy (ARUPS) system, which is designed to measure various organic solids such as molecular crystals, organic semiconductors, and conducting polymers. This beamline consists of a plane-grating monochromator (PGM), a sample preparation chamber with a fast-entry load-lock chamber, a measurement chamber (base pressure 1×10^{-10} Torr), a cleaning chamber (base pressure 1×10^{-10} Torr), and a sample evaporation chamber (base pressure 3×10^{-10} Torr). The cleaning chamber is equipped with a back-view LEED/AUGER, an ion gun for Ar^+ sputtering, and an infrared heating unit. The PGM consists of premirrors, a plane grating, focusing mirror, and a post-mirror, with an exit slit. It covers the wide range from 2 to 130 eV with two exchanging gratings (G1: 1200 l/mm, G2: 450 l/mm) and five cylindrical mirrors. The toroidal mirror focuses the divergent radiation onto the sample in the measurement chamber. The spot size of the zeroth-order visible light at the sample surface is approximately 1×1 mm^2. Figure 1 shows the throughput spectra of PGM (slit = 100 μm). The energy resolution at a slit width of 100 μm was found to be $E/\Delta E$ = 1000 in the wavelength range from 2 to 130 eV. A hemispherical electron energy analyzer of 75 mm mean radius with an angular resolution less than 2° can be rotated around the vertical and horizontal axes. The sample mounted on a manipulator (temperature range 14–320 K) can also be rotated around two axes.

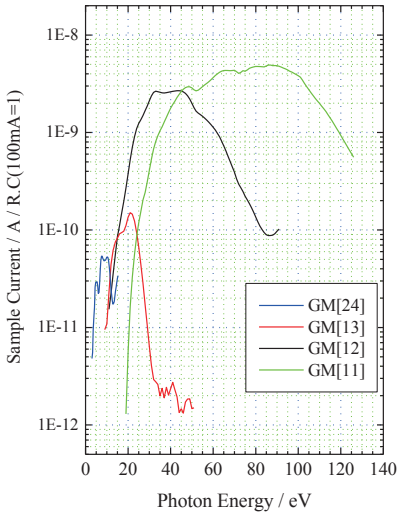

Fig. 1. Throughput spectra of plane-grating monochromator at BL8B (slit = 100 μm).

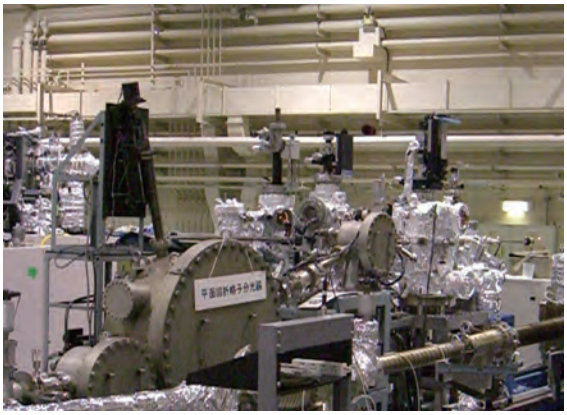

Fig. 2. A photo of BL8B.

▼Technical Data

Monochromator	Plane-grating monochromator
Wavelength Range	9-600 nm
Resolution	E / ΔE = 1000
Experiments	Angle-resolved ultraviolet photoemission spectroscopy

UVSOR User 1

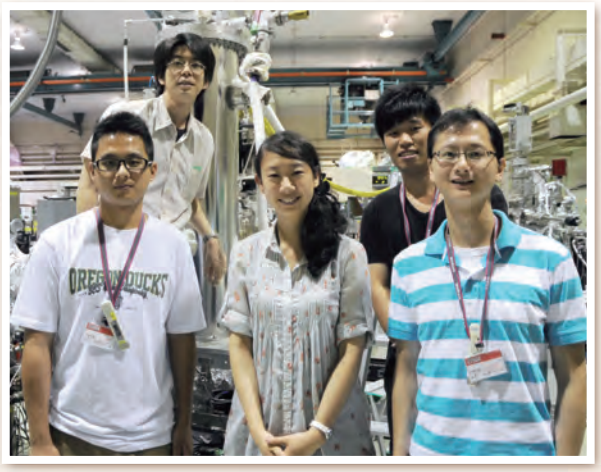

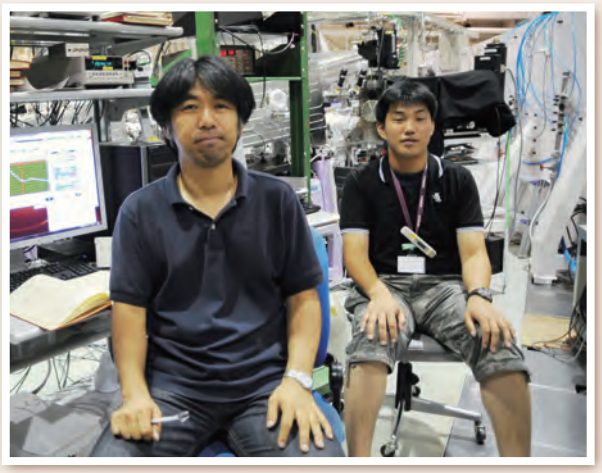

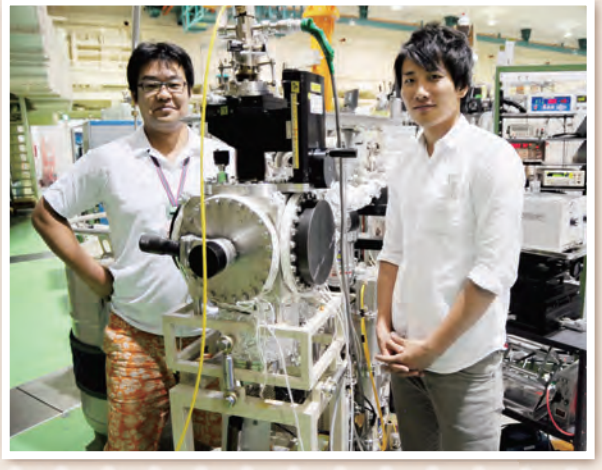

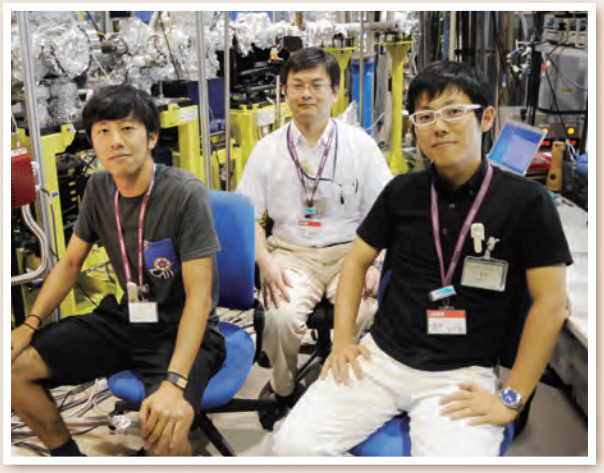

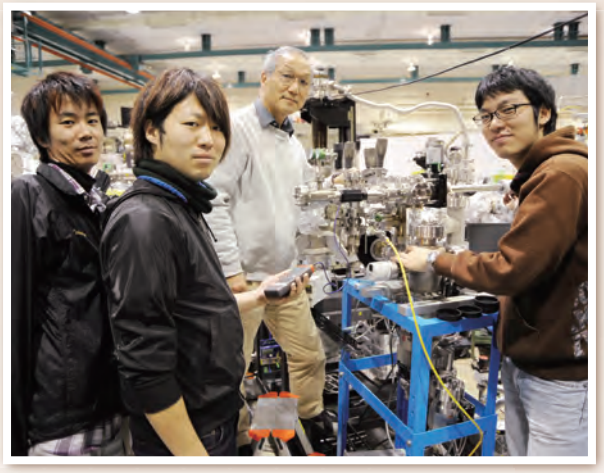

III-1

Accelerators and Instruments

Light sources

Development of 90° Bend-Type Spin-Rotator for Inverse Photoemission Spectroscopy

Y. Kajiura [1], T. Inagaki [1,3], N. Yamamoto [1,2], M. Hosaka [2], A. Mano [2], Y. Takashima [1,2], T. Konomi [3] and M. Katoh [2,3]

[1] *Graduate School of Engineering, Nagoya University, Nagoya, 464-8603*
[2] *Nagoya University Synchrotron Radiation Research Center, Nagoya, 464-8603*
[3] *UVSOR Facility, Institute for Molecular Science (IMS), Okazaki, 444-8585*

Transmission type (NEA-GaAs) spin-polarized electron sources, in which pump laser light is injected from the backside of the photocathodes and the polarized beam is extracted from the front side, have been developed. By using this type of photocathodes, the high brightness of ~2×10^7 A.cm^{-2}.sr^{-1} and the high polarization of ~90% were achieved [1, 2].

At UVSOR, we are planning to apply this type of photocathodes to the Spin-resolved Inverse Photoemission Spectroscopy. For this purpose, a compact spin rotator is needed. A spin rotator enables us to obtain arbitrary direction of electron spin. Furthermore, to suppress the degradation of beam qualities, a compact (shorter length) electron transfer system is essential. Therefore, we have designed and manufactured a compact spin rotator combined with the 90° bending function.

Arbitrary spin direction according to the beam direction is obtained by applying magnetic and electric forces simultaneously [3]. The designed spin rotator consists of in-situ spherical electrodes (curvature radius of 50mm and electric poles gap of 5mm), and a C-type bending magnet. We have designed the electro and magnetic components based on numerical calculations by using the Poisson code (2D) and Radia code (3D) [4]. The beam trajectories were also evaluated by using the GPT code.

From the electrode structure described above, the curvature radius of 50 mm and magnetic pole gap of > 48 mm were required for the bending magnet. Because the beam trajectories evaluated by using only electric or magnetic field should be equal and the vacuum chamber should be placed in the space between the magnet and the electrodes. In the simple C-type magnet case, it is difficult to satisfy the requirement for beam curvature due to the fringing field. Then we have employed two sets of return yoke and shield pole for both inject and extract sides.

As the result of the design, the spin-rotator size was decided 198mm x 175mm x 130 mm (W, D, H). Based on the numerical designs, we manufactured the bending magnet and the vacuum chamber (Fig.1). The magnetic coil parameters were decided in the consideration of wire-heating and current accuracy. The coil consists of 30-turns electric wires and the operation current is calculated to be around 7A.

Figure 2 shows the measurement field values and it is found that the result can be reproduced the numerical calculation values with sufficient accuracy.

The beam trajectories were also evaluated from various designed fields. In the case that only the magnetic field is applied, which corresponds to the parallel spin direction mode, the maximum beam discrepancy between obtained and ideal trajectories was obtained and estimated to be + 1.04 mm. Because the acceptable discrepancy for beam transfer is ±1.8 mm, it is confirmed that the designed spin rotator has sufficient performance.

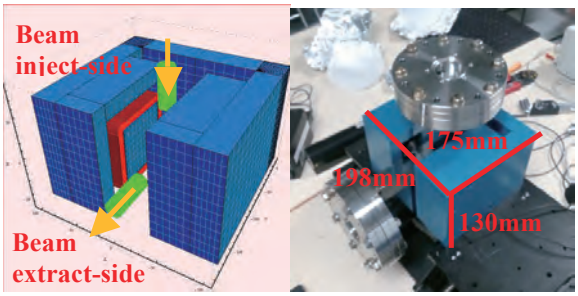

Fig. 1. 3D analysis model and fabricated spin rotator

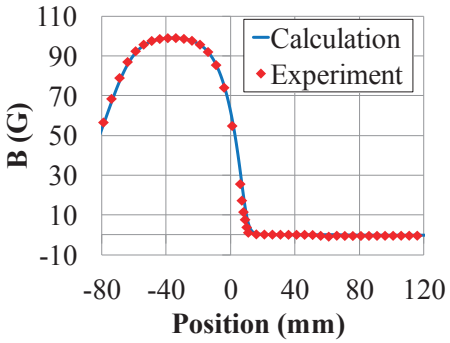

Fig. 2. Result of magnetic field measurement.

[1] N. Yamamoto, T. Nakanishi *et al*., J. Appl. Phys. **103** (2008) 064905.
[2] X. G. Jin, N. Yamamoto *et al*., Appl. Phys. Ex. **1** (2008) 045002.
[3]Andersen W. H. J., J. Appl. Phys. **18** (1967)1573.
[4]RADIA_URL: "http://www.esrf.fr/machine/support/ids/Public/Codes/software.html"

Light sources

Development of Temporal Response Measurement System for Transmission-Type Spin Polarized Photocathodes

T. Inagaki[1,2], N. Yamamoto[1], Y. Kajiura[1], T. Konomi[2], Y. Okano[3], M. Adachi[4], X. G. Jin[1], M. Hosaka[1], Y. Takashima[1] and M. Katoh[2]

[1]*Nagoya University, Nagoya 464-8601, Japan*
[2]*UVSOR Facility, Institute for Molecular Science, Okazaki 444-8585, Japan*
[3]*Laser Research Center for Molecular Science, Okazaki 444-8585, Japan*
[4]*High Energy Accelerator Research Organization (KEK), Tsukuba 305-0801, Japan*

We have developed transmission-type spin polarized photocathodes with negative electron affinity (NEA). The spin-polarized electron beam is essential for "International Linear Collider" and so on. It is also expected to be applied for "Spin-resolved Inverse Photoemission Spectroscopy" [1].

In order to measure the temporal response of photocathodes, we developed the electron pulse length measurement system with 20 kV DC gun (Fig. 1). In this system by using an rf deflecting cavity, the electron beam is kicked transversely according to the rf phase position and the longitudinal pulse structure is projected to the transverse plane. We have employed the resonance mode of TM120. The resonance frequency is 2614 MHz for the rf cavity and the resonance frequency corresponds to the multiple of RF acceleration frequency of UVSOR storage ring, so the laser can be synchronized with UVSOR accelerator is used for the pump laser [2]. Temporal response of the photocathodes is evaluated by comparing the electron pulse structure and the pump laser pulse length. The pump laser pulses are provided by a mode-locked Ti:sapphire oscillator. In the present system by using a pulse stretcher, the pulse length of the pump laser can be selected in the range between 20 ps and 45 ps (Fig. 2).

In the process of the rf cavity manufacturing, we measured the induced magnetic properties on the beam axis by bead perturbation method and it is consistent with the designed value. After the installation of the rf cavity to electron gun system, the beam deflecting test was carried out and it is found that the maximum induced field was about 1.4 G with the input rf power of 5 W. This field strength is consistent with the designed value and enough for deflecting the 20 keV electron beam.

Furthermore, we carried out the comprehensive test for our developed system with the GaAsP photocathode with thickness of 600 nm. To realize the laser transmissibility, the photocathode was fabricated on GaP substrate. As the results, 48.3 ps electron beam pulse is obtained with 40.5 ps laser pulse. Then the temporal response of this photocathode is estimated to be about 7.8 ps and we considered that this result is consistent in view of the thickness of GaAsP active layer [3].

Finally, in near future we are planning to shorten the pump laser to 1 ps by improving the pulse stretcher and we will make systematic measurement for the various transmission-type photocathodes.

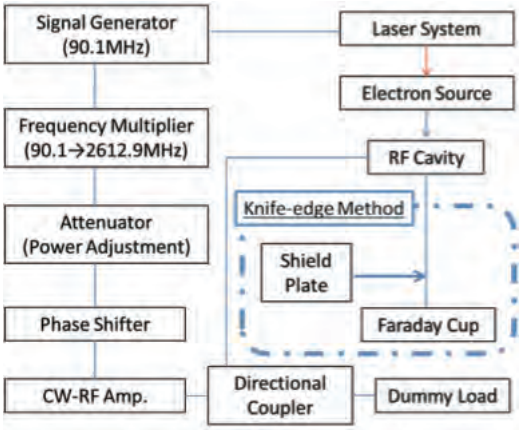

Fig. 1. Measurement system of temporal response.

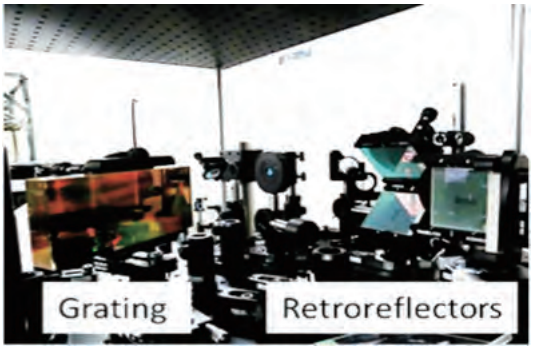

Fig. 2. Stretcher.

[1] N. Yamamoto, doctoral thesis, Nagoya University (2007).
[2] T. Niwa, master's thesis, Nagoya University (2013).
[3] X. Jin, Institute for Advanced Research, Nagoya University, Applied Physics Express 6 (2013) 015801, "High-Performance Spin-Polarized Photocathodes Using a GaAs/GaAsP Strain-Compensated Superlattice".

Light Sources

Study on Vacuum Ultraviolet Coherent Harmonic Generation Using Relativistic Electron Beam and Laser

S. Sekita[1], M. Hosaka[2], N. Yamamoto[1,2], Y. Takashima[1,2], K. Hayashi[3], J. Yamazaki[3], T. Konomi[3] and M. Katoh[3]

[1]*Graduate School of Engineering, Nagoya University, Nagoya 464-8603, Japan*
[2]*Nagoya University Synchrotron Radiation Research Center, Nagoya 464-8603, Japan*
[3]*UVSOR, Institute for Molecular Science, Myodaiji-cho, Okazaki 444-8585, Japan*

At UVSOR-III, we are developing a coherent VUV light source using coherent harmonic generation (CHG) technique. An optical klystron, consisting of two Apple-II type undulators and an electro-magnetic buncher, has been already installed in BL1U. Recently, we installed a VUV spectrometer at the U1 experimental end station and made a CHG experiment. Figure 1 shows a schematic diagram of the measurement system including the spectrometer and figure 2 shows a photograph of the actual system.

In the experiment, we employ Ti:Sa laser with 800 nm wavelength and 100 fsec pulse width as a seed light source and observe 3rd-CHG (266 nm) using the spectrometer. Figure 3 shows the measured CHG spectrum.

The measured spectral width is 2.2 nm and assuming Fourier-transform-limited pulse the pulse duration is 50 fs. The value is shorter than the incident laser pulse width. Measured CHG intensity is 30 times of the SR intensity (Fig. 4), however the value is weaker than that of the calculated one [1]. This suggests that the interaction with the laser takes place not in the whole bunch but only limited transverse region due to poor alignment between the laser and the electron bunch. In the near future, we are going to install an improved laser alignment system.

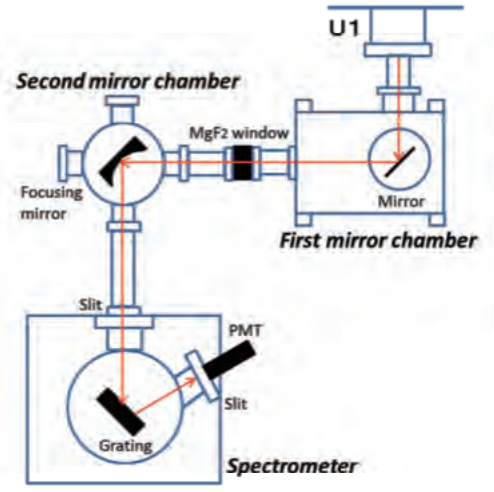

Fig. 1. Schematic of the measurement system for the CHG experiment.

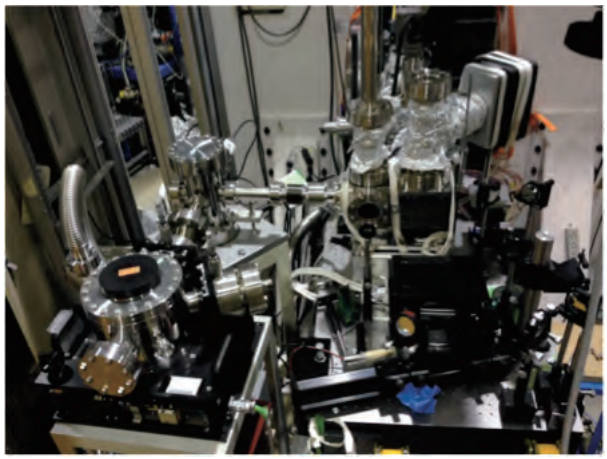

Fig. 2. Photograph of the measurement system.

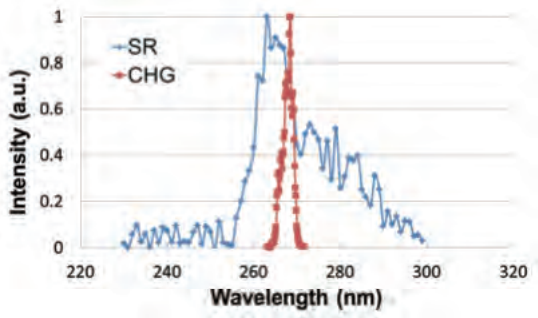

Fig. 3. Observed 3rd-CHG spectrum compared with spontaneous synchrotron radiation.

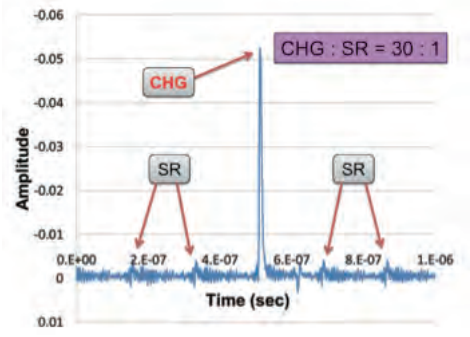

Fig. 4. Observed CHG radiation intensity

[1] S. Sekita, Master's Thesis, Nagoya University (2014).

Light Sources

Development of Deep Ultraviolet Pulse Compressor for Coherent Harmonic Generation Experiments

H. Zen[1], T. Konomi[2,3] and M. Katoh[2,3]
[1]*Institute of Advanced Energy, Kyoto University, Uji 611-0011, Japan*
[2]*UVSOR Facility, Institute for Molecular Science, Okazaki 444-8585, Japan*
[3]*The Graduate University for Advanced Studies (SOKENDAI), Okazaki 444-8585, Japan*

The Coherent Harmonic Generation (CHG) from relativistic electron beam through the Free Electron Laser (FEL) interaction with high power laser is promising way to generate short pulse EUV coherent radiation [1]. However, power saturation occurs when the incident laser pulse is too strong and it limits the number of photon in a pulse [2]. In conventional laser, Chirped Pulse Amplification (CPA) technique is commonly used for avoiding damage or power saturation and to obtain high output power. We proposed utilization of CPA to CHG technique to overcome the saturation problem [3].

We are planning to make proof of principle experiment at the wavelength of 266 nm, the 3rd harmonics of Ti-sapphire laser. For the experiment, we need a pulse duration measurement system and a DUV pulse compressor.

In this fiscal year, we have constructed a DUV pulse compressor. The schematic diagram is shown in Fig. 1. The pulse compressor consists of a DUV grating, a periscope, 500-mm linear translation stage, a roof mirror and dielectric mirrors. The group velocity dispersion (i.e. compression factor) of this compressor can be controlled by changing the position of roof mirror. Figure 2 shows the photograph of the developed compressor. In this compressor, DUV laser pulse experiences four times diffraction on the same grating.

In order to adjust the compressor and check the efficiency, DUV laser pulses (λ = 266 nm) are generated by 3rd harmonic generation of Ti-Sapphire laser using 2nd and 3rd harmonic generation crystals. After finishing the adjustment of compressor, the incident and transmitted DUV laser power were measured by a power meter (PH10I-Si-USB). As the result, the measured incident power was 470 μW and transmitted power was 120 nW. The measured efficiency or transmittance of the compressor was 2.6×10^{-4} and calculated diffraction efficiency of the grating was around 13%. The diffraction efficiency of the grating measured in manufacturer at 300 nm and Littrow configuration was around 65%. The measured diffraction efficiency was significantly lower than that. We are planning to make further investigation on the polarization and incident angle dependence of diffraction efficiency to achieve higher transmission.

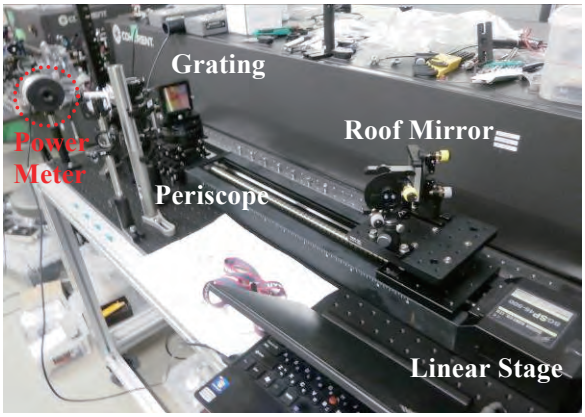

Fig. 2. Photograph of the developed pulse compressor

[1] R. Prazeres *et al.*, Nucl. Inst. Meth. A **304** (1991) 72-76.
[2] T. Tanikawa *et al.*, Appl. Phys. Exp. **3** (2010) 2702.
[3] H. Zen *et al.*, Proc. of FEL2011 (2012) 366-369.

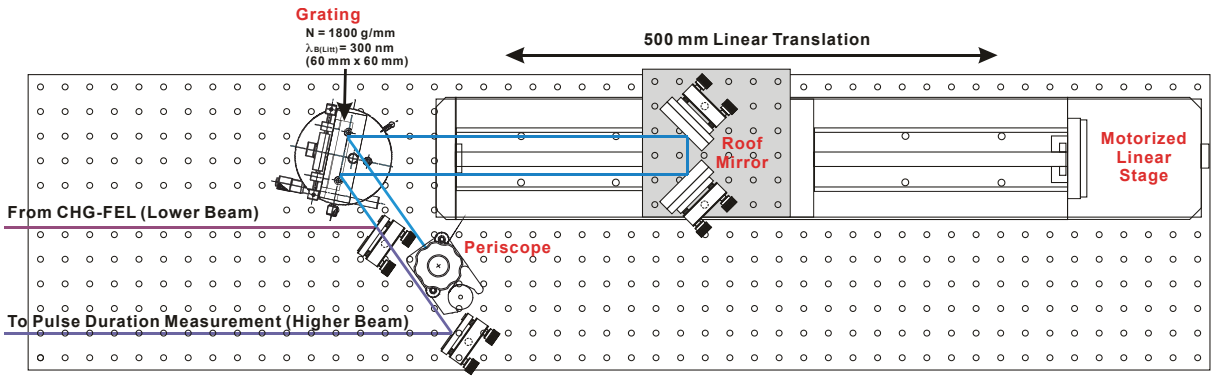

Fig. 1. Schematic drawing of pulse compressor.

Others

Performance Evaluation of New Type Nuclear Emulsion with Electron Beam

K. Ozaki[1], S. Aoki[1], K. Kamada[1], E. Shibayama[1], S. Takahashi[1], S. Tawa[1], F. Mizutani[1], H. Kawahara[2], H. Rokujo[2] and GRAINE collaboration

[1]*Department of Human Environment Science, Kobe University, Kobe 657-8501, Japan*
[2]*Graduate School of Science, Nagoya University, Nagoya, 464-8602, Japan*

We are promoting GRAINE project [1], which is balloon-borne experiment to explore the gamma-ray astrophysics with nuclear emulsion.

Nuclear emulsion is a 3-dimensional tracking detector with 0.1 μm precise position resolution. Nuclear emulsion records the track of silver grains produced by trajectory of charged particle (see Fig. 1). Self-production of new type emulsion has developed at Nagoya University since 2010. The performance evaluation of new type emulsion is presented. This work is mainly for next balloon experiment of GRAINE in 2014, Australia.

In order to control / improve the sensitivity to the charged particle, four types of emulsions which are changed the amount of silver halide were developed at Nagoya University. Emulsion films were made by coating emulsion on both side of plastic base. These films were exposed to electron beam at UVSOR to evaluate their sensitivity. After development the films, the measurement of the numbers of silver grains was done with optical microscope.

Figure 2 shows the result of measurement of Grain Density (GD: counts of silver grains per 100μm) for four types of emulsions. Development time is 25 minutes for all types. There is good correlation between GD and the amount of silver halide. GD of conventional nuclear emulsion (OPERA film [2]) is about 30, so we could succeed to improve the sensitivity by increasing the amount of silver halide. While multiple coulomb scattering increases due to the increasing the amount of silver halide, so there is trade-off.

It is also important to evaluate about characteristic of long-term preservation of new type emulsion film. In the case of GRAINE, it takes about 6 months from film production to balloon flight. This time we have evaluated about the highest silver halide type of emulsion. Films were exposed to electron beam at UVSOR just after production, and 1, 2.4, 3.8, 4.9 months after production. Preservation environment is shielded place with lead block at room temperature and humidity (about 14-20 degree and 40-60 %RH). After development the films, the measurement of GD was done with optical microscope.

Figure 3 shows the result of long-term preservation of new type emulsion film. Development time is 20 minutes mainly, but film of 3.8 months after is 25 minutes. Black and red circle means difference of measurement person. GD is almost stable after 5months. There is no problem about characteristic of long-term preservation to perform the GRAINE and other experiments.

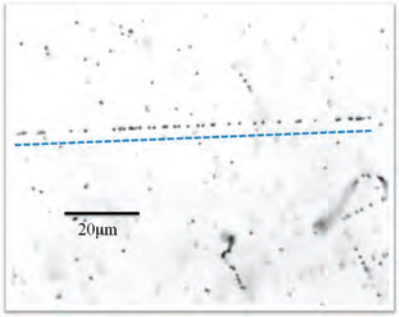

Fig. 1. Microscopic view of emulsion recorded charged track.

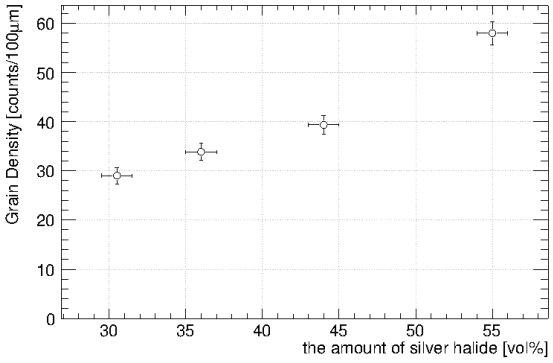

Fig. 2. The amount of silver halide dependence of Grain Density.

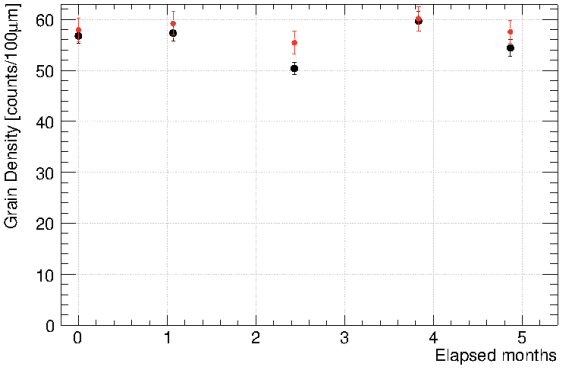

Fig. 3. Characteristic of long-term preservation of new type emulsion film.

[1] S. Aoki *et al.*, <arXiv: 1202. 2529 [astro-ph.IM]>.
[2] T. Nakamura *et al.*, Nucl. Instr. Meth. A **556** (2006) 80.

BL2B

Reconstruction of the Beamline BL2B for Development of Photoelectron Spectroscopy for Organic Materials

S. Kera[1], K. R. Koswattage[1,2], K. Yonezawa[1], J. P. Yang[1], Y. Nakayama[1], K. K. Okudaira[1] and H. Ishii[1]

[1] *Graduate School of Advanced Integration Science, Chiba 263-8522, Japan*
[2] *UVSOR Facility, Institute for Molecular Science, Okazaki 444-8585, Japan*

Electronic/optical devices based on π-conjugated molecular semiconductors have moved out of the field of the academic curiosity and are now regarded as valuable brilliant technologies as found for organic field-effect transistors and organic photovoltaics etc. However the fundamental pictures of the intrinsic electronic and optical properties are often hindered by the presence of chemical and physical imperfections, eg. chemical impurities, energetic and structural disorder. Thus, the development in the surface science technique and the availability of research stations at synchrotron facility suited for characterizing the wide range of molecular materials is desired for achieving the fundamental understanding.

The bending-magnet beamline of BL2B is developed by Prof. Mitsuke *et al.*[1,2], where the 18-m spherical grating monochromator (Dragon type) with three gratings (G1 – G3) and four mirrors (M1 – M4) to achieve a high-resolution and photon flux and had been used for gas-phase experiments. The monochromator can cover the energy range of 23-205 eV, a resolving power of 2,000-8,000 and photon flux of more than 10^{10} photons/s[2].

We started the reconstruction of the beamline for photoelectron spectroscopy of molecular solids in September 2013. In the monochromator, it is necessary to insert two plane mirrors M2 and M3 across the photon-beam between G3 grating and S2 slit in order to get precious light from G3 grating. These mirrors should be removed from the optical path when G1 or G2 grating is employed. However, there was a problem of the linear motion of the mirror system due to a deformation of a vacuum rod in between mirror and motor system. A new vacuum rod has been replaced (TOYAMA) in order to solve the malfunction of the M2 and M3 mirror system.

A UHV chamber *so called* monitoring chamber has been placed downstream of the refocusing mirror chamber. The monitoring chamber contains three linear motion feedthroughs, where a silicon photodiode for absolute photon flux measurement (AXUV-100, IRD), a sapphire plate to monitor the photon-beam position, a Au mesh of the size 100 to monitor the relative photon flux and for the beamline alignment. The third feedthrough is to equip the filters to attenuate higher order light and, at the present foil structure of Al/Mg/Al filter (LUXEL) is attached. The same chamber can be also employed for gold evaporation.

A new interlock system has been introduced to ensure the safety of users as well as prevent damage to the beamline and storage ring in case of accidents. The safety interlocks at six vacuum valves of the beam line are controlled by a system with vacuum gauge readings. There is a touch-panel display and the screen show a schematic drawing of the beamline along with vacuum valve status. Further, two power distribution units have been built for proper handling the electricity in the beam line.

A new end-station for the photoelectron spectroscopy equipped with a hemispherical analyzer (SCIENTA R3000) and a liquid-He-cooled cryostat (temperature range of 15-400 K) with 5-axis stage is transferred from Chiba Univ. The experimental chambers have been adjusted to place for the photon-beam trajectory.

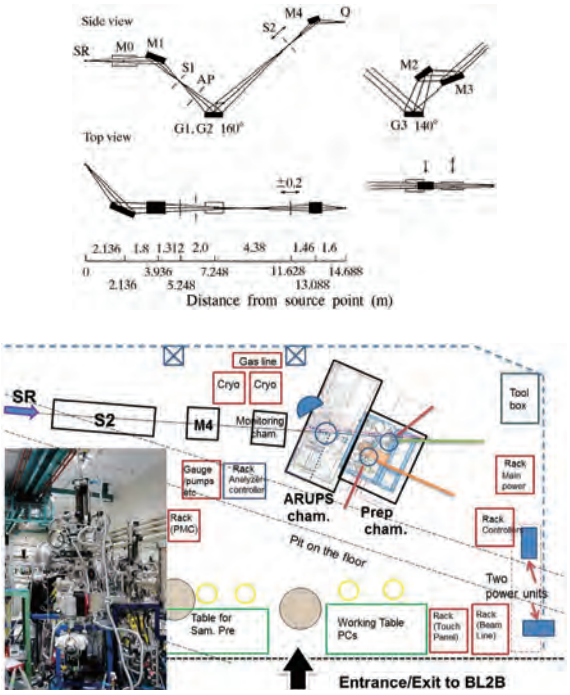

Fig. 1. (top) BL2B equipped with an 18-m SGM. Two optical paths with including angles of 160° for G1 and G2 and 140° for G3 are indicated. S2: exit slit; Q: sample point (after ref [1]). (bottom) Schematic layout of BL2B.

[1] H. Yoshida and K. Mitsuke, J. Synch. Rad. **5** (1998) 774.
[2] M. Ono, H. Yoshida and K. Mitsuke, Nucl. Instrum. Meth. Phys. Res. A **467-468** (2001) 577.

BL3B

Observation of VUV Emission from Al_2O_3 and Nd:LaF_3 Crystals

M. Kitaura[1], S. Kurosawa[2,3], J. Pejchal[2], K. Fukui[4], K. Nakagawa[5], S. Watanabe[6], A. Ohnishi[1], K. Ogasawara[6], M. Hasumoto[7] and M. Sakai[7]

[1]*Department of Physics, Faculty of Science, Yamagata University, Yamagata 990-8560, Japan*
[2]*Institute for Materials Research, Tohoku University, Sendai 980-8679, Japan*
[3]*New Industry Creation Hatchery Center, Tohoku University, Sendai 980-8679, Japan*
[4]*Department of Electrical and Electronics Engineering, University of Fukui, Fukui 910-8507, Japan*
[5]*Graduate School of Human Development and Environment, Kobe University, Kobe 657-8501, Japan*
[6]*School of Science and Technology, Kwansei University, Sanda 669-1337, Japan*
[7]*UVSOR facility, Institute for Molecular Science, Okazaki 444-8585, Japan*

Since 2011, the BL3B beamline offfers many researchers for the opportunity of spectroscopy experiment using VIS, UV and VUV photons to many researcher [1]. One of the next targets is to extent observable emission range to higher-energy side. Few VUV emission spectroscopic experiments have been performed in synchrotron radiation facilities. The SUPERLUMI station at HASYLAB in DESY was the only experimental setup for VUV emission spectroscopy; however, it still remains closed at present. We have installed the spectroscopy system consisting of two MgF_2 lenses, a CCD detector (Princeton Instruments SX-100B) and a monochromator (Acton VM-502) at the BL3B. To check whether this system works, we have measured VUV emission and excitation spectra of Al_2O_3 and Nd^{3+}-doped LaF_3 (Nd:LaF_3) crystals at 9 K. These crystals have been known to show VUV emission at low temperatures [2, 3].

Figure 1 shows the emission and excitation spectra of pure Al_2O_3 crystals. Blue squares clearly show that an emission band appears around 7.51 eV under excitation at 8.92 eV. This band is excited in the fundamental absorption band of Al_2O_3. These data are in agreement with those published previously [2], where the 7.51 eV band was attributed to the radiative annihilation of self-trapped excitons (STEs).

Emission and excitation spectra of Nd:LaF_3 crystals are shown in Fig. 2. As indicated by blue squares, a sharp emission peak is observed around 7.08 eV under excitation at 7.75 eV. The 7.08 eV band is excited in the $4f \rightarrow 5d$ absorption region of Nd^{3+} ions (red squares). This feature suggests that the 7.08 eV band is assigned to the $5d \rightarrow 4f$ transition of Nd^{3+} ions. The observed spectra are almost the same as those in Ref [3]. Another band is seen around 5.74 eV, also being assigned to the $5d \rightarrow 4f$ transition of Nd^{3+} ions.

We will install a focus mirror system the nex year to collect VUV emission more efficiently next year. This is vital for the detection of VUV emission, because the sensitivity of the detector such as PMT and CCD is relatively low in the VUV range. Furthermore, the experimental setup for the time-resolved emission and excitation spectroscopy in the wide energy range from VIS to VUV will be also installed for the investigation of photo-excited state dynamics in crystalline solids.

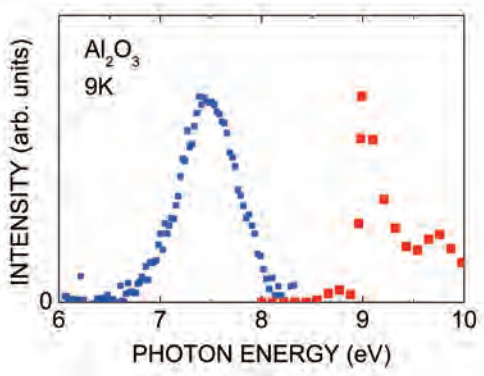

Fig. 1. Emission (blue) and excitation spectra (red) for the Al_2O_3 crystal. The emission and excitation spectra were measured at 9K for 8.92 eV excitation and 7.51 eV emission.

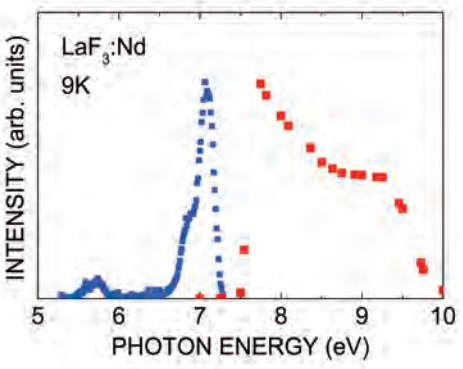

Fig. 2. Emission (blue) and excitation spectra (red) for the Nd^{3+}-doped LaF_3 crystal. The emission and excitation spectra were measured at 9K for 7.75 eV excitation and 7.08 eV emission.

[1] K. Fukui *et al.*, J. Synchrotron Rad. **21** (2014) 452.
[2] V. V. Harutunyan *et al.*, Eur. Phys. J. B **12** (1999) 35.
[3] P. Dorenbos *et al.*, J. Lumin **69** (1996) 229.

BL7B

Stokes Parameters Measured by VUV Spectral Ellipsometer

T. Saito[1], K. Ozaki[2] and K. Fukui[2]
[1]*Faculty of Engineering, Tohoku Inst. Tech., Sendai 982-8577, Japan*
[2]*Faculty of Engineering, Univ. of Fukui, Fukui 910-8507, Japan*

Ellipsometers are known as powerful tools to determine optical properties such as optical constants of thin films or bulk materials [1]. For typical ellipsometers, the photon beam entering the sample should be highly polarized or its polarization state should be characterized. Contrary to typical ellipsometers, the one developed [2] is capable to determine the photon source Stokes parameters as well as the sample optical constants.

Figure 1 shows a schematic structure of the VUV ellipsometer. Monochromatic radiation hits a sample specimen at an angle of incidence of 67.5˚ or 45˚. The reflected beam is detected with an inclined photodiode with an angle of incidence of about 40˚. The ellipsometer chamber can be rotated around the axis of the incidence with angle α using a rotational feedthrough with magnetic sealing fluid. The analyzer unit can also be rotated around the reflected beam from a sample with angle β. Intensity measurements in the several combinations of α and β make it possible to analytically solve all the unknown parameters, that is, the Stokes parameters of the incident radiation, optical constants of the sample and detector polarization characteristics of the detector.

We used the ellipsometer at the normal incidence monochromator beamline, BL7B at UVSOR for three sample mirrors, Au, AlN and AlN photodiode. Complex refractive indices of AlN obtained were published elsewhere [3-4]. Figure 2 shows Stokes parameters obtained for the radiation emerging from BL7B. Note that measurements were repeated three times for each sample incidence angles of 45˚ and 67.5˚ by changing the sample mirrors. Although the data of S_2 and S_3 are somehow scattered, the data of S_1 shows better reproducibility independent of the sample mirror.

Considering the rather large vertical accepting angle, the results obtained are considered to be reasonable. It should be also mentioned that the polarization, in principle, could be different depending on the electron beam condition such as beam position and beam emittance in the storage ring. Although we were not able to attribute the cause of the scatter of S_2 and S_3, it can be probable that the electron beam instability of the storage ring and/or difference in illuminating condition in the beamline optics is partly responsible for it since we observed rather big changes in Stokes parameters over many times measurements.

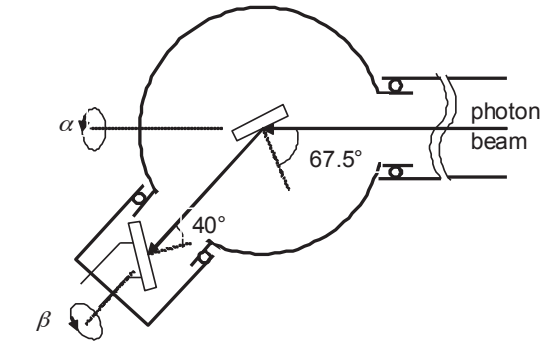

Fig. 1. Schematic layout of the ellipsometer.

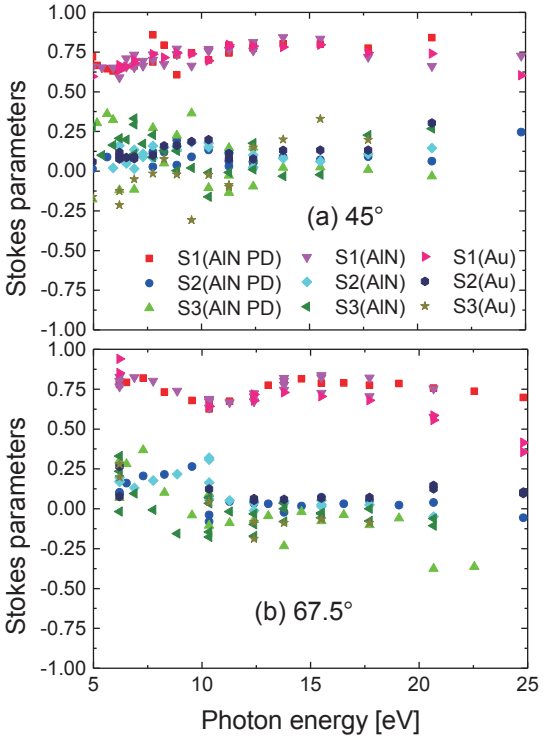

Fig. 2. Stokes parameters obtained by the ellipsometer using 3 different samples. The angle of incidence to the sample: (a) 45˚ and (b) 67.5˚.

[1] D. E. Aspnes, in: E. D. Palik (Ed.), *Handbook of Optical Constants of Solids* (Academic Press, Boston, 1985).
[2] T. Saito, M. Yuri and H. Onuki, Rev. Sci. Instrum. **66** (1995) 1570.
[3] K. Ozaki *et al.*, UVSOR Activity Report **38** (2010) 105.
[4] T. Saito *et al.*, Thin Solid Films, available online 12 March 2014
(http://dx.doi.org/10.1016/j.tsf.2014.02.099).

BL7B

Efficiency Measurement of a Holographic Concave Grating for VUV Solar Spectro-Polarimetry

H. Hara[1,2], M. Kasuga[2], T. Kobiki[1], K. Miyagawa[2] and N. Narukage[3]
[1]*National Astronomical Observatory of Japan, Mitaka 181-8588, Japan*
[2]*Department of Astronomy, School of Science, The University of Tokyo, Tokyo, 113-0033 Japan*
[3]*Institute of Space and Astronautical Science, JAXA, Sagamihara, 252-5210, Japan*

We are developing a payload of a sounding rocket experiment named the Chromospheric Lyman-Alpha Spectro-Polarimeter (CLASP) [1] (Fig. 1). CLASP is an instrument to detect low-level polarization signals with an order of 0.1% photometric sensitivity in the H Lyman-alpha line at 121.6 nm for the measurement of magnetic fields in the upper chromosphere and transition region of the Sun. A holographic-ruled spherical concave grating of 110 mm diameter with a 3000 gr/mm groove density is used in the spectro-polarimeter that requires a high efficiency (>0.18). The grating for the experiment was fabricated by Horiba Jobin Yvon (HJY), which has rich heritages for providing the flight gratings in the space programs.

In parallel with developing the flight optics, we have been developing the grating for the future use in space astronomy with domestic companies. One of the programs is to make a high-efficiency holographic concave grating in collaboration with Shimadzu Corporation. The grating specification is almost the same as that of the CLASP flight grating. It has a spherical concave surface of 110mm effective area with groove density of 3,000 gr/mm and a rectangular groove shape reshaped by the ion-beam etching process. Three gratings fabricated this time are master gratings. The grating substrate is fused silica, while Zerodur is used for the CLASP replica gratings. Al/MgF_2 is coated on the grating surface to enhance the diffraction efficiency.

Figure 3 shows the absolute grating efficiency of one of three gratings measured at the beam line BL7B. Although non-uniformity in efficiency is found over the effective grating aperture, the efficiency is good enough for the specification for the CLASP grating, and is comparable to the CLASP flight gratings that have been fabricated by HJY. The reflectance of the witness sample mirror coated by Al/MgF_2 with the concave grating is 0.75 at 121nm, so that the 30–40% groove efficiency has been achieved. Other two gratings have also shown good absolute efficiency of 0.24-0.28 with better uniformity over the grating surface, though they partially have areas with low efficiency of 0.05 due to the local failure of groove formation.

This work was supported by a Grant-in-Aid for Scientific Research (B) (No. 23340052) from the Ministry of Education, Culture, Sports, Science and Technology of Japan.

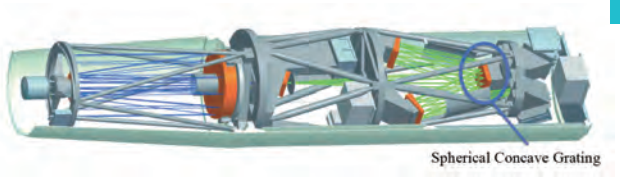

Fig. 1. Concave grating in the CLASP polarimeter.

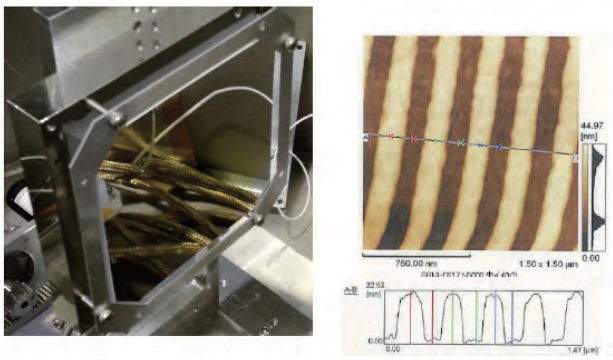

Fig. 2. (left) Holographic spherical concave grating fabricated by Shimadzu Corporation and (right) its groove profile.

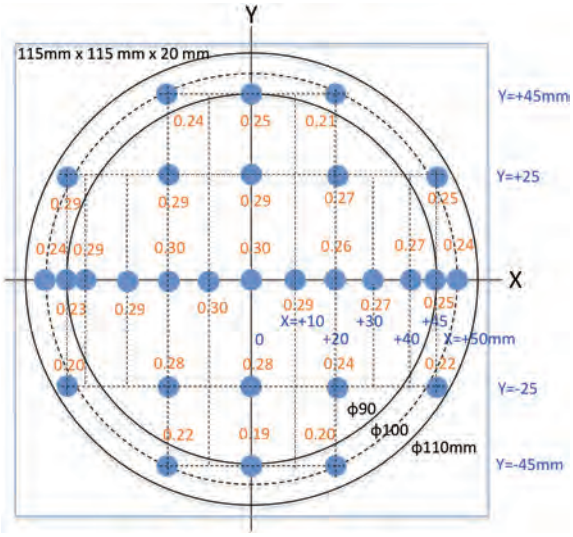

Fig. 3. Absolute grating efficiency of the holographic concave grating measured at 121nm in red characters.

[1] R. Kano *et al.*, SPIE **8443** (2012) 84434F.

BL7B

Performance Verification of Flight Filter Unit for CLASP Slit-Jaw System

M. Kubo[1], N. Narukage[1], G. Giono[2], R. Ishikawa[1], S. Ishikawa[1], K. Aoki[3], T. Kobiki[1], Y. Suematsu[1], T. Bando[1] and R. Kano[1]

[1]*National Astronomical Observatory of Japan, Tokyo 181-8588, Japan*
[2]*Department of Astronomical Science, Graduate University for Advanced Studies (SOKENDAI), Tokyo 181-8585, Japan*
[3]*Department of Astronomy, University of Tokyo, Tokyo 113-0033, Japan*

CLASP is a sounding rocket program, for the first time, to detect the linear polarization signal in Lyman alpha (121.567nm) emitted from the upper chromosphere or transition region of the Sun [1]. The telescope of CLASP focuses a solar image on a slit, and the light passing through the slit feeds into the spectropolarimeter that measures the spectra of the linear polarization. The outside of the slit has a mirror surface, and the solar image outside the slit is reflected to the slit-jaw system. The slit-jaw system will obtain Ly-alpha images by focusing optics with a pair of Ly-alpha narrow band filters. The images are used to select the instrument pointing during flight and to help the interpretation of the data obtained by the spectropolarimeter.

A filer unit (Fig.1) of the slit-jaw system holds a pair of Ly-alpha filters. The Ly-alpha filters are developed by the Acton Optics & Coatings. The diameter of the filter is one inch and its thickness is 2.5mm. The filter unit is fabricated by the Genesia Corporation. Their designs are based on measurements of prototype of Ly-alpha filters in FY2011 [2].

The transmissivity in Ly-alpha and the visible light rejection performance of the Ly-alpha filters are important for obtaining Ly-alpha images because the amount of photons in the visible light is much higher than photons in Ly-alpha wavelength. Figure 2 shows the transmissivity of a witness sample that is coated simultaneously with the flight Ly-alpha filters. The transmissivity is 10% in the Ly-alpha wavelength and less than 10^{-3} % for the visible light. The measured transmissivity satisfies our requirements, and then the visible light contamination is less than 1% in the Ly-alpha images. We conclude that the flight Ly-alpha filters are successfully fabricated.

A pair of Ly-alpha filters is mounted at the angle of incidence (AOI) of 0 degree, and the coated surfaces of the two filters face each other at a distance of 5mm. The ghost images are created by the reflection on the back and coated surfaces of a filter, and by the reflection between two filters. The Ly-alpha images though the flight filter unit are taken by CCD camera at AOI = 0 and AOI=±10 degrees (Fig.3). We have confirmed no issue of the ghost images created by the filter unit: (1) the intensity of ghost beams to the main beam is less 1%, (2) the distance between the ghost beam and main beam is expected value (about 1.7mm in the case of AOI=±10 degree), and (3) there is no unexpected ghost pattern.

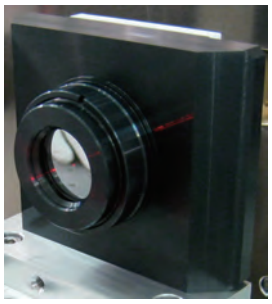

Fig. 1. Photo of the CLASP filter unit.

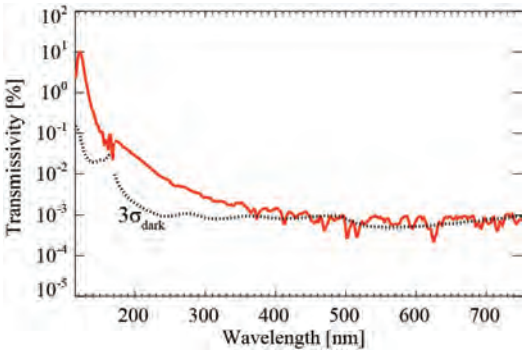

Fig. 2. Transmissivity of the Ly-alpha filter (red line).

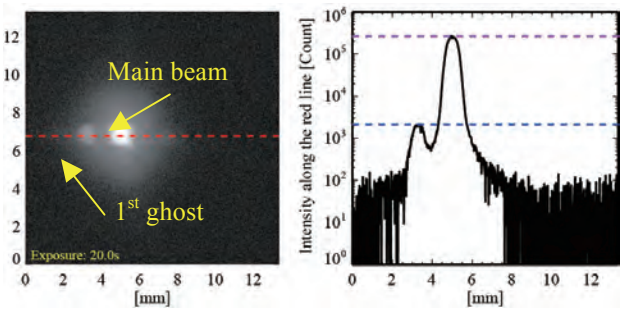

Fig. 3. *Left:* Main beam and ghost beam image created by the filter unit at the AOI of 10 degree. *Right:* Intensity along the dashed red line in the left panel.

[1] R. Kano *et al.*, SPIE **8443** (2012) 84434F.
[2] M. Kubo *et al.*, UVSOR Activity Report **39** (2011) 43.

BL7B

Waveplate Axis Alignment for the CLASP Sounding Rocket

S. Ishikawa[1], G. Giono[2], R. Ishikawa[1], N. Narukage[1], R. Kano[1] and T. Bando[1]
[1]*National Astronomical Observatory of Japan, Tokyo 181-8588, Japan*
[2]*Department of Astronomical Science, Graduate University for Advanced Studies (SOKENDAI), Tokyo 181-8585, Japan*

The Chromospheric Lyman-Alpha SpectroPolarimeter (CLASP) is a sounding rocket experiment to observe the linear polarization profile of the Lyman-alpha line (vacuum ultraviolet, 121.6 nm) from the Sun for the magnetic field measurement in the upper chromosphere and transition region [1]. CLASP uses a continuously rotating MgF_2 half-waveplate [2] and reflecting polarization analyzer to measure the Lyman-alpha linear polarization. A digital signal to trigger the CCD camera exposure is sent out from the motor every 22.5-degree rotation of the waveplate to drive the linear polarization degree and angle. To measure the polarization angle precisely, it is necessary to align the waveplate on the motor with a small angle uncertainty. The estimated polarization angle uncertainty from the CCD photon noise is 0.8-degree, and the goal was to align the waveplate with respect to the motor with better than 0.8-degree. Before this alignment experiment, the waveplate angle is adjusted just by looking at a reference marking-off on the waveplate edge by eye, and the uncertainty is not smaller than a few degrees.

We measured the relative angle between the waveplate and motor with the UVSOR BL7B beam with the wavelength of the Lyman-alpha light, and adjusted the waveplate angle. The experimental setup is shown in Fig. 1 and Fig. 2. We made the linearly polarized Lyman-alpha beam by the UVSOR beam with a reflecting polarization analyzer. The polarized beam is going through the rotating waveplate, and the polarization direction changes continuously. The linear polarization component parallel to the certain direction is extracted by the reflecting polarization analyzer and a time profile of the intensity of the extracted component is recorded by a photodiode. The recorded time profile, which is called the polarization modulation, and the exposure synchronization signal are recorded simultaneously. The rotation speed of the motor is 4.8 seconds per one rotation; therefore we measured the signals with the high sampling frequency of 1 kHz to estimate the waveplate angle with the better precision than 0.1-degree (one sampling interval of 1 ms corresponds to 0.075-degree).

We estimated the deviation angle of the waveplate with respect to the motor to be 0.66-degree from the obtained polarization modulation (shown in Fig. 3). We adjusted the waveplate angle to cancel the deviation. After the adjustment, we measured the polarization modulation and the exposure synchronization signal again, and the deviation was ~0.05-degree. Therefore, we confirmed that the waveplate angle is successfully aligned and the remained deviation was much less than the requirement.

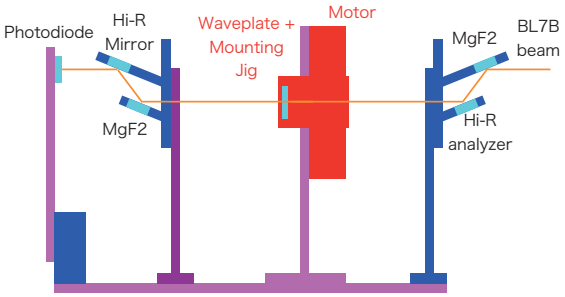

Fig. 1. Overview of the experimental setup.

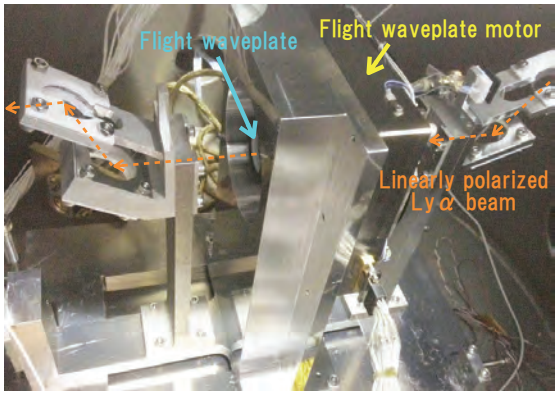

Fig. 2. Photo of the experimental setup.

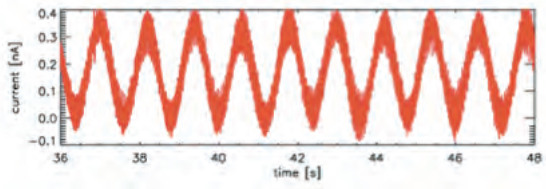

Fig. 3. Obtained polarization modulation. Only a part (10 seconds, ~2 waveplate rotation) of the obtained data is plotted.

[1] R. Kano *et al.*, SPIE **8443** (2012) 84434F.
[2] R. Ishikawa *et al.*, Appl. Optics. **52** (2013) 8205.

BL7B

Development of Mechanically Ruled Grating for the VUV Application

R. Ishikawa[1], S. Ishikawa[1], R. Kano[1], T. Bando[1], M. Koyama[2], Y. Enokida[2], T. Sukegawa[3] and S. Tsuneta[4]

[1]*National Astronomical Observatory of Japan, Mitaka, 181-8588, Japan*
[2]*Corporate Production Engineering Headquarters, CANON Inc., Kawasaki, 212-8602, Japan*
[3]*Corporate R&D Headquarters, CANON Inc., Utsunomiya, 321-3292, Japan*
[4]*Institute of Space and Astronautical Science, Japan Aerospace Exploration Agency, Sagamihara, 252-5210, Japan*

For the vacuum-ultraviolet (VUV; λ < 200nm) applications, holographic gratings have been widely used, but here we focus on the capability of a mechanically ruled grating, since it is flexible in choice of groove density and surface figure compared with the holographic grating. As a first step of the development of a mechanically ruled VUV grating, we have fabricated a test sample made of NiP with the groove density of 5000 lines/mm and the effective area of 10 mm x 10 mm, and evaluated the performance at the UVSOR BL7B. Since we consider the possibility to apply this grating to the CLASP sounding rocket experiment [1] in the future, which intends to measure linear polarization at the hydrogen Lyman-α line (121.6 nm), our experiment was done with a focus on this wavelength. For the reference, we have also performed the measurement of the NiP plane mirror made by cutting work.

Figure 1 shows the photograph of the surface shape of the grating sample observed with the Atomic Force Microscope (AFM), and the micro-roughness is found to be very good with 0.6 nm RMS, indicating very low stray light. Figure 2 represents the reflectivity of 0th order with the angle of incidence (AOI) of 5 deg for TE (electric vector is parallel to the groove) and TM (electric vector is perpendicular to the groove). We found significant difference in the reflectivity between two incident polarization states; the reflectivity for TM is lower than that for TE, and the difference becomes larger at longer wavelength (λ>120 nm). At the wavelengths of 183 nm and 217 nm (shown with dotted lines in Fig. 2), the TM reflectivity represents the local maximum, and these wavelengths correspond to the wavelengths, where +1st and -1st orders disappear for the grating with groove density of 5000 lines/mm at AOI=5deg. The diffraction efficiency of +1st and -1st orders at 121.6 nm is found to be 6.4% and 7.8% for TM and 11.0% and 12.1% for TE. The similarity in the reflectivity among +1st and -1st orders indicates that the groove shape is symmetrical, while the higher efficiency for TE indicates that the groove depth is not optimized for 121.6 nm (see next paragraph for more detail). We also find that the reflectivity of plane mirror sample at AOI=5deg is 28% at 121.6 nm. Thus, the relative diffraction efficiency of our grating sample is estimated to be 22 - 43%.

The measured reflectivity of the NiP plane mirror from 115 to 300 nm allows us to evaluate the optical constant of NiP and simulate the diffraction efficiency of the NiP grating. We found that the 0th order reflectivity and diffraction efficiency at +/-1st orders are consistent with the simulation results with the groove depth of 45 nm, and the groove depth of 28 nm gives us the well-balanced diffraction efficiency between TE and TM. We also found that the simulation depends strongly on the optical constant of the material, and the evaluation is necessary for the development of the grating.

The relative diffraction efficiency of our sample is large and reproduced by the simulation. The difference in efficiency between TE and TM, which should be avoided in the polarization measurement, can be suppressed by optimizing the groove depth. Thus, we conclude that the first step of the development of mechanically ruled gratings was successfully done. Next step is to develop the coating to enhance the absolute diffraction efficiency.

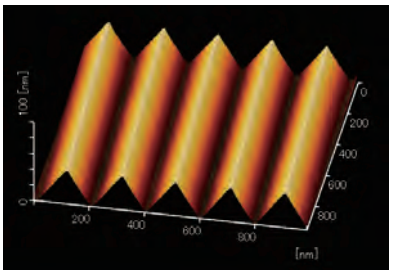

Fig. 1. Photo of grating surface.

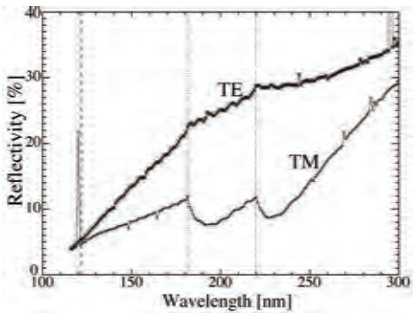

Fig. 2. Reflectivity of NiP grating sample at 0th order with AOI=5 deg for TE and TM.

[1] R. Kano *et al*., SPIE **8443** (2012) 84434F.

BL7B

Birefringence of MgF_2 in the Vacuum Ultraviolet and Development of an MgF_2 Half-Waveplate

R. Ishikawa[1], R. Kano[1], T. Bando[1], Y. Suematsu[1], S. Ishikawa[1], Y. Katsukawa[1], M. Kubo[1], N. Narukage[1], H. Hara[1], S. Tsuneta[2], H. Watanabe[3], K. Ichimoto[4], K. Aoki[5] and K. Miyagawa[5]

[1]*National Astronomical Observatory of Japan, Mitaka, 181-8588, Japan*
[2]*Institute of Space and Astronautical Science, Japan Aerospace Exploration Agency, Sagamihara, 252-5210, Japan*
[3]*Unit of Synergetic Studies for Space, Kyoto University, Kyoto 607-8417, Japan*
[4]*Kwasan and Hida Observatories, Kyoto University, Takayama 506-1314, Japan*
[5]*Department of Astronomy, School of Science, The University of Tokyo, Tokyo 113-0033, Japan*

Spectro-polarimeteric observations in the vacuum-ultraviolet (VUV) region are expected to be developed as a new astrophysics diagnostic tool for investigating space plasmas with temperatures of $>10^4$ K. A team of researchers from Japan, the USA, Spain, France, and Norway has been developing the high-throughput chromospheric Lyman-alpha spectro-polarimeter (CLASP), which is aiming to measure the linear polarization of the hydrogen Lyman-α line (λ = 121.567 nm) for the first time [1]. Precise measurements of the difference in the extraordinary and ordinary refractive indices are required for developing accurate polarimeters, but reliable information on the birefringence in the VUV range is difficult to obtain. We have measured the birefringence of magnesium fluoride (MgF_2) around 121.57 nm at the BL7B beamline using prototype of MgF_2 waveplates, and developed a flight half-waveplate for the CLASP rocket experiment. Our waveplates consist of two stacked MgF_2 plates with slightly different thicknesses and their principal axes are rotated by 90° with respect to each other.

A schematic of our experimental setup is shown in Fig. 1. We employed three MgF_2 plates set at Brewster's angle (59°). Using two MgF_2 plates, linearly polarized light in the horizontal direction with a polarization degree of >99.999% was directed onto a waveplate sample. With this configuration, we measured the intensities I_{obs} at ϕ=0° and ϕ=45° (ϕ is the angle of the principle axis of a waveplate from the horizontal direction), and calculated the ratio which is a function of phase retardation δ, $A(\lambda)=I_{obs}(\phi=45°)/I_{obs}(\phi=0°)=[(1+PER)+(1-PER)\cos\delta(\lambda)]/2$. The polarization extinction ratio (PER) is the ratio of the p-polarization reflectivity to the s-polarization reflectivity. From the amplitude A(λ), we determined δ as a function of wavelength and then derive the birefringence $n_e - n_o$ using $\delta = 2\pi (n_e - n_o)(d_1 - d_2)/\lambda$, where $d_1 - d_2$ is a thickness difference of two stacked MgF_2 waveplate. One of the difficulties in this measurement is the assignment of phase without 2π ambiguities. To achieve this, we measured several waveplate samples with different thickness differences (see [2] for more detail).

Figure 2 shows the birefringence of MgF_2 as a function of wavelength, derived from the phase retardation measurement of the waveplate sample with $d_1 - d_2$ = 15.755 μm. We found that $n_e - n_o$ = 0.004189 ± 0.000039 at 121.57 nm. Based on this birefringence, we fabricated the flight waveplate with $d_1 - d_2$ = 14.51 μm, and measured the phase retardation to be 2π at the BL7B. Thus, we conclude that we successfully completed the development of a half-waveplate for the CLASP experiment.

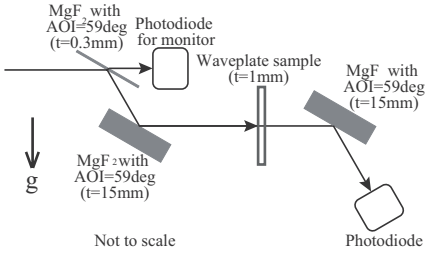

Fig. 1. Schematic of the experimental setup.

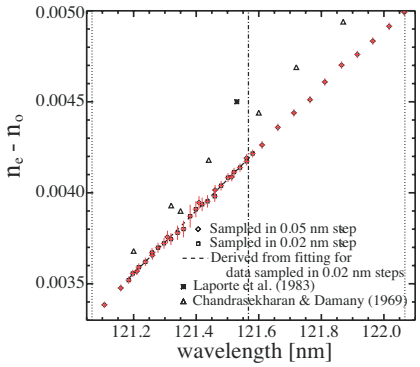

Fig. 2. Birefringence of MgF_2. Values measured in previous studies [3, 4] are also shown.

[1] R. Kano *et al.*, SPIE **8443** (2012) 8443F.
[2] R. Ishikawa *et al.*, Appl. Optics. **52** (2013) 8205.
[3] V. Chandrasekharan and H. Damany, Appl. Opt. **8** (1969) 671.
[4] P. Laporte *et al.*, J. Opt. Soc. Am. **73** (1983) 1062.

UVSOR User 2

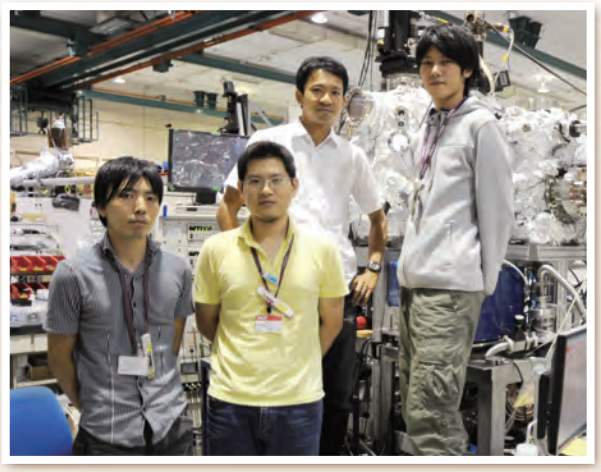

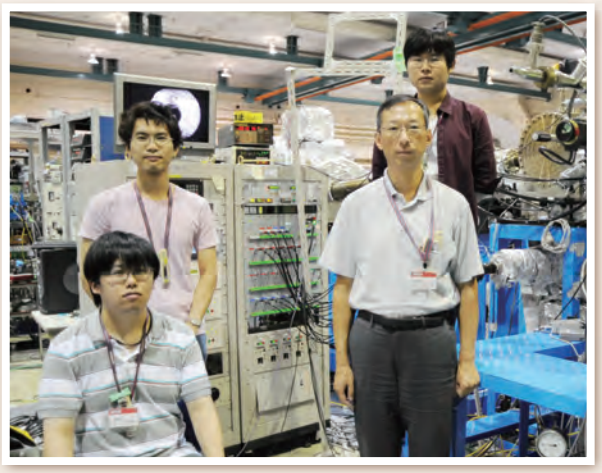

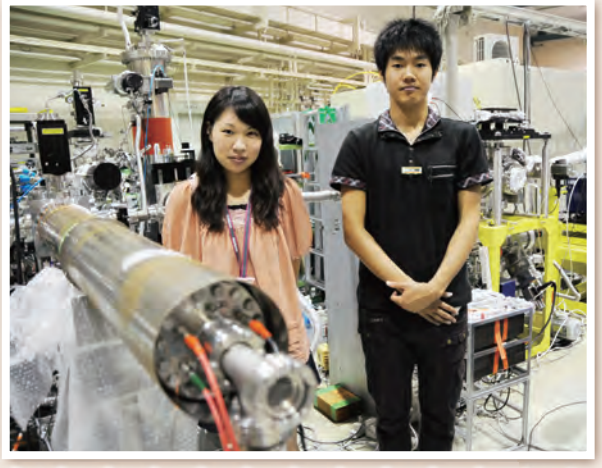

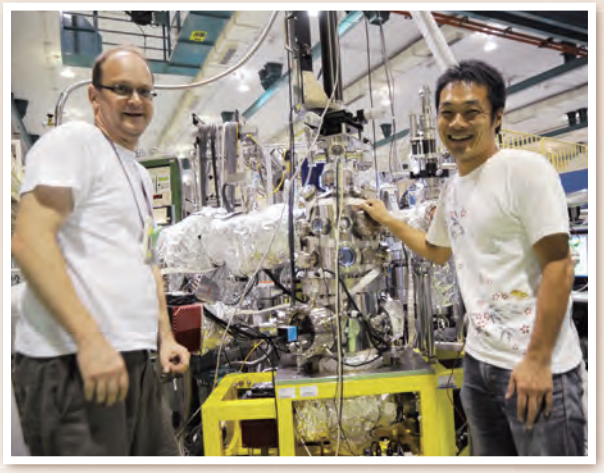

Ⅲ-2

Materials Sciences

Highlight

BL7U

Electron-Phonon Coupling Investigation in Highly Oriented Pyrolytic Graphite by Angle-Resolved Photoelectron Spectroscopy

S. Tanaka[1], M. Matsunami[2,3] and S. Kimura[2,3,4]

[1]*The institute of Scientific and Industrial Research, Osaka University, Ibaraki 567-0047, Japan.*
[2]*UVSOR Facility, Institute for Molecular Science, Okazaki 444-8585, Japan.*
[3]*School of Physical Sciences, The Graduate University for Advanced Studies (SOKENDAI), Okazaki 444-8585, Japan.*
[4]*Graduate School of Frontier Biosciences, and Department of Physics, Osaka University, Suita 565-0871, Japan.*

Electron-phonon coupling (EPC) plays an important role in solid state physics. The EPC has been analyzed via the self-energy $\Sigma^{el-ph}(E,T)$ in the quasiparticle spectral function, which is determined with the integral of the Eliashberg function $\alpha^2F(\hbar\omega,q)$ with the energy and momentum of the phonon, by using the angle-resolved photoelectron spectroscopy (ARPES). Here, we demonstrate an experimental method in which the elemental process of EPC, that is a scattering of the electron by the phonon in the solid, can be investigated [1].

Figure 1(a) presents a series of surface-normal ($\pm 5^{\circ}$) photoelectron spectra for HOPG (highly oriented pyro-lytic graphite) at 50 K in the region near the Fermi level with several photon energies (hν). The feature that we focus on here is the step-like edges located at either 154 meV or 67 meV with respect to the Fermi level, those are clearly demonstrated by the differentials of the photoelectron intensity with the binding energy along with that of a gold film as shown in Fig. 1(b). The π-band of the graphite crosses the Fermi level at the K(H) point, and no electronic states are located near the Fermi level at the Γ(A) point, that is observed in the present spectra. We therefore conclude that the observed electron emission is due to EPC and that the energy of the step matches the energy of the phonon that is involved. The 154- and 67-meV steps are ascribed to the transverse optical (TO), and the out-of-plane acoustic (ZA) and/or out-of-plane optical (ZO) phonon of graphite at the K(H)-point, respectively. Figure 1 (c) plots the intensities of the steps at 154 and 67 meV in the surface-normal photoelectron spectra as a function of the photon energy. These intensities represent the electron-scattering intensities from K(H) to Γ(A) by the phonons at the K(H) point in the Brillouin zone. The black (red) solid line is the Lorentzian curve, where the center and width energies are 11.05 and 0.92 eV (6.0 and 1.2 eV), respectively. This hν-dependence indicates that the final photoexcitation state is definitely defined by the photon energy and that this state determines the phonon branch that can scatter the electron. Note that this photon-energy dependence clearly demonstrates that we are observing EPC among the electrons in bands of the solid. The photoexcitation process that accompanies electron-phonon scattering is widely known as the "indirect transition" that is often observed in semiconductor materials.

The transition probabilities of the indirect transition can be formulated as

$$W_{0,k\to f,k'} = \frac{2\pi}{\hbar}\frac{\langle f,k'|\hat{H}_{EPC}|i,k\rangle^2\langle i,k|e\cdot\hat{A}|0,k\rangle^2}{(\hbar\omega_{0i}-\hbar\omega)^2}\delta(\hbar\omega-\hbar\omega_{0f}-\hbar\omega_s)$$
$$+\frac{2\pi}{\hbar}\frac{\langle f,k'|e\cdot\hat{A}|i',k'\rangle^2\langle i',k'|\hat{H}_{EPC}|0,k\rangle^2}{(\hbar\omega_{i'f}-\hbar\omega)^2}\delta(\hbar\omega-\hbar\omega_{0f}-\hbar\omega_s)$$

where the matrix elements of the optical transition and EPC among the electronic bands in graphite are included. This is the first measurement of the matrix elements of the EPC by ARPES. Additional insights about electron-phonon scattering in the solid will be gained from further research using this method. A comparison with the results of theoretical calculations of the intensity of the electron-phonon interaction while resolving the energy and momentum of all the contributing electronic states and phonons will lead to deeper insight into EPC in solids.

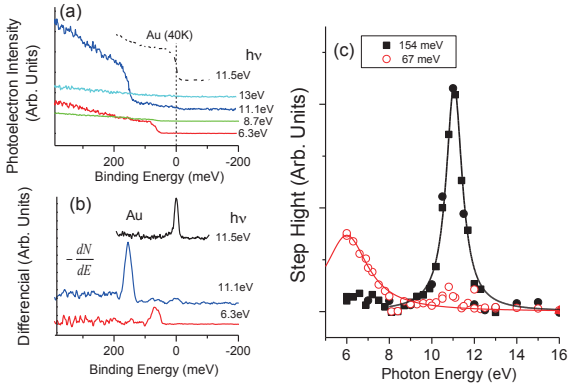

Fig. 1. (a) Surface-normal photoelectron spectra of graphite at 50K. (b) Differentials of photoelectron intensity with the binding energy. (c) Height of the steps observed in the photoelectron spectra as a function of the photon energy.

[1] S. Tanaka, M. Matsunami, and S. Kimura, Sci. Rep. 3, 3031; DOI:10.1038/srep03031 (2013).

BL1B

Experimental Study of Electronic States on Solids Using THz Beamline

A. Irizawa
The Institute of Science and Industrial Research, Osaka University, Ibaraki 567-0047, Japan

The optical study is one of the most powerful techniques for the investigation of electronic states on solids. There can be obtained the great deal of information about the electronic band structure, the symmetry of crystal structure, and the dielectric property. In the respect of experimental affinity, the optical study is extremely compatible with the multiple conditions such as low temperature, high magnetic field, and high pressure. In the case of strongly correlated electron systems, it is well known that the temperature is one of the decisive factors for the electronic state. The considerable types of phase transition are induced by the change of the temperature. Particularly, the multiferroic compounds can be controlled of its physical properties mutually by the external fields such as magnetic, electronic, and elastic ones. The other particular condition, the pressure will directly affect the electron-electron interactions through the change of lattice constants. The beamline 1B in UVSOR is the new one adjusted for the investigations at low temperature and at extremely low-energy region of THz. There is Martin-Puplett type interferometer moved from BL6B and the cryostat covering the temperature between 10 K and 300 K. In this report, I tried to use this newly installed beamline and aimed to get more low energy spectra for samples we use to deal. In the beginning, I prepared some typical compounds having absorption bands in THz region for transmittance experiment.

However, the experiments were resulted in preliminary ones. There were several problems in the alignment process of optical axis. Several upper stream mirrors were lost their original positions after an electrical power down. Also step motion motors for mirror alignment were not fixed even in motion controlled mode. Therefore, every machine time after several month was dedicated for find the light. Fortunately a visible light was also on the same optical axis, we can explore the THz light following it as a loadstar. On the way, I believed to find the THz light but it might not be true one. There were two different type spectra, both the synchrotron light and a black body like light. The later one with rather broad spectrum might be originated in thermally activated mirrors or something near the optical axis (unproved).

Next time, those problems accompanied by the first time experiment will be fixed and the study might be proceeded.

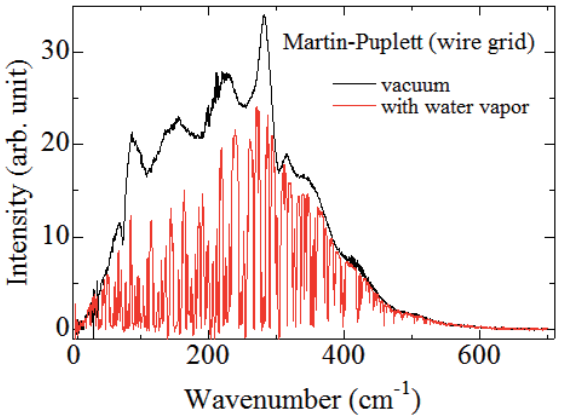

Fig. 1. Difference of light source spectra through blank (vacuum) and water vapor (air). (But the light was said to be ‘another’ origin.).

BL1B

Teraheltz Spectra of Nano Porous Gold

T. Awano
Department of Electronic Engineering, Tohoku Gakuin University, Tagajo 985-8537, Japan

It is well known that bulk Au is inert. However, Au nanoparticles with several-nanometer-scale sizes are catalytically active for several chemical reactions such as the decomposition of formaldehyde and oxidation of CO. The catalytic activity depends on the size of nanoparticles. The nanoparticles with diameters in the range of 2 to 5 nm show the highest activity for oxidation. Nanoporous Au (NPG) with 10–50 nm pore size also shows catalytic activity for oxidation.

Recently, TiO_2 is being widely used for photocatalysis of various materials. TiO_2 has a different activity with crystal structure for different wavelengths. It has been reported that composite materials of TiO_2 with Au or Pt nanoparticles enhance TiO_2 catalytic activity. TiO_2 plays an active role in the decomposition of water to generate OH radicals. It is supposed that the plasmonic electromagnetic effect of Au or Pt enhances the catalytic activity of TiO_2. In addition, since pores of NPG are able to trap the TiO_2 particles on its surface, NPG seems to be a photocatalytic nanocomposite because of enhancement of the catalytic activity by the electromagnetic effect. We have found that NPG acts as a promoter to produce OH radicals using TiO_2. We report optical properties of NPG in this paper to investigate electromagnetic and plasmonic origin of the promotor effect [1].

Figure 1 shows THz-reflectivity spectra of the NPG films on gold-evaporated substrate measured at BL1B. These spectra were connected with other spectral range between millimeter wave and UV. Dielectric constants were obtained by K-K analysis.

Plasmon fitting by classical Drude model in energy loss function spectra is shown in Fig. 2. In the Drude model,

$$\varepsilon = \varepsilon_\infty \left(1 - \frac{\omega_p^{\,2}}{\omega^2 + \gamma^2} + i\frac{\gamma\omega_p^{\,2}}{\omega(\omega^2 + \gamma^2)}\right)$$

$$\omega_p = \sqrt{\frac{4\pi Ne^2}{m^* \varepsilon_\infty}}$$

where is the plasma frequency, γ is dumping factor and ε_∞ is dielectric constant at high frequency. Energy loss function, Im(1/ε), is proportional to absorption intensity by transverse wave. The plasmon fitting parameters are summarized in Table 1. Systematic decrease of the plasma frequency with pore size increment was observed. Plasma frequency of bulk gold is 8.6eV, therefore, these ω_p for pore samples are much small. The promoter effect seems to be related with small values of these parameters. The origin of pore size dependence of the promoter effect is still not clear.

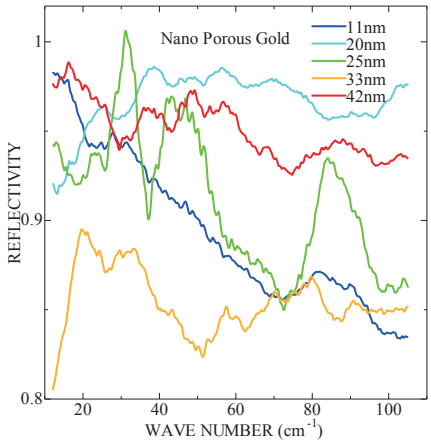

Fig. 1. Reflectivity spectra of nano-porous gold films on Au/SiO_2 glass substrates.

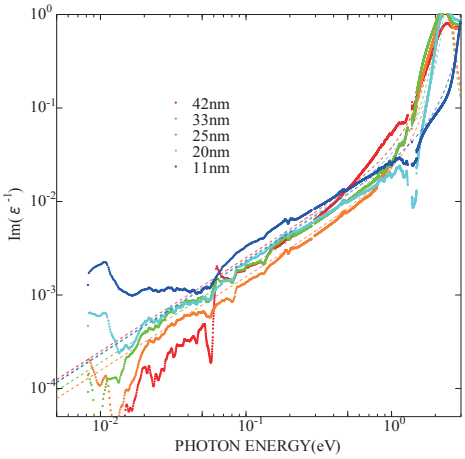

Fig. 2. Drude curve fitting of the energy loss function spectra of NPG membranes on quartz substrates. Dashed lines show fitting curves for each pore size sample.

Table 1. Plasmon parameters.

pore size (nm)	ω_p (eV)	γ (eV)	ε_∞
42	2.3	0.06	2.2
33	2.4	0.01	9
25	2.3	0.025	4
20	2.6	0.02	8
11	3.6	0.03	10

[1] S. Kuwano-Nakatani, Y. H. Han, T. Takahashi and T. Awano, Advanced Electromagnetics **2** (2013) 5.

BL2A

Fluorescence Yield XANES Measurement of Thin Film by Silicon-Drift Detector

H. Murata[1], K. Okada[2,3], D. Kobayashi[2], K. Hirose[2] and T. Yamamoto[3]

[1]*Advanced Key Technologies Division, National Institute for Materials Science, Tsukuba 305–0044, Japan*

[2]*Institute of Space and Astronautical Science, Japan Aerospace Exploration Agency, Sagamihara 252-5210, Japan*

[3]*Faculty of Science and Engineering, Waseda University, Shinjuku 169-8555, Japan*

X-ray absorption near edge structure (XANES) is a powerful tool to reveal local environments of materials with an elemental selectivity. Since it is difficult to prepare the suitable thin samples for transmission mode in soft X-ray region, two alternative techniques, total electron yield (TEY) and fluorescence yield (FY) were usually employed for measurements. FY method gives bulk-sensitive information while TEY does surface-sensitive one. [1] For FY method, there are two suitable sample conditions. One is thin and concentrated, and the other is thick and diluted. Otherwise FY spectra were distorted by the "self-absorption effect". In addition, counting loss of a detector also affects XANES spectra.

Recently, a silicon-drift detector (SDD), which is high-efficient and energy-dispersive detector, was introduced in UVSOR and now we can measure XANES by both TEY and partial fluorescence yield (PFY) at the same point sequentially. In this study, we reported Si-*K* XANES of SiO_2 film measured by both of TEY and PFY.

Si-*K* XANES spectra were measured at BL2A in UVSOR by TEY with drain current and PFY with SDD. The X-ray fluorescence spectra were deconvoluted with gauss functions. Incident X-ray beam was monochromatized with a InSb-(111) ($2d$ = 7.481 Å) double crystals monochromator. The samples were SiO_2 glass, Si powder and a SiO_2 film formed on *p*-Si (SiO_2/*p*-Si). The thickness of the film was 1 μm.

Figure 1(a) shows Si-*K* XANES of SiO_2/*p*-Si and references. The component of SiO_2 was observed in both of the TEY and the PFY spectra of SiO_2/*p*-Si. In the PFY spectrum, it was also found that a contribution derived from *p*-Si around 1840 eV (indicated an arrow). This indicated that PFY spectra reflect on information below 1μm from the surface for Si-*K* XANES.

Compared between the TEY and the PFY spectra, the white line in the PFY spectrum of SiO_2/*p*-Si was underestimated even if the contribution of *p*-Si was removed. This was the mainly caused by the counting loss of SDD since dead time was around 10 % at the white line, as shown in Fig. 1(b).

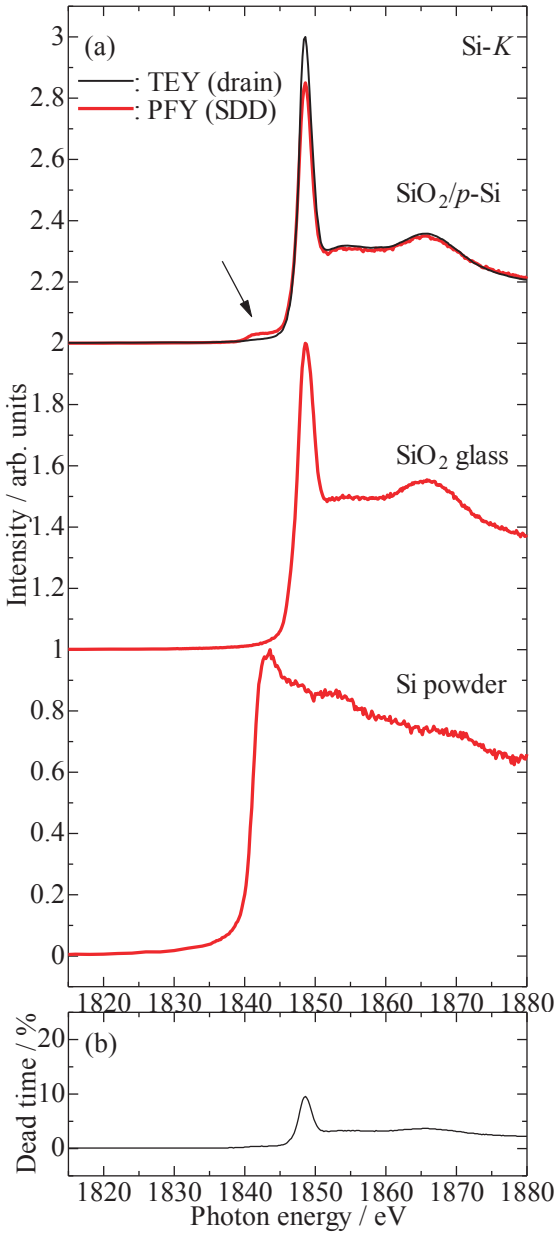

Fig. 1. (a) Si-*K* XANES of the SiO_2/*p*-Si and references. (b) Dead time of SDD for SiO_2/*p*-Si.

[1] T. Yamamoto and K. Kawabata, UVSOR Activity Report **40** (2009) 126.

BL2A

Soft X-Ray Photoluminescence and Photoluminescence Excitation Spectra of AlGdN around Gd M_{IV} Edge

K. Fujita[1], K. Fukui[1] and K. Yamamoto[2]

[1]*Department of Electrical and Electronics Engineering, University of Fukui, Fukui 910-8507, Japan*
[2]*Far-Infrared Region Development Research Center, University of Fukui, Fukui 910-8507, Japan*

III-V nitride semiconductors doped with the rare earth elements are promising light emitting devices in a wavelength range from visible to ultraviolet. Gd^{3+} ion is known as the light emitting material having ~ 3.9 eV emission line by $^6P_{7/2}$ (lowest excited state) → $^8S_{7/2}$ (ground state) 4*f* intra- transition. This emission energy (3.9 eV) is higher than the band gap energy of GaN, so we should use AlN or AlGaN as the host semiconductor materials for Gd. In previous work [1], a sharp 3.9 eV line emission was clearly observed from AlGdN, and its photoluminescence (PL) excitation (PLE) spectra in a energy range between 3 and 7 eV showed that the emission process was host excitation. We also showed that PLE spectra of this 3.9 eV line around Al K edge (1.55 ~ 1.6 keV) and Gd M_{IV} edge (1.2 ~ 1.25 keV) show very similar to total electron yield (TY) spectrum [2]. They indicate that there is a process which transfers energy from band-to-band transition in the matrix to 4*f* intra-transition of Gd^{3+} ion. They also indicate that this 3.9 eV emission does not observed by the intra-atomic 4*f* to 4*f* excitation of Gd^{3+}, but clearly observed by the allowed intra-atomic 3*d* to 4*f* excitation. Then, we carried out soft X-ray (SX) PL measurements around both Al K edge and Gd M_{IV} edge and their PLE measurements with TY measurements to investigate the relaxation process of excited inner core electrons.

AlGdN thin film was grown in a MBE system with a RF-plasma assisted radical cell on the Si-face of (0001)-oriented 6H-SiC substrate. The thickness of the sample is about 120 nm. Concentration of Gd^{3+} ions is 13% ($Al_{0.87}Gd_{0.13}N$). All SX-PL, PLE and TY measurements were carried out at room temperature (RT) with a silicon drift detector (SDD).

Figure 1 shows the PL spectra of AlGdN at RT. The excitation energy is 1215 eV. Peaks less than 1000 eV including the largest peak around 900 eV and above the excitation energy are SX emission lines of Cu sample holder and "sum peaks" by SDD itself, respectively. Emission line due to Gd^{3+} intra-atomic transition is found around 1200 eV as a small peak. This peak is observed only when the excitation photon energy is near and higher than Gd M_{IV} edge energy. PLE spectrum of this peak and TY spectrum are plotted in Fig. 2(a) and (b), respectively. It is found that the spectrum feature of PLE spectrum is very similar to that of TY spectrum which is clearly explained by the $3d^{10}4f^7 \rightarrow 3d^9 4f^8$ transition array [3].

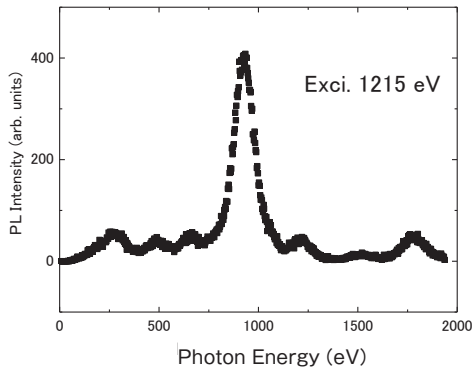

Fig. 1. PL spectrum of $Al_{0.87}Gd_{0.13}N$ at RT.

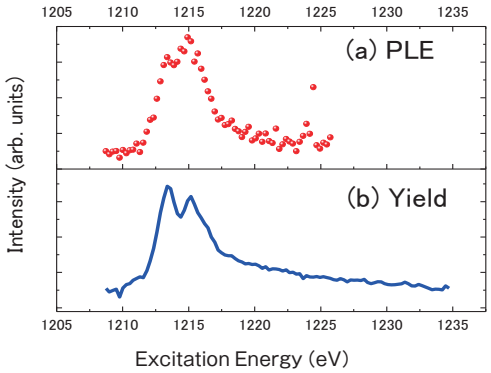

Fig. 2. PLE (a) and TY (b) spectra of $Al_{0.87}Gd_{0.13}N$ at RT.

[1] K. Fukui *et al.*, Phys. Stat. Sol. (c) **7** (2010) 1878.
[2] K. Fujita *et al.*, UVSOR Activity Report **40** (2012) 95.
[3] C. Bonnelle *et al.*, J. Phys. B **10** (1977) 795.

BL2A

Chemical State Analyses of Ag Species Loaded on Ga_2O_3 Photocatalysts

T. Yoshida[1], M. Yamamoto[2], N. Yamamoto[2] and S. Yagi[1]
[1]*EcoTopia Science Institute, Nagoya University, Furo-cho, Chikusa-ku, Nagoya 464-8603*
[2]*Department of Applied Chemistry, Graduate School of Engineering, Nagoya University, Nagoya 464-8603*

CO_2 reduction is important not only for the energy storage as usable and value-added products but for the abatement of CO_2 as a greenhouse gas. Especially, photocatalytic reduction of CO_2 with water is environment-friendly and attractive as the artificial photosynthesis. It has been reported that Ga_2O_3 shows photocatalytic activity for CO_2 reduction with water to produce CO as well as for water splitting to H_2 and O_2, and Ag loading on Ga_2O_3 (Ag/Ga_2O_3) promotes the CO_2 reduction [1].

In the present study, Ag L_3-edge XAFS measurements were performed to clarify the chemical states and the local structures of Ag species in Ag/Ga_2O_3 samples.

The reaction tests were carried out with a fixed-bed flow reactor. Photocatalysts (mass: 0.2 g) were put into the reactor cell under flowing CO_2 gas. When we exposed this reactor cell to UV light for 1 h, a $NaHCO_3$ aqueous solution was added to this reactor cell in dark condition. After an hour, UV light irradiation was started. Analysis of products was performed using a thermal conductivity detector gas chromatography (TCD-GC, Shimadzu GC-8A).

X-ray absorption fine structure (XAFS) measurements were carried out at the beam line 2A station of UVSOR-II at the Institute for Molecular Science and the beam line 6N1 station of Aichi Synchrotron Radiation Center. Ag L_3-edge XANES spectra of the samples were measured at room temperature in total electron yield mode and the fluorescent X-ray yield mode with a silicon drift detector (Vortex Electronics).

The results of photocatalytic reduction of CO_2 with water are summarized in Table 1. All samples exhibited photocatalytic activity for CO_2 reduction to produce CO, H_2 and O_2. The amount of CO production over 0.1 wt% Ag/Ga_2O_3 is larger than that over bare Ga_2O_3. It is confirmed that the Ag loading promotes CO_2 reduction.

Figure 1 shows Ag L_3-edge XANES spectra of silver-loaded gallium oxide samples (Ag/Ga_2O_3) together with those of Ag and Ag_2O reference samples. The spectrum feature in the post-edge region reflects the local structure around the target Ag atom, that is, the coordination symmetry and electronic state of the Ag atom. The XANES spectrum of 1 wt% Ag/Ga_2O_3 [Fig.1 (b)] exhibits a sharp absorption (whiteline) at 3354 eV due to the oxidized Ag as well as the fine resonance peaks at 3380, 3399 eV characteristic of the metallic Ag. This result suggests that Ag metal particles are partially oxidized in 1 wt% Ag/Ga_2O_3. Note that the absorption peaks due to the Ag metal and oxides are weak in the spectrum of 0.1 wt% Ag/Ga_2O_3 and indistinct broad feature is observed. It seems that the Ag particles are atomically dispersed by connecting directly to Ga_2O_3.

Table 1. The results of photocatalytic reduction of CO_2 with water over Ga_2O_3 and Ag loaded Ga_2O_3 catalysts.

photocatalyst	amount of CO (μmol/h)	amount of H_2 (μmol/h)
Ga_2O_3	0.2	2.5
0.1 wt% Ag/Ga_2O_3	2.1	5.2
1 wt%	1.1	0.8

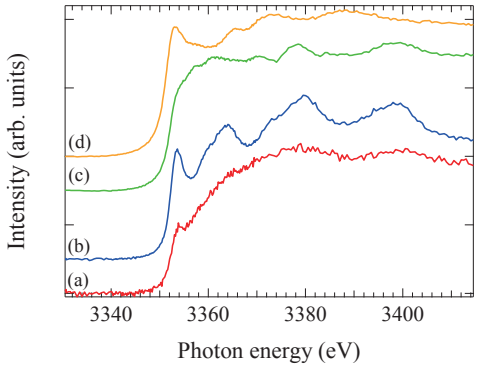

Fig. 1. Ag L_3-edge XANES spectra of (a) 0.1 wt% Ag/Ga_2O_3, (b) 1 wt% Ag/Ga_2O_3, (c) Ag foil and (d) Ag_2O.

[1] K. Koci, K. Mateju, L. Obalova, S. Krejcikova, Z. Lacny, D. Placha and L. Capek, Appl. Catal., B: Environ. **96** (2010) 239.

BL2A

Local Structure Investigation of FAU Zeolite Prepared from Si Based Waste Materials

M. Sato[1], M. Togo[2], Y. Inoue[2], K. Hara[2] and A. Nakahira[1,2]
[1]*Kansai Center for Industrial Materials Research, Tohoku University, Osaka 599-8531, Japan*
[2]*Department of Material Science, Osaka Prefecture University, Osaka 599-8531, Japan*

Blast furnace slag (BF slag) is one of the industrial waste materials, and efficient use of the BF slag has been sought for a long time. BF slag is obtained as a by-product in an iron manufacturing process, and generation amount is about 25 million tons per year in Japan. It has been widely used as mixture material and fine aggregate for cement, road bed, source of rock wool, dressing and ground improvement materials because of its hydraulic property. Since the consumption amount of BF slag is smaller than its generation amount, however, additional efficient use of BF slag has been strongly desired.

In a previous study, LTA Na-P1 and FAU type zeolite were successfully synthesized using BF slag and some kinds of waste glass. To synthesize the FAU zeolite in a single phase, optimum aging time about 150 hours was necessary, and the ratio between Na-P1 and FAU zeolite changed strongly depending on the aging time as shown in Fig. 1. Therefore, Si-K and Al-K edge XAFS was measured to investigate the effect of aging time to the local structure around both atoms.

BF slag, waste glass, $NaAlO_2$ and NaOH were used as starting materials. Si/Al ratio was controlled at around 2. The starting materials and 2 mol/L NaOH solution were encapsulated into a Teflon vessel, and aged for several periods. After aging, they were hydrothermally treated at 368 K for 72 hours. After that, obtained products were also filtered and dried at 323 K for overnight.

Al-K and Si-K edge XANES spectra of obtained samples before and after hydrothermal synthesis were measured by fluorescence mode using InSb double-crystal monochrometer for Si-K and KTP double-crystal monochrometer for Al-K at BL-2A station of UVSOR.

Figure 2 shows Al-K edge XANES spectra of samples before hydrothermal treatment. Obtained spectra of samples were resembled with starting material and no changes were observed by aging. This result indicates that the local structure around Al atom does not changed during the aging. On the other hand, Al-K edge XANES spectra of the sample after hydrothermal treatment were resembled to that of commercial FAU zeolite. Similar results were obtained in the case of Si-K edge XANES spectra.

From these results, the aging does not affect to the local structure of Al and Si in sample and it is suggested that the frameworks of zeolite is determined at the point of nucleation during hydrothermal synthesis.

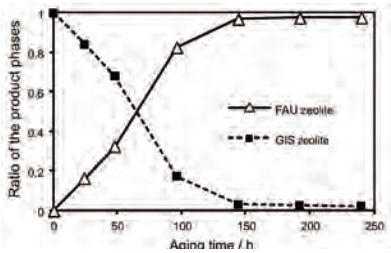

Fig. 1. Relationship between generation phase and aging time.

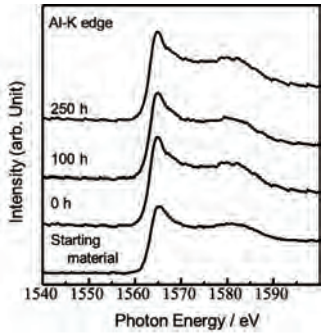

Fig. 2. Al-K edge XANES spectra of samples, which before hydrothermal synthesis, prepared at different aging period.

BL2A

Partial Fluorescence Yield XANES Measurements for Ultra-Dilute Dopants by Silicon-Drift Detector

H. Murata[1], T. Taniguchi[1] and T. Yamamoto[2]
[1]*Advanced Key Technologies Division, National Institute for Materials Science, Tsukuba 305–0044, Japan*
[2]*Faculty of Science and Engineering, Waseda University, Shinjuku 169-8555, Japan*

Fluorescence yield (FY) method of X-ray absorption near edge structure (XANES) is suitable for ultra-dilute dopants. In hard X-ray region, it is possible to measure 10 ppm dopants [1]. On the other hand, FY has following difficulties in soft X-ray region: low fluorescence yield and overlap of characteristic X-ray. Recent progress of light sources and detectors, such as top-up mode and energy dispersive silicon drift detector (SDD), made us enable to measure XANES of ultra-dilute dopants even in soft X-ray region. In UVSOR, a SDD was introduced for soft X-ray spectroscopy.

Cubic boron nitride (*c*-BN) has a similar crystal structure and features to diamond. It is a good matrix for soft X-ray spectroscopy since it consists of only light elements. It was interesting that a large rare-earth cation, Ce^{3+}, is substituted for N-site with surrounding B vacancies [2] and thus it is essential to investigate local environments of dopants in *c*-BN. In this report, we present an attempt of XANES measurements for ultra-dilute dopants in *c*-BN by partial fluorescence yield (PFY) with SDD.

S-*K* XANES spectra were measured by PFY with SDD at BL2A in UVSOR. The X-ray fluorescence spectra were deconvoluted by gauss functions. We also consider the component of elastic scattering. Incident X-ray beam was monochromatized with a InSb-(111) ($2d$ = 7.481 Å) double crystals monochromator. The sulfur-doped *c*-BN (*c*-BN:S) samples were synthesized under high-pressure and high-temperature conditions. Samples were mounted by carbon tape on Al sample holder.

Figure 1 shows typical X-ray fluorescence spectra of *c*-BN:S at different incident energy. Besides characteristic X-ray from the sample, B-*K*, N-*K* and S-*K*, it was also observed additional characteristic X-ray, C-*K*, O-*K*, Fe-*L* and so on. These derived from the optical and measurement system, such as a chamber, a monochromator and carbon tape, for example.

Since the sample contains only trace sulfur, the S-*K* signals were weak, about 1 cps at the peak. However, long dwell time (20 sec/points, 3 h/spectra) enabled us to obtain good XANES spectra, as shown in Fig. 2. It was noted that total electron yield method with drain current could not detect S-*K* XANES at all. A detailed analysis of local environments of sulfur in *c*-BN is in progress using first-principles calculations.

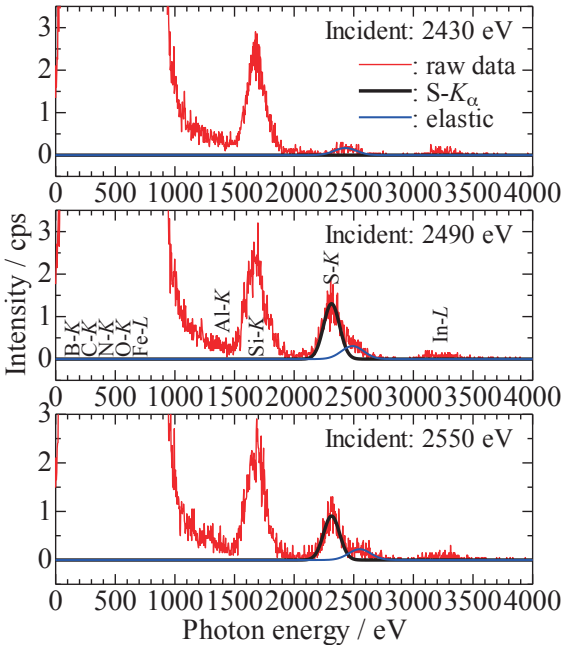

Fig. 1. Typical X-ray fluorescence spectra of *c*-BN:S measured by SDD at different incident energy.

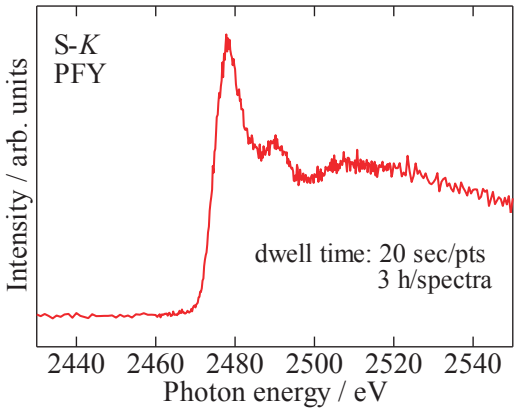

Fig. 2. S-*K* XANES of *c*-BN:S measured by PFY with SDD

[1] I. Tanaka *et al.*, Nat. Mater. **2** (2003) 541–545.
[2] R. Ishikawa *et al.*, Phys. Rev. Lett. **110** (2013) 065504.

BL2A

Evaluation of Local Structures of Si for LTA Nano-Zeolite on the Grinding Process

A. Nakahira[1,2], T. Tagami[1], H. Kanayama[1], H. Sakaguchi[1], K. Hara[1], Y. Inoue[1], M. Sato[2] and H. Aritani[3]

[1]*Faculty of Engineering, Osaka Prefecture University, Gakuencho, Sakai 599-8531, Japan*

[2]*Osaka Center, IMR, Tohoku University, Gakuencho, Sakai 599-8531, Japan*

[3]*Saitama Institute of Technology, Fukaya 369-0293, Japan*

Zeolites have the unique 3D micropore networks. They are one of aluminosilicate minerals commonly used as various commercial adsorbents and other applications. For example, zeolites are in fact widely used in petroleum industry as a catalyst for the preparation of advanced materials. Furthermore, they are used to extract nitrogen purification from air to increase oxygen content for both industrial and medical purposes Recently, in addition, they are applicable to water purification, and also Cs purification in nuclear accidents. However, in order to expand the applications of zeolite in various industrial fields, furthermore modification of microstructures and morphology is needed for zeolites. [1-3] For example, a lot of attentions are focused on the synthesis of the finely nanosized zeolite powders by various novel processing. Although many novel processing are attempted to synthesize the nano-sized zeolite powders, the finely nano-sized zeolite powders were synthesized by the mechanical mixing processing in this study. And the local structures were investigated for finely nano-sized zeolite powders prepared by the mechanical mixing processing.

Commercial LTA type zeolite was prepared. Nano-sized zeolite was synthesized by the following method. The powder of this LTA type zeolites powder was milled for 30 min and 120min by the mechanical milling method with the high energy forces. After the milled and ground nano-sized LTA type zeolite powder were characterized by XRD method, FT-IR and TG-DTA. The microstructures of nano-sized LTA type zeolite powder were observed by SEM. The local structures around Si for the products of nano-sized LTA type zeolite powder were characterized by measuring X-ray adsorption near edge structure (XANES) at BL02A in UV-SOR.

The evaluation of XRD for ground fine-zeolite and reference LTA was carried out. XRD results showed that after the mechanical mixing processing for 30 min and 120min the ground products were also identified to be LTA type. The results indicated that the obtained fine-zeolite products were LTA type zeolites. Products obtained after the mechanical mixing processing had the average particle of a few hundred nanometer in diameter, suggesting the nano-sized LTA zeoite powders were successfully obtained by after the mechanical mixing processing for 2 hs

Figure 1 shows the XANES spectra of zeolites and reference materials. As shown in Fig. 1, XANES spectra of sample obtained after the mechanical mixing processing for 30 min to 120 min the same spectra as the LTA without mechanical mixing. These results suggest nano-sized LTA zeoite powders possess the good crystallinity and also the same local structure of Si after the mechanical mixing processing.

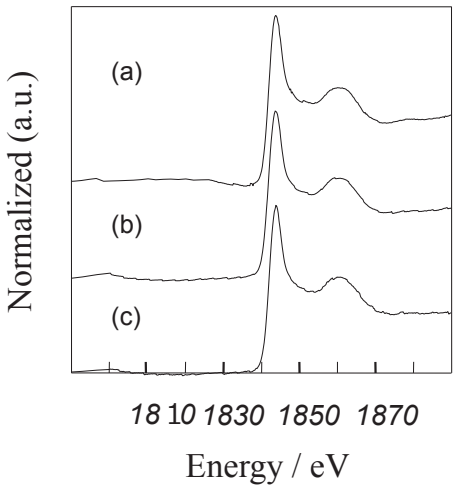

Fig. 1. Si XANES spectra of zeolites and reference materials. (a)commercial LTA, (b)30min, and (c)120min.

[1] C. D. Chang, A. J. Silvestri, Journal of Catalysis **47** (1977) 249–259.

[2] T. Wakihara, R. Ichikawa, J. Tatami, A. Endo, K. Yoshida, Y. Sasaki, K. Komeya and T. Meguro, Cryst. Growth Des. **11** (1977) 955–958.

[3] A. Nakahira, S. Nishimura, H. Aritani, T. Yamamoto S. Ueda, J. Mater. Sci. **36** (2001) 1885-89.

BL2A

Ag-L and P-K Edge XAFS Measurement of Antibacterial HAp

M. Sato[1], H. Sakaguchi[2], Y. Inoue[2] and A. Nakahira[1,2]

[1]*Kansai Center for Industrial Materials Research, Tohoku University, Osaka 599-8531, Japan*

[2]*Department of Material Science, Osaka Prefecture University, Osaka 599-8531, Japan*

Hydroxyapatite ($Ca_{10}(PO_4)_6(OH)_2$, HAp) is a chief component of our hard tissue and it shows excellent biocompatibility and osteoconductivity. Therefore, it has been widely used as an alternate of hard tissue in an orthopedic surgical procedure. However, bacterial infection has been a major problem in orthopedic surgery. Therefore, the development of a new implant which can prevent a bacterial infection during surgery is strongly desired.

There are many studies to provide an antibacterial effect for implant by the doping of some kinds of metal elements. In these elements, silver, copper and zinc are understood to show and excellent antibacterial effect with very small amount of use.

In this study, Ag doped HAp were prepared by conventional hydrothermal process, and local structure around P and Ag atom was investigated by XAFS measurement.

0.1 mol/L $Ca(NO_3)_2$, $(NH_4)_2HPO_4$ and $AgNO_3$, solutions were used as starting materials. These solutions were mixed up each other becoming the ratio of Ca to P of 1.67 and the ratio of Ag changed from 0.5 to 10 mol% for Ca of HAp in a Teflon vessel, and pH of mixed solution was adjusted to 10. After mixing, they were hydrothermally treated at 423 K for 24 hours. Obtained solutions were filtered and dried at 323 K for overnight.

Ag-L and P-K edge XANES spectra of obtained Ag-HAp powders were measured in a total electron yield mode and fluorescence mode by SDD detector using InSb double-crystal monochrometer at BL-2A station in UVSOR. For XAFS measurement, commercial HAp, $AgNO_3$ and $Ag_3(PO_4)$ were used as references.

From the XRD analysis, HAp generated for all samples as a main phase. In addition, metal Ag was generated for the sample prepared at the ratio of Ag more than 2 mol% for Ca of HAp. ICP measurement showed that the actual amount of Ag in obtained sample is about one tenth of additive amount.

Figure. 1 shows P-K edge XANES spectra of samples prepared in Ag ratio of 0.5 and 1 mol%. Since obtained P-K edge XANES spectra of sample was resembled that of commercial HAp, it is clarified that the local structure around P atom does not change by doping of Ag. From this result, the possibility of Ag substitution into HAp structure was suggested.

On the other hand, since we did not obtain the clear spectra for Ag-L edge of sample in this measurement, we will study continuously to obtain the clear Ag-L edge XAFS spectrum.

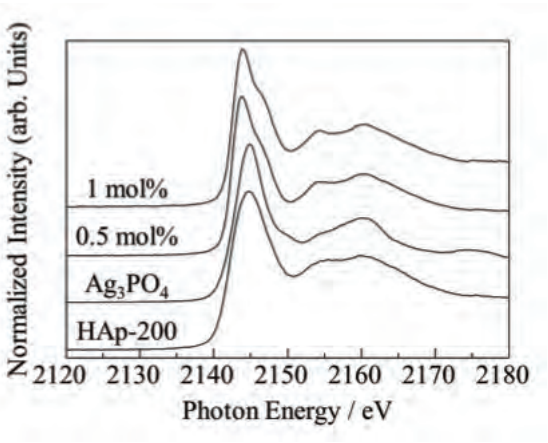

Fig. 1. P-K edge XANES spectra of obtained samples.

[1] M. Sato, S. Yamamoto, Y. Nishio, Y. Takamatsu and A. Nakahira, UVSOR Activity Report **38** (2011)115.

[2] M. Sato, Y. Kawabe, S. Misu, S. Hayashi and A. Nakahira, UVSOR Activity Report **39** (2012)81.

[3] M. Sato, T. Nagayasu, S. Hayashi and A. Nakahira, UVSOR Activity Report **40** (2013)126.

BL2A

Investigation of Local Structure of Ca-Based Materials Synthesized from Granulated Blast Furnace Slag

M. Sato[1], M. Togo[2], T. Morinaga[2], S. Fujihara[2] and A. Nakahira[1,2]
[1]*Kansai Center for Industrial Materials Research, Tohoku University, Osaka 599-8531, Japan*
[2]*Department of Material Science, Osaka Prefecture University, Osaka 599-8531, Japan*

Blast furnace slag (BF slag) is one of the industrial waste materials and generates about 25 million tons per year in Japan. BF slag mainly consisted from SiO_2, CaO and Al_2O_3. Fe, Ti and Mn are included as trace elements. By focusing on this composition of BF slag, it can be recognized that the ratio of Si, Ca and Al is close to a tobermorite, and the ratio of Si and Al is also close to a zeolite.

In a previous study, tobermorite, Ca-based layered double hydroxide (LDH) and calcium phosphate were successfully synthesized using BF slag. In these materials, tobermorite is one of the most important calcium silicate materials and has been widely used architectural materials such as autoclaved lightweight concrete (ALC) and fire-resistant building materials. Tobermorite has layer structure of that SiO_4 tetrahedra sandwiches CaO sheet and cation exchange ability by substituting a part of Si by Al ion.

It has been clarified that the Al substituted tobermorite has selectivity for cation such as alkali metal and alkali-earth metal ions.

Since tobermorite also has a high selectivity for Cs ion, it has been suggested that can use for handling of nuclear waste. Therefore, XAFS measurement was conducted to investigate a local structure around Si and Al atom of obtained tobermorite.

BF slag, quartz powder and CaO powder were used as starting materials. BF slag was ball-milled to become particle size less than 75μm. Ca/(Si+Al) ratio was controlled in the range from 0.8 to 1.2 by addition of quartz or CaO powder. Mixed powder and distilled water was encapsulated into a Teflon vessel, and then it was hydrothermally treated at 453 K for 24 and 48 h with rotation speed of 20 rpm. After that, obtained products were filtered and dried at 323 K for overnight.

Al-K and Si-K edge XANES spectra of obtained samples were measured by fluorescence mode by SDD using InSb double-crystal monochrometer for Si-K and KTP double-crystal monochrometer for Al-K at BL-2A station of UVSOR.

From the Si-K edge XANES spectra, the spectrum of sample prepared at Ca/(Si+Al) = 1.0 was resembled with that of commercial tobermorite, and significant change of spectrum by rotation during a hydrothermal synthesis did not observed .

Figure 1 shows Al-K edge XANES spectra of sample prepared by hydrothermal synthesis using BF slag. Obtained spectra showed similar trend to Si-K edge XANES spectra, and local structure around Al atom changed depending on the ratio between Ca and Si+Al. These results suggested that the Al-substituted tobermorite was synthesized by using BF slag, and the possibility to use tobermorite as not only architectural materials, but also environmental purification materials was indicated.

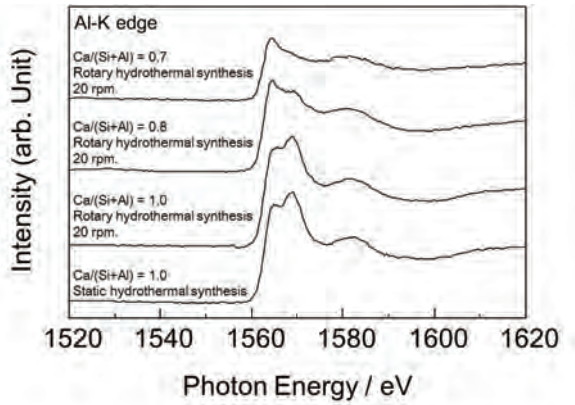

Fig. 1. Al-K edge XANES spectra of samples prepared by static and rotary hydrothermal synthesis at 453 K for 48 h.

BL2A

Structural Evaluation of Novel Piezoelectric Ceramics

A. Nakahira[1,2], H. Kanayama[1], T. Tagami[1], S. Togo[1], S. Fujihara[1], T. Morinaga[1], M. Sato[2] and H. Aritani[3]

[1]*Faculty of Engineering, Osaka Prefecture University, Gakuencho, Sakai 599-8531, Japan*

[2]*Kansai Center, IMR, Tohoku University, Gakuencho, Sakai 599-8531, Japan*

[3]*Saitama Institute of Technology, Fukaya 369-0293, Japan*

Piezoelectric ceramics are widely used as piezoelectric, electro-optic and non-liner optic devices in modern society. Among piezoelectric ceramics, PZT ($Pb(Zr_x,Ti_{1-x})O_3$) is used extensively in the world, but it contains lead damaging human health and environment. In order to solve this problem of PZT, the development of lead-free piezoelectric ceramics are desired. Much attention is attracted to niobium based complex oxide, $KNbO_3$ with the perovskite-type structure as one of the promising ceramics instead of PZT ceramics [1-3]. $KNbO_3$ ceramics have the higher curie temperature (435 °C) and energy conversion rate (0.69) of $KNbO_3$ than that of another post PZT materials.

$KNbO_3$ was synthesized by the electrode reaction process in KOH solution as electrolyte using metal niobium plate (10 × 20 × 0.2 mm) as an anode and carbon (C) rod (φ5 × 100 mm) as cathode. The distance between Nb and C electrodes was about 40 mm in the beaker. The reaction was continued until Nb plate was completely dissolved under 100 mA / cm^2 of current density supplied direct current power. Then, the precipitation obtained during the reaction was filtered and collected by centrifugation. The solid product was frequently washed and air-dried at 50 °C. For the comparison, $KNbO_3$ (KN-ref) as a reference material was prepared by the solid reaction process at 1150 to 1250 °C. Products were characterized with some techniques such as XRD, FT-IR, TG/DTA and the microstructures were observed with SEM. The local structures around K for the products of the solid product powder were characterized by measuring X-ray adsorption near edge structure (XANES) at BL02A station of UVSOR in Okazaki.

As a result of XRD diffraction patterns and SEM images, finely nano-sized $KNbO_3$ powder was synthesized in 1 M KOH solution. SEM observations indicated that obtained $KNbO_3$ powder with several hundred nanometer in diameter were synthesized. On the contrary, $KNbO_3$ (KN-ref) as a reference material prepared by the solid reaction process had the particle size with 5 to 10 micrometer in diameter, i.e. micro-sized $KNbO_3$ (KN-ref) powders. These results suggest that the fine nan-sized $KNbO_3$ powders were successfully obtained from the electrode reaction process.

Figure 1 shows the XANES spectra of synthesized by the electrode reaction process products (nano KN) and a reference material ($KNbO_3$: KN-ref). XANES spectra of sample obtained the same spectra as the reference micron-sized $KNbO_3$ (KN-ref). These results suggest the fine nano-sized $KNbO_3$ powders synthesized by the electrode reaction process possess the good crystallinity and also the same local structure of K–edge as the reference $KNbO_3$ (KN-ref).

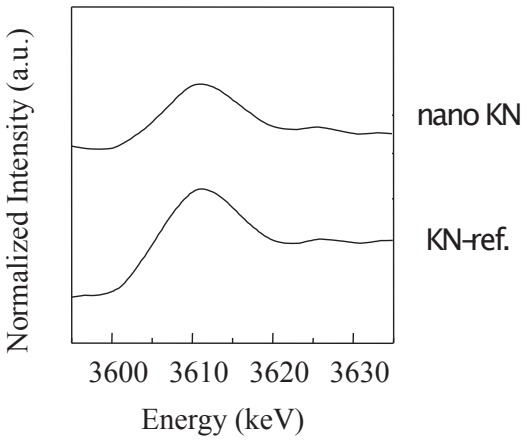

Fig. 1. K-edge XANES spectra of nano-sized $KNbO_3$ and a reference material (micro-sized $KNbO_3$ (KN-ref)).

[1] T. R. Shrout *et al*., Journal of Electroceramics **19** (2007) 111-124.
[2] I. Nowak *et al*., Chemical Reviews **99** (1999) 3603-3624.
[3] C. H. Lu *et al*., Materials Letter **34** (1998) 172-176.

BL3B

Intrinsic Luminescence and Energy Transfer from Self-Trapped Excitons in Scandium Borates upon Vacuum UV Excitation

N. Kodama, A. Abe, Y. Morisawa, T. Sakashita and T. Takahashi
Faculty of Engineering and Resource Science, Akita University, Akita 010-8502, Japan

The intrinsic luminescence characteristics were investigated for self-trapped excitons (STEs) in polycrystalline samples of the binary scandium borates $LaSc_3(BO_3)_4$(LSB), $YSc(BO_3)_2$(YSB), and $LuSc(BO_3)_2$(LuSB), in which absorption of vacuum ultraviolet (VUV) light by the host can facilitate efficient energy transfer from the STEs to Re^{3+} (Re^{3+} = Sm^{3+}, Gd^{3+}, or Tb^{3+}) ions.

Emission and excitation spectra were measured at temperatures in the range 7.8-293 K using the Ultraviolet Synchrotron Orbital Radiation (UVSOR) facility. All of the borates were found to exhibit intense intrinsic emissions in the UV region under VUV excitation at 70 and 160 nm, and the decay times were determined. These emissions were assigned to recombination of STEs possibly associated with bandgap excitations, or to molecular transitions in the BO_3^{3-} group. The emission spectra for undoped LSB under VUV excitation at temperatures of 7.8-293 K were characterized by three distinct broad bands at 253 nm (I), 323 nm (II), and 379 nm (III), as shown in Fig. 1(a). These features are similar to those found in the emission spectra for single-crystal LSB. The emission spectra for undoped YSB and LuSB at 293 K are shown in Fig. 1(b). For undoped YSB, two broad emission bands were present in the temperature range 15-293 K, the first centered at 258 nm (I) and the second at 320 nm (II). Undoped LuSB exhibited a single strong broad emission at 250 nm in the temperature range 14.9-293 K.

For undoped LSB, the decay times for emissions I, II, and III were less than 10 ns, 115 ns and 3.4 μs, respectively. For undoped YSB, the decay time for emissions I and II were 120 and 550 ns, respectively. By analogy with the STE states in alkali halides [1], the fast decay components II in LSB and I in YSB originate from singlet STE states with center and/or off-center configurations. The fast component I in LSB may have the same origin, and may also have a contribution from energy transfer to impurities or defects near the STE. In contrast, the slow components III in LSB and II in YSB are thought to originate from a triplet STE with an off-center configuration. Energy transfer from the STEs to Re^{3+} ions at temperatures between 7.8 or 14.9 and 293 K was evidenced by a decrease in STE emissions and shortened decay times in LSB doped with Sm^{3+}, Gd^{3+} or Tb^{3+}, and YSB doped with Gd^{3+}. The STE emission intensity decreased with increasing Re^{3+} concentration (1-40 at.%), accompanied by the appearance of intense emissions associated with Re^{3+} at 7.8 K for Sm^{3+}-doped LSB (Fig. 2(a)), and at 14.9 K for Tb^{3+}-doped LSB (Fig. 2(b)). This suggests efficient energy transfer from the STEs to the Re^{3+} ions. Re^{3+} doping also caused a decrease in the decay times for the STE emissions, which is consistent with the decrease in the time-averaged STE emission intensity. This provides further evidence for energy transfer from the STEs to the Re^{3+} ions. In the case of LSB at a temperature of 293 K, the energy transfer rates determined from time-resolved measurements were 1.6×10^6 s^{-1} (STE II) and 7.0×10^{-4} s^{-1} (STE III) for 5 at.% Gd^{3+} doping, and 2.1×10^6 s^{-1} (STE II) and 8.0×10^{-4} (STE III) for 5 at.% Tb^{3+} doping.

The observed energy transfer rates are within an order of magnitude of estimates based on dipole-dipole or dipole-quadrupole energy transfer. For both LSB and YSB, the ratio of the STE II and III emission intensity in doped samples to that in undoped samples gradually increased with temperature. This temperature dependence is shown in Fig. 3 for Sm^{3+}- and Tb^{3+}-doped LSB, and suggests that energy transfer from STEs to Re^{3+} ions is thermally activated and probably related to exciton mobility.

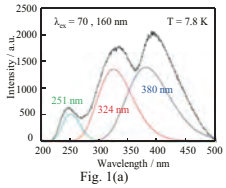

Fig. 1(a)

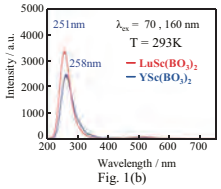

Fig. 1(b)

Fig. 1. Emission spectra for undoped samples at excitation wavelengths of 70 and 160 nm: (a) LSB at 7.8 K, and (b) YSB and LuSB at 293 K.

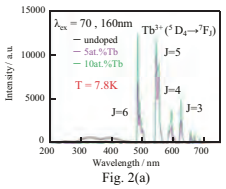

Fig. 2(a)

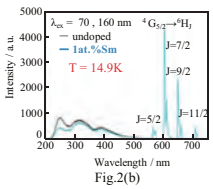

Fig.2(b)

Fig. 2. Emission spectra for samples at 15 K and excitation wavelengths of 70 and 160 nm : (a) undoped and Sm^{3+}-doped LSB, and (b) undoped and Tb^{3+}-doped LSB.

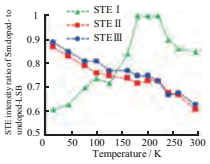

Fig.3(a)

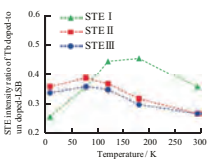

Fig.3 (b)

Fig. 3. Temperature dependence of ratio of STE intensity for doped LSB to that for undoped LSB: (a) Sm^{3+} doping, and (b) Tb^{3+} doping.

[1] K. Kan'no *et al.*, Pure & Appl. Chem. **69** (1997) 1227.

BL3B

Analysis of Optical Properties for Pr^{3+}-Doped $Y_3Sc_2Al_3O_{12}$

S. Watanabe[1], K. Ogasawara[1], S. Ishii[2] and M. Kitaura[2]
[1]*School of Science and Technology, Kwansei Gakuin University, Sanda 669-1337, Japan*
[2]*Deptartment of Physics, Faculty of Science, Yamagata University, Yamagata 990-8560, Japan*

The 4*f*-4*f* and 4*f*-5*d* transitions of lanthanide (Ln^{3+}) ions have drawn attention for potential application as luminescent materials. The garnet-type oxides are chemically and structurally stable among inorganic compounds. Therefore, to date, Ln^{3+}-doped garnet-type oxides have been widely used as commercial materials. The analysis of the optical properties due to the 4*f*-4*f* and 4*f*-5*d* transitions, however, remains limited, since they originate in the complicated mulitplet structures. In addition, the many-body effects and relativistic effects coexist in these issues. In this study, the optical properties of Pr^{3+}-doped $Y_3Sc_2Al_3O_{12}$ have been investigated, experimentally and theoretically.

Pr^{3+}-doped $Y_3Sc_2Al_3O_{12}$ polycrystalline sample was prepared by the solid-state reaction. The concentration of Pr^{3+} ion was 1 mol%. The experimental excitation spectrum at 10 K was measured monitoring the emission at 333 nm. We analyzed the $4f^2$-$4f^15d^1$ transitions of Pr^{3+} ions in $Y_3Sc_2Al_3O_{12}$ based on first-principles many-electron configuration interaction calculations [1, 2].

Figure 1 shows the experimental excitation spectrum and theoretical absorption spectrum for Pr^{3+}-doped $Y_3Sc_2Al_3O_{12}$. The fundamental absorption of $Y_3Sc_2Al_3O_{12}$ host crystal is located above 6.7 eV. This result agrees with the excitation spectrum of non-doped $Y_3Sc_2Al_3O_{12}$ host crystal. Compared to the theoretical $4f^2$-$4f^15d^1$ absorption spectrum of Pr^{3+}, the peaks at 4.2 – 6.0 eV can be attributed to the $4f^2$-$4f^15d^1$ transitions of Pr^{3+} ions The configuration analysis of many-electron calculations clearly indicates that the separations among main peaks are due to crystal field splitting of the Pr-5*d* levels, while splitting between the main peaks and subpeaks is due to spin-orbit interaction of the Pr-4*f* levels. The subpeaks are due to transitions to two-electron excitation states based on a shake-up process.

Figure 2 shows the emission spectra for Pr^{3+}-doped $Y_3Sc_2Al_3O_{12}$ measured at 10 K under excitation at various photon energies. The sharp peaks at 480 – 800 nm originate in the $4f^2$intraconfiguration transitions of Pr^{3+} ions, which can be attributed to the $^3P_0 \rightarrow {}^3H_J$ transitions. The broad bands at 300 – 400 nm are considered to be either the excitonic emission of $Y_3Sc_2Al_3O_{12}$ host crystal or the 5*d*-4*f* emission of Pr^{3+} ions. Unfortunately, we have little information on these bands. Further spectroscopy experiments in the UV-VUV region are needed to assign the origins of these two bands.

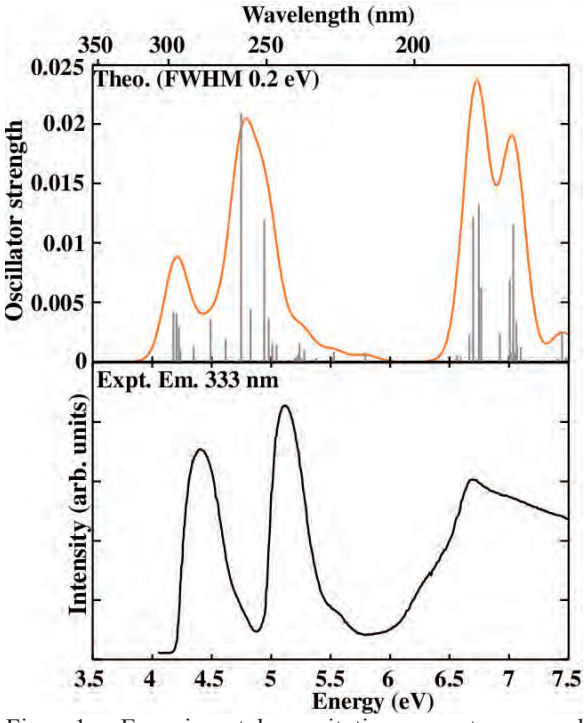

Fig. 1. Experimental excitation spectrum and theoretical absorption spectrum for Pr^{3+}-doped $Y_3Sc_2Al_3O_{12}$.

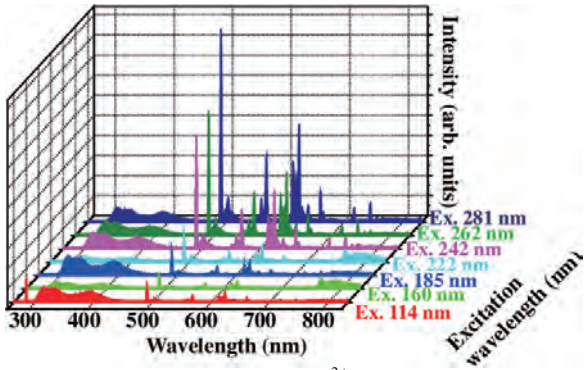

Fig. 2. Emission spectra for Pr^{3+}-doped $Y_3Sc_2Al_3O_{12}$.

[1] K. Ogasawara *et al.*, Phys. Rev. B **64** (2001) 143.
[2] S. Watanabe *et al.*, Phys. Rev. B **81** (2010) 125128.

BL3B

Optical Spectra and Electronic Structure of $SrCeO_3$ Crystals

H. Numata[1], M. Kitaura[1], S. Watanabe[2], K. Ogasawa[2], S. Kurosawa[3,4], K. Yubuta[3], A. Ohnishi[1] and M. Sasaki[1]

[1]*Department of Physics, Faculty of Science, Yamagata University, Yamagata 990-8560, Japan*
[2]*Department of Chemistry, School of Science and Technology, Kwansei University, Sanda 669-1337, Japan*
[3]*Institute for Materials Research, Tohoku University, Sendai 980-8679, Japan*
[4]*New Industry Creation Hatchery Center, Tohoku University, Sendai 980-8679, Japan*

CeO_2 is characterized by so-called mixed valency, which is caused by mixing between $4f^0$ and $4f^1\underline{L}^{-1}$ configurations in the ground state, where $\underline{L}^{-1}$ denotes the hole in the valence band mainly composed of O-2*p* orbitals [1]. This feature comes from hybridization between the Ce-4*f* and O-2*p* orbitals. Indications of the mixed valency have been found in photoemission and X-ray absorption spectra [2]. On the other hand, it has been pointed out that the reflectivity spectrum also exhibits an evidence for the mixed valency: A prominent reflectivity peak around 13 eV has been assigned to an appearance of $4f^2\underline{L}^{-2}$ configuration.

$SrCeO_3$ is also regarded as a mixed valent compound [3], because of similarities in photoemission and X-ray absorption spectra. In addition, this material is known as one of typical proton conductors. Despite the important material in both of basic science and industrial application, the fundamental optical constant spectra such as absorption and reflectivity spectra, and its electronic structure have been few reported so far. One of the reasons for this is the difficulty for the crystal growth of $SrCeO_3$. Recently, we have succeeded the crystal growth of $SrCeO_3$ by using a Floating zone technique.

In the present study, we have measured reflectivity and absorption edge spectra of $SrCeO_3$ crystals at 300 K. The results are shown in Fig. 1(a). As indicated by a red solid curve, the fundamental absorption starts at 2.2 eV. This energy is lower than that determined from the diffuse refection spectrum [4]. The reflectivity spectrum (red solid curve) consists of three parts: 3.4-6.3 eV (part I), 6.3-16.5 eV (part II), and 16.5-40 eV (part III). Referred to the calculated energy band structure, the part I, II, and III are assigned to O-2*p*→Ce-4*f*, O-2*p*→Ce-5*d*, Ce-5*p*→Ce-5*d* transitions, respectively. The agreement between experimental and theoretical spectra is good, as shown in Figs. 1(a) and 1(b). Several peaks in the part II are due to the crystal field splitting of the Ce-5*d* orbital. In the part III, a peak appears around 27.9 eV. Considering the $5p^55d^1$ configuration of a Ce^{3+} ion, it is expected that the transition between $^1P_1$ and $^1S_0$ multiplets occurs in the part III. Thus, we assign the 27.9 eV peak to the $^1S_0 \rightarrow {}^1P_1$ transition. Drastic increase in reflectivity can be seen below 3.4 eV. This would be influenced by the reflection at the back of the crystal, because it occurs in the energy region below the fundamental absorption edge. Since the absorption coefficient is negligibly weak below 3.4 eV, the monochromatic synchrotron radiation light can penetrate inside the crystal.

As mentioned above, it is expected that the experimental reflectivity spectrum exhibits a peak due to the excitation of the $4f^2\underline{L}^{-2}$ configuration. Actually, Fig. 1(a) shows such a peak around 12 eV. On the other hand, Fig. 1(b) also exhibits a prominent peak around 11.9 eV. Since the 11.9 eV peak is connected to the critical point of the joint density of state, it is not likely to attribute the 11.9 eV peak in Fig. 1(a) to the excitation of the $4f^2\underline{L}^{-2}$ configuration.

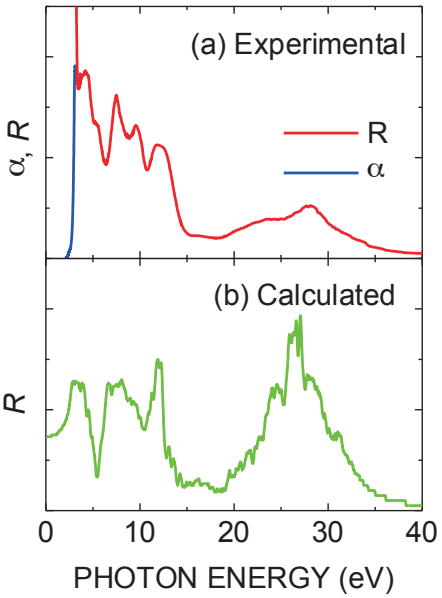

Fig. 1. (a) Reflectivity (red line) and absorption adge (blue line) spectra of $SrCeO_3$ crystals, measured at 300 K. (b) Theoretical reflectivity spectrum (green line).

[1] A. Fujimori *et al.*, Phys. Rev. B **28** (1983) 2281.
[2] M. Niwano *et al.*, J. Phy. Soc. Jpn. **57**(1988) 1489.
[3] M. Matsumoto *et al.*, J. Electron Spectrosc. Relat. Phenom. **78** (1996) 179.
[4] F. Goubin *et al.*, Chem. Mater. **16** (2004) 662.

BL3B

Energy Transfer from I^- Centers to Au^- Centers in Co-doped NaCl:I^-, Au^- Crystals

T. Kawai and K. Yuasa
Graduate School of Science, Osaka Prefecture University, Sakai 599-8531,

Alkali halide crystals have the wide band-gap up to the vacuum ultra violet energy region and are a suitable candidate host for doping of impurity ions. Though many experimental investigations have been performed on alkali halide crystals doped with impurity ions, energy transfer between two kind of impurity ions in co-doped alkali halide crystals are comparatively less studied [1, 2]. In this study, we have investigated the energy transfer from I^- centers to Au^- centers in NaCl crystals co-doped with I^- and Au^- ions.

Figure 1 shows the absorption spectrum of NaCl:Au^- and the luminescence spectrum of NaCl:I^- at room temperature (RT). In NaCl:Au^-, the A, C, D_1, and D_2 absorption bands due to the Au^- centers are observed at 4.18, 5.54, 6.25, and 7.10 eV, respectively [3]. In NaCl:I^-, the luminescence band due to the one-center type localized exciton appears at 5.32 eV [4]. The 5.32 eV luminescence band in NaCl:I^- has an overlap with the C absorption band at 5.54 eV in NaCl:Au^-. The fact indicates the potential of the energy transfer from the I^- center to the Au^- center in co-doped NaCl:I^-, Au^- crystals.

Figure 2 shows the excitation spectra in NaCl:Au^-, NaCl:I^-, and co-doped NaCl:I^-, Au^- crystals at RT. The 5.32 eV luminescence band in NaCl:I^- is efficiently excited in the energy region between 6.5 and 7.2 eV, where the absorption band due to one-center type localized exciton is located. In NaCl:Au^-, the luminescence band at 3.99 eV, which corresponds to the A' luminescence band due to the Au^- centers, is efficiently excited at the A, C, D_1, and D_2 absorption bands. In the co-doped NaCl:I^-, Au^- crystal, the excitation spectrum for the A' luminescence band at 3.99 eV has the broad band around 6.66 eV in addition to the A, C, D_1, and D_2 bands. Since the 6.66 eV band corresponds to the excitation band for the 5.32 eV luminescence band in NaCl:I^-, the fact implies the existence of the energy transfer from the I^- center to the Au^- center in the co-doped NaCl:I^-, Au^- crystal.

From the absorption intensity of respective absorption bands, the concentrations of the I^- and Au^- centers in the co-doped NaCl:I^-, Au^- crystal are estimated to be about 3.0×10^{19} and 1.0×10^{15} cm^{-3}, respectively. Thus, the average distance between the I^- center and its nearest neighboring Au^- center is about 2.0 nm. The distance of 2.0 nm indicates the potential of the energy transfer mechanism of Förster type. In order to clarify the energy transfer mechanism from the I^- center to the Au^- center in the co-doped NaCl:I^-, Au^- crystals, the measurements of the decay kinetics of the luminescence are needed.

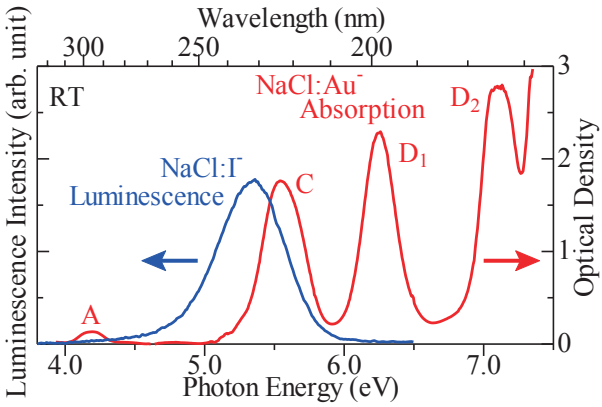

Fig. 1. Luminescence spetrum (blue) of NaCl:I^- and absorption spectrum (red) of NaCl:Au^- at RT.

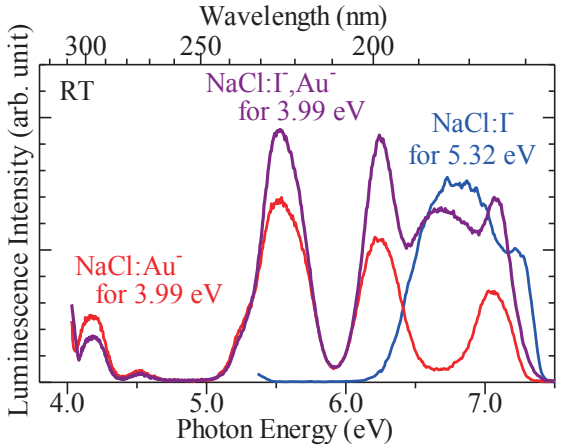

Fig. 2. Excitation spectra of NaCl:Au^- (red), NaCl:I^- (blue), and co-doped NaCl:I^-, Au^- (purple).

[1] A. F. Muñoz and J. O. Rubio, Phys. Rev. B **38** (1988) 9980.
[2] A. Méndez, *et al.*, J. Lumin. **79** (1998) 269.
[3] F. Fischer, Z. Physik **231** (1970) 293.
[4] I. Akimoto, *et al.*, Phys. Status Solidi C **6** (2009) 342.

BL3B

Photoluminescence Study on Structural Deformation of $LaAlO_3$ Induced by Ion Implantation

M. Harima, Y. Horii, T. Morimoto and Y. Ohki
Waseda University, 3-4-1 Ohkubo, Shinjuku-ku, Tokyo 169-8555, Japan

High permittivity (high-*k*) materials such as $LaAlO_3$ or $YAlO_3$ are expected as a gate insulator in advanced MOS devices. In the manufacturing process of semiconductors, ion implantation through a gate dielectric to a Si substrate is often used to adjust the threshold voltage of a metal oxide semiconductor (MOS) device [1]. However, ion implantation may induce localized electronic states in the forbidden band and defects resulting from degradation of crystallinity.

In the present study, the effects of implantation of P^+ or B^+ ions on the structural change of single crystal $LaAlO_3$ were examined. Before and after ion implantation, optical absorption, photoluminescence (PL) and X-Ray diffraction (XRD) were measured.

In Fig. 1, an optical absorption edge is seen at about 5.6 eV. This edge, which corresponds to the band gap energy of $LaAlO_3$, is scarcely affected by the ion implantation.

Figure 2 shows PL spectra. As shown in Fig. 2(a), a broad PL peak due to the oxygen vacancy appears at around 2.8 eV [2]. The intensity of this PL, which is also detectable in amorphous samples [3], scarcely changes after the ion implantation. In addition, three sharp PL peaks were detected at 1.62, 1.65, and 1.69 eV as shown in Fig. 2(b). The intensities of the three PLs become smaller by ion implantation. These PLs are due to Cr^{3+} that are present in $LaAlO_3$ as impurities [4]. It is known that this type of PL appears only when the samples are crystalline [5]. These results indicate that the ion implantation degrades the crystallinity of $LaAlO_3$.

Figure 3 shows in-plane XRD spectra. The XRD peak intensity at $2\theta = 23.5^{\circ}$ is decreased by the ion implantation. One important thing is that the depth measurable by XRD is too shallow to evaluate the crystallinity of the area where ions had passed through. In this regard, PL measurements can cover the whole ion-implanted area.

To conclude, it has become clear that deformation of crystal structure of $LaAlO_3$ is induced by ion implantation.

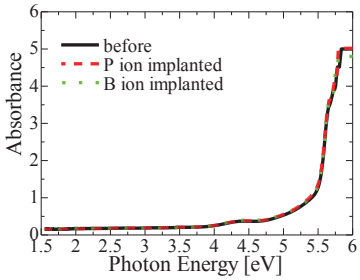

Fig. 1. Optical absorption spectra observed before and after the implantation of P^+ or B^+ ions at a fluence of 10^{15} cm^{-2}. Note that the three spectra overlap each other.

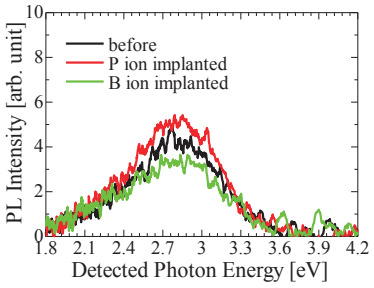

(a)

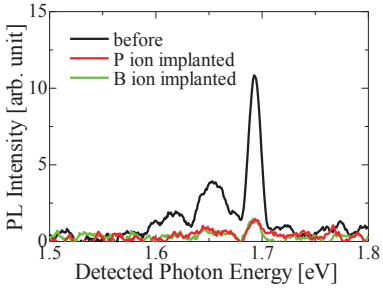

(b)

Fig. 2. PL spectra induced by the irradiation of 5.0-eV (a) and 6.4-eV (b) photons observed before and after the implantation of P^+ or B^+ ions at a fluence of 10^{15} cm^{-2}.

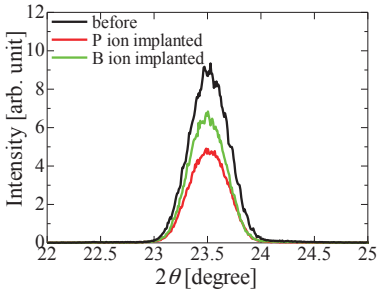

Fig. 3. In-plane XRD patterns observed before and after the implantation of P^+ or B^+ ions at a fluence of 10^{15} cm^{-2}.

[1] B. Razavi and T. Kuroda, *Design of Analog CMOS Integrated Circuits* (Tokyo; Maruzen, 2003).
[2] E. Hirata *et al.*, Jpn. J. Appl. Phys. **49** (2010) 091102.
[3] H. Nishikawa *et al.*, Phys. Rev. Lett. **72** (1994) 2101.
[4] D. Yamasaka *et al.*, Jpn. J. Appl. Phys. **52** (2013) 071501.
[5] J. Heber *et al.*, Z. Phys. **246** (1971) 261.

BL3B

Observation of VUV Emission from Er/Nd:LuF_3 Crystals

S. Kurosawa[1,2], J. Pejchal[2], M. Kitaura[3], K. Fukui[4], K. Nakagawa[5], S. Watanabe[6], A. Ohnishi[3], K. Ogasawara[6], M. Hasumoto[7] and M. Sakai[7]

[1] *Institute for Materials Research, Tohoku University, Sendai 980-8679, Japan*
[2] *New Industry Creation Hatchery Center, Tohoku University, Sendai 980-8679, Japan*
[3] *Deptartment of Physics, Faculty of Science, Yamagata University, Yamagata 990-8560, Japan*
[4] *Department of Electrical and Electronics Engineering, University of Fukui, Fukui 910-8507, Japan*
[5] *Graduate School of Human Development and Environment, Kobe University, Kobe 657-8501, Japan*
[6] *School of Science and Technology, Kwansei University, Sanda 669-1337, Japan*
[7] *UVSOR facility, Institute for Molecular Science, Okazaki 444-8585, Japan*

The development of new fast radiation detection systems employing the vacuum ultraviolet (VUV) scintillators has been started in the recent past. In these systems, the fast VUV scintillators can be coupled with advanced VUV photodetectors, such as position-sensitive gas electron multipliers (GEM), micro-pixel chambers or VUV-sensitive photomultipliers with CsI-coated photocathodes [1,2]. One of the candidates considered for the VUV scintillator is the Nd-doped $BaLu_{1.2}Y_{0.8}F_8$ (BaYLuF). The fast VUV emission around 185 nm with a decay time of several nanoseconds is due to the allowed 5d-4f transition of the Nd^{3+} ion. Even more favorable properties, such as significantly elevated scintillation efficiency and emission shifted to even shorter wavelengths were found for LuF_3 single crystals [3]. Shorter emission wavelength usually matches better the sensitivity of the mentioned VUV photodetectors.

Recently, we tried to improve the energy transfer from the host matrix to the Nd^{3+} luminescence center by Tm-codoping. As the Tm^{3+} 5d-4f emission spectrum coincides with the Nd 4f-5d absorption band, the energy would migrate over the Tm^{3+} 5d levels to the Nd^{3+} ones. This was successfully proved [4], even though the improvement of the overall scintillation efficiency was not significant.

Since Er^{3+} has also emission lines in the VUV region, other co-dopant effect with Er is investigated in this study; LuF_3 codoped with 1-mol% Er / Nd 1 –mol% and 1 mol% Er doped LuF_3 samples were grown by micro-pulling down method. In order to show the energy transfer, we measured the emission spectra using BL3B beam line at UVSOR.

Figure 1 shows the emission spectra of the LuF_3Er1% sample excited at 135nm at 9K and LuF_3Er1%Nd1% excitd at 145nm at 9K. The result for Er-doped sample shows presence of both low-spin and high-spin transitions at 160 and 165nm, respectively. For the ErNd codoped sample no Er^{3+} emission is observed at all, even though the sample is excited in the Er^{3+} absorption band. This proves the energy transfer from the Er^{3+} to Nd^{3+} ions.

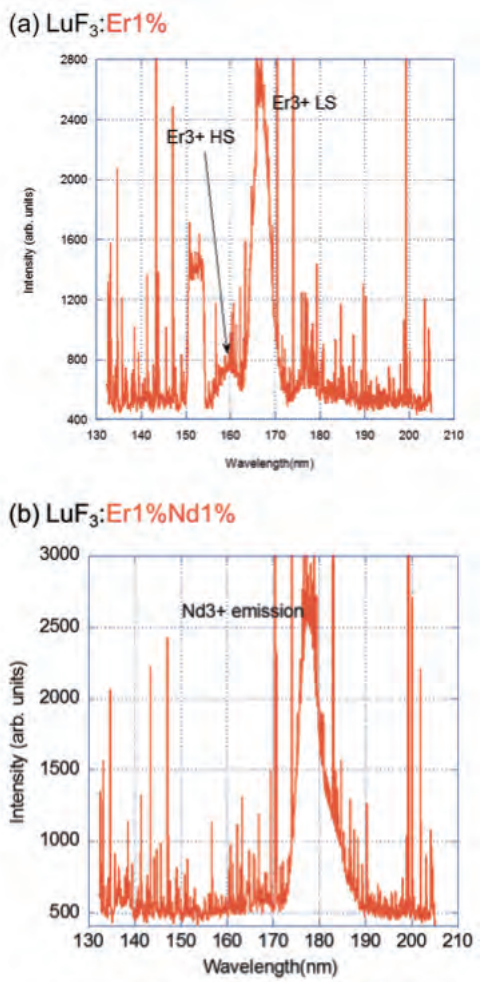

Fig. 1. Emission spectra of the LuF_3Er1% sample excited at 135nm at 9K (a) and LuF_3Er1%Nd1% excitd at 145nm at 9K (b).

[1] R. Chechik, A. Breskin, Nucl. Instr. and Meth. A **595** (2008) 116-131 and references therein.
[2] S. Kurosawa, J. Pejchal *et al*., J. Instrumentation **7** (2012) C03013.
[3] T. Yanagida, N. Kawaguchi, K. Fukuda *et al*., Nucl. Instr. Meth. A **659** (2011) 258–261.
[4] J. Pejchal, K. Fukuda, M. Nikl *et al*., IEEE Trans. Nucl. Sci. **59** (2012) 2177-2182.

BL3B

Optical Spectroscopy of Rare-Earth Doped $Y_3Al_5O_{12}$ (RE=Ce, Eu, Tb, Pr) Single Crystals

M. Yamaga, K. Takagi, T. Kishita, D. Susuki and H. Watanabe
Department of Mathematical and Design Engineering, Gifu University, Gifu 501-1193, Japan

Current white LEDs with high efficiency and brightness are composed of an InGaN-based blue LED and a yellow phosphor in the powder form of Ce^{3+}-doped $Y_3Al_5O_{12}$ (Ce:YAG). As the emission from Ce:YAG lacks the red component of the spectrum, the white light has a low color-rendering value. In order to obtain warm white light and an appropriate color rendering value, it is required to add the red emission by codoping Ce^{3+} and other rare-earth ions, such as Pr^{3+}, Eu^{3+} and Tb^{3+}. Such enhancement of the red component may be achieved through energy transfer between Ce^{3+} and codoped ions.

Rare-earth doped YAG single crystals were prepared using the Czochralski method by NIMS. Optical measurements at 300 K were done at BL3B.

Figure 1 shows the optical absorption spectra of Ce:Pr:YAG, Ce:Eu:YAG, Ce:Eu:Tb:YAG, and Ce:YAG. The absorption spectrum of Ce^{3+} in YAG consists of four bands with peaks at 205, 228, 340 and 458 nm, being due to the 4f→5d transitions of Ce^{3+}. In Ce:Pr:YAG, the intense broad bands at 237 and 290 nm other than the Ce^{3+} bands are due to the 4f→5d transitions of Pr^{3+}. The fairly weak lines around 600 nm is assigned to the $^3H_4 \rightarrow {}^1D_2$ transition of Pr^{3+}. The intense broad band below 240 nm in Ce:Eu:YAG is due to the charge transfer transitions to Eu^{3+} or the 4f→5d transitions of Eu^{3+}, whereas the fairly weak line at 400 nm is due to the $^7F_0 \rightarrow {}^5D_3$ transition of Eu^{3+}. In Ce:Eu:Tb:YAG, a new intense broad band with a peak at 270 nm other than the broad bands in Ce:Eu:YAG is due to the 4f→5d transitions of Tb^{3+}.

Figure 2 shows the emission spectra observed in (a) Ce:YAG, (b) Ce:Pr:YAG, (c) Ce:Eu:YAG, and (d) Ce:Eu:Tb:YAG. Excitation at 340 and 458 nm in the Ce^{3+} absorption bands for (a) Ce:YAG produced the broad emission bands with double peaks due to the 5d→4f ($^2F_{5/2}$, $^2F_{7/2}$) transitions of Ce^{3+}. In (b) Ce:Pr:YAG, excitation at 610 nm, corresponding to the $^3H_4 \rightarrow {}^1D_2$ transition of Pr^{3+}, produced the several sharp emission lines in the range from 610 to 830 nm, being assigned to the $^1D_2 \rightarrow {}^3H_J$ (J=4,5,6) transitions. The emission spectrum excited at 291 nm consists of two broad bands at 320 and 380 nm, several sharp weak lines in the wide range from 490 to 830 nm, and the weak Ce^{3+} emission band. On the other hand, excitation at 458 nm produced the weak Pr^{3+} emission lines at 610, 640 and 830 nm other than the intense Ce^{3+} emission band. In (c) Ce:Eu:YAG, the emission spectrum excited at 220 nm consists of the weak sharp lines at 592, 609, 630, and 709 nm due to the $^5D_0 \rightarrow {}^7F_J$ (J=1,2,3,4) transitions of Eu^{3+}. In (d) Ce:Eu:Tb:YAG, excitation at 271 nm produced the intense sharp lines at 385 nm and (490, 550, 590 and 625) nm and the weak Ce^{3+} emission band. These sharp lines are assigned to the $^5D_3 \rightarrow {}^7F_6$ and $^5D_4 \rightarrow {}^7F_J$ (J=6,5,4,3) transitions in this series. The emission spectrum excited at 220 nm consists of the sharp lines from both Eu^{3+} and Tb^{3+} and the Ce^{3+} emission band.

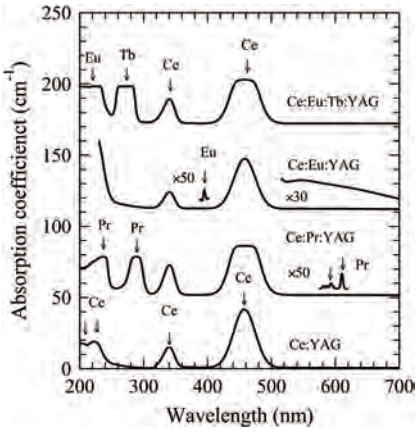

Fig. 1. Absorption spectra for rare-earth doped YAG crystals.

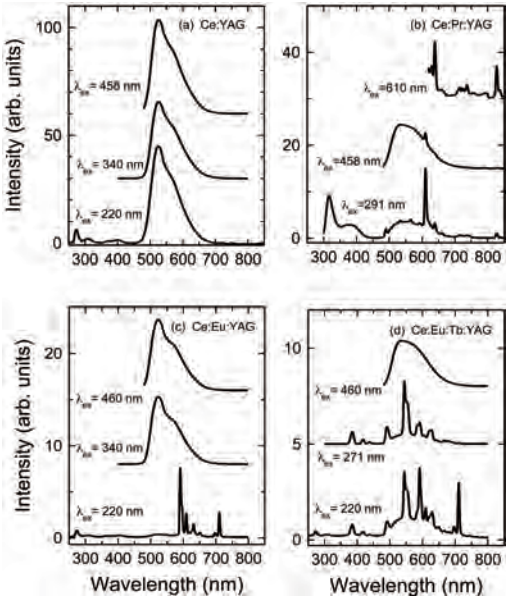

Fig. 2. Emission spectra for rare-earth doped YAG crystals.

BL3B

Optical Properties of Amorphous Carbon Nitride Thin Films

D. Itoh[1], K. Fukui[1] and K. Yamamoto[2]

[1]*Department of Electrical and Electronics Engineering, University of Fukui, Fukui 910-8507, Japan*

[2]*Far-Infrared Region Development Research Center, University of Fukui, Fukui 910-8507, Japan*

Amorphous Carbon Nitride (a-CN_x) is known to have interesting mechanical, electrical and optical properties. In the case of optical properties, it is expected that a-CN_x becomes cheap white LED material, because photoluminescence (PL) of a-CN_x spreads over the visible (VIS) region. However, PL spectrum of a-CN_x has sample preparation condition dependences. Recently, it is found that laser irradiated a-CN_x thin film after depositing shows much higher PL intensity than that of as-deposited a-CN_x thin film [1]. Then, we have been measuring laser irradiated a-CN_x to investigate its luminescence mechanism and growth condition dependences by using combined excitation emission (CEE) spectroscopy.

All samples are deposited on Si substrates by the RF-sputtering method at Ryukoku University. Their thickness is about 1 um. Laser-irradiation time to as-deposited samples is 240 minutes by using He-Cd laser (325 nm) with 20 mW. All CEE spectra have been measured at BL3B [2].

Figures 1 and 2 show CEE spectra at 20 K of as deposited (a-CN_x(A)) and laser irradiated a-CN_x thin films (a-CN_x(L)), respectively. Higher intensity regions are represented by warm colors. PL spectra widely spread in VIS region, though their width becomes narrower after laser irradiation. Photon energies of PL peak and PL excitation of both a-CN_x(A) and a-CN_x(L) are ~3.3 eV and 4.5, 5.5 eV, respectively. However, maximum intensity of a-CN_x(L) is 90 times larger than that of a-CN_x(A).

Figure 3 shows emission spectra of a-CN_x(A) and a-CN_x(L) at the excitation energies of 4.6 eV and 5.5 eV. Asymmetric line shape of each spectrum can be decomposed by two Gaussian type emission bands. Higher energy side band has its peak at 3.5 eV in all spectra. However, lower energy side peak shifts from 2.9 eV to 3.1 eV after laser irradiation. These higher and lower energies are correspond to the energy gaps between π* and π, σ* and N_{LP} (nitrogen lone pair) bands, respectively, following from Nitta's band diagram [3]. According to C 1s XPS results, contribution of sp^2 bonding decreases and that of sp^3 one increases after laser irradiation. Since these XPS results are probably explain as the decrease of the overlap between σ* and π* bands, and increase energy gap of N_{LP}-σ* [4] after laser irradiation. Then, it is supposed that the degree of hybridization of σ* and π* bands is important to understanding the effect of the laser irradiation.

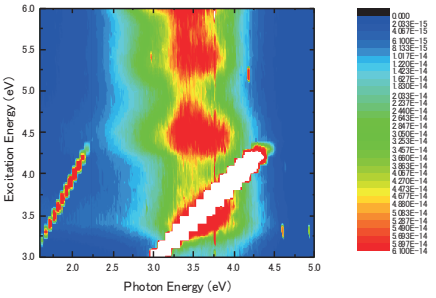

Fig. 1. CEE Spectrum of as-deposited a-CN_x.

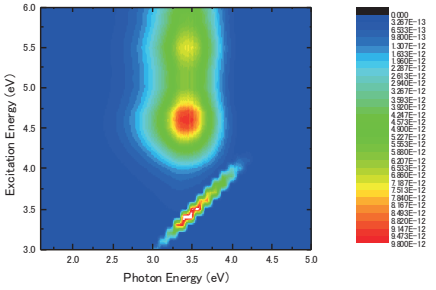

Fig. 2. CEE Spectrum of laser irradiated a-CN_x.

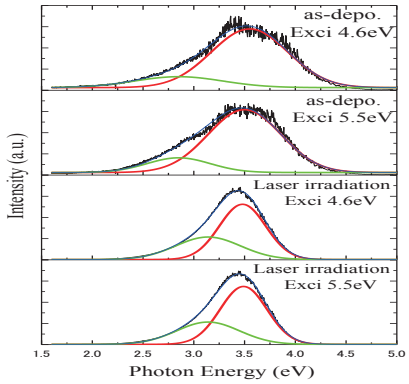

Fig. 3. Emission Spectra of as-deposited and laser irradiated a-CN_x at the excitation energies of 4.6 and 5.5 eV.

[1] M. Satake *et.al.,* 2013 JSAP Autumn Meeting–28p-PB3-11.

[2] K. Fukui *et.al.,* J synchrotron Rad. **21** (2014) 452.

[3] S. Nitta, Oyo Buturi **69** (2000) 7 (in Japanese).

[4] Y. Zhang *et.al.,* Sci. Rep. **3** (2013) 1943.

BL4U

The Effect of PFI on the Microstructural Aggregates of PEDOT:PSS by Scanning Transmission X-Ray Microscopy

M. W. Lin[1], H. W. Shiu[1], Y. L. Lai[1], T. F. Guo[2] and Y. J. Hsu[1]
[1]*National Synchrotron Radiation Research Center, Hsinchu, Taiwan 300, Republic of China*
[2] *Department of Photonics, National Cheng Kung University, Tainan, Taiwan 701, Republic of China*

A spin-casted conducting polymer PEDOT:PSS (poly(3,4-ethylenedioxythiophene): poly(styrenesulfonate)) forms a hole-injection layer with a gradient work function tuned by self-organization of the PFI, which resulted in a remarkably improved device efficiency of organic light-emitting diodes and organic photovoltaics. From previous X-ray photoelectron spectroscopy (XPS) measurements, we found the sulfide component is increased, while the PSS concentration decreases after the addition of PFI. However, the PFI is rich at the surface and its concentration gradually decreases with depth. We therefore investigated whether if the morphology change of PFI aggregation on surface is caused by the interplay between PEDOT:PSS and PFI. To study the chemical morphology with several blended polymers, the Scanning Transmission X-ray microscopy (STXM) measurements were utilized to explore the heterogeneous structure and chemical properties of PEDOT:PSS:PFI composited polymers at S *L*-edge.

Near-edge X-ray absorption fine structure (NEXAFS) taken at S *L*-edge (Figs. 2(a) and (b)) in beamline BL4U identifies major characteristic peaks for PEDOT:PSS and PFI unambiguously (Chemical structures are shown in Fig. 1). The spectra of PEDOT:PSS display strong intensity in the energy range between 170 to 175 eV which are associated with the sulfonic acids groups, energy range between 165 to 170 eV corresponding to sulfur atoms in PEDOT (Fig. 2(a)) . In Fig. 2(b), the PFI has a strong absorption between 170 to 175 eV, which are associated with the sulfonic acids in PFI. The 3D optical density (OD) images were acquired to discriminate the composition and structure change caused by PFI. Figure 3 (a) and (b) exhibit OD images of PEDOT:PSS and PEDOT:PSS:PFI, extracted from 3D images, respectively. Despite several large spots caused by dusts, the obtained imaging at 166.8 eV (which is characteristic peak of PEDOT) for PEDOT:PSS:PFI film(Fig. 3 (b)) has denser dark particles in compared to pure PEDOT:PSS film(Fig. 3 (a)). As a result, the addition of PFI tends to aggregate on surface. The obtained data indicates that the blending of PFI on PEDOT:PSS generates high concentration of PFI-covered surface and cause the re-distribution of sulfonic acids group in PEDOT:PSS. The OD images for PEDOT:PSS and PEDOT:PSS:PFI are hence different. Also, the results from STXM greatly resembles with our XPS findings, the adding PFI re-arrange the distribution of PEDOT:PSS. It should be noted that the obtained OD image was not divided by the pre-edge image (for example at 160 eV) due to the beamlight around 160 eV to 180 eV exists periodic distribution of dark and bright. Again, the periodic distribution minimizes the absorption contrast attributed by the sample. Nonetheless, from the STXM results, we still found the PFI changes the distribution of PEDOT:PSS. The result is important to explain how the PFI influence the interplay of PEDOT:PSS compositions.

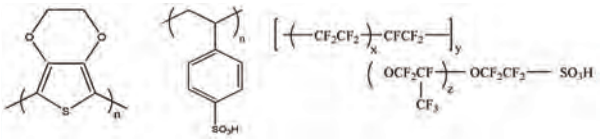

Fig. 1. The chemical structures of conducting polymers used in this study.

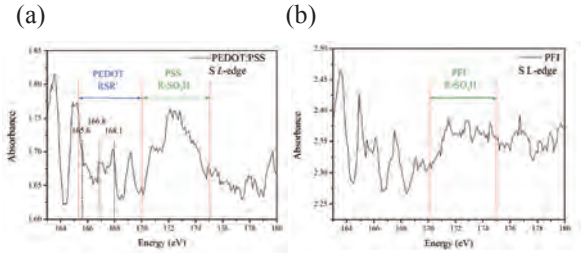

Fig. 2. S *L*-edge NEXAFS of the (a) PEDOT:PSS and (b) PFI.

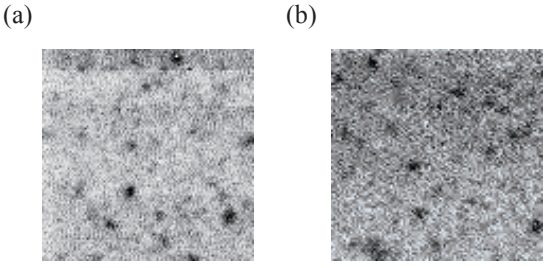

Fig. 3. The OD image for S *L*-edges extracted from 3D images of (a) PEDOT:PSS and (b) PEDOT:PSS:PFI.

[1] T. W. Lee, Y. Chung, O. Kwon, and J. P. Park , Adv. Funct. Mater. **17** (2007**)** 390.

BL4U

Observation of the Origin of d^0 Magnetism in ZnO Nanostructures Using X-Ray-Based Microscopic and Spectroscopic Techniques

S. B. Singh[1], Y. F. Wang[1], J. W. Chiou[2], W. F. Pong[1], T. Ohigashi[3] and N. Kosugi[3]
[1]*Department of Physics, Tamkang University, Tamsui 251, Taiwan*
[2] *Department of Applied Physics, National University of Kaohsiung, Kaohsiung 811, Taiwan*
[3] *Editorial Board, UVSOR Facility, Institute for Molecular Science, Okazaki 444-8585, Japan*

In present report, efforts have been made to elucidate the origin of d^0 magnetism[1,2] in ZnO nanocactus (NC) and nanowires (NW) using X-ray-based microscopic and spectroscopic techniques. The magnetic hysteresis curve obtained in an applied field revealed that the saturation magnetization in ZnO NC exceeded that of the NW. Figure 1 shows the O *K*-edge scanning transmission X-ray microscopy (STXM) and corresponding x-ray absorption near-edge structure (XANES) spectra of the ZnO nanostructures. The experiments were performed at the 4U beamline. The O *K*-edge STXM stack mappings were recorded at two randomly selected regions in ZnO NC (NC-1 and NC-2) and NW (NW-1 and NW-2) respectively (see Figs. 1a-d). The insets in the figures also present corresponding scanning electron microscopy images that help to identify the regions and can be used to verify the STXM images. To overcome the signal-to-noise ratio of the XANES spectra obtained from specific mapping areas in the STXM images, the O *K*-edge STXM-XANES spectra in Fig. 1(e) were obtained as the sum of the XANES spectra in the regions that are bordered by yellow dashed lines, as shown in NC-1, NC-2, NW-1 and NW-2. According to the dipole-transition selection rule, the features at ~535-550 eV are attributed to the electron excitations from O 1*s*-derived states to $2p_{x,y}$-derived (along the bilayer) and O $2p_z$-derived (along the ***c*** axis) states, which are approximately proportional to the density of the unoccupied O 2*p*-derived states.[3] The intensities of the O *K*-edge STXM-XANES spectra of NC-1 and NC-2 are clearly higher than those of NW-1 and NW-2. The STXM-XANES results consistently demonstrate that the population of defects at the O sites in ZnO NC is larger than in the NW and confirming the enhanced density of states of O 2*p*-derived states, as the population of defects and dangling bonds at/above E_{CBM} or E_F in ZnO NC exceeds that in the NW. The experimental results are also consistent with the measurements of extended X-ray absorption fine structure spectroscopy, X-ray excited optical luminescence spectroscopy and X-ray magnetic circular dichroism. The STXM-XANES resesult strongly support the arguments that the origin of magnetization is attributable to the O 2*p* orbitals rather than the Zn 3*d* orbitals.

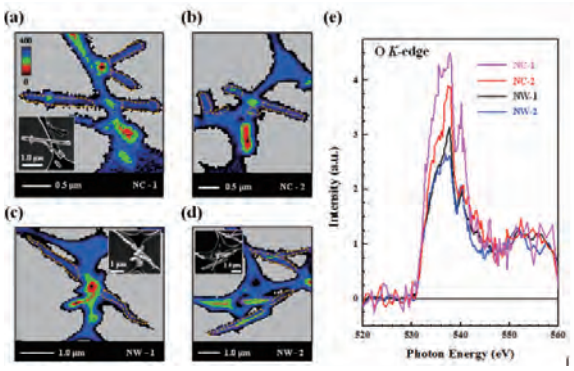

Fig. 1. **(a)-(d)** O *K*-edge STXM images of two selected regions in ZnO NC (NC-1 and NC-2) and NW (NW-1 and NW-2), respectively. **(e)** corresponding O *K*-edge XANES spectra of regions bordered by yellow dashed lines in ZnO NC (NC-1 and NC-2) and ZnO NW (NW-1 and NW-2). The insets show the corresponding SEM images.

[1] T. A. Dietl *et al.*, Nat. Mater. **9** (2010) 965.
[2] S. Z. Deng *et al.*, ACS Nano **4** (2010) 495.
[3] J. W. Chiou *et al.*, Appl. Phys. Lett. **85** (2004) 3220.

BL4U

STXM Study on Fluorescence Mechanism of Nanocarbon-Silica Composites

S. Kawasaki, Y. Ishii and H. Song
Nagoya Institute of Technology, Gokiso, Showa, Nagoya 466-8555, Japan

In order to solve the energy and environmental problems, we have to reduce our energy consumption. For that purpose, it is highly expected to replace the normal fluorescent lamps by LED lamps. However, it is not a very easy task, because the present white LED light does not have the same photoluminescence profile as normal fluorescent lamps have. To reproduce the good profile, we need fluorescent materials which can emit good white light under weak ultra-violet light produced by LED. Recently, we found that a kind of mesoporous carbon-silica composite can emit very broad white light.[1-3] The detailed mechanism of the PL property is not clarified yet. In order to elucidate the mechanism, electronic structures of nanocarbon fragments included in the light emitting mesoporous carbon-silica composites should be investigated.

We prepared several kinds of chemically modified nanocarbon materials such as oxidized carbon nanotubes, oxidized graphenes, carbon nanotubes including some functional molecules inside their hollow cores and so on. Oxygen K edge X-ray absorption spectra were observed using UVSOR BL4U Scanning Transmission X-ray Microscopy (STXM).

STXM observations of several kinds of nanocarbon materials were performed. Here, I report on the observation of the carbon nanotube sample in which anthraquinone molecules were encapsulated. The encapsulation of anthraquinone was carried out by exposing the SWCNT sample to anthraquinone gas in an evacuated glass tube. The open-end SWCNT sample and the organic molecule powder sample in the evacuated glass tube were heated at 200ºC for 10 hours. After the heat-treatment, the SWCNT sample was washed several times with ethanol in order to remove the physically adsorbed organic molecules on the SWCNT surface. The encapsulation was confirmed by XRD and N_2 adsorption experiments. Figure 1 shows STXM spectra of the anthraquinone molecule sample and the the carbon nanotube sample in which anthraquinone molecules were encapsulated (A@SWCNT). We could observe a peak of the anthraquinone sample at around 529 eV very clearly. On the other hand, for the A@SWCNT sample, two peaks were observed at around 529.2 eV and 531.5 eV. The latter peak was the absorption peak of polymer microgrids of TEM sample holder which was used to mount the A@SWCNT sample. Therefore, the peak position of anthraquinone molecule shifted from 529 eV to 529.2 eV by encapsulating it in carbon nanotubes. The energy shift was occurred probably due to the charge transfer from nanotubes to anthraquinone molecules.

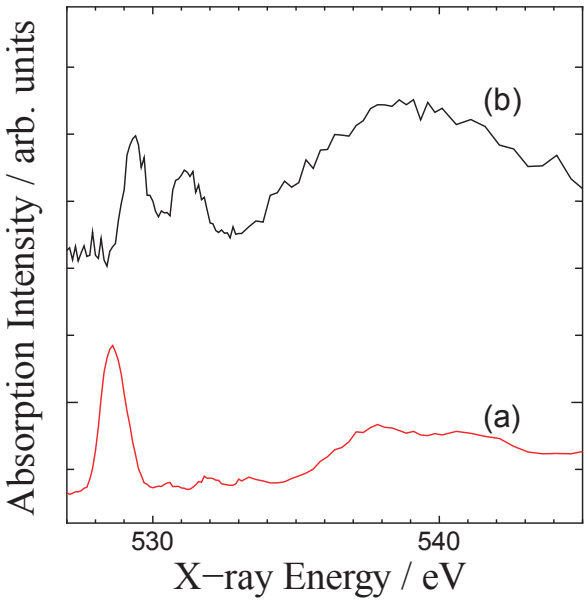

Fig. 1. Oxygen K-edge X-ray absorption spectra of (a) the anthraquinone molecule sample and (b) the A@SWCNT sample.

[1] Y. Ishikawa, S. Kawasaki, Y. Ishii, K. Sato and A. Matsumura, Jpn. J. Appl. Phys. 51, 01AK02, (2012)
[2] Y. Ishikawa, K. Sato, S. Kawasaki, Y. Ishii, A. Matsumura and S. Muto, physica status solidi (a) **209** (2012) 1022.
[3] Y. Ishii, A. Matsumura, Y. Ishikawa and S. Kawasaki, Jpn J. Appl. Phys. **50** (2011) 01AF06-1.

BL4U

X-Ray Linear Dichroism of Sodium Titanate Nanoribbons Measured with *in situ* Azimuthal Sample Rotation in STXM

X. H. Zhu[1], T. Ohigashi[2], A. P. Hitchcock[1], C. Bittencourt[3], P. Umek[4] and P. Krüger[5]
[1]*Brockhouse Institute for Materials Research, McMaster University, Hamilton, ON L8S 4M1, Canada*
[2]*UVSOR Facility, Institute for Molecular Science, Okazaki 444-8585, Japan*
[3] *University of Mons, 7000 Mons, Belgium*
[4] *Institute Jožef Stefan, 1000 Ljubljana, Slovenia*
[5] *Graduate School of Advanced Integration Science, Chiba University, Chiba 263-8522, Japan*

Titanate nanostructures are potential active materials in applications such as lithium ion batteries, gas sensors, photocatalysts, and dye sensitized solar cells [1]. This study used scanning transmission X-ray microscopy (STXM) to investigate the electronic structure of sodium titanate nanoribbons ($NaTiO_x$-NR) prepared by hydrothermal treatment of anatase TiO_2 [2]. We measured the Ti 2p and O 1s absorption spectra and X-ray linear dichroism (XLD) of individual nanoribbons using a newly implemented *in situ* azimuthal sample rotation device. While XLD in $NaTiO_x$-NR has been studied previously in a full field microscope [3], the ability to examine XLD of an identical nanostructure is an advantage of the STXM approach. Figure 1 is a STXM image of the sample, and images of the 6 orientations at which Ti 2p and O 1s image sequences (stacks) were measured.

Figure 2 presents O 1s spectra of a small portion of one nanoribbon extracted from the aligned optical density (OD) O 1s stacks. Through careful energy calibration an apparent energy shift in the lowest energy band was identified. This shift is caused by differences in the XLD of two adjacent states (split t_{2g} band). A similar apparent shift in the Ti $2p_{3/2} \rightarrow t_{2g}$ band was noted previously, and reproduced in this work (not shown). The Ti 2p and O 1s stacks can be reduced to dichroic maps by fitting to spectra characteristic of the sample parallel and perpendicular to the fixed horizontal E-vector, as shown in Fig. 3 for one orientation of the O 1s data. Detailed analysis and comparison to the results of multichannel multiple scattering with atomic multiplet (Ti 2p) and density functional (O 1s) calculations by Krüger (Chiba) is in progress.

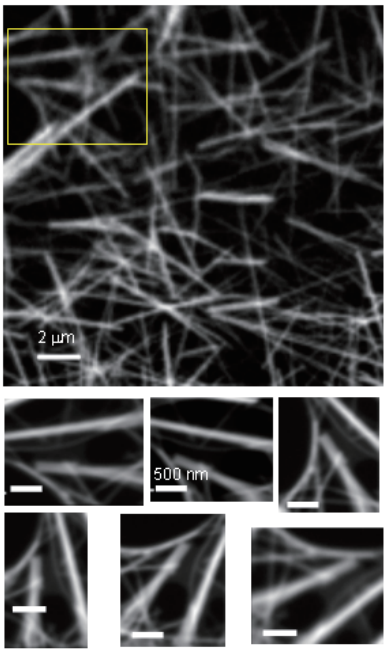

Fig. 1. STXM OD image at 460 eV of the $NaTiO_x$ nanorod sample. The yellow box is the area for XLD study using *in situ* azimuthal rotation. Lower panel is average O 1s stacks for the 6 orientations.

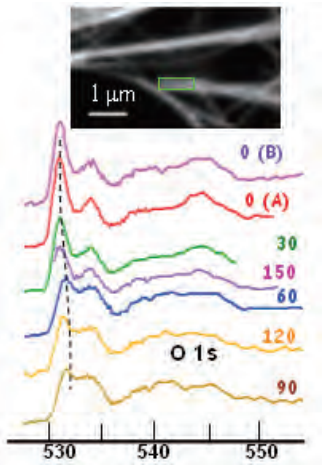

Fig. 2. O 1s spectra as a function of angle between sample and E-vector for the region in the green box.

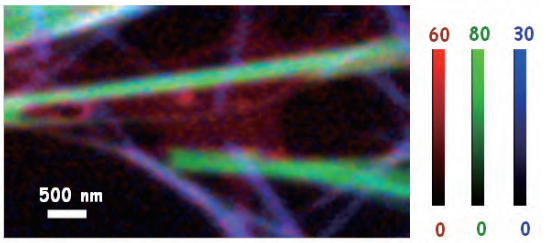

Fig. 3. Color composite of component maps (holey carbon support, parallel, perpendicular) from singular value decomposition analysis of an O 1s stack.

[1] D. Walsh *et al., Titanate and Titania nanotubes*. (Cambridge Univ. Press, 2009)
[2] P. Umek *et al.*, J. Nanosci. & Nanotech. **7** (2007) 3502.
[3] P. Guttman *et al.*, Nature Photonics **6** (2011) 25.

BL4U

The Influence of N 2*p* Vacancy on the Electronic Structure of (*p*, *n*)-Type GaN Nanowires Studied by Scanning Transmission X-Ray Microscopy

Y. F. Wang[1], W. F. Pong[1], L. W. Tu[2], J. W. Chiou[3], T. Ohigashi[4] and N. Kosugi[4]
[1]*Department of Physics, Tamkang University, Tamsui 251, Taiwan*
[2]*Department of Physics, National Sun Yat-Sen University, Kaohsiung 804, Taiwan*
[3]*Department of Applied Physics, National University of Kaohsiung, Kaohsiung 811, Taiwan*
[4]*Editorial Board, UVSOR Facility, Institute for Molecular Science, Okazaki 444-8585, Japan*

In this report, scanning transmission X-ray microscopy (STXM) was utilized to investigate the effect of N 2*p* vacancy on the electronic structure of *p*- and *n*-type GaN, which were grown on the same piece of nanowire top and bottom area, respectively. As shown in Fig. 1, the scanning electron microscope (SEM) measurement revealed that GaN nanowires were ~1500 nm long and ~50 nm in diameter. Figure 2 presents the N *K*-edge STXM and corresponding x-ray absorption near-edge structure (XANES) spectra of the (*p*, *n*)-type GaN. The experiments were performed at the 4U beamline. The N *K*-edge STXM stack mappings were recorded at two selected regions in GaN nanowire top (*p*-type-1 and *p*-type-2) and bottom (*n*-type-1 and *n*-type-2) regions (see Fig. 2a). To overcome the signal-to-noise ratio of the XANES spectra obtained from specific mapping areas in the STXM images, the N *K*-edge STXM-XANES spectra in Fig. 2(b) were obtained as the sum of the XANES spectra in the regions that are bordered by white color, as shown in *p*-type-1, *p*-type-2, *n*-type-1, and *n*-type-2. According to the dipole-transition selection rule, the features at ~398-413 eV are attributed to the electron excitations from N 1*s*-derived states to $2p_{x,y}$-derived (along the bilayer) and N $2p_z$-derived (along the ***c*** axis) states, which are approximately proportional to the density of the unoccupied N 2*p*-derived states.[1] The intensities of the N *K*-edge STXM-XANES spectra of *p*-type GaN are significantly higher than those of *n*-type GaN, which reflects the increase in the number of unoccupied N 2*p*-derived states. In other words, the STXM-XANES results demonstrate that the population of defects at the N sites in *p*-type is larger than in the *n*-type and confirming the enhanced density of states of N 2*p*-derived states, as the population of defects and dangling bonds at/above E_{CBM} or E_F in *p*-type GaN exceeds that in the *n*-type GaN. The STXM-XANES results intensely support the arguments that the amount of N 2*p* vacancy affects the electric conductivity, carrier concentration, and carrier mobility of *p*-type GaN nanowires.

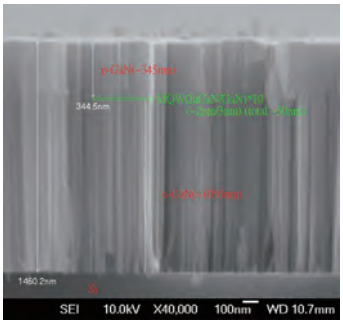

Fig. 1. SEM image of the GaN nanowires. The *p*- and *n*-type GaN were grown on the nanowire top and bottom area, respectively.

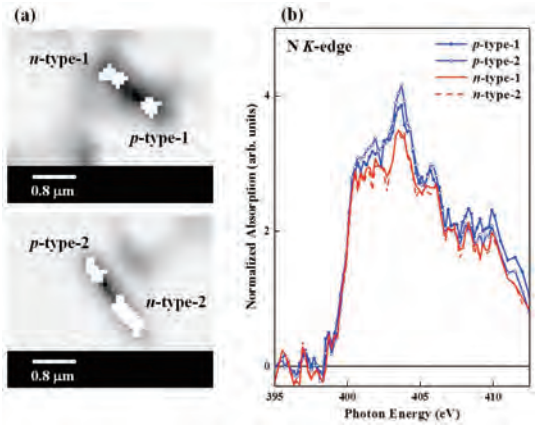

Fig. 2. **(a)** N *K*-edge STXM images of two selected regions in GaN nanowire top (*p*-type-1 and *p*-type-2) and bottom (*n*-type-1 and *n*-type-2), respectively. **(b)** The corresponding N *K*-edge XANES spectra of the top (*p*-type-1 and *p*-type-2) and bottom (*n*-type-1 and *n*-type-2) regions.

[1] J. W. Chiou *et al.*, Appl. Phys. Lett. **81** (2002) 3389.

BL4U

Comprehensive Characterization of Monolithic Polymers by Scanning Transmission X-Ray Microscopy (STXM)

D. Arrua[1], T. Ohigashi[2], Y. F. Wang[2], J. Hoon[1], N. Kosugi[2] and E. Hilder[1]

[1] *Australian Centre for Research on Separation Science (ACROSS), School of Chemistry, University of Tasmania, Private Bag 75, Hobart 7001, Australia*

[2] *UVSOR Facility, Institute for Molecular Science, Okazaki 444-8585, Japan*

Monolithic polymers are a new generation of stationary phases for chromatography, offering significant benefits over currently particle-based materials. The main characteristic of these materials is the presence of large through-pores which permits the use of high flow rates at low backpressures [1]. However, improvements in this technology rely on being able to accurately characterize the porous structure and new characterization techniques are needed to better understand the polymer morphology and its optimization. In this sense, the relatively high penetration power of X-rays would allow a comprehensive analysis of the radial and longitudinal heterogeneity of the monolithic materials developed in our research group.

The characterization by STXM of polymer monoliths was performed at the BL4U beamline of the UVSOR synchrotron radiation facility. To obtain a suitable sample for STXM studies, the macroporous methacrylate monolith with encapsulated divinylbenzene (DVB) nanoparticles was embedded with an aliphatic epoxy resin specially designed for STXM analysis [2]. The experiments were performed at the O 1s edge. Figure 1 shows the O 1s NEXAFS spectra for the polymer monolith and the embedding resin. The spectrum for the methacrylate scaffold has a peak at 531 eV which is characteristic of the O 1s→$\pi^*_{C=O}$ transition in esters. The O 1s spectrum of the epoxy resin has little or no absorption at this energy and therefore there is good contrast between the resin and the polymeric scaffold. The DVB nanoparticles were not possible to be observed due to lack of contrast at the O edge.

Figure 2 shows color-coded composite maps of the porous polymer embedded with the epoxy resin. These color coded composites display the spatial distribution of the polymer scaffold relative to the embedding resin.

Ongoing studies in our research group are focused in the characterization of polymer monoliths containing nanostructures with different functionality and the use of other photon energies (e.g. C 1s and N 1s) to get a better understanding of the distribution of the nanostructures within the polymeric scaffold.

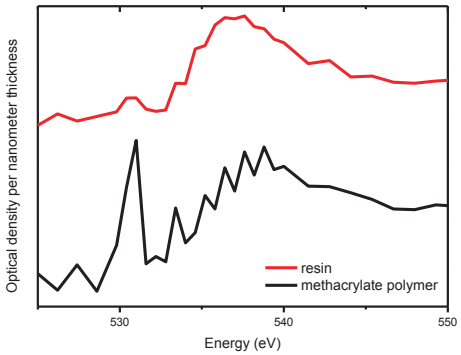

Fig. 1. NEXAFS spectra of the methacrylate scaffold (black) and the TTE epoxy resin (red).

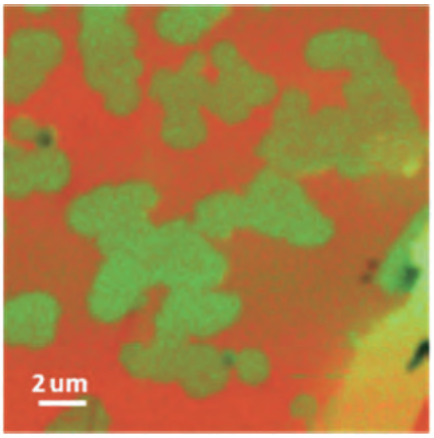

Fig. 2. Color composite of STXM derived component maps of methacrylate-based polymer (green) and TTE resin (orange).

[1] R. D. Arrua *et al.*, Analyst **137** (2012) 5179.
[2] A. P. Hitchcock *et al.*, J. Electron Spectrosc. **156** (2007) 467.

BL4B

O K-Edge XAS of Electrocatalytic Manganese Oxide

Y. Aoki[1,2], K. Kikutani[1], E. Tsuji[1] and H. Habazaki[1]
[1]*Faculty of Engineering, Hokkaido University, Sapporo 060-8628, Japan*
[2]*PRESTO, JST, Kawaguchi 332-0012, Japan*

In naturally occurring photosystem II (PSII), the water oxidation reaction proceeds with extraordinary high catalytic activity, where a μ-oxo bridged tetrameric Mn cluster (Mn_4CaO_5) serves as the multielectron oxidation catalyst within a complex protein environment [1, 2]. Thus, the Mn clusters of photosynthetic organisms have triggered extensive research efforts to develop efficient water oxidation catalysts composed of the inexpensive and abundant element Mn. In a recent year, various manganese oxides, such as MnO_2, $BaMnO_3$, $LaMnO_3$ etc. has been reported to show an excellent electrocatalytic properties for oxygen evolution by electrochemical water splitting [3, 4]. Suntivich *et al* reported that hole on oxygen make an important role for oxygen evolution catalysis of manganese oxide [4]. Such a hole probably evolves by mixing of ligand-to-metal charge transfer state related to the covalency of Mn-O bonding. O K-edge XAS spectroscopy can direct evidence of unoccupied state of solids. Accordingly, it is of fundamental and technological important to study the manganese oxide system by using this technique in order to clarify the relationship between oxygen hole and electrocatalysis. In this study, we investigate O K-edge spectra of various manganese oxide and those of peroxide and superoxide.

Here, the O K-edge spectra of manganese oxides $KMn^{VII}O_4$, $BaMn^{IV}O_3$ and $Mn^{IV}O_2$ were measured. $KMnO_4$ and MnO_2 were purchased from Aldrich and $BaMnO_3$ was prepared by solid state reaction. The spectra of MgO, BaO_2 and KO_2 were measured as a reference of oxide (O^{2-}), peroxide (O^-) and superoxide (O_2^-). The powder specimens were attached to the folder with carbon tape and to measure the adsorption by total electron yield method.

O K-edge XAS spectra of the manganese oxide samples were shown in Fig. 1(a). The Mn atoms in MnO_2 and $BaMnO_3$ take octahedral coordination with oxygen atoms. Therefore, the two peaks near O K-edge at around 529 and 531 eV can be assigned to the transition anti-bonding t_{2g} and e_g states, respectively. In case of $KMnO_4$, the Mn-O clusters take tetrahedral coordination, so that the peaks at around 528 and 530 eV can be assigned to the transition to anti-bonding t_2 and e symmetric states, respectively.

The O K-edge spectra are clearly changed by changing oxidation state of oxide anions, as shown in Fig. 1(b). The peroxide and superoxide show clear pre-edge peak at around 529 eV, provably due to the antibonding O-O states, even though MgO does not show pre-edge features because of strong ionic character of Mg-O bonding.

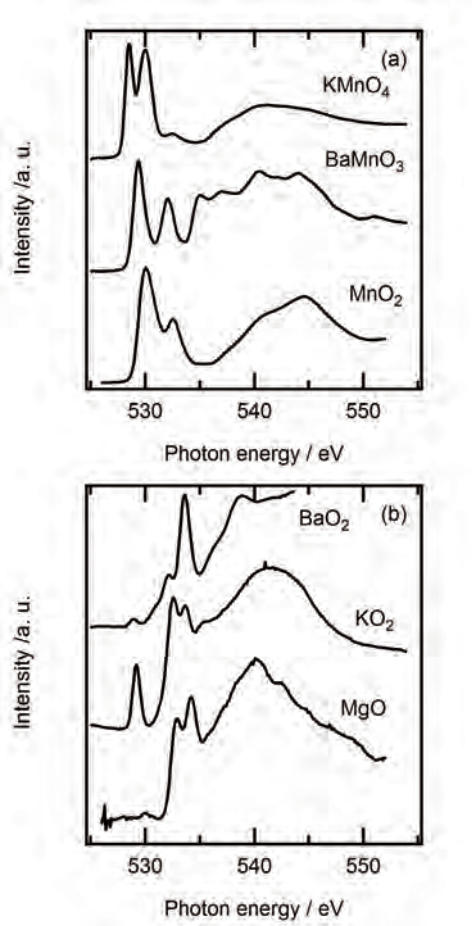

Fig. 1. O K-edge spectra of (a) various manganese oxides and (b) oxides with various oxidation state of O atoms.

[1] J. H. Alstrum-Acevedo *et al*., Inorg. Chem. **44** (2005) 6802.
[2] G. C. Dismukes, R. Brimblecombe, G. A. N. Felton, R. S. Pryadun, J. E. Sheats, L. Spiccia and G. F. Swiegers, Acc. Chem. Res. **42** (2009) 1935.
[3] F. Jiao and H. Frei, Energy Environ. Sci. **3** (2010) 1018.
[4] J. Suntvichi *et al*., J. Phys. Chem. C **118** (2014) 1856.

BL4B

Correlation between Oxygen Functional Groups and Magnetic Properties in Graphene Oxides Using X-Ray Magnetic Circular Dichroism

Y. F. Wang[1], S. B. Singh[1], J. W. Chiou[2], W. F. Pong[1], Y. Takagi[3] and T. Yokoyama[3]
[1]*Department of Physics, Tamkang University, Tamsui 251, Taiwan*
[2]*Department of Applied Physics, National University of Kaohsiung, Kaohsiung 811, Taiwan*
[3]*Editorial Board, UVSOR Facility, Institute for Molecular Science, Okazaki 444-8585, Japan*

In present study, three different samples i.e. graphene oxide (GO), medium reduce graphene oxide (MRGO) and highly reduce graphene oxide (HRGO) where studied using x-ray magnetic circular dichroism (XMCD) technique. Magnetic study (M-H loop) shows room temperature ferromagnetism in GO sample whereas gradual increases of paramagnetic contribution were observed after photo-thermal reduction process (in MRGO and HRGO samples). Figures 1a and 1b display the C and O *K*-edge XMCD spectra respectively, with the photo-helicity of incident x-rays parallel (μ^+) and anti-parallel (μ^-) to the direction of magnetization of the GO sample. The XMCD experiments were performed at the 4B beamline. In Fig. 1a (top panel), spectral features observed in the regions 283-289 eV and 289-315 eV are ascribed to C 1*s*→ π* and C 1*s*→ σ* transitions, respectively. The difference was observed in both π*- and σ*-states when applied the magnetic field in opposite directions (see bottom panel). In Fig. 1b (top panel), spectral features observed in the regions 528-535 eV and 535-545 eV are ascribed to O 1*s*→ π* and O 1*s*→ σ* transitions, respectively. The XMCD signal was also observed in O *K*-edge when applied the magnetic field in opposite directions (bottom panel, see Fig. 1b). The origin of XMCD signal confirms that oxygen functional groups playing important role in origin of magnetism in GO sample. The presence of various oxygen funtion groups were clearly observed in x-ray photoelectron spectroscopy and scanning transmission x-ray microscopy study in GO sample. The presence of oxygen functional groups on GO surface was related to ferromagnetism, whereas consumption of oxygen function groups after photo-thermal reduction process was related to paramagnetic contribution in MRGO and HRGO samples.

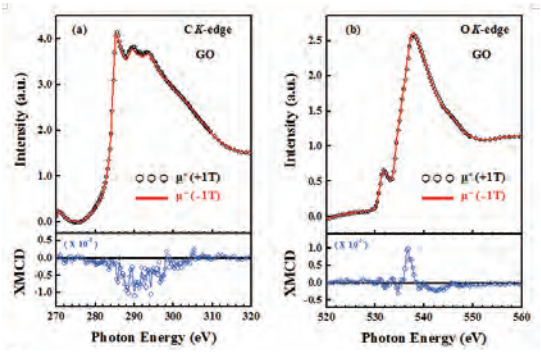

Fig. 1. **a)** (Top panels) display the C *K*-edge x-ray absorption near-edge structure (XANES) spectra of GO sample, with the photo-helicity of incident x-rays parallel (μ^+) and anti-parallel (μ^-) to the direction of magnetization. Bottom panel represents the XMCD spectra of GO sample. **b)** (Top panels) display the O *K*-edge XANES spectra of GO sample, with the photo-helicity of incident x-rays parallel (μ^+) and anti-parallel (μ^-) to the direction of magnetization. Bottom panel represents the XMCD spectra of GO sample.

[1] M. Weser *et al*., Phys. Chem. Chem. Phys. **13** (2011) 7534.
[2] A. Ganguly *et al*., J. Phys. Chem. C **115** (2011) 17009.

BL4B

Investigation on Electrochemical Property of Al_2O_3-Coated Li-Excess Mn-Based Layered Positive Electrode Material

T. Okumura[1], M. Shikano[1], K. Takada[2] and H. Kobayashi[1,2]

[1]*Research Institute for Ubiquitous Energy Devices, National Institute of Advanced Industrial Science and Technology (AIST), Ikeda, 563-8577, Japan*

[2]*Faculty of Chemistry, Materials and Bioengineering, Kansai University, Suita, 564-8680, Japan*

The layered Li_2MnO_3-$LiMO_2$ (M = transition metal) materials are one of the promising positive electrode materials for lithium secondary battery. Especially, it has been reported that $Li[Mn_{0.56}Ni_{0.17}Co_{0.07}Li_{0.2}]O_2$ displayed an initial discharge capacity of ca. 280 mAh/g in the voltage range of 2.5 to 4.8 V and maintained a reversible capacity of ca. 250 mAh/g after 50 cycles. On the other hand, the decomposition of the electrolyte proceeded on the positive electrode material above 4.5 V is a problem to be solved for realizing long cycle life. Recently several efforts have been made to improve the cycle performance through surface modification of positive electrode materials, but limited efforts have been made to improve the cycle performance through surface modification of Li-excess Mn-based layered materials. In this paper, the effect of Al_2O_3-coating on electrochemical properties was studied in $Li_{1.20}Mn_{0.55}Ni_{0.16}Co_{0.09}O_2$.

Surface modificated-$Li_{1.20}Mn_{0.55}Ni_{0.16}Co_{0.08}O_2$ was prepared by mechanochemical reaction with nano-Al_2O_3 using NOB-MINI (Hosokawa Micron Co.). The particle morphology was measured by SEM. Crystal and electronic structures were investigated by synchrotron XRD (BL19B2 at SPring-8) and XAFS (BL7C at PF, BL4B at UVSOR, and BL27SU at SPring-8) measurements. The crystal structure and bondlength were determined using the analysis programs RIETAN-FP and REX2000. Electrochemical property was measured using coin-type cells with Li/1M $LiPF_6$ in EC:DMC(1:2) /samples

The XRD and SEM results showed that the 5wt% Al_2O_3-coated sample (Test conditions; 2000 rpm and 5 min.) was well defined layered phase without additional impurity peak and the Al_2O_3 particles with the order of 10-20 nm were uniformly distributed over the surface of $Li_{1.20}Mn_{0.55}Ni_{0.16}Co_{0.08}O_2$ particles. The hard X-ray XAFS results clarified that both pristine and 5wt% Al_2O_3-coated samples showed almost the same valence states of M cations. These results indicated that the mechanochemical reaction gave no damage to the bulk structure of $Li_{1.20}Mn_{0.55}Ni_{0.16}Co_{0.09}O_2$. On the other hands, the soft X–ray XANES results clarified that the surface of $Li_{1.20}Mn_{0.55}Ni_{0.16}Co_{0.09}O_2$ was covered by Al_2O_3 particles as shown in Fig. 1. Electrochemical tests showed that the cycle dependence of discharge capacity retention at 318 K was improved for the 5wt% Al_2O_3-coated sample as shown in Fig. 2. In this paper, it is revealed that the mechanochemical Al_2O_3-coating process is an effective way of improving the cycle performance at high temperature.

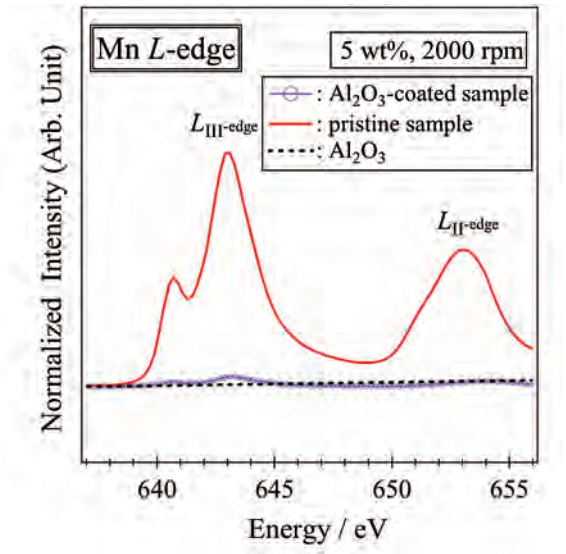

Fig. 1. Mn L-edge XANES spectra for pristine and Al_2O_3-coated samples together with Al_2O_3.

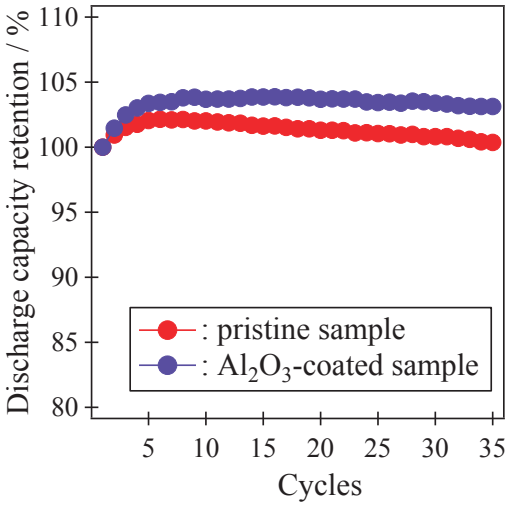

Fig. 2. Cycle dependence of discharge capacity retention at 318 K for pristine and Al_2O_3-coated samples.

[1] A. Ito *et al*., J.Power Sources **183** (2008).
[2] H. Kobayashi *et al*., Solid State Ionics
DOI: 10.1016/j.ssi.2013.09.045.

BL4B

Valence State Analysis of Mn and Fe Ions in $Bi_4Ti_3O_{12}$

K. Nishimura[1], T. Yoshioka[1] and T. Yamamoto[1,2]

[1]*Faculty of Science and Engineering, Waseda University, Shinjuku 169-8555, Japan*

[2]*Institute of Condensed-Matter Science, Waseda University, Shinjuku 169-8555, Japan*

Dilute Magnetic Materials (DMMs) have been extensively investigated because of their potential applications in spintronics. Recently, it was reported that $Bi_4Ti_3O_{12}$ doped with dilute Fe ions show both ferroelectric and ferromagnetic properties, i.e., multiferroic property, at room temperature [1]. Although it is essential to know the local environment of doped magnetic ions for the understandings of the mechanism of room-temperature ferromagnetism, such analysis has often been skipped for DMMs. We have studied Mn and Fe codoped In_2O_3 by the analysis of X-ray absorption spectra (XAS) [2, 3]. In the current study, the valence state of Mn and Fe ions in $Bi_4Ti_3O_{12}$ is investigated by the Mn- and Fe-$L_{2,3}$ XAS measurements.

All the samples were synthesized by the solid-state reaction method changing concentrations of doped Mn and Fe ions. Reagent grade powders of Bi_2O_3, TiO_2, Mn_2O_3 and Fe_2O_3 were mixed and ground in an agate mortar, which were calcined at 1023 K for 5 hours in air. Resultant powers were remixed and reground, and pressed into a cylindrical pellet form, which were sintered at 1223 K for 5 hours in air.

Mn- and Fe-$L_{2,3}$ XAS were collected at BL4B in UVSOR by total electron yield method. Sample powers were mounted on the first Cu-Be dinode of the electron multiplier using carbon adhesive tape. Synchrotron radiation from the storage ring was monochromatized by a varied-line-spacing plane grating (800 lines/mm). Energy resolution (E/ΔE) of the incident beam was set to 3000.

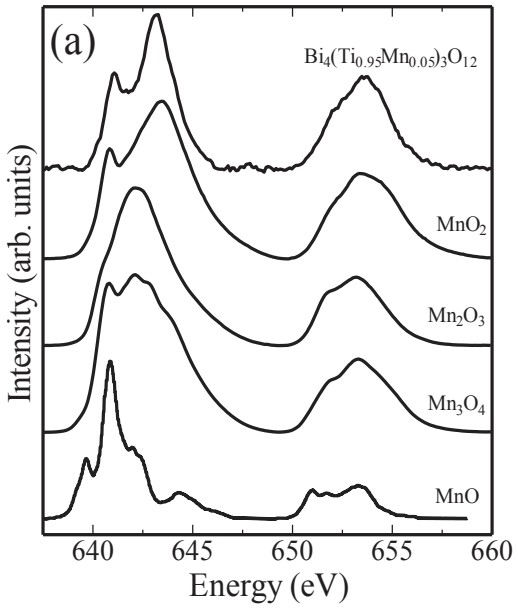

Fig. 1(a). Observed Mn-$L_{2,3}$ XAS of Mn-doped $Bi_4Ti_3O_{12}$ and those of Mn oxides.

Observed Mn- and Fe- $L_{2,3}$ XAS are shown in Figs. 1(a) and (b), respectively, with those of metal oxides for comparisons. Mn-L_3 XAS of Mn-doped $Bi_4Ti_3O_{12}$ shows similar profile as that of MnO_2, which indicates that valence state of Mn ions in $Bi_4Ti_3O_{12}$ are 4+. On the other hand, that of Fe ions can be determined as 3+ by the same comparisons in Fig. 1(b).

In summary, we have successfully determined the valence states of doped dilute Mn and Fe ions in $Bi_4Ti_3O_{12}$ by XAS analysis.

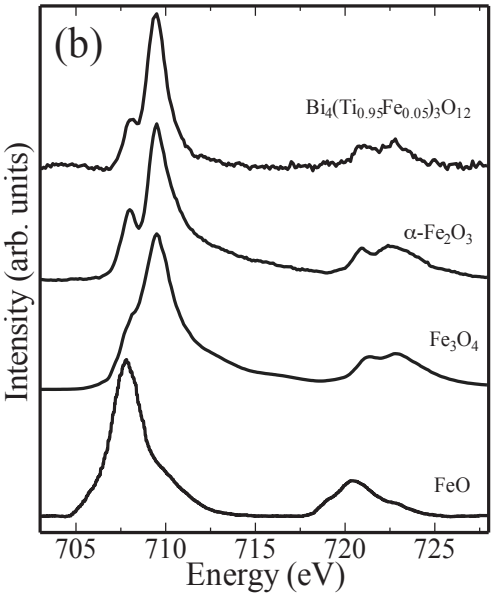

Fig. 1(b). Observed Fe-$L_{2,3}$ XAS of Fe-doped $Bi_4Ti_3O_{12}$ and those of Fe oxides.

[1] X. Q. Chen *et al.*, Solid State Comm. **150** (2010) 1221.

[2] T. Okazaki *et al.*, Solid State Comm. **151** (2011) 1749.

[3] S. Nishida *et al.*, UVSOR Activity Reports 2012, (2013) 99.

BL5U

Electronic Structures of the ZrNiSn Half-Heusler Thermoelectric Material

H. Miyazaki[1], T. Nakano[2], M. Inukai[2], K. Soda[3] and Y. Nishino[2]

[1]*Center for Fostering Young and Innovative Researchers, Nagoya Institute of Technology, Nagoya 466-8555, Japan*

[2]*Department of Frontier Materials, Nagoya Institute of Technology, Nagoya 466-8555, Japan*

[3]*Department of Quantum Engineering, Graduate School of Engineering, Nagoya University, Nagoya 464-8603, Japan*

Half-Heusler *M*NiSn and *M*CoSb (*M* = Ti, Zr, Hf) alloys with a valence electron count of 18 are considered to be semiconductors with a narrow band gap [1] and a promising class of thermoelectric materials with their large dimensionless figure of merit *ZT* [2, 3]. Numerous half-Heusler ZrNiSn-based alloys have been investigated, and *ZT* values of 0.52 (p-type) and 1.0 (n-type) (at 1000 K) have been reported for the $Zr_{0.5}Hf_{0.5}CoSb_{0.8}Sn_{0.2}$ [2] and $Zr_{0.4}Hf_{0.6}NiSn_{0.98}Sb_{0.02}$ [3] alloys, respectively. Although the optimization of the thermoelectric performance of half-Heusler ZrNiSn-based alloys has been extensively investigated, the mechanism by which the thermoelectric properties are improved has not been clarified. To clarify the origin of the large thermoelectric properties, we investigate the electronic structures of the ZrNiSn alloy by photoemission spectroscopy (PES).

Soft X-ray and ultraviolet PES measurements were performed using the BL27SU and BL5U beamlines at the SPring-8 and UVSOR-III synchrotron radiation facilities. Clean surfaces for the PES measurements were obtained by *in-situ* fracturing with a knife edge at 10 K under ultra-high vacuum. The Fermi level (E_F) and total energy resolution were determined by the Fermi edge of evaporated gold films. The total energy resolutions were set to 160 and 50 meV at the excitation photon energies ($h\nu$) of 1000 and 50 eV, respectively.

Figure 1(a) shows the photon-energy-dependent valence band spectra and density of states (DOS) determined by electronic band structure calculations using a theoretical lattice parameter of a = 6.154 Å. The experimental spectra are normalized with respect to their integrated intensity on the whole valence band up to E_B = 12 eV. The overall features of the photoemission spectra of ZrNiSn are in good agreement with the DOS results, even though a shift to higher binding energies is observed compared with the predicted values. Figures 1(b) shows the photoemission spectra near E_F at $h\nu$ = 50 for the ZrNiSn alloy and a Au film. The intensity of the photoemission spectra of the Au film gradually decreases from 0.4 eV to a value near the E_F and changes as a Fermi distribution curve at the E_F. The bandgap was not observed in the photoemission spectra within the total energy resolution of the present measurements. The observed intensity at E_F and the inflection point suggests the existence of a semi-metallic in-gap state, that is to say, pseudo-gap, which is inconsistent with the predicted semiconductor-like band structure for the ZrNiSn alloy [1].

Thus, an improvement in the thermoelectric properties can be achieved by material design based on the pseudo-gap electronic structure of half-Heusler ZrNiSn-based alloys.

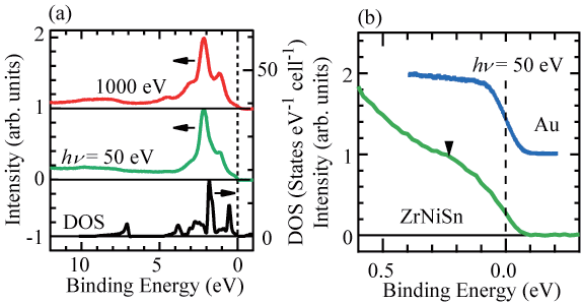

Fig. 1. (a) Photoemission spectra at excitation-photon energies $h\nu$ of 50 and 1000 eV, and calculated DOS for the ZrNiSn alloy. (b) hotoemission spectra near the Fermi edge at $h\nu$ = 50 eV for the ZrNiSn alloy and a Au film.

[1] J. Tobola *et al.*, J. Phys. Condens. Mat. **10** (1998) 1013.
[2] S.R. Culp *et al.*, Appl. Phys. Lett. **93** (2008) 022105.
[3] C. Yu *et al.*, Acta Mater. **57** (2009) 2757.

BL5U

Metal-Insulator Transition in Pyrite-Type $Ni_{1-x}Cu_xS_2$

K. Usui[1], S. Osawa[2], H. Kondo[1], M. Kato[1,2], J. Iwasaki[3], K. Niwa[2,3], K. Kusaba[2,3], M. Hasegawa[2,3] and K. Soda[1,2]

[1]*Department of Quantum Engineering, Graduate School of Engineering, Nagoya University, Nagoya 464-8603, Japan*

[2]*Department of Physical Science and Engineering, School of Engineering, Nagoya University, Nagoya 464-8603, Japan*

[3]*Department of Crystalline Materials Science, Graduate School of Engineering, Nagoya University, Nagoya 464-8603, Japan*

Pyrite-type transition-metal dichalcogenides MX_2 exhibit rich variety of electronic and magnetic properties due to the electron correlation and hybridization effects. In particular, NiS_2 is classified as a charge-transfer-type insulator [1], while CuS_2 is a p-band metal, showing superconductivity [2]. It is interesting to clarify the effects of solid solution between insulating NiS_2 and metallic CuS_2 on the electronic structure and related properties. In this study we have studied the valence band spectra near the Fermi level E_F of $Ni_{1-x}Cu_xS_2$ to clarify the origin of the x-dependence of their electronic properties.

Photoelectron measurements were carried out at 10 K in angle-integrated mode. Specimens of $Ni_xCu_{1-x}S_2$ were polycrystals synthesized under a high pressure of 6.5 GPa at a temperature of ~920 K with use of multi-anvil cell. Their clean surfaces were prepared for the measurement by scraping them with a diamond file. Total energy resolution was estimated as ~0.1 eV at the excitation photon energy of 60 eV. The origin of the binding energy E_B was set to the Fermi energy E_F determined by measuring the Fermi edge of an evaporated Au film on the sample holder.

Typical valence-band spectra near E_F of $Ni_xCu_{1-x}S_2$ are compared with each other in Fig.1. Numerals in the right-hand side of the figure show the intensity at E_F normalized with the intensity (*i.e.* the edge jump) linearly extrapolated from the spectral intensity between E_B = 0.2 ~ 0.3 eV to E_F. The normalized intensity at E_F is ~0.5 of the edge jump for CuS_2, indicating its metallic nature, gradually decreases with the Cu content x decreasing, and becomes ~0.2 for NiS_2, suggesting that NiS_2 has a semimetallic or semiconducting (insulating) feature, as reported [2, 3]. For NiS_2, fine structures are also recognized near E_F, which might imply that NiS_2 is not a simple semiconductor.

Figure 2 shows the electric conductivity at 300 K for $Ni_{1-x}Cu_xS_2$ in comparison with the spectral intensity at E_F. The conductivity decreases gradually as the Cu content x reduces from 1 to 0.1, and then steeply from x = 0.1 to 0, qualitatively consistent with the x-dependence of the spectral intensity at E_F; the metal-insulator transition occurs between x = 0 and 0.1. Here we propose a mechanism for the metal-insulator transition as follows; holes are injected into the S3p-derived fully-occupied valence band of Mott-insulating NiS_2 from the metallic S3p-band (or states) of CuS_2. Hence the substitution of Cu for Ni may make $Ni_{1-x}Cu_xS_2$ metallic in a wide Cu content x range.

Cu and Ni 2p core-level spectroscopy will provide further support to the above-mentioned mechanism.

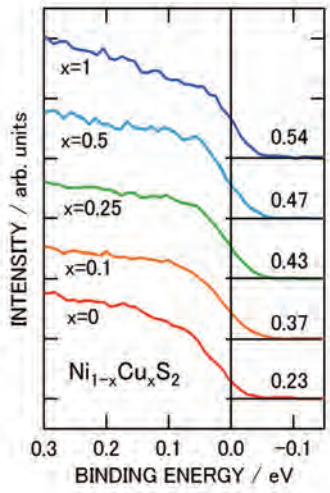

Fig. 1. Photoelectron spectra near E_F of $Ni_{1-x}Cu_xS_2$.

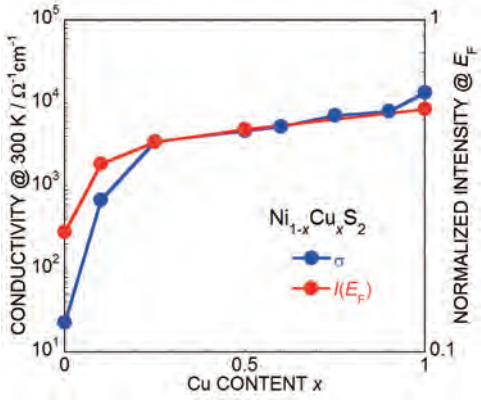

Fig. 2. Electric conductivity and spectral intensiy at E_F of $Ni_{1-x}Cu_xS_2$.

[1] J. Kunes *et al.*, Phys. Rev. B **81** (2010) 025122.
[2] H. Ueda *et al.*, Phys.Rev.B **65** (2002) 155104.
[3] K. Mamiya *et al.*, Phys. Rev. B **58** (1998) 9611.

BL5U

Angle-Resolved Photoemission Study of Insulator-to-Metal Transition of $Sm_{1-x}Y_xS$

M. Kaneko[1,2], M. Sato[3], T. Ito[1,4], K. Imura[3], T. Hajiri[1,2], M. Matsunami[2,5], S. Kimura[2,6], H. S. Suzuki[7] and N. K. Sato[3]

[1]*Graduate School of Engineering, Nagoya University, Nagoya 464-0818, Japan*
[2]*UVSOR Facility, Institute for Molecular Science, Okazaki 444-8585, Japan*
[3]*Graduate School of Science, Nagoya University, Nagoya 464-8603, Japan*
[4]*Nagoya University Synchrotron Radiation Research Center, Nagoya University, Nagoya 464-8603, Japan*
[5]*School of Physical Sciences, The Graduate University for Advanced Studies (SOKENDAI), Okazaki 444-8585, Japan*
[6]*Graduate School of Frontier Biosciences and Physics Department, Osaka University, Osaka 565-0871, Japan*
[7]*National Institute for Materials Science, Tsukuba 305-0047, Japan*

Samarium monosulfide (SmS) is a prototypical valence fluctuating compound that exhibits an insulator (black) – to – metal (golden) phase transition by applying external pressure [1]. To elucidate the origin of this anomalous phase transition, the experimental investigation of the electronic structure across the phase transition has been desired.

By using the three-dimensional (3D) ARPES at UVSOR-III BL5U, we investigated the electronic structure near the Fermi level (E_F) of $Sm_{1-x}Y_xS$, where the similar black-golden phase transition has been realized by the substitution of Sm by yttrium in SmS at ambient pressure [2]. For example, the color and electronic properties of $Sm_{1-x}Y_xS$ changes from $x = 0$: black insulating (BI) ($x = 0$), black metallic (BM) ($x = 0.03$, 0.13), to golden metallic (GM) phase ($x = 0.25$, 0.32, 1).

Figure 1 shows the band structure near E_F around the X point of $Sm_{1-x}Y_xS$ obtained by the present 3D-ARPES experiment. From the comparison with our previous study [2], the electronic structure near E_F of $Sm_{1-x}Y_xS$ consists of the Sm^{2+} 4*f* multiplet structures and the electron-pocket at the X point with Sm (Y) *d* character appearing at the metallic phase. With increasing x, the Sm^{2+} 4*f* multiplet structure gradually shifts to lower binding energies. Furthermore, we found that the Sm 4*f* feature at the black phase ($x = 0 \sim 0.13$) shows sizable dispersion (dashed line), while one at the golden phase ($x = 0.25$, 0.32) is non-dispersive. With respect to the electron pocket (circles), we found that there exists anomalous narrowing of the Sm 5*d* feature at the BM phase, while the electron pocket shows a free-electron like parabolic dispersion at the GM phase. Furthermore, the high-energy shift of the electron pocket becomes intensively small from BM to GM phase. Taking account that the $x = 1$ (YS) is a reference of the localized Sm^{3+} electron system, the present ARPES observation of the dispersive (non-dispersive) features of Sm^{2+} 4*f* multiplet structure as well as the narrowing (free-electron like dispersion) of Sm 5*d* electron pocket at the BM (GM) phase might suggest the change of Sm 4*f* electron character from itinerant to localized one across the BM-GM phase transition of $Sm_{1-x}Y_xS$.

[1] P. Wachter: in Handbook on the physics and chemistry of rare earths, edited by K. A. Gschneidner, Jr. *et al*., (North-Holland, Amsterdam, 1994), Vol. **19**, p. 383.
[2] K. Imura *et al*., J. Korean Phys. Soc. **62** (2013) 2028.
[3] V. N. Antonov *et al*., Phys. Rev. B **58** (1998) 6807.

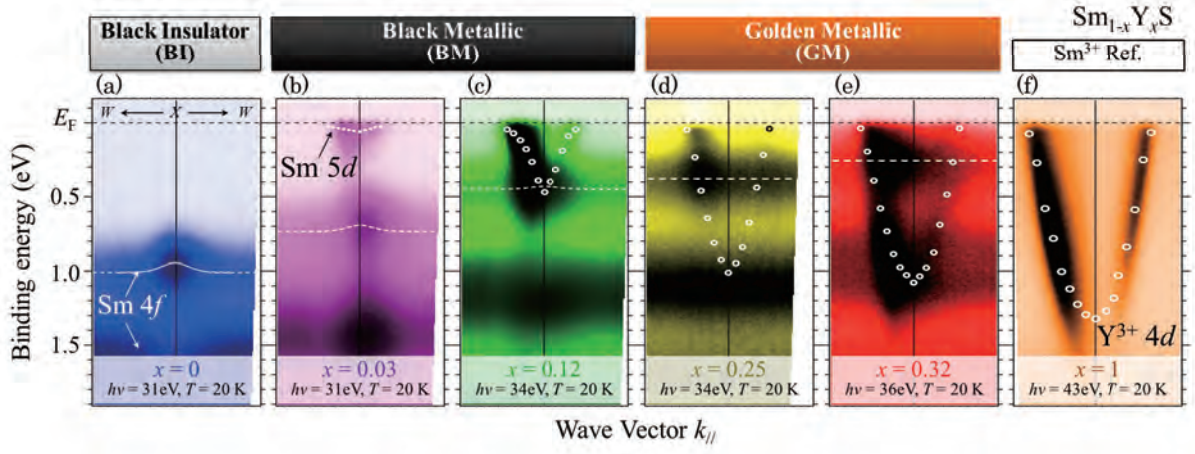

Fig. 1. Band structure of the $Sm_{1-x}Y_xS$ ($x = 0$ (a), 0.03 (b), 0.13 (c), 0.25 (d), 0.32 (e), and 1 (f)). Dashed lines (open circles) are guide for Sm 4*f* (Sm 5*d* (Y 4*d*)) features, respectively.

BL5U

Angle-Resolved Photoemission Study on LuPtSb

E. Tsuiki[1], M. Kaneko[1], T. Hosokawa[1], T. Ito[1,2], T. Hajiri[1,3], S. Kimura[3,4], M. Matsunami[3,5], K. Imura[6] and S. Suzuki[7]

[1]*Graduate School of Engineering, Nagoya University, Nagoya 464-8603, Japan*
[2] *Nagoya University Synchrotron Radiation Research Center, Nagoya University, Nagoya 464-8603, Japan*
[3]*UVSOR Facility, Institute for Molecular Science, Okazaki 444-8585, Japan*
[4]*Graduate School of Frontier Biosciences and Physics Department, Osaka University, Osaka 565-0871, Japan*
[5]*School of Physical Sciences, The Graduate University for Advanced Studies (SOKENDAI), Okazaki 444-8585, Japan*
[6] *Graduate School of Science, Nagoya University, Nagoya 464-8603, Japan*
[7]*National Institute for Materials Science, Tsukuba 305-0047, Japan*

Several years ago, new kind of functional materials that are neither the metal nor the insulator, so called Topological Insulator, were discovered. In topological insulators, the bulk properties are characterized as semimetal or insulating, while the surface ones, as unique metal. In the surface metallic state, the band shows linear (Dirac cone) dispersion between the bulk, which in fact observed by angle-resolved photoemission spectroscopy (ARPES) on $TlBiSe_2$ [1].

Semi-metallic half-Heusler compound XYZ (X,Y: Rare earth or transition element, Z: pnictogen) with the lattice distortion have been expected to be a topological insulator [2]. By changing combination of X, Y, and Z atoms, the ground state changes from topologically trivial (semiconducting) to non-trivial (semi-metallic) as the characteristic energy difference between the Γ_6 and Γ_8 bands changes from negative to positive. Furthermore, it is predicted that there is a possibility of controlling functionalities (superconductivity, magnetism, and abnormal carrier) in addition to the topologically insulating states. On the other hand, there are few experimental evidences of the existence of the topologically trivial to non-trivial border at the electronic structure of half-Heusler ternary compounds so far.

In this study, we have performed angle-resolved photoemission spectroscopy (ARPES) on LuPtSb, , which has been expected to be located on the non-trivial border [2, 3], to clarify the intrinsic electronic structure of this system as the starting point.

Figure 1(b) shows ARPES spectra along cut1 passing through the Γ point in the fcc Brillouin zone (BZ) (Fig. 1(a)) of LuPtSb obtained by utilizing $h\nu$ = 61 eV photons. To show the dispersive features clear, the second-derivative ARPES intensity plot of Fig. 1(b) is shown in Fig. 2 (a). We found that the highly-dispersive features around the Γ point seems to be similar between the experiment and the calculation (Fig. 2(b)).

On the other hand, we found two types of Fermi surfaces (FSs) around the BZ center and boundary, respectively. The former is formed by the small electron-pocket whose bottom merges with the hole-like dispersion around 100 meV, while the latter by the large electron-pocket appearing symmetrically with respect to the Γ point. Thus the experimental electronic structure near E_F of the LuPtSb shows strong contrast to the calculation where the zero-gap states at E_F form a point-like FS at the BZ center. To elucidate the effect of the FS formation at LuPtSb to the systematic change of the electronic structure of half-Heusler ternary compounds, systematic ARPES study on the trivial border system, YPtSb etc., is intended.

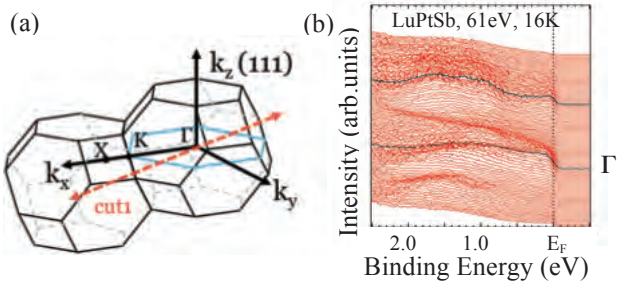

Fig. 1. (a) fcc Brillouin zone of LuPtSb. (b)ARPES spectra along cut1 from Fig.1(a) obtained by using hν = 61eV photons.

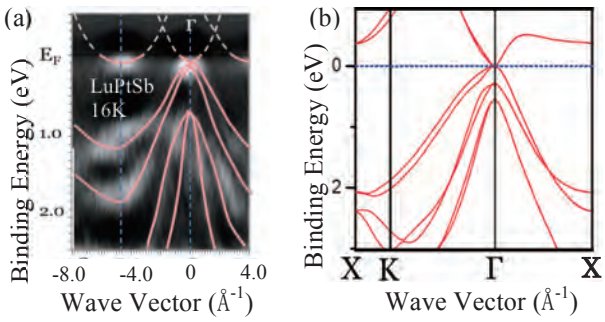

Fig. 2. (a) Second-derivative ARPES image of Fig. 1. Thick lines are guide for eyes. (b) Band structure calculation of LuPtSb along the Γ KX line.

[1] T. Sato *et al*., Phys. Rev. Lett. **105** (2010) 136802.
[2] S. Chadov *et al*., Nature Mat. **9** (2010) 541.
[3] W. Al-Sawai *et al*., Phys. Rev.B **82** (2010) 125208.

BL5U

Photoemission Study of $Mg_xZn_{1-x}O$ Synthesized under High Pressure

K. Takahama[1], R. Eguchi[2], D. Shimada[3], M. Kato[1], K. Niwa[2,3], K. Kusaba[2,3], M. Hasegawa[2,3] and K. Soda[1,3]

[1]*Department of Quantum Engineering, Graduate School of Engineering, Nagoya University, Nagoya 464-8603, Japan*

[2]*Department of Physical Science and Engineering, School of Engineering, Nagoya University, Nagoya 464-8603, Japan*

[3]*Department of Crystalline Materials Science, Graduate School of Engineering, Nagoya University, Nagoya 464-8603, Japan*

Wide band-gap semiconductor ZnO and its related solid solutons have received much interest for a variety of applications such as electronic and optoelectronic devices, catalysts, gas sensors, and transparent conductive films. Under high pressures, ZnO crystalizes in NaCl structure (B1) with a band gap E_G of 2.45 eV and can form solid solutions with B1-type MgO of E_G ~ 7.7 eV in wide concentration range. Hence it is expected from band structure calculations [1] that the band gap of $Mg_xZn_{1-x}O$ may increase with x. Thus we have investigated the electronic band structure, in particular band gap, of n-type semiconductor $Mg_xZn_{1-x}O$ by use of photoelectron spectroscopy.

Photoelectron measurement was performed at room temperature. Specimens of B1-type $Mg_xZn_{1-x}O$ were synthesized at high temperatures of 1173 K under high pressure of 6.5 GPa, and their clean surfaces for the photoelectron measurement were prepared by scraping them with a diamond file. The origin of the binding energy E_B was set to the Fermi energy E_F of an evaporated film on the sample holder.

Figure 1 shows valence-band spectra of $Mg_xZn_{1-x}O$ recorded with weak photon intensity to prevent from the charging-up effect as possible. Spectral intensities are normalized with the integrated intensity up to E_B = 20 eV. Densities of states (DOS) for B1-type $Mg_xZn_{1-x}O$ are calculated by a full-potential linearized augmented plane wave (FLAPW) method with WIEN2k code [2] and GGA-PBE approximation [3] for the exchange-correlation energy and they are also presented for comparison in the figure, where the DOS's are plotted as a function of energy relative to the conduction minimum (CVM) indicated by a broken line and are shifted by 5 eV towards the high binding energy side (in the lower abscissa), compared to the experimental spectra.

Overall spectral features agree fairly well with the calculated DOS except for a band at E_B ~ 15 eV, the origin of which is unknown at present. Taking account of the n-type semiconductor, the band gap can be estimated from the binding energy of the valence band onset, which is indicated by arrows in Fig.1. Observed band gaps are about 2~3 times larger than calculated ones, as known as the underestimation of the band gap by the band structure calculation [4]. As is already reported [1], the calculated band gap increases gradually with the Mg content x. For cubic $Mg_xZn_{1-x}O$ epitaxial films (x > 0.6), it has been reported that E_G > 6 eV [5]. However, the present experimental band gap seems almost unchanged or slightly decreased as x is increased. At present this discrepancy has not been clarified yet; it might arise from the Fermi level pining due to surface defect states such as those of oxygen deficiency. Charging-up effects might smear out fine structures and the band onset. Further study is intended on the dependences on specimens and the content x.

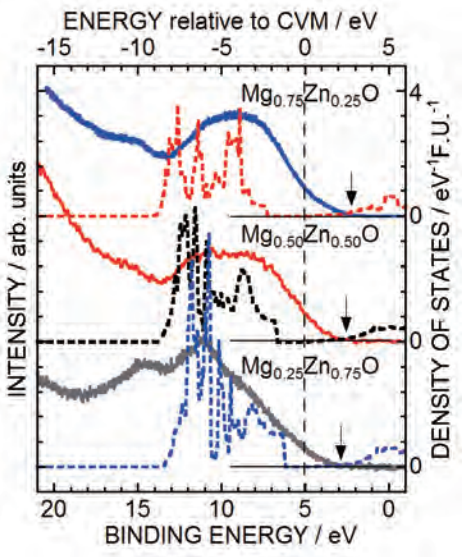

Fig. 1. Photoelectron spectra and calculated densities of states of $Mg_xZn_{1-x}O$.

[1] F. Z. Aoumeur-Benkabou *et al.*, Model. Num. Sim. Mater. Sci. **2** (2012) 60.
[2] P. Blach *et al.*, Comput. Phys. Commun. **59** (1990) 399-415.
[3] J. P. Perdew *et al.*, Phys. Rev. Lett. **77** (1996) 3865.
[4] D. Fritsch *et al.*, Appl. Phys. Lett. **88** (2006) 134104
[5] S. Choopun *et al.*, Appl. Phys. Lett. **80** (2002) 1529.

BL5U

Resonance Photoemission Study on Electronic Structure of $Fe_{2-x}VAl_{1+x}$

S. Osawa[1], Y. Yamada[2], H. Miyazaki[3], M. Kato[1], Y. Nishino[2] and K. Soda[1]
[1]*Department of Quantum Engineering, Graduate School of Engineering, Nagoya University, Nagoya 464-8603, Japan*
[2] *Department of Frontier Materials, Graduate School of Engineering, Nagoya Institute of Technology, Nagoya 466-8555, Japan*
[3]*Center for Fostering Young and Innovative Researchers, Nagoya Institute of Technology, Nagoya 466-8555, Japan*

Heusler-type intermetallic compound Fe_2VAl and related alloys have attracted much attention as thermoelectric materials with a pseudogap around the Fermi level E_F in its electronic structure [1]. In $Fe_{2-x}VAl_{1+x}$, both the p-type and n-type thermoelectric powers are enhanced on the off-stoichiometric change in the Fe/Al ratio, while the semiconductor-like temperature dependence of the electrical conductivity is observed for $x > 0.08$; it can be explained by thermal excitation between the pseudogap like semiconductor and the weak localization caused by the random occupation of the excess Al at the Fe sub-lattice for $x > 0.12$ [2]. Analysis of the core-level spectra suggests that the V3*d* states may appear just below E_F. Thus we have performed the Fe3*p*-3*d* resonance photoemission study to clarify the V3*d* partial density of states (DOS) by suppressing the Fe3*d* states on the anti-resonance as well as the Fe3*d* partial DOS by the on-resonance enhancement.

The photoemission measurement was carried out at 7 K with the energy resolution of ~70 meV in an angle integrated mode. Polycrystalline specimens of $Fe_{2-x}VAl_{1+x}$ were *in situ* fractured with a knife edge to prepare clean surfaces for the measurement. Origin of the binding energy E_B is set to E_F by measuring a Fermi edge of a gold film evaporated onto the sample holder.

Figure 1 shows typical on-resonance (recorded at the excitation photon energy $h\nu$ of 55 eV) and anti-resonance (at $h\nu$ = 52 eV) valence-band spectra for x = 0, 0.08 and 0.18. Here, the spectra are subtracted backgrounds due to the secondary electrons from by an iteration method [3] and normalized with the intensity of the V3*d*-derived band at E_B = 1.5 eV, although the hybridized Fe3*d* states contribute to the band at 1.5 eV in the on-resonance spectra.

As seen in Fig. 1, the Fe3*d*-derived bands are located around E_B = 0.7 and 3 eV; they are enhanced at $h\nu$ = 55 eV, compared to the V3*d*-derived band at 1.5 eV, due to the Fe3*p*-3*d* resonance. The band at E_B ~ 6 eV in the anti-resonance spectra is attributed to the *s*-like hybridized states; it is shifted to the high binding energy side and enhanced in the on-resonance spectra, which is ascribed to the Auger-like emission near the 3*p*-3*d* resonance. Small shift of the main 3*d* valence-band as a whole is recognized to the low binding energy side with x increased. This is due to the decrease in the valence electron counts by substitution of the excess Al for Fe, as expected in a rigid band model [1]. On the other hand, the anti-resonance spectra show that the spectral intensity near E_F is increased with x, while the intensity at E_F, in particular for x = 0.08 and 0.18, does not change so much for the on-resonance spectra. Thus the V3*d* states grow just below E_F with increasing x ($x > 0.08$), as suggested [2], although the surface states may affect the spectra [4]. The Fe3*d*-derived states are also increased near E_F for x = 0.08 and 0.18 in comparison with Fe_2VAl.

These states near E_F act as the impurity states at the edges of the semimetallic conduction and valence bands, leading to the weak localization and the mobility gap. This also suggests the importance of the relaxation time factor for thermoelectric properties as well as the factors of DOS and its energy derivative.

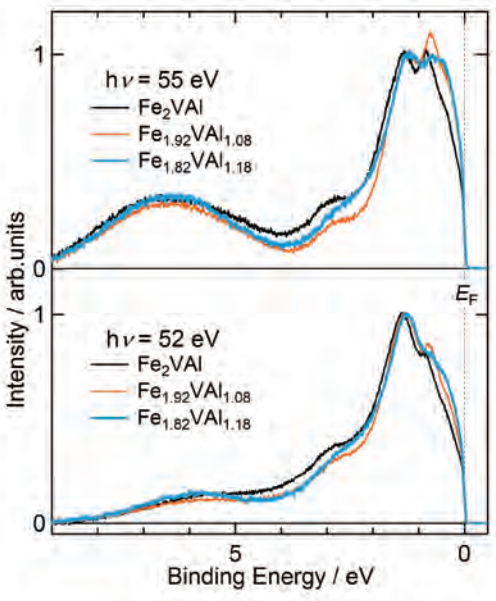

Fig. 1. Valence-band spectra of $Fe_{2-x}VAl_{1+x}$.

[1] Y. Nishino, IOP Conf. Series: Mater. Sci. Eng. **18** (2011) 142001.
[2] K. Soda *et al.*, J. Phys. Soc. Jpn. *in press*.
[3] K. Soda *et al.*, J. Phys. Soc. Jpn. **60** (1991) 3059.
[4] H. Miyazaki *et al.*, J. Vac. Sci. Technol. A **24** (2006) 1464.

BL5B

Reflectance Measurement of Fluoride Output-Coupler for Cavity High-Harmonic Generation in VUV

K. Wakui, K. Hayasaka and T. Ido
National Institute of Information and Communications Technology, Tokyo 184-8795, Japan

Intracavity high-harmonic generation of near infrared femtosecond (fs) frequency combs using a passive enhancement cavity has extended accessible wavelength of frequency combs, realizing precision spectroscopy in the extreme ultraviolet [1]. Lower harmonics at 150-200 nm vacuum ultraviolet (VUV) also attract interests because conventional optics are barely available using fluoride material. In addition, each comb components are well separated thanks to high repetition rate, and rather small phase shift from the nonlinear media maintains the regular comb structures in this wavelength. Therefore its application to a precision spectroscopy at the VUV wavelengths is anticipated.

Among various important atomic transitions, the time and frequency community has been interested in the use of $^1S_0 - {}^1P_1$ transitions in alkaline-earth-like ions for state detection in the optical clock based on the proposal by Dehmelt in 1982 [2]. Moreover, a clock transition in a single thorium nucleus has been intensively studied for realizing hyper-accurate frequency standard [3]. However, they all exist in VUV region and the direct excitation has never been realized because of the difficulty in development of continuous-wave (CW) coherent laser source in that wavelength range. Alternatively, the single frequency-comb component of the high-rep VUV combs may be able to act as a "quasi-CW" laser and thus to work as a state detection laser. In the case of such ions including Al^+, a simple estimation indicates that single-mode VUV power in the order of 10 pW might yield fluorescent photons sufficient for the state detection. The single comb components of the high-rep VUV combs may supply this level of average intensity. This approach also opens a way to simultaneous detection of multiple ions, which may overcome limited stability of the single-ion clocks. Indium ion ($^{115}In^+$) provides an ideal test bed for this approach [4], where the 159 nm radiation generated as the 5th harmonic of a Ti:S laser can excite the $^1S_0 - {}^1P_1$ transition. In our intracavity HHG setup with the repetition rate of 110 MHz, a total average intensity in the order of 10 μW may provide sufficient for In^+ detection, whereas it has been limited to 1.5 μW in our previous report [5].

The output coupling of high harmonics from the cavity is the key to scale up the yield of intracavity HHG. Several methods were previously demonstrated using e.g. bulk sapphire windows as Brewster plates [6, 7], a diffraction grating carved onto a NIR mirror [8], and on an anti-reflection-coated grazing incidence plate [9]. Here, we design and demonstrate a new type of VUV output-coupler (VUV-OC). The VUV-OC consists of a SiO_2 substrate of ~100 um thickness with a fluoride-multilayer coating on one of its surfaces. The VUV-OC's reflectance is designed to be >80% at 153-163 nm and >90% at 159 nm for p-polarized VUV light, while it works as a Brewster plate at the incident angle of ~55 degree, that corresponds to a Brewster angle to SiO_2 at 795 nm. We confirmed the reflectance in VUV using the beamline facility (BL5B) in UVSOR. As shown in Fig. 1, the reflectance of ~90% was measured at 159 nm as designed. We also demonstrate an efficient output-coupling method using the VUV-OC for our HHG experiment. The final yield of the HHG currently amounts to 4.2 μW at 159 nm, which is almost three times larger than previous work in spite of ~20% reduction of the NIR inside the cavity.

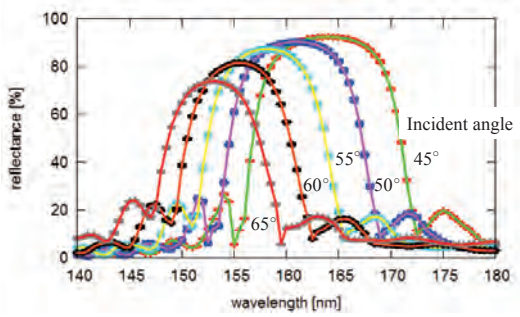

Fig. 1. Reflectance of the fluoride output coupler.

[1] A. Cingös *et al.*, Nature **482** (2012) 68.
[2] H. Delmelt, IEEE Trans. Instrum. Meas. 83 (1982) **IM-31**.
[3] E. Peik and Ch. Tamm, Europhys. Lett. **61** (2003) 181.
[4] K. Hayasaka, Appl. Phys. B **107** (2012) 965.
[5] K. Wakui, K. Hayasaka and T. Ido, Proc. SPIE **8132**, Time and Frequency Metrology III, 813204 (2011).
[6] R. J. Jones, K. D. Moll, M. J. Thorpe and J. Ye, Phys. Rev. Lett. **94** (2005) 193201.
[7] Ch. Gohle *et al.*, Nature **436** (2005) 234.
[8] D. Yost, T. Schibli and J. Ye, Opt. Lett. **33** (2008) 1099.
[9] Y. Y. Yang *et al.*, Opt. Express **19** (2011) 1954.

BL5B

Reflectance of Hypothetical Meteors in EUV Spectral Range

T. Hamaguchi, M. Kuwabara, K. Isashiki, K. Uji and I. Yoshikawa
Graduate School of Science, the University of Tokyo, Hongo 113-8654, Japan

We have measured the surface reflectivities in the EUV spectral ranges, of two examples (NWA 4423、NWA 645) which are hypothetical meteors. We have selected (3, 5) among the combinations of (G,M) and always employed Al/Mg/Al filter to avoid the higher-order spectral contamination. Each result is shown in Fig. (Fig. 2 shows the reflectivity of NWA 4423, Fig. 3 is NWA 645). Please note that the statistical error of NWA 4423 reflectivity measurement is over-plotted, but it is so small (approximately 1/1000) that you might not identify it.

These measurements will be useful, when the albedo of solid planets needs to be studied.

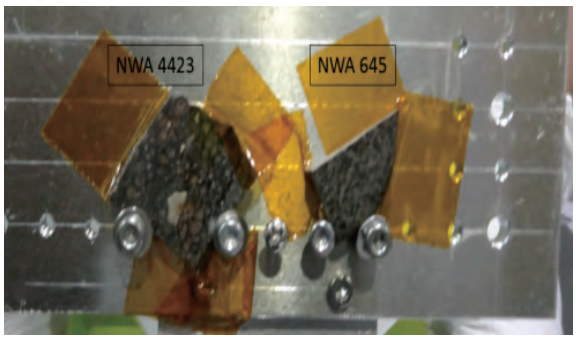

Fig. 1. Two examples of hypothetical meteors (left) NWA 4423, (right) NWA 645.

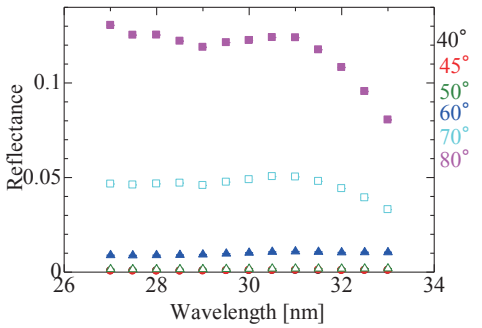

Fig. 2. NWA 4423 reflectivity.

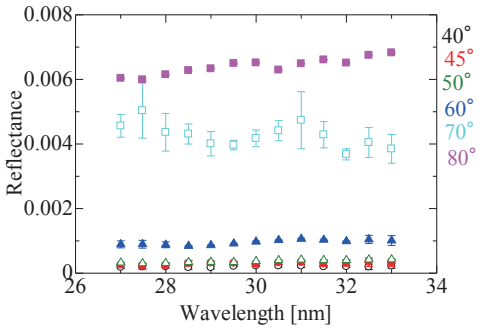

Fig. 3. NWA 645 reflectivityt.

BL6B

Far-Infrared Reflective Study of Alkali Niobate Ceramics

T. Yamazaki, M. Kato, K. Tsuchida and K. Kakimoto
Graduate School of Engineering, Nagoya Institute of Technology, Nagoya 466-8555, Japan

Alkali niobate ceramics are one of the promising candidates for lead-free piezoelectric materials. Especially, Li(Na,K)NbO_3 solid solution shows excellent piezoelectric properties and high Curie temperature. In our previous work, we demonstrated that the small ionic diameter Li substitution induces monoclinic *Pm* phase using synchrotron X-ray, EXASF and FT-IR analyses. It is expected that *Pm* phase involves piezoelectric properties. The present work reports the spectroscopic characterization of *Pm* phase using infrared (IR) technique.

The $Li_{0.02}(Na_{0.5}K_{0.5})_{0.98}NbO_3$ (LNKN02) ceramics were obtained by conventional solid state reaction. The surface of the LNKN sample was mirror polished for IR reflectivity measurement. The spectra were corrected by using Michelson interferometer (Bruker, IFS66v). The measured reflectivity data was fitted using the equation (1) and (2), as mentioned below.

$$R = \left|\frac{\sqrt{\varepsilon(\omega)} - 1}{\sqrt{\varepsilon(\omega)} + 1}\right|^2 \qquad (1)$$

$$\varepsilon(\omega) = \varepsilon_\infty + \sum_n \frac{\omega_{np}^2}{\omega_{no}^2 - \omega^2 - n\gamma_n\omega} \qquad (2)$$

Where, ε_∞ is the high- frequency dielectric constant, ω_p and ω_o are the plasma and longitudinal frequencies, and γ is the damping constant.

The reflectivity spectra of LNKN02 in the temperature range from 10 to 290 K are shown in Fig.1. Remarkable difference in spectra is found below 30 K. Figure 2 shows the imaginary part of complex dielectric constant, which was calculated by fitting result using equations (1) and (2). Five peaks were assumed around 600 cm^{-1} using $(Na_{0.5}K_{0.5})NbO_3$ (NKN) data[1] and group factor analysis. Three peaks are related to *Bmm2* phase which represents NKN and two peaks are related to *Pm* phase. The *Pm* ratio calculated by fitting peaks area was about 26 % at 290 K. Figure 3 shows the calculated *Pm* ratio for LNKN02 ceramics at various temperatures. The *Pm* ratio is found to independent of temperature with the decrease in temperature from 290 to 190 K. At 170 K, *Pm* ratio increased suddenly and further temperature induces the decrease in *Pm* ratio gradually. Finally, the *Pm* ratio decreases about 10 % at 30 K. It can therefore be suggested that LNKN02 ceramics indicate two phase transitions from 290 to 10 K which is different from those of the pure NKN phase.

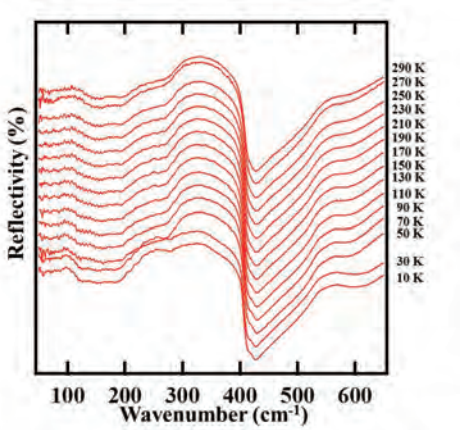

Fig. 1. The reflectivity spectra of LNKN02.

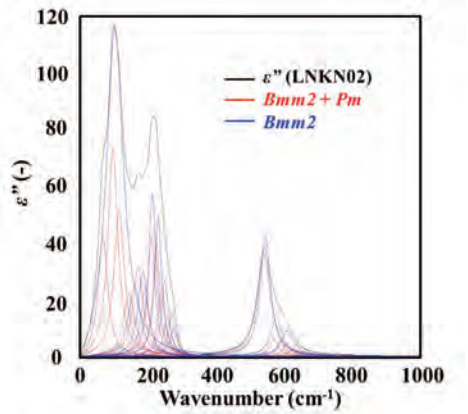

Fig. 2. The imaginary part of complex dielectric constant for LNKN02 at 290 K

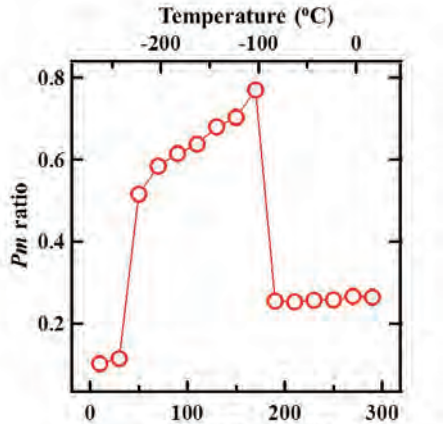

Fig. 3. Temperature dependence of the *Pm* ratio for LNKN02 ceramics.

[1] M. D. Fontana *et al.*, Phys. Stat. Sol. *(b)* **103** (1981) 211.

BL6B

Final State of Ultrashallow Thermal Donors Formed in Carbon- and Hydrogen-Doped Czochralski Silicon Crystals

A. Hara and T. Awano
Department of Electronic Engineering, Tohoku Gakuin University, Tagajo 985-8537, Japan

In the past, we have reported on ultrashallow thermal donors (USTDs) formed in carbon- and hydrogen-doped Czochralski silicon (CZ Si) crystals after annealing at 480°C [1,2]. In this study, we evaluated the final state of USTDs.

Carbon-doped CZ Si samples were doped with hydrogen by annealing them in wet oxygen at 1300°C for 60 min. The samples were then cooled to room temperature by rapidly exposing them to air. For carbon doping, the Si melt for preparing the ingot was doped with carbon powder during CZ Si crystal growth. Transmission spectra were obtained using the far-IR spectrometer of the BL6B beamline at the liquid-He temperature using a flowing cryostat.

Figure 1(a) shows the spectra of USTDs and shallow thermal donors (STD(H)s) after annealing at 480°C for various durations. It has been reported that STD(H)s are hydrogen-like donors and are generated in hydrogen-doped CZ Si crystals at approximately 450°C [3]. USTD-A and USTD-B are generated in an initial stage of annealing at 480°C and eliminated after long-term annealing at the same temperature. Finally, the intensities of only two peaks, namely, USTD-C and USTD-D, are remarkable at 480°C-65h. Figure 1(b) shows USTDs formed after annealing for 40 hours at 450°C, 480°C, and 510°C, respectively. The spectrum of the USTDs at 450°C-40h is nearly the same as that at 480°C-20h in Fig. 1(a). Moreover, the spectrum at 510°C-40h is nearly the same as that at 480°C-65h in Fig. 1(a), and only two peaks, USTD-C and USTD-D, are remarkable. Figure 1(c) shows the spectra of the USTDs at 480°C-40h followed by additional annealing at each temperature higher than 480°C for 15 min. The spectrum with additional annealing at 550°C is nearly the same as that at 480°C-52h and the spectrum at 600°C is nearly the same as that at 480°C-65h. Also, in this case, only two peaks, namely, USTD-C and USTD-D, are remarkable, and their intensity decreases with annealing above 620°C.

As mentioned in our previous report, our model for generating USTDs comprises the following: in the first stage, STD(H)s are generated at high formation speeds and, in the second stage, carbon modulates the electronic structure of STD(H)s. The fact that similar spectra are obtained with short-duration annealing with increasing annealing temperature indicates that thermally activated processes are concerned with the generation of USTDs. According to our model, carbon acted as a modulator and had to migrate to STD(H)s. It is a thermally activated process. USTD-A and USTD-B are generated in the initial stage of annealing at 480°C and eliminated after long-term annealing at the same temperature. Thus, these are not the final states of USTDs, but intermediate products. The USTD-C and USTD-D are believed to be the final states of USTDs, because all experimental results show the survival of only these two peaks. The final form of these two USTDs is consistent with the generation of two STD(H)s in the initial stage. These results support our proposed mechanism of formation.

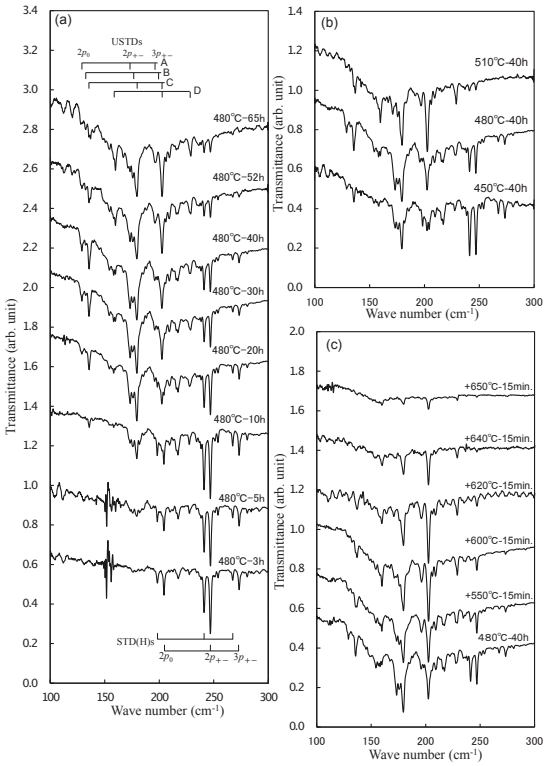

Fig. 1. (a) Annealing behavior of USTDs at 480°C; (b) temperature dependence of USTDs with annealing for 40 h; (c) annealing behavior of USTDs after 40 h followed by additional annealing for 15 min at a higher temperature than 480°C.

[1] A. Hara, T. Awano, Y. Ohno and I. Yonenaga, Jpn. J. Appl. Phys. **49** (2010) 050203.
[2] A. Hara and T. Awano, UVSOR Activity Report **40** (2013) 103.
[3] R. C. Newman, J. H. Tucker, N. G. Semaltianos, E. C. Lightowlers, T. Gregorkiewicz, I. S. Zevenbergen and C. A. J. Ammerlaan, Phys. Rev. B **54** (1996) R6803.

BL6B

Electronic States on Solids Probed by a FIR-THz Light Using the Synchrotron Radiation

A. Irizawa
The Institute of Science and Industrial Research, Osaka University, Ibaraki 567-0047, Japan

Optical study is one of the most powerful techniques for investigating electronic states on solids. There can be obtained the great deal of information about the electronic states, a band structure, a symmetry of crystal structure, and a dielectric response. In view of experimental affinity, the optical study is extremely compatible with multiple conditions such as low temperature, high magnetic field, and high pressure. The observation of electronic states can be concluded with only optical operations. In the case of strongly correlated electron systems, it is well known that the temperature is one of the decisive factors for the electronic state. The considerable types of phase transition are induced by the change of the temperature. Particularly, the multiferroic compounds can be controlled of its physical properties mutually by the external fields such as magnetic, electronic, and elastic ones. The other particular condition, the pressure will directly affect the electron-electron interactions through the change of lattice constants. The beamline 6B in UVSOR is adjusted for the investigations at low temperature and high pressure in the extremely low-energy region of FIR-THz. There equips two type interferometers of both Michelson and Martin-Puplett type. In this report, we have performed the optical transmittance measurements in the longest wavelength region for several compounds having peculiar absorption bands there.

The selected experimental components are the Michelson type interferometer and the Si-bolometer detector with the liquid-He flow type cryostat for controlling the temperature from 300 K down to 13 K. The transmittance was obtained from the ratio of optical transmission spectra between the sample and polypropylene as a matrix for samples. The concentration of samples is around 5%wt for the matrix. They were installed on the sample holder and the transmittance was measured through the tapered hole of 4mm in diameter.

The transmittances are obtained in the energy range between 40 and 600 cm^{-1} as shown in Fig. 1. Here we can confirm the red shift of absorption bands with increasing temperature. The transmittances are nearly 1 at lower energies and go down to zero in higher energies. It means that both CuO and Cu_2O are insulating and the gaps are around there. Small amount of CuO can be recognized in Cu_2O, but the samples are almost single phases. We notice that the shift of absorption bands around 150 cm^{-1} between CuO and Cu_2O. This must be due to the difference of bonds between Cu and O and is originated in the difference of valence. At the same time, experiments in THz region using FEL in Osaka University are in execution. The information obtained using FT-IR is useful for the high power light source experiments.

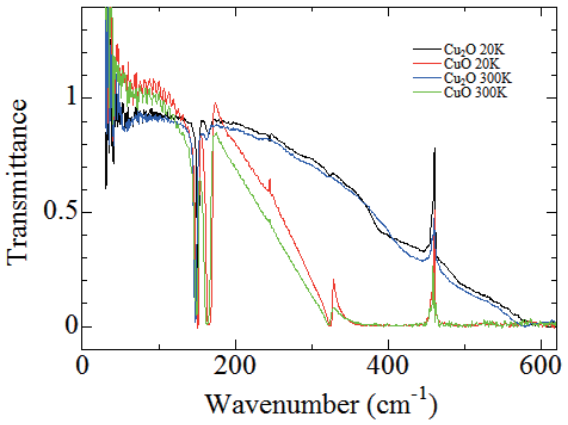

Fig. 1. Temperature change of transmittance of CuO and Cu_2O at the FIR-THz region.

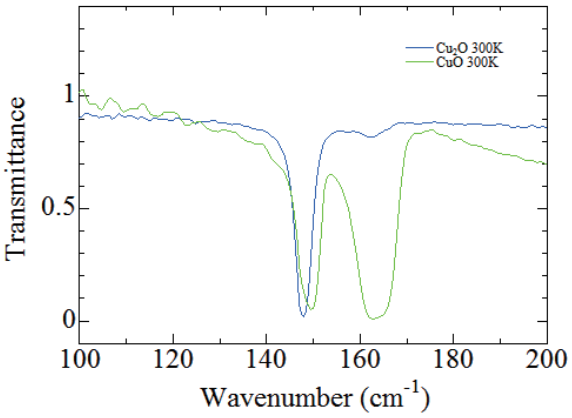

Fig. 2. Expansion near the absorption bands at 300 K.

BL6B

Macroscopic Randomness of Carrier Density in $Sm_{0.83}Y_{0.17}S$

S. Kimura[1], K. Imura[2] and N. K. Sato[2]
[1] *Graduate School of Frontier Biosciences and Department of Physics, Osaka University, Suita 565-0871, Japan*
[2] *Department of Physics, Nagoya University, Nagoya 464-8603, Japan*

Inhomogeneity or randomness of samples is important to investigate the origin of the physical properties of materials because local distortion becomes a trigger of a phase transition [1]. The origin of the insulator-to-metal transition, namely black-golden phase transition (BG transition), of SmS by applying an external pressure is under debate [2], one of candidates of such phenomena, i.e., the BG transition originates from inhomogeneity and/or spatial distribution of distortion. However, it is difficult to obtain the information of local electronic structures of samples. In the study, to obtain the spatial distribution of carrier density in the vicinity of the BG transition, the spatial distribution of the infrared reflectivity spectrum of $Sm_{0.87}Y_{0.17}S$, which is located near the BG transition at ambient pressure [3].

The experiment was performed at the infrared imaging end station of BL6B using a 16-channel linear array MCT detector [4]. The spatial resolution and the sampling points were set to be about 6 μm and 64×64 points, respectively. The total measurement time was about 40 min.

Figure 1a is a visible image of $Sm_{0.87}Y_{0.17}S$. Almost all the area is black (black phase), but tiny areas are changed to gold (golden phase), which indicates the coexistence of both phases. Reflectivity spectra taken at the four different points on the sample are shown in Fig. 1b. The spectra are much different from one another, two of four spectra have a bending part indicated by arrows, which wavenumber corresponds to the plasma edge of free carriers (ω_p). ω_p^2 is proportional to the carrier density. Other two spectra have the plasma edge above the accessible wavenumber of 6000 cm^{-1}, but the intensity at around 6000 cm^{-1} corresponds to the carrier density owing to the spectral shape of a free carrier Drude formula.

The images at several wavenumbers are shown in Figs. 1c1–1c4. The image at the wavenumber of 800 cm^{-1} shown in Fig. 1c1 is almost monochrome except for low reflectivity at cracks on the sample. This implies that the plasma edge of the monochrome area is located at the wavenumber above 800 cm^{-1}. At higher wavenumbers, the image becomes more inhomogeneous. The image at 3000 cm^{-1} in Fig. 1c3 is the most inhomogeneous owing to the distribution of the wavenumber of the plasma edge around 3000 cm^{-1}. In addition, the difference of the golden area from the black area in the visible image of Fig. 1a is only observed in the image at 5700 cm^{-1} in Fig. 1c4.

In comparison with the visible image in Fig. 1a, the reflectivity of the golden area at 3000 cm^{-1} in Fig. 1c3 is similar to the black area but the part at the right lower side has a stripe pattern despite the constant black phase in the visible image. This suggests that the inhomogeneity of carrier density appears in the black phase.

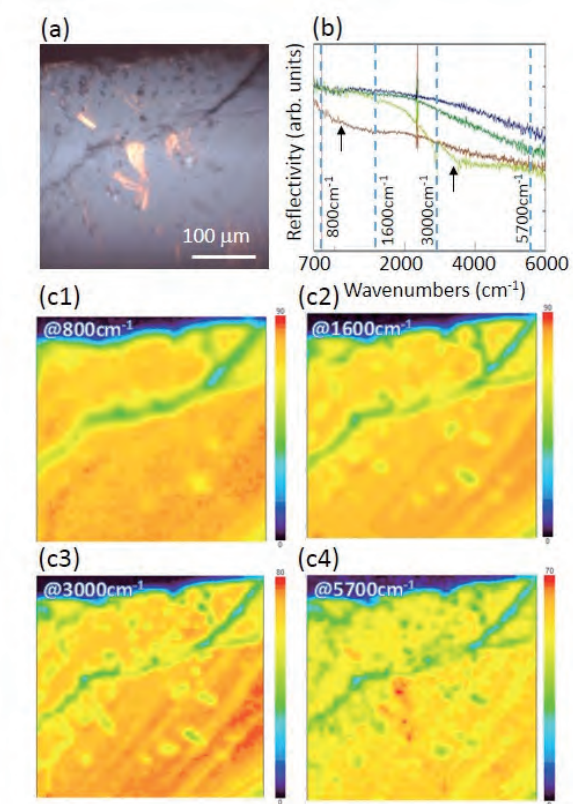

Fig. 1. (a) Visible image of a measured sample of $Sm_{0.83}Y_{0.17}S$. (b) Four spectra at different positions on the sample. Reflectivity intensities at 800 cm^{-1} (c1), 1600 cm^{-1} (c2), 3000 cm^{-1} (c3), and 5700 cm^{-1} (c4).

[1] e.g. L. Zhang, C. Israel, A. Biswas, R. L. Greene and A. de Lozanne, Science **298** (2002) 805.
[2] P. Wachter, *In Handbook on the Physics and Chemistry of Rare Earth* (North-Holland, 1994) **19** (1994) 383.
[3] K. Imura, T. Hajiri, M. Matsunami, S. Kimura, M. Kaneko, T. Ito, Y. Nishi, N. K. Sato and H. S. Suzuki, J. Korean Phys. Soc. **62** (2013) 2028.
[4] S. Kimura, T. Katsumata and J. Koshobu, UVSOR Activity Report **40** (2013) 45.

BL7U

Observation of the Phonon Dispersion in Single-Crystalline Graphite by Angle-Resolved Photoelectron Spectroscopy

S. Tanaka[1], M. Matsunami[2,3] and S. Kimura[2,3,4]

[1]*The institute of Scientific and Industrial Research, Osaka University, Ibaraki 567-0047, Japan.*
[2]*UVSOR Facility, Institute for Molecular Science, Okazaki 444-8585, Japan.*
[3]*School of Physical Sciences, The Graduate University for Advanced Studies (SOKENDAI), Okazaki 444-8585, Japan.*
[4]*Graduate School of Frontier Biosciences, and Department of Physics, Osaka University, Suita 565-0871, Japan.*

Recently, we demonstrated an experimental method using the angle resolved photoelectron spectroscopy in which the elemental process of EPC (electron-phonon coupling), that is a scattering of the electron by the phonon in the solid, can be investigated in HOPG (highly oriented pyro-lytic graphite) [1]. Since HOPG is polycrystalline material, the dispersion of the phonon involved could not discussed in detail in the previous work. Here, we report the phonon dispersion of the graphite involved in the indirect transition in single-crystalline graphite.

Figure 1(a) presents a series of angle-resolved photoelectron spectra of graphite at 12 K in the region near the Fermi level with the photon energies of 11.1eV, which gives a resonant enhancement in the intensity of step-like edges near 160meV[1]. Here we focus on these step-like edges, which are provided by the energy-shift from the Fermi-edge due to the electron-phonon scattering from the K(A)-point of the Brillouin zone, where the π-band crosses the Fermi level in graphite. The energy of the step, therefore, matches the energy of the phonon that is involved[1]. Two possible scattering geometry when the electron at the K and K' points are scattered into the point on the Γ-K line, along which the ARPES is measured, are displayed in Fig. 1(b). According to these schemes, phonon dispersions along the K'-Γ(1) and K-M(2) lines are probed simultaneously in the present case. We applied the least squares method to fit the ARPES data by a phenomenological step-function as

$$f(x) = y_0 + c(X_C - x) + [a(X_C - x) + b]\left[1 - \mathrm{erf}\left\{\frac{(X_C - x)}{\sqrt{2}w}\right\}\right],$$

[shown as grey lines in Fig.1(a)] in order to obtain a value (X_C) of an energy for the step with respect to the Fermi level. The results are shown as dots in Fig. 1(c) for two directions of the phonon momentum vector simultaneously. Solid lines are results of GW-calculation for LO (longitudinal optical), LA (longitudinal acoustic), and TO (transverse optical) phonon branches. Dotted line presents that of the LDA-calculation of the TO branch [2]. Note that there are no practical differences reported between GW and LDA calculations for LO and LA branches. It is obvious that only the TO branch calculated with GW-method agrees with the experiments. It is known that the difference between the LDA and GW calculations is usually caused by the Kohn anomaly, which is due to the electron-phonon coupling in the solid.

An important feature we should point out is the fact that the LO- or LA-phonon branches are not observed here. This indicates that the probability of the indirect transition accompanying with the electron scattering by the LO- and LA- phonons are significantly smaller than that by the TO-phonons. It is difficult to ascribe these to the dipole selection rule, since the K_5 symmetry of the LO and LA-phonons and the K_1 symmetry of the TO phonon cannot be distinguished when the initial state of the indirect transition is the K_6 symmetry as in this case. Therefore, it should be attributed to the difference in the magnitude of the matrix element for the electron-phonon scattering of these phonon modes.

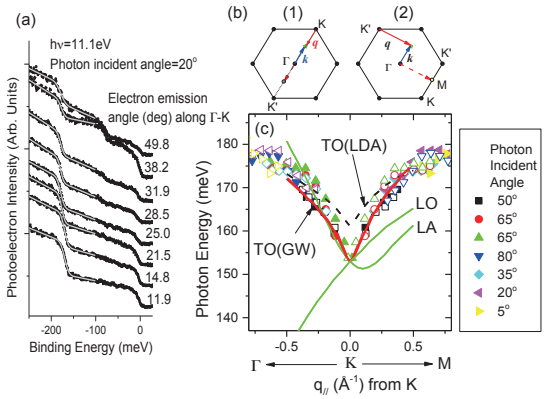

Fig. 1. (a) Angle-resolved photoelectron spectra of single-crystalline graphite. (b) Two possible electron-phonon scattering geometry when the electron at the K and K' points is scattered into the point on the Γ-K line. (c) Phonon dispersion derived from the ARPES (dots), GW-calculation (solid lines) and LDA-calculation (dotted lines)[2].

[1] S. Tanaka, M. Matsunami and S. Kimura, Sci. Rep. 3, 3031; DOI:10.1038/srep03031 (2013).
[2] A. Grüneis *et al.*, Phys. Rev. B. **80** (2009) 085423.

BL7U

Photoemission Studies on Rashba & Dresselhaus Effect Systems

W. Jung[1], S. Cho[1], Y. Kim[1], B. Kim[1], Y. Koh[1],
J. Seo[1], M. Matsunami[2], S. Kimura[2,3] and C. Kim[1]
[1]*Institute of Physics and Applied Physics, Yonsei University, Seoul, Korea*
[2]*UVSOR Facility, Institute for Molecular Science, Okazaki 444-8585, Japan*
[3]*Graduate School of Frontier Biosciences, Osaka University, Suita 565-0871, Japan*

Topological insulators with strong spin-orbit coupling have recently been studied in our group. [1, 2]. We found existence of orbital angular momentum (OAM) through theoretical calculation as well as circular dichroism ARPES experiments. [1, 2] The OAM is found to greatly affect the surface electronic structure. We expect that OAM also greatly affect the electronic structures of semiconductors such as CdTe, InSb and GaAs that possess inversion symmetry breaking (ISB) and resulting electric field.

Semiconductor materials have recently been extensively studied for their spintronic applications. An important example is spin-field-effect transistor (spin-FET) proposed by Datta and Das [3] in the light of controllability of spin precession motion of electrons through the Rashba and Dresselhaus spin-orbit coupling effects. [4, 5, 6]. As we expect OAM in these materials greatly affects the electronic structure, it is also expected that OAM has strong influence on Rashba and Dresselhaus effects, therefore in turn on the spintronic properties.

Compound semiconductors such as InSb, CdTe, GaAs have zinc blende structure with ISB in the bulk. They have three hole bands at the Γ-point (occupied states). They are heavy and light hole bands with J=3/2, and a split off band with J = 1/2. The energy splitting (Δ) between J=3/2 and 1/2 states due to spin-orbit coupling is the order of hundred meV. To explain this band splitting they normally apply Dresselhaus Hamiltonian. Then the effective one-body Hamiltonian becomes:

$$H = H_0 + H_D$$

$$H_D = \gamma[\sigma_x k_x(k_y{}^2 - k_z{}^2) + cyclic\ permutations]$$

Here, H_D is the Hamiltonian for the Dresselhaus effect, σ is Pauli matrix, and γ the material dependent spin-orbit coupling constant. However, we believe it is OAM instead of the spin that determines the energy. Therefore, we expect an OAM pattern similar to a spin pattern. To study the OAM pattern in semiconductors, we have performed circular dichroism ARPES on semiconductors.

CdTe single crystals were purchased as wafers. ARPES measurement was performed at the beam line 7U of UVSOR-III. Samples were cleaved in situ at room temperature and the chamber pressure was better than 5×10^{-11} Torr. ARPES spectra were acquired with a hemispherical photoelectron analyzer (MBS A-1). We used linearly polarized as well as left and right circularly polarized (LCP and RCP) light with the photon energy in the range of 9–34 eV.

As for the OAM textures, we used circularly polarized light on GaAs, InP, InAs of zinc blende semiconductors. Figure 1 shows so obtained ARPES data. Clear band dispersions are observed. Circular dichroism data (LCP-RCP data) shows complex pattern, implying a complex OAM textures in the material. All these prove that there is significant OAM in the material. This is rather surprising, considering the strong crystal field in the system.

On the other hand, we could not reach the Γ-point with low-energy photons due to the limitation of the beam line in spite of the importance of the Γ-point data. It is expected that three-dimensional bulk band structure of GaAs and InSb should give us new information. Therefore, we will perform the three-dimensional ARPES to obtain the complete bulk electronic structure.

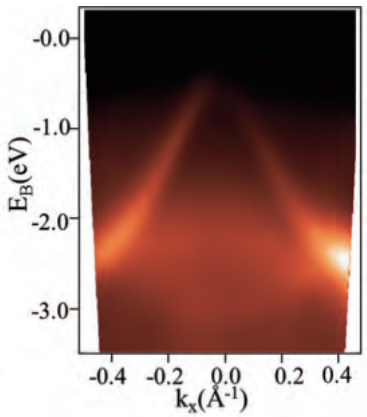

Fig. 1. ARPES results from GaAs (110) bulk state measured with 21 eV photons at the Γ-point.

[1] S. R. Park *et al.,* PRL **107** (2011) 156803.
[2] B. Y. Kim *et al.,* PRB **85** (2012) 195402.
[3] S. Datta *et al.,* Appl. Phys. Lett. **56** (1990) 665.
[4] Y. A. Bychkov *et al.,* JETP Lett. **39** (1984) 78.
[5] J. Schliemann *et al.,* PRL. **90** (2003) 146801.
[6] X. Cartoixà, D *et al*., APL. **83** (2003) 1462.

BL7U

Low-Photon-Energy Polarization-Dependent Angle-Resolved Photoemission Study on Quasi-One Dimensional Organic Conductor $(TMTSF)_2SbF_6$

M. Mitamura[1], T. Hajiri[1,2], T. Ito[1,3], S. Kimura[2,4] and T. Nakamura[4,5]

[1] *Graduated School of Engineering, Nagoya University, Nagoya 464-8603, Japan*

[2] *UVSOR Facility, Institute for Molecular Science, Okazaki 444-8585, Japan*

[3] *Nagoya University Synchrotron Radiation Research Center, Nagoya University, Nagoya 464-8603, Japan*

[4] *School of Physical Sciences, The Graduate University for Advanced Studies (SOKENDAI), Okazaki 444-8585, Japan*

[5] *Institute for Molecular Science, Okazaki 444-8585, Japan*

The Bechgaard salts $(TMTSF)_2X$ (where X is one of the anions PF_6, ClO_4, etc.) belong to a family of highly anisotropic organic conductors [1]. The quasi-one-dimensional (Q1D) structure of these materials allows for a variety of ground states from a Peierl's-like spin density wave (SDW) insulator to a metallic state, to a superconducting state, as anion and/or pressure are changed [1].

In this study, we have performed polarization dependent angle-resolved photoemission spectroscopy (ARPES) on single-crystalline $(TMTSF)_2SbF_6$ to clarify the effects of the Q1D TMTSF molecular chain and the interchain coupling on the electric structure. ARPES measurements were performed at UVSOR-III BL7U by utilizing the bulk-sensitive low photon energy (hν = 8 eV) as well as the micro focus beam (15×100 μm^2).

Figure 1 (a) and (b) shows the polarization-dependent ARPES images near the Fermi level (E_F) along TMTSF-chain direction (*a*-axis) measured at T = 30 K with *p* (E // a) and *s* (E ⊥ a) polarized photons, respectively. In Fig. 1 (a), we found a highly-dispersive feature which approaches E_F around k = 0.2 Å^{-1}. On the other hand, the dispersive feature becomes intensively weak in Fig. 1 (b). Taking account of the selection rules associated with the *p* orbital of TMTSF molecules, initial states with the even- (odd-) symmetry with respect to a mirror plane are selectively observed with *p*- (*s*-) polarized light. Thus the observed dispersive feature increasing with *p*-polarization geometry can be ascribed to the *p* orbital which forms the Q1D TMTSF chain along *a*-axis.

Figure 2 (a) and (b) shows the angle (θ_{bc}) dependent ARPES spectra near E_F measured with *p* and *s* polarized photons, respectively. We found a strong reduction of spectral weight near E_F as increasing (decreasing) θ_{bc} from the normal emission angle (θ_{bc} =0°) in Fig. 2 (a). Since the mirror plane symmetry of *p*-polarization geometry does not change with θ_{bc}, the observed reduction might come from the decreasing mean free path for the intrachain *p* orbital. On the other hand, the cross section for the interchain orbital will be changed with θ_{bc} in *s*-polarization geometry. Though the change of the spectral weight in Fig. 2 (b) is weak, we found slight increase of the spectral weight around 0.3 eV with increasing θ_{bc} from 5° to -15° (see Fig. 3). We expect that the observed change of the spectral weight in Fig.3 is suggestive of the existence of the weak interchain coupling in $(TMTSF)_2SbF_6$. To elucidate the role of the interchain coupling in the anomalous properties, the further study is intended.

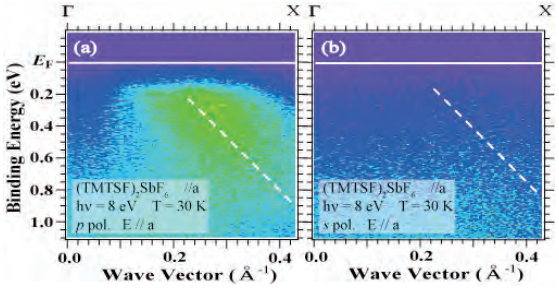

Fig. 1. ARPES images of $(TMTSF)_2SbF_6$ along TMTSF-chain direction measured at T = 30 K with *p* (a) and *s* (b) polarized light. Dashed line is guide for TMTSF band dispersion.

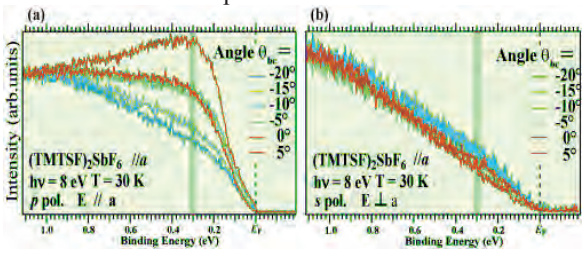

Fig. 2. Interchain angle-dependence of EDC at $k = k_F$ (0.2 Å^{-1}) of $(TMTSF)_2SbF_6$ measured at T = 30 K with *p* (a) and *s* (b) polarized light.

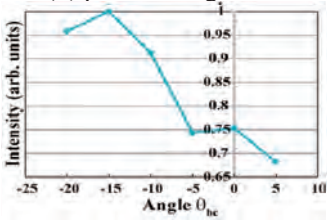

Fig. 3. θ_{bc} dependence of the ARPES spectral weight around 0.3 eV in Fig. 2 (b).

[1] T. Ishiguro *et al.*, *Organic Superconductors* (Springer - Verlag, Berlin, 1998).

BL7U

High-Resolution ARPES Study of SnTe(111): Observation of Two Types of Dirac-Cone Surface States

Y. Tanaka[1], T. Shoman[1], K. Nakayama[1], S. Souma[2], T. Sato[1], T. Takahashi[1,2], M. Novak[3], K. Segawa[3] and Y. Ando[3]

[1]*Department of Physics, Tohoku University, Sendai 980-8578, Japan*
[2]*WPI Research Center, Advanced Institute for Materials Research, Tohoku University, Sendai 980-8577, Japan*
[3]*Institute of Scientific and Industrial Research, Osaka University, Ibaraki, Osaka 567-0047, Japan*

Topological crystalline insulators (TCIs) are a new class of topological materials where an inverted bulk-band gap leads to unusual gapless surface states (SSs) that are protected by point-group symmetries of the crystal, in particular, mirror symmetry [1, 2]. The TCI phase has been experimentally verified on the (001) surface of the narrow-gap semiconductor SnTe, in which characteristic double-Dirac-cone SSs are observed on the projection of the (110) mirror plane [3]. While the existence of topologically protected Dirac-cone SSs is theoretically guaranteed on *any surface containing a mirror plane,* it has not been experimentally verified whether the topological SSs indeed exist on other surface-plane orientations like (111) and how the surface band structure depends on the symmetry of each surface orientation. This point is of crucial importance for understanding the interplay between the crystal symmetry and the topological protection in TCIs.

In this study, we have performed angle-resolved photoemission spectroscopy (ARPES) on the (111) surface of SnTe whose bulk and surface Brillouin zones (BZs) are displayed in Fig. 1(a). By utilizing the high-resolution and variable-photon-energy ($h\nu$) capabilities of the beamline BL7U, we have succeded in revealing two types of mirror-symmetry-protected Dirac-cone SSs, which originate from the bulk-band inversion at the L points [4].

Figure 1(b) represents Fermi-surface mapping results on the (111) surface of SnTe with $h\nu = 23$ eV. We identify bright intensity centered at the $\bar{\Gamma}$ point as well as relatively weak intensity at the $\bar{\mathrm{M}}$ point, which reflects the periodicity of the (111) surface. The observed intensity at E_F around the $\bar{\Gamma}$ point originates from a linearly dispersive hole-like band near E_F as seen from Fig. 1(c). The near-E_F band dispersion [Fig. 1(d)] extracted from the numerical fittings of the MDCs with two Lorentzians reasonably overlaps with each other within the experimental uncertainties irrespective of photon energies. This result strongly suggests the existence of a Dirac-cone SS centered at the $\bar{\Gamma}$ point. We also found a linearly dispersive hole-like band which crosses E_F around the $\bar{\mathrm{M}}$ point as displayed in Fig. 1(e). The $h\nu$ independence in the dispersion [see Fig. 1(f)] demonstrates that the observed linearly dispersive band originates from a Dirac-cone SS centered at $\bar{\mathrm{M}}$, indicating that there exist four Dirac cones in the surface BZ, one centered at $\bar{\Gamma}$ and three at $\bar{\mathrm{M}}$. As seen from Fig. 1(a), the (110) mirror plane of the bulk BZ lies along the $\bar{\Gamma}$– $\bar{\mathrm{M}}$ line of the surface BZ. Since a single L point at which bulk-band inversion takes place is projected onto either the $\bar{\Gamma}$ or $\bar{\mathrm{M}}$ points, a single Dirac cone is produced centered at those time-reversal-invariant momenta (on the projection of the mirror plane), consistent with the present observation. The present ARPES result on the (111) surface, together with our previous study on the (001) surface [3], establishes an essential role of the crystal mirror symmetry and the bulk-band inversion in realization of the TCI phase.

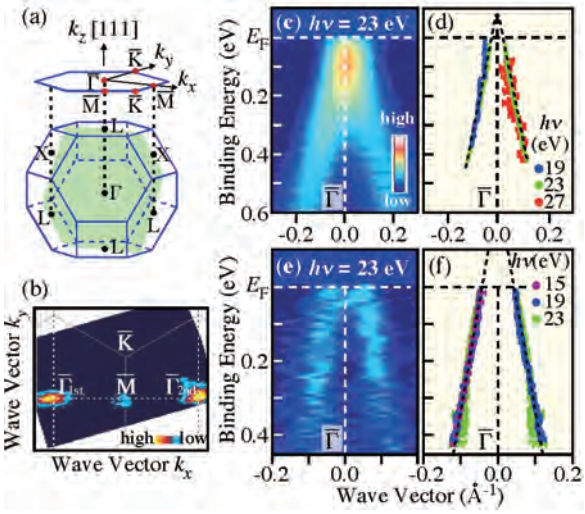

Fig. 1. (a) Bulk fcc BZ and corresponding hexagonal (111) surface BZ of SnTe. Green shaded area represents the (110) mirror plane. (b) ARPES intensity mapping at E_F at T = 30 K plotted as a function of in-plane wave vector. (c) Intensity plot of the second derivatives of the momentum distribution curves (MDCs) across the cut crossing the $\bar{\Gamma}$ point for $h\nu$ = 23 eV. (d) Comparison of the band dispersions for different photon energies extracted by fitting the MDCs. (e) and (f) Same as (c) and (d), respectively, but measured along the cut crossing the $\bar{\mathrm{M}}$ point.

[1] L. Fu, Phys. Rev. Lett. **106** (2011) 106802.
[2] T. H. Hsieh *et al.*, Nature Commun. **3** (2012) 982.
[3] Y. Tanaka *et al.*, Nature Phys. **8** (2012) 800.
[4] Y. Tanaka *et al.*, Phys. Rev. B **88** (2013) 235126.

BL7U

An ARPES Study of the Electronic Structure of $CsBi_4Te_6$

S. T. Cui[1], S. Kong[1], G. B. Zhang[1], Z. Sun[1], C. Xiao[2], Y. Xie[2], M. Matsunami[3] and S. Kimura[3,4]

[1]*National Synchrotron Radiation Laboratory, University of Science and Technology of China, Hefei, Anhui 230029, People's Republic of China*

[2] *Hefei National Laboratory for Physical Sciences at Microscale, University of Science and Technology of China, Hefei, Anhui 230026, People's Republic of China*

[3]*UVSOR Facility, Institute for Molecular Science, Okazaki 444-8585, Japan*

[4]*Graduate School of Frontier Biosciences, Osaka University, Suita 565-0871, Japan*

Topological insulators are a new quantum state of matter with gapless surface states inside of the bulk energy gap. $(Bi, Sb)_2(Te, Se)_3$ series of compounds have been extensively studied as topological insulators. On the other hand, $(Bi, Sb)_2(Te, Se)_3$ series have been widely used as thermoelectric materials. Indeed, the excellent properties of thermoelectric materials are mainly due to the nature of the novel electronic structures of these topological insulators. Thus, it is an interesting topic to search $(Bi, Sb)_2(Te, Se)_3$-derived thermoelectric materials for topological insulators.

$CsBi_4Te_6$ is an excellent thermoelectric material [1], with thermoelectric properties better than $(Bi, Sb)_2(Te, Se)_3$ at low temperature. Recently, it has also been found that a slight hole-doping can induce superconductivity in this compound [2]. Figure 1 shows the crystal structure of $CsBi_4Te_6$. In this material, the Bi_2Te_3 framework is reconstructed, so $CsBi_4Te_6$ bears no resemblance to the corresponding binary compound. Thus it is important to investigate whether this excellent thermoelectric material can host topological insulating states. Moreover, it is of great interest to study whether the topological insulator states can coexistence with superconductivity in this material.

We performed ARPES experiments on $CsBi_4Te_6$ at BL7 of UVSOR at T=30K, with 20 meV energy resolution and 0.5° angular resolution, under an ultrahigh vacuum of 6×10^{-11} mbar.

Figure 1 shows the electronic band structure over a large energy scale near the zone center. The band structure calculations show that $CsBi_4Te_6$ is a narrow-gap semiconductor [3], while the electrical conductance measurements show that this material bears metallic properties. The inset of Fig. 1(a) exhibits evident spectral weight near the Fermi level, which is consistent with the metallic conductivity in this material [3]. These metallic spectral weight however could arise from the conduction band with slight electron doping.

A close inspection of the near-E_F states can reveal more details of the electronic structure. Figure. 2(b) shows the spectral weight distribution in the yellow frame in Fig. 2(a). It is very interesting that there likely exists Dirac-cone-like spectral weight within the band gap of this material. Although more experiments should be carried out to reveal the true nature of these states, it is possible that novel electronic states may exist in this thermoelectric material.

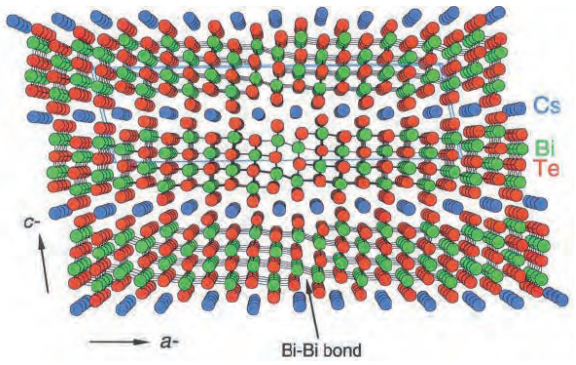

Fig. 1. The crystal structure of $CsBi_4Te_6$ looking down the *b* axis.

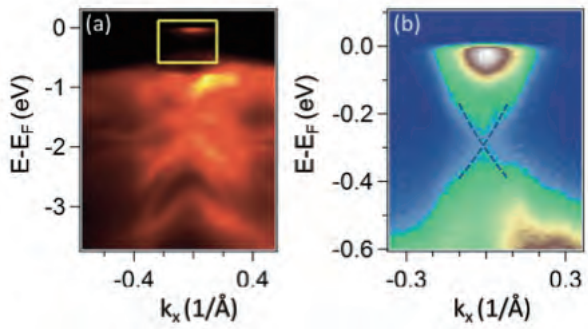

Fig. 2. (a) Band structure of $CsBi_4Te_6$. (b) Near-E_F Dirac-cone-like dispersions, which were taken from the yellow frame in (a).

[1] D. Y. Chung *et al.*, Science **287** (2000) 1024.
[2] C. D. Malliakas *et al.*, J. Am. Chem. Soc. **135** (2013) 14540.
[3] D. Y. Chung *et al.*, J. Am. Chem. Soc. **126** (2004) 6414.

BL7U

Three-Dimensional Anisotropic Superconducting Gap of Over-Doped $BaFe_{1.8}Co_{0.2}As_2$

T. Hajiri[1,2], T. Ito[1,3], M. Matsunami[2,4], B. H. Min[5], Y. S. Kwon[5] and S. Kimura[2,4]

[1]*Graduate School of Engineering, Nagoya University, Nagoya 464-8603, Japan*
[2]*UVSOR Facility, Institute for Molecular Science, Okazaki 444-8585, Japan*
[3]*Nagoya University Synchrotron Radiation Research Center, Nagoya University, Nagoya, 464-8603, Japan*
[4]*School of Physical Sciences, The Graduate University for Advanced Studies (SOKENDAI), Okazaki 444-8585, Japan*
[5]*Department of Emerging Materials Science, DGIST, Daegu 711-873, Republic of Korea*

In iron pnictide superconductors, one of the most attractive issues is the position of nodes in the three-dimensional (3D) electronic structures, because the position of nodes is the most important information for the origin of the superconductivity as well as the symmetry of the superconducting (SC) order parameter. Angle-resolved photoemission spectroscopy (ARPES) is one of the most powerful tools to investigate the SC-gap structures. Importantly, the SC-gap structure in the 3D momentum space can be revealed by ARPES using synchrotron radiation. In this report, we show the 3D-ARPES results of the over-doped $BaFe_{1.8}Co_{0.2}As_2$ (T_c ~ 22.5 K) using UVSOR BL7U "SAMRAI" end-station. In this material, the nodal behavior was reported [1,2].

Figures 1(a) and 1(b) show the out-of-plane electron Fermi surfaces (FSs) in the ΓMAZ plane and in-plane FSs determined by experiments, respectively. The symmetrized ARPES spectra above T_c (T = 35 K) and below T_c (T = 12 K) at several FS angles (θ) measured with the photon energy $h\nu$ = 14 eV are shown in Figs. 1(c) and 1(d). At the outer electron FS in Fig. 1(c), the spectral weight at Fermi level at $|\theta|$ = 177.2° are suppressed with decreasing temperature, indicating the opening the SC gap. At $|\theta|$ = 92.3°, however, no temperature dependence appears. In contrast to the outer electron FS, the inner electron FS shows substantially isotropic SC gaps as shown in Fig. 1(d). We summarized the θ-dependence of the SC-gap size of both electron FSs around the A and M points in Figs. 1(e) and 1(f), respectively. The only outer electron FS has an anisotropic SC gap with nodes or gap minima around the longer axis of the ellipsoid-shaped FS.

Focusing on the electron FSs at the intermediate region between the M and A points taken at $h\nu$ = 19 eV shown in Figs. 1(g) and 1(h), both electron FSs show substantially isotropic SC gaps. Therefore, the nodes exist only around the longer axis of the ellipsoid-shaped outer electron FS at around the M ($h\nu$ = 24 eV) and A ($h\nu$ = 14 eV) points. Our observation suggests that the appearance of superconductivity of this material originates from not only spin fluctuation but also orbital fluctuation.

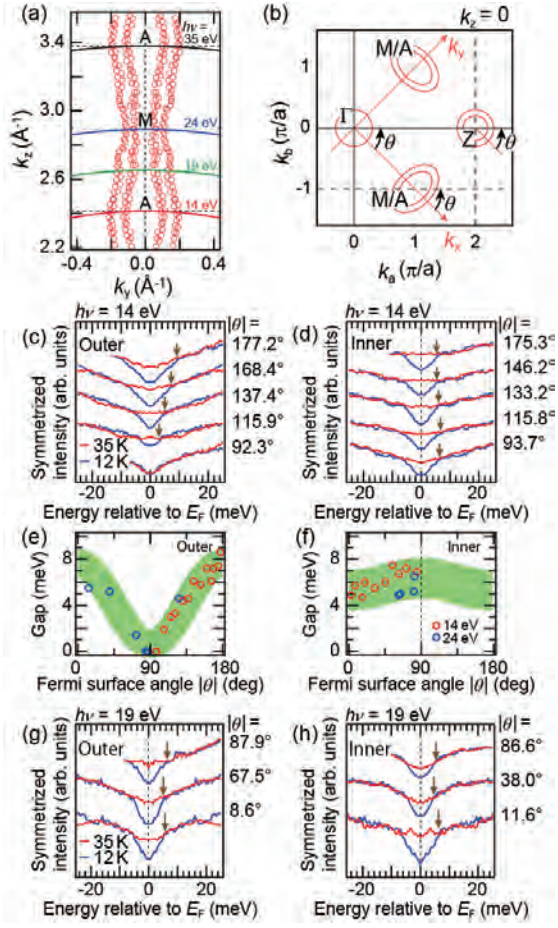

Fig. 1. (a) Out-of-plane electron FSs in the ΓMAZ plane. (b) Schematic in-plane FSs. (c,d) Symmetrized ARPES spectra taken at $h\nu$ = 14 eV with selected θ of the outer and inner electron FSs, respectively. (e,f) θ-dependence of the SC-gap size around the M and A points. (g,h) Same as (c,d) but taken at $h\nu$ = 19 eV.

[1] D. -J. Jang *et al.*, New J. Phys. **13** (2011) 023036.
[2] T. Hajiri *et al.*, arXiv:1311.4990 (2013).

BL7U

Carrier Concentration Dependence of Superconducting Gap in $Bi_2(Sr,RE)_2CuO_{6+d}$ (RE = La, Nd, Sm)

H. Sakamoto[1], A. Yamamoto[1], M. Matsunami[2], S. Kimura[2] and T. Takeuchi[1,3,4,5]

[1]*Department of Crystalline Materials Science, Nagoya University, Nagoya 464-8603, Japan*
[2]*UVSOR Facility, Institute for Molecular Science, Okazaki 444-8585, Japan*
[3]*Ecotopia Science Institute, Nagoya University, Nagoya 464-8603, Japan*
[4]*Toyota Technological Institute, Nagoya 468-8511, Japan*
[5] *Promoting Individual Research to Nurture the Seeds of Future Innovation, Japan Science and Technology Agency, Tokyo 102-8666, Japan*

The relation between the pseudogap and the stability of superconducting state had been intensively discussed. Some experimental results supported the scenario of the pseudogap as the pre-formed superconducting gap, but many other experiments suggested that the pseudogap developing around the anti-node direction is caused by an unidentified mechanism that is different from the Cooper pair formation and, therefore, prevents the electrons near the anti-nodal region from forming the Cooper pairs. The electrons near the node, on the other hand, are not affected by the pseudogap, and the Bose condensation of the Cooper-pairs still takes places to stabilize the superconducting state.

Despite a huge number of investigations being performed after the discovery of high-T_c cuprate superconductors, the collective excitation leading to the formation of Cooper-pairs has not been fully identified yet. In order to gain deep insight into such collective excitation, it is of great importance to know the temperature-, momentum-, and carrier concentration- dependences of superconducting gap. Unfortunately, however, the pseudogap developing at the underdoped condition has made it difficult to reveal the temperature-, momentum-, and carrier concentration- dependences of superconducting gap.

The relation between the carrier concentration dependence of superconducting gap and the carrier concentration dependence of T_c especially at the underdoped region, on the other hand, has not been fully investigated yet, because the highly developed pseudogap covers the very wide momentum and the superconducting gap persists only in the limited portion in the vicinity of nodal direction where the energy-width of superconducting gap stays in very small values.

In this study, therefore, we carefully investigated the very small superconducting-gap $\Delta(\phi) = \Delta_0 \cos\phi$ persisting near the nodal direction ($\phi = 0$) for a series of $Bi_2(Sr,RE)_2CuO_{6+d}$ (RE = La, Nd, Sm) superconductors of various hole-concentrations by means of ultra-high-energy-resolution laser induced ARPES. By additionally employing the synchrotron radiation ARPES measurements at BL7U in UVSOR, we investigated the shape of the Fermi surface and the size of the pseudogap as a function of carrier concentration.

Figure 1 shows the hole concentration dependence of superconducting gap Δ_0 and T_c of $Bi_2(Sr,RE)_2CuO_{6+d}$ (RE = La, Nd, Sm) determined by means of ARPES measurements. The pseudogap develops when the rare earth element of small ionic radius is used for the substitute of Sr. The difference in T_c for the different series of $Bi_2(Sr,RE)_2CuO_{6+d}$ is, therefore, attributed to the development of pseudogap.

The hole-concentration dependence of Δ_0 shows universal behavior regardless of the rare earth element involved in the samples. It obviously increases with decreasing hole concentration at overdoped region. After becoming maximal at around p = 0.23 holes/Cu, it turns out to be reduced with decreasing hole concentration. The value of p = 0.23 holes/Cu providing maximum Δ_0 is definitely different from p = 0.16 holes/Cu that has been generally considered for the optimally doped condition.

We should stress, as a consequence of this study, that the formability of Cooper-pair is less sensitive to out-of-plane disordering. It is also very important to find the collective excitation that can strongly affect the energy and momentum of conduction electrons at p = 0.23 holes/Cu.

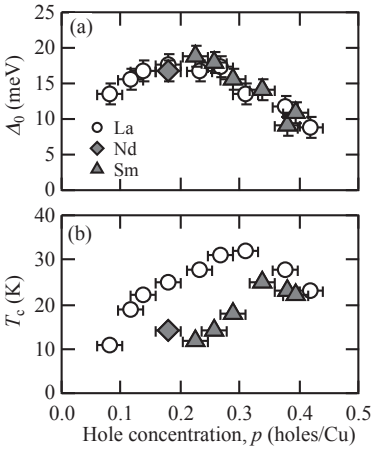

Fig. 1. Hole concentration dependence of (a) superconducting gap Δ_0 and (b) T_c of $Bi_2(Sr,RE)_2CuO_{6+d}$ (RE = La, Nd, Sm) determined by means of ARPES measurements and (b) that of.

BL7B

Electronic Status of Ce^{3+} in Glass Host by Characterizing Photoluminescence of Ce^{3+} Doped $20Al(PO_3)_3$–80LiF Glass Scintillator

T. Shimizu[1], Y. Minami[1], R. Arita[1], M. Tsuboi[1], T. Nakazato[2], T. Hori[1], K. Fukuda[1], K. Yamanoi[1], Y. Shinzato[1], R. Sogi[1], N. Sarukura[1], H. Azechi[1], M. Cadatal-Raduban[3], T. Murata[4], S. Fujino[5], H. Yoshida[6], T. Suyama[7], K. Fukuda[7], A. Yoshikawa[8], N. Sato[9], H. Kan[9] and K. Kamata[9]

[1]*Institute of Laser Engineering, Osaka University, Suita 565-0871, Japan*
[2]*Research Institute for Science & Technology, Tokyo University of Science, Noda 278-8510, Japan*
[3]*Centre for Theoretical Chemistry and Physics, Institute of Natural and Mathematical Sciences, Massey University, Albany, Auckland, 0632 New Zealand*
[4]*Kumamoto University, Kumamoto 860-8555, Japan*
[5]*Kyushu University, Fukuoka 812-8581, Japan*
[6]*Ceramic Research Center of Nagasaki, Higashisonogi-gun 859-37, Japan*
[7]*Hamamatsu Photonics K.K., Hamamatsu 430-8587, Japan*
[8]*Institute for Materials Research, Tohoku University, Sendai 980-8577, Japan*
[9]*Furukawa Co. Ltd., Tokyo 100-8370, Japan*

The realization of nuclear fusion is highly expected to satisfy the energy demand in the future. Fusion plasma diagnostics at higher plasma areal density than 3 g/cm^2 is one of the biggest breakthrough in nuclear fusion research. Scattered-neutron diagnostics [1] utilizing Pr^{3+}-doped $20Al(PO_3)_3$-80LiF (APLF+Pr) glass scintillator is expected to achieve plasma areal density measurement in fusion core. APLF+Pr, which have high sensitivity for scattered neutrons and fast response time about 5.4 ns, is the key factor of the measure. In addition, recent research indicated that APLF+Ce also have great characteristics as neutron scintillator [2]. In this work, we report the optical properties of APLF+Ce at various temperature for investigation of electronic status of Ce^{3+}.

We have measured Photoluminescence (PL) spectra and Photoluminescence Excitation (PLE) spectra of APLF+Ce for 0.5 and 3.0 mol % Ce^{3+} concentrations at 30K, 100K, 200K, and 300K. APLF+Ce glass samples which size are 25 mm in diameter and 10 mm in thickness are used. The experiment was conducted at BL7B utilizing G2 grating. Each sample was put inside a vacuum chamber maintained at a vacuum level of 10^{-6} Pa and was excited by the synchrotron radiation. An optical fiber was used to guide luminescence from the sample to the spectrometer. The spectrometer consists of a liquid nitrogen-cooled charge coupled device (CCD) camera for PL measurement and a photomultipliertube (PMT) for PLE measurement. The temperature of samples was controlled by liquid helium cryostat and heater.

The PL spectra of APLF+Ce for 0.5 and 3.0 mol % Ce^{3+} concentrations excited by 220 nm radiation at 30 K and 300 K are shown in Fig. 1. The luminescence intensity of both samples remain nearly unaffected by temperature change. The emission peak of APLF+0.5 mol % Ce^{3+} was around 330 nm wavelength. On the other hand, one of APLF+3.0 mol % Ce^{3+} was around 343 nm wavelength. This difference result from expanding of 5d bandwidth in Ce^{3+} with increasing of Ce^{3+} concentration. The PLE spectra of samples, emission wavelength is 331 nm, at various temperature are shown in Fig. 2. Both crystal show broad excitation spectrum and the peak wavelength are around 270 nm.

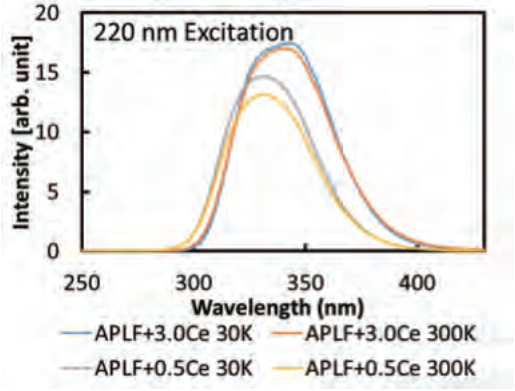

Fig. 1. PL spectra of APLF+Ce.

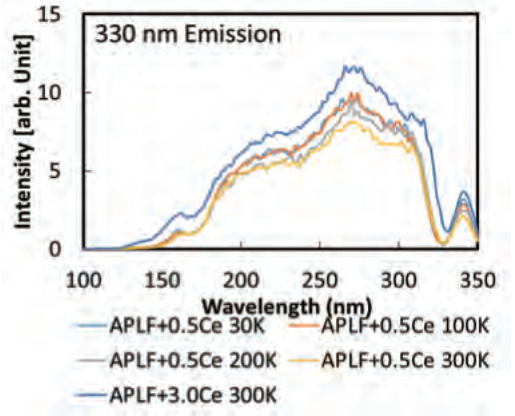

Fig. 2. PLE spectra of APLF+Ce.

[1] M. Moran *et al.*, Rev. Sci. Instrum. **75** (2004) 3592.
[2] IEEE TRANSACTIONS ON NUCLEAR SCIENCE. **59** (2012) 2256.

BL7B

Reflection Spectra of Ternary Zinc Bismuth Phosphate Glasses in the Ultraviolet Region

N. Kitamura
National Institute of Advanced Industrial Science and Technology, Osaka 563-8577, Japan

Bismuth phosphate glasses, which have high refractive index and low deformation temperature, are candidate materials for producing high performance optical components such as compact lenses and diffractive optics. It is of interest that a zinc bismuth phosphate glass system has two distinct glass-forming regions; orthophosphate and isolated phosphate structures are dominant in the region that the atomic ratio O/P is higher than 3.5 and metaphosphate and pyrophosphate structures are dominant in the region of O/P < 3.5[1, 2]. We have reported the glass structure and local structure around bismuth ions in a previous work [2, 3]. Absorption edge energy is related to the interconfigurational transition from $6s^2$ to $6s^16p^1$ of the Bi^{3+} ion. However, the energy level in the glass system is not clear yet. In the present study, reflectivity of the bismuth phosphate glasses has been measured to investigate compositional dependence of the band structure in the vacuum ultraviolet region.

Binary xBi_2O_3-$(100-x)P_2O_5$ glasses (x=15, 25 and 30 mol%), ternary $yZnO$-$(30-y/2)Bi_2O_3$-$(70-y/2)$ P_2O_5 glasses (y=10, 20 and 30 mol%) and 50ZnO-50 P_2O_5 glass were prepared by using a conventional liquid-quench method. Reflectivity of optically polished samples was measured in the photon energy region of 4-12 eV with an incident angle of 10° at the BL7B. Figure 1 shows reflection spectra of the binary and un-doped ZnO-P_2O_5 glass. Distinct reflection peak and broad contour were respectively observed at around 5 eV and 6-8 eV by comparing the spectrum for the undoped ZnO-P_2O_5 glass. The peak and contour are assigned to the $6s^2 \rightarrow 6s^16p^1$ transition in the Bi^{3+} ion [2, 4]. We know that transitions from the ground state ($^1S_0$) to excited states $^3P_0$ and $^3P_2$ are spin-forbidden. Therefore, the lower distinct peak is expected to the $^1S_0 \rightarrow {}^3P_1$ transition and the next contour could be due to the $^1S_0 \rightarrow {}^1P_1$ transition. In the binary Bi_2O_3-P_2O_5 glass system, the distinct peak shifted toward lower energy side with Bi_2O_3 concentration. Moreover, both the band structure tended to broaden with increasing the concentration. It could be due to distortion of BiO_6 tetrahedron which was found in high energy diffraction measurement [5].

On the other hand, reflection spectra of ternary $yZnO$-$(30-y/2)Bi_2O_3$-$(70-y/2)$ P_2O_5 glasses are shown in Fig. 2. As shown in the figure, the distinct peak did not shifted with the change of Bi_2O_3 concentration, while the intensity of the band increased with the concentration. It was consistent with that the absorption edge energy was less dependent on the concentration in the ternary glass system with O/P<3.5 [2]. The band structure of ternary glass with O/P>3.5 will be measured in near future.

This work was supported by Nippon Sheet Glass Foundation for Materials Science and Engineering.

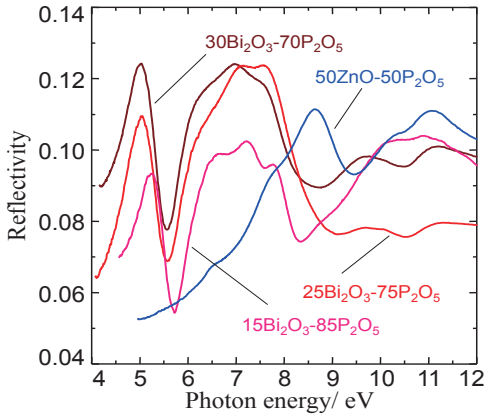

Fig. 1. Reflection spectra of binary xBi_2O_3-$(100-x)$ P_2O_5 and ZnO-$50P_2O_5$ glasses.

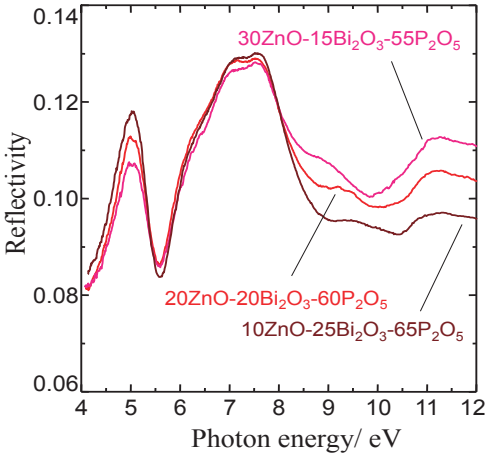

Fig. 2. Reflection spectra of ternary $yZnO$- $(30-y/2)Bi_2O_3$-$(70-y/2)P_2O_5$ glasses.

[1] B. Elouadi *et al.*, Phase Trans. **13** (1988) 219.
[2] N. Kitamura, K. Fukumi, J. Nakamura, T. Hidaka, H. Hashima, Y. Mayumi and J. Nishii, Mater. Sci. Eng. B **161** (2009) 91-95.
[3] N. Kitamura and K. Fukumi, J. Ceram. Soc. Jpn. **121** (2013) 355-360.
[4] G. Blasse and A. Bril, J. Chem. Phys. **48** (1968) 217-222.
[5] N. Kitamura, *et al.*, 23th International Congress on Glass 2013, in preparation.

BL7B

Anomalous Domain-Wall Conductance in Pyrochlore-Type $Nd_2Ir_2O_7$ on the Verge of the Metal-Insulator Transition

J. Fujioka[1], K. Ueda[1], Y. Takahashi[1], T. Suzuki[2], S. Ishiwata[1], Y. Taguchi[2], M. Kawasaki[1,2] and Y. Tokura[1,2]

[1]*Department of Applied Physics, University of Tokyo, Tokyo 113-8656, Japan*
[2]*RIKEN Center for Emergent Matter Science (CEMS), Wako 351-0198, Japan*

The topological quantum phase of condensed matter has been of great interest since the discovery of the topological insulator. A spectacular feature of topological insulator is the emergence of the topologically protected surface state, whereas the bulk is characterized by a gapped electronic state. Recently, Wan *et al*. have predicted another class of unconventional topological quantum state, that is, Weyl semimetal (WSM). WSM is a zero gap semiconductor(semimetal) which is characterized by the *k*-linearly dispersing bands near the Fermi energy and by the emergence of topologically-protected edge state at the sample surface.

Pyrochlore-type $R_2Ir_2O_7$ (R = trivalent rare-earth or Y ion) has attracted much attention since it is one of the promising candidates for the realization of WSM due to the interplay between electron correlation and strong spin-orbit coupling inherent to heavy 5*d* elements. Among a series of $R_2Ir_2O_7$, R = Nd undergoes metal-insulator transition accompanying with all-in all-out type magnetic ordering at T_N = 32 K, where all the spins on the vertices of tetrahedron point either inwards or outwards to its center. Recent study suggests that its ground state could be a Mott insulator in vicinity to WSM [2]. In order to characterize this unconventional phase, the observation of edge state at sample surface or magnetic domain wall (DW) is essential.

In this article, we report the spectroscopic observation of metallic state at antiferromagnetic DW in $Nd_2Ir_2O_7$ [3]. The antiferromagnetic DW shows Drude-like optical response with minimal damping constant of ~ 2 meV, contrary to the fully-gapped electronic structure in bulk.

We measured reflectivity spectra for polycrystals of $Nd_2Ir_2O_7$ between 12 meV and 5 eV using Fourier-transform spectrometer and grating-type spectrometer in temperature range between 5 K and 290 K. We obtained the reflectivity between 5 and 40 eV at room temperature by using synchrotron radiation at BL7B in UVSOR. We determined complex optical constants through the Kramers-Kronig transformation with proper extrapolations of reflectivity in the low and high energy regions. We also obtained the optical conductivity spectra below 8 meV by the terahertz time-domain spectroscopy in a transmission configuration.

Figure 1 (a) shows the reflectivity spectra up to 40 eV. Below T_N, the reflectivity in low energy region is significantly suppressed, indicative of the opening of the charge gap. Figure 1 (b) shows the real parts of the optical conductivity spectra below 8 meV at 4 K. Here, the black solid line denotes the conductivity for multi-domain state [$\sigma_{ut}'(\omega)$] obtained at 0 T after cooling under zero magnetic field(untrained state), whereas the red one denotes the spectra for single-domain state[$\sigma_t'(\omega)$] obtained at 0 T once the field applied(trained state). $\sigma_{ut}'(\omega)$ shows Drude response below 4 meV, whereas $\sigma_t'(\omega)$ monotonically decreases as lowering energy. In order to examine the charge dynamics of DW in more detail, we have deduced the real ($\Delta\sigma'(\omega) = \sigma_{ut}'(\omega) - \sigma_t'(\omega)$) and imaginary ($\Delta\sigma''(\omega) = \sigma_{ut}''(\omega) - \sigma_t''(\omega)$) part of the DW optical conductivity spectra. Figure 1 (c) shows $\Delta\sigma'(\omega)$ (red solid line) and $\Delta\sigma''(\omega)$ (blue solid one). The broken lines corresponds to fitting 1 curve with Drude model with scattering rate of 2 meV, indicating that highly metallic state is realized at the magnetic DW. Such anomalous DW conductance could be relevant with the topological edge state relevant to WSM

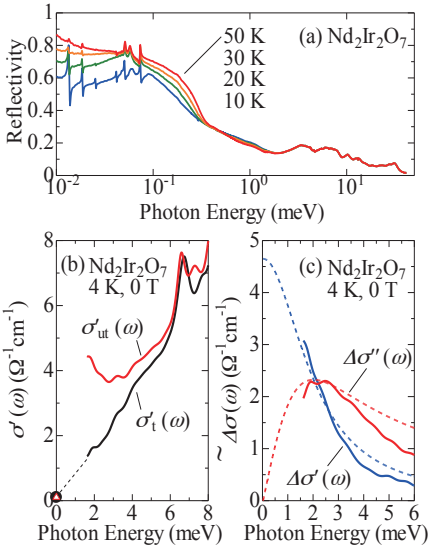

Fig. 1. (a)Reflectivity and (b) (c) optical conductivity spectra for $Nd_2Ir_2O_7$ at various temperatures.

[1] X. Wan *et al*., Phys. Rev. B **83** (2011) 205101.
[2] K. Ueda *et al*., Phys. Rev. Lett. **109** (2012) 136402.
[3] K. Ueda *et al*., Phys. Rev. B **89** (2014) 075127.

BL7B, BL8B

Measurement of Transmittance and Reflectance of $LiTi_2O_4$ and UPS Measurement of Multi-Alkali Surface

R. Inagaki[1,2], T. Konomi[2], T. Tokushi[2], M. Katoh[2], E. Kako[3], S. Yamaguchi[3], Y. Kobayashi[3], N. Yamamoto[4], M. Hosaka[4], Y. Takashima[4], S. Shiraki[5], T. Hitosugi[5], K. K. Rasika[6] and Y. Okano[7]

[1]*Graduate School of Engineering, Nagoya University, Nagoya 464-8603, Japan*
[2]*UVSOR facility, Institute for Molecular Science, Okazaki 444-8585, Japan*
[3]*High Energy Accelerator Research Organization, KEK, Tsukuba, 305-0801, Japan*
[4]*Nagoya University Synchrotron radiation Research center, Nagoya 464-8603, Japan*
[5]*WPI-AIMR, Tohoku University, Sendai 980-8577, Japan*
[6]*Graduate School of Advanced Integration Science, Chiba 263-8522, Japan*
[7]*Laser center, Institute for Molecular Science, Okazaki 444-8585, Japan*

In UVSOR, a VUV free electron laser based on superconducting linear accelerator with high pulse repetition about 1MHz is being designed for the next generation light sources. We are developing an electron gun for the new accelerator by combining superconducting RF cavity and photocathode. We propose a back-illuminated multi-alkali photocathode with transparent superconductor $LiTi_2O_4$ [1]. We consider that to clarify the transmittance / reflectance of the substrate and deposition state of multi-alkali is important in making the photocathode.

In this study we measured the transmittance and reflectance of $LiTi_2O_4$ in R.T. and 25.5K at BL7B, UVSOR-Ⅲ. Furthermore, we performed a Ultraviolet Photoelectron Spectroscopy of gold surface was deposited multi-alkali (K_2CsSb) at BL8B, UVSOR-Ⅲ to elucidate the bonding state of alkali metal atoms in the course of deposition.

Figure 1(a) shows a transmittance of $LiTi_2O_4$ of 70nm and 90nm thickness at R.T. and 25.5K. Figure 1(b) shows a reflectance of $LiTi_2O_4$ of 70nm and 90nm thickness at R.T. and 25.5K. The transmittance at R.T. is about 70% in the range of 350nm and 600nm. These results are consistent with the measurement results at Tohoku University [2]. At 25.5K, the transmittance of only substrate ($MgAl_2O_4$) was higher than that of at R.T. in all measurement wavelength range but transmittance and reflectance of $LiTi_2O_4$ did not change significantly.

Figure 2 shows a spectrum of Au surface deposited K_2CsSb. The results suggests that three alkali metals were not compounded, it was only stacked. This is because the substrate temperature during the deposition was lower than the bonding temperature.

We plan to measure the transmittance and reflectance below superconducting transition temperature (<12K) and to perform a UPS in the actual deposition condition.

We are grateful to T. Hitosugi and S. Shiraki, WPI-AIMR Tohoku Univ. for provision of $LiTi_2O_4$ samples.

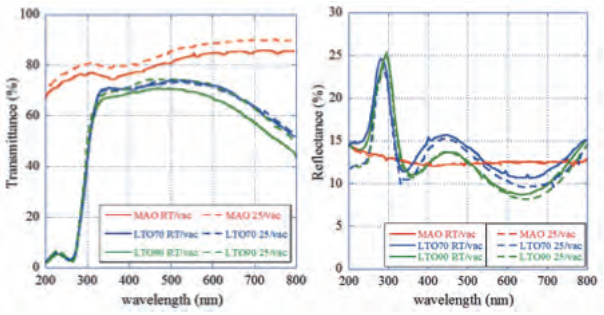

(a) (b)

Fig. 1. (a) Transmittance comparison of 70nm and 90nm thickness of $LiTi_2O_4$ at R.T. and 25.5K (b) Reflectance comparison of 70nm and 90nm thickness of $LiTi_2O_4$ at R.T. and 25.5K.

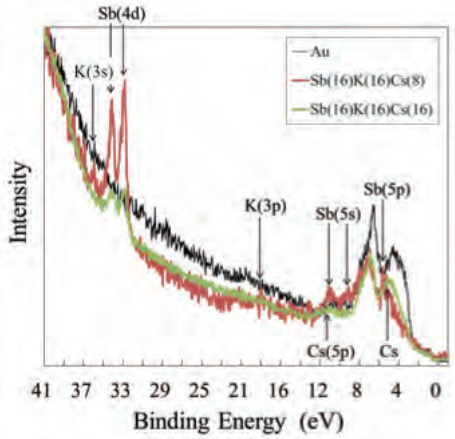

Fig. 2. Spectrum of Au surface was deposited K, Cs and Sb. (Black; Spectrum of Au, Red; Spectrum of surface deposited Sb: 16nm, K: 16nm and Cs: 8nm, Green; Spectrum of surface deposited Cs; 8nm on the sample of the red line)

[1] T. Hitosugi, N. Yamada, S. Nakao, Y. Hirose, and T. Hasegawa, Phys. Status Aolidi A 207, No.7, 1529-1537 (2010).
[2] A. Kumatani, T. Ohsawa, R. Shimizu, Y. Takagi, S. Shiraki *et al.,* Appl Phys. Lett. **101** (2012) 123103.

BL7B

Ultraviolet Photoluminescence of Gd^{3+} in Inorganic Materials under Vacuum Ultraviolet Excitation

K. Ueda[1], Y. Shimizu[1], Y. Taira[2] and Y. Inaguma[2]

[1] *Department of Materials Science, Graduate school of Engineering, Kyushu Institute of Technology, Kitakyushu 804-8550, Japan*

[2] *Department of Chemistry, Faculty of Science, Gakushuin University, Tokyo 171-8588, Japan*

Several ions such as Gd^{3+}, Ce^{3+}, Pb^{2+}, Bi^{3+} and Eu^{2+} are known as UV luminescent centers. Among them, only the Gd^{3+} emission center gives a sharp emission peak at approximately 310 nm in UV-B region. The sharp emission, which is attributed to the inner shell 4f–4f transition from ^6P_J to $^8S_{7/2}$ in the Gd^{3+} ions, can be used as a light source for not only lighting application but also medical application such as phototherapy for skin disease [1], transillumination for DNA analysis [2]. Because Gd^{3+} doped phosphors usually have large band gaps in the VUV region, efficient UV emission from doped Gd^{3+} ions necessitates intense VUV excitation. In this study, Gd^{3+} doped $YAlO_3$ were prepared and the fundamental UV photoluminescence (PL) properties were investigated by VUV excitation.

The polycrystalline samples of $(Y_{1-x}Gd_x)AlO_3$ (x=0.00-0.30) were prepared by a polymerized complex method, using Y_2O_3, Gd_2O_3, $Gd(NO_3)_3{\cdot}6H_2O$, $Al(NO_3)_3{\cdot}9H_2O$ as starting materials. Citric acid monohydrate and propylene glycol (PG) were used to form the polymerized complex gels. The sample powders were obtained by heating at 1400 °C in air. The obtained powders were pressed into pellets and sintered at 1400 °C in air. The phases in the samples were identified by the powder X-ray diffraction (XRD) using a Rigaku RINT 2100 diffractometer (CuKα radiation). The emission and excitation spectra were measured in the beamline BL7B at the UVSOR facility.

Each sample was identified as a distorted perovskite type phase with a space group Pnma. Because the unit cell volumes increased with Gd^{3+} concentration x, it was confirmed that Gd^{3+} was dissolved into the host lattices. Figure 1 shows PL spectra observed in $(Y_{1-x}Gd_x)AlO_3$ at room temperature along with the excitation energies for host lattice as a function of x. All samples showed Gd^{3+} emission peaks at 314 nm originating from $^6P_{7/2}$ to $^8S_{7/2}$ transition. The maximum PL intensity was observed at x=0.03 and concentration quenching occurred above x=0.03. The excitation energies for host lattices, that gave the maximum PL intensity, decreased with increasing x.

Figure 2 shows PL excitation spectra of $(Y_{1-x}Gd_x)AlO_3$. Intense peaks, that were assignable to host excitation, were observed in the wavelength range from 150 to 180 nm. The variation of the wavelength probably indicates the decrease in the band gaps of the host materials. Although shoulder peaks were observed at 120 nm and 200 nm, their origins are unknown at the present time.

Consequently, $(Y_{1-x}Gd_x)AlO_3$ was found to exhibit intense Gd^{3+} UV emission and showed promise as a UV phosphor upon VUV excitation.

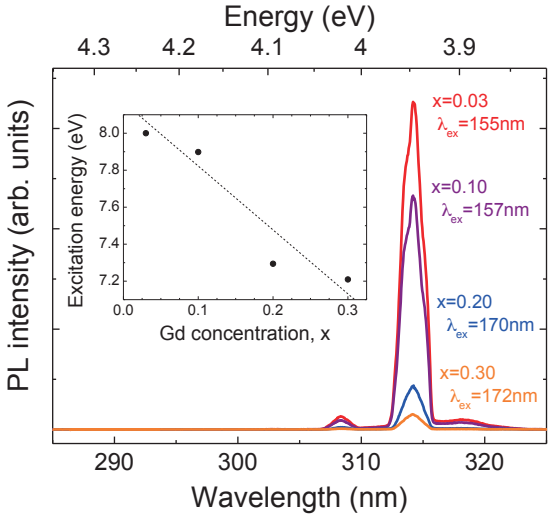

Fig. 1. Gd^{3+} photoluminescence spectra in $(Y_{1-x}Gd_x)AlO_3$. Inset shows excitation energies for host lattices as a function of x.

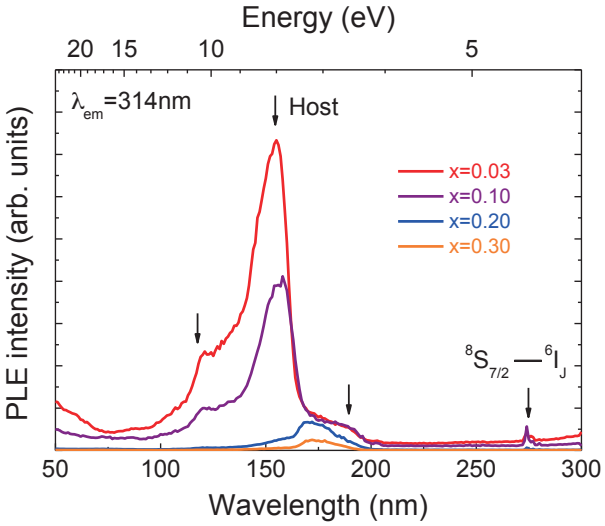

Fig. 2. PL excitation spectra of $(Y_{1-x}Gd_x)AlO_3$.

[1] R. P. Sonekar, S. K. Omanwar, S. V. Moharil, S. M. Dhopte, P. L. Muthal and V. K. Kondawar, Opt. Mater. **30** (2007) 622.

[2] S. Okamoto, R. Uchino, K. Kobayashi and H. Yamamoto, J. Appl. Phys. **106** (2009) 013522.

BL7B

Scintillation and Luminescence Properties of a Single $CsCaCl_3$ Crystal

M. Koshimizu[1], N. Yahaba[1], R. Haruki[2], F. Nishikido[3], S. Kishimoto[4] and K. Asai[1]

[1] *Department of Applied Chemistry, Graduate School of Engineering, Tohoku University, Sendai 9800-8579, Japan*

[2] *Advanced Science Research Center, Japan Atomic Energy Agency, Ibaraki 319-1195, Japan*

[3] *Molecular Imaging Center, National Institute of Radiological Sciences, Chiba 263-8555, Japan*

[4] *Institute of Materials Structure Science, High Energy Accelerator Research Organization, Tsukuba 305-0801, Japan*

Auger-free luminescence (AFL), or core-valence luminescence, is a radiative electronic transition between the valence band and the outermost core band. This luminescence is observed only for insulator crystals in which the band-gap energy is larger than the energy difference between the valence band and the outermost core band. AFL is known to be a fast luminescence process whose decay time constant is typically of the order of nanoseconds or less. Therefore, insulator materials that exhibit AFL are applicable as to fast-response scintillators.

Thus far, BaF_2 has been the most successful example of scintillators exhibiting AFL. Its scintillation has a fast component corresponding to AFL, whose decay time constant is as short as 0.8 ns [1]. Owing to this fast decay combined with relatively high light yields, BaF_2 has been used for applications in which good timing characteristics are necessary. However, its scintillation also has a long decay component corresponding to self-trapped excitons (STEs). The decay time constant of the long component has been reported to be 600 ns [1]. Thus, the long component limits the usage of BaF_2 in several applications, such as measurements with a high counting rate. AFL has also been observed in other binary halide crystals.

In this paper, we report the scintillation properties of a ternary halide crystal, $CsCaCl_3$. The origin of the scintillation is discussed on the basis of the luminescence characteristics under VUV irradiation.

Figure 1 shows the luminescence time profiles for excitation at 84 and 200 nm. For the excitation at 84 nm, we observed fast luminescence decay in the entire range of the broad band at 300 nm, and Fig. 1 illustrates the time profiles at short- and long-wavelength regions of the band. The decay time constant was estimated to be 2.3 ns, which is consistent with the result reported in a previous paper [2].

Figure 2 shows the scintillation time profile of $CsCaCl_3$. The decay behavior was satisfactorily fitted with a sum of two exponential-decay components and a time-independent component. The fast component had a decay time constant of 2.3 ns, which is consistent with that of the luminescence shown in Fig. 1. Thus, a fast scintillation component due to AFL was successfully obtained. The fast component accounts for 58% of the total scintillation. The slow component had a decay time constant of 14 ns, and this component accounts for only 4% of the scintillation. The time-independent component accounts for 38%, and this component is considered to have a decay time constant much longer than 624 ns, which is the period of the successive X-ray pulses. The components having a long decay time constant are presumably ascribed to the luminescence at defects or impurities and STE emission.

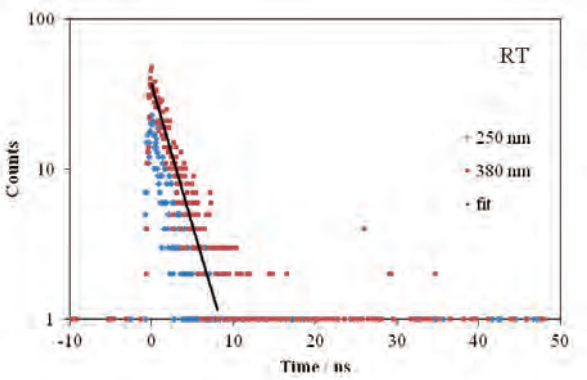

Fig. 1. Luminescence time profiles of $CsCaCl_3$ under irradiation of VUV photons at 88 nm.

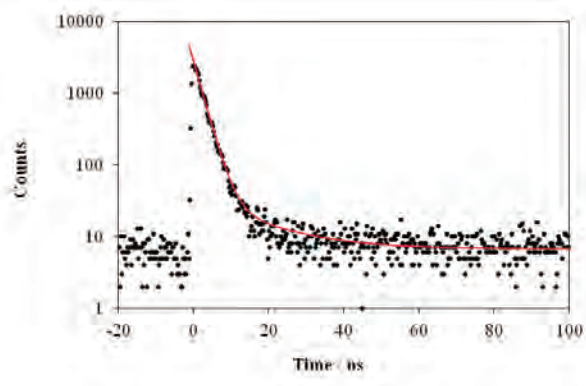

Fig. 2. Scintillation time profile of $CsCaCl_3$.

[1] M. Laval, *et al.*, Nucl. Instrum. Methods **206** (1983) 169.

[2] I. A. Kamenskikh, *et al.*, Rev. Sci. Instrum. **63** (1992) 1447.

BL7B

Insulator-to-Metal Transition of $Sm_{1-x}Y_xS$

K. Imura[1], M. Saito[1], M. Matsunami[2,3], H. S. Suzuki[4], S. Kimura[2,3] and N. K. Sato[1]
[1]*Department of physics, Graduate School of Science, Nagoya University, Nagoya 464-8602, Japan*
[2]*UVSOR Facility, Institute for Molecular Science, Okazaki 444-8585, Japan*
[3]*School of Physical Sciences, The Graduate University for Advanced Studies, Okazaki 444-8585, Japan*
[4]*Nuclear Scattering Group, National Institute for Materials Science, Tsukuba 305-0047, Japan*

Samarium monosulfide (SmS) is a prototypical compound that exhibits a phase transition by applying external pressure. This phase transition is accompanied by a color change from black to golden-yellow, namely black-to-golden (BG) transition [1]. It is well known that the electrical resistivity shows an energy gap of about $E_g \sim 0.1$ eV at ambient pressure. Although this energy gap decreases as increasing pressure, it is still unsolved how energy gap changes in the vicinity of the critical pressure of the BG transition.

In order to study an electronic structure as well as a mechanism of this phase transition, angle resolved photoemission spectroscopy or optical conductivity measurements are powerful techniques. However, pressure studies are very difficult for these experiments.

On the other hand, it has been reported that the BG transition is also induced by site substitution [2]. Then we focused onto the $Sm_{1-x}Y_xS$ system and performed optical conductivity measurement in order to reveal the relationship between the insulator to metal transition and the BG transition.

A detailed description of single crystal growth of $Sm_{1-x}Y_xS$ (x = 0, 0.17, 0.33) was shown in elsewhere [3]. The reflectivity measurement in the vacuum-ultraviolet, ultraviolet and visible region i.e., the photon energy region of 1.2-25 eV, was performed at the BL7B which consists of a 3-m normal incidence monochrometer. The optical conductivity spectra were obtained from the Kramers-Kronig (KK) analysis of the reflectivity spectra.

The BG transition of $Sm_{1-x}Y_xS$ is observed in the vicinity of x = 0.17. Figure 1 shows photon energy dependence of the reflectivity spectra [$R(\omega)$] of x = 0 (black color), 0.17 (black color) and 0.33 (gold color) at room temperature. The reflectivity in the infrared region of x = 0 is low in the whole energy region excepting a sharp reflection at $\hbar\omega \sim 23$ meV due to an optical phonon, reflecting an insulating behavior of pure SmS. At x = 0.17, however, a large reflectivity is observed although the system is still in black phase. The plasma edge of x = 0.33 is located at higher energy than x = 0.17 reflecting an increasing of carrier density.

Figure 2 shows the optical conductivity [$\sigma(\omega)$] as a function of photon energy calculated using the KK transformation from the reflectivity spectra. Closed circles show the DC conductivity values. The Drude structure is clearly observed at x = 0.17 and 0.33, and the systems show metallic behavior. These results indicate that the insulator-to-metal transition is not a trigger of the BG transition of Y-substituted SmS.

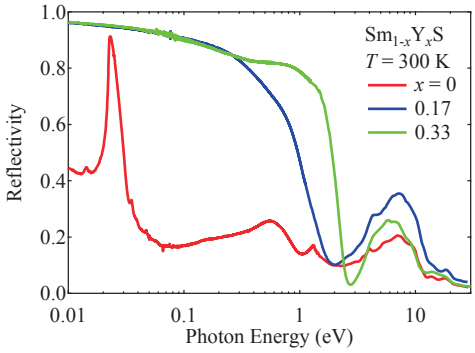

Fig. 1. The reflectivity spectra as a function of photon energy of $Sm_{1-x}Y_xS$ (x = 0, 0.17, 0.33) at T = 300 K.

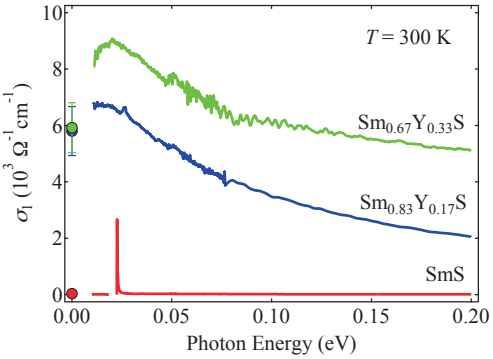

Fig. 2. Photon energy dependence of the optical conductivity calculated using the Kramers - Kronig transformation. Closed circles show DC conductivity value obtained from the conventional 4 probe method.

[1] P. Wachter, *In Handbook on the Physics and Chemistry of Rare Earth* (North-Holland, 1994) **19** (1994) 383.
[2] T. Penny and F. Holtzberg, Phys. Rev. Lett. **34** (1975) 322.
[3] K. Imura, T. Hajiri, M. Matsunami, S. Kimura, M. Kaneko, T. Ito, Y. Nishi, N. K. Sato and H. S. Suzuki, J. Korean Phys. Soc. **62** (2013) 2028.

BL7B

Anomalous Energy Transfer Route from Gd^{3+} to Ce^{3+} Ions in $Ce:Gd_3Al_2Ga_3O_{12}$ Crystals

A. Sato[1], M. Kitaura[1], S. Kurosawa[2,3], K. Kamada[3], A. Ohnishi[1], M. Sasaki[1] and K. Hara[4]
[1]*Department of Physics, Faculty of Science, Yamagata University, Yamagata 990-8560, Japan*
[2]*Institute for Materials Research, Tohoku University, Sendai 980-8577, Japan*
[3]*New Industry Creation Hatchery Center, Tohoku University, Sendai 980-8579, Japan*
[4]*Research Institute for Electronics, Shizuoka University, Hamamatsu 432-8011, Japan*

It is well known that the addition of Gd^{3+} ions works effectively for an enhancement of Ce^{3+} 5*d*-4*f* emission in inorganic phosphors [1]. The fundamental process is elucidated by the energy transfer from Gd^{3+} to Ce^{3+} ions ($Gd^{3+}\rightarrow Ce^{3+}$ energy transfer). The spectral overlap between the Gd^{3+} 4*f*-4*f* emission and Ce^{3+} 4*f*-5*d* absorption bands are necessary for the $Gd^{3+}\rightarrow Ce^{3+}$ energy transfer, and the route is usually opened from the lowest energy $(4f)^7$ excited state of the Gd^{3+} ion to the $(5d)^1$ excited state of the Ce^{3+} ion. Beside the spectral overlap, an appearance of phosphorescence in the Ce^{3+} 5*d*-4*f* emission is also worthwhile to note. The Gd^{3+} 4*f*-4*f* emission is electric-dipole forbidden, while the Ce^{3+} 5*d*-4*f* emission is electric-dipole allowed. When the Ce^{3+} 4*f*-5*d* excitation occurs through the energy transfer from the Gd^{3+} ion excited, the decay curve for the Ce^{3+} 5*d*-4*f* emission ranges from μs to ms.

The Ce-doped $Gd_3Al_2Ga_3O_{12}$ (Ce:GAGG) crystal attracts much attention as an inorganic scintillator for the detection of X- and γ-rays [2]. So far, we have investigated photoluminescence (PL) properties of Ce:GAGG crystals at the BL3B beamline of UVSOR [3, 4]. The PL-excitation (PLE) spectra for the Ce^{3+} 5*d*-4*f* emission exhibited narrow peaks around 4 and 4.5 eV, which are due to Gd^{3+} 4*f*-4*f* absorption. This fact suggests that the $Gd^{3+}\rightarrow Ce^{3+}$ energy transfer process occurs in Ce:GAGG. This process is supported by the existence of phosphorescence in the decay curve for the Ce^{3+} 5*d*-4*f* emission.

In the present study, we have found an anomalous $Gd^{3+}\rightarrow Ce^{3+}$ energy transfer route in Ce:GAGG crystals under the single bunch operation of UVSOR. Figure 1(a) demonstrates that a fast rise component with the lifetime of dozens of nanosecond appears in only the decay curve for Ce^{3+} 4*f*-5*d* emission measured under excitation in the Gd^{3+} 4*f*-4*f* absorption around 4.5 eV. This component was not observed under excitation in the Ce^{3+} 4*f*-5*d* absorption (Fig. 1(b)) and host GAGG absorption (Fig. 1(c)). Furthermore, it was confirmed that the fast rise does not appear under excitation in the Gd^{3+} 4*f*-4*f* absorption around 4 eV. Therefore, it is most likely that the fast rise component is caused by the excitation in Gd^{3+} 4*f*-4*f* absorption around 4.5 eV. Details of such an anomalous energy transfer route are unknown at present, so we are analyzing the route using the Dieke diagram.

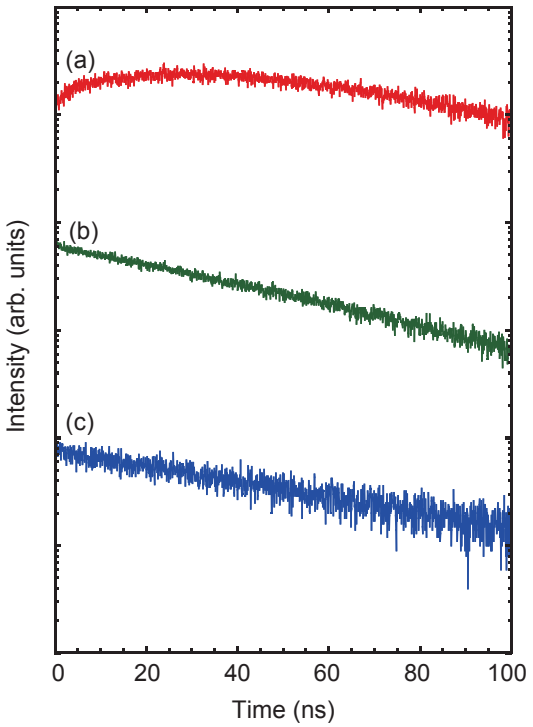

Fig. 1. Decay curves for the Ce^{3+} 5*d*-4*f* emission from the Ce:GAGG crystal, which were measured at 11 K under excitation at 4.5 eV (a), 3 eV (b) and 6.5 eV (c). The concentration of Ce^{3+} ion was 1.5 mol%. The decay curves were vertically shifted for clarity.

[1] M. Nikl *et al*., Appl. Phys. Lett., **77** (2000) 2159.
[2] K. Kamada *et al*., J. Cryst. Growth **352** (2012) 88.
[3] M. Kitaura *et al*., J. Appl. Phys. **115** (2014) 083517.
[4] A. Satoh *et al*., Jpn. J. Appl. Phys. (in press).

UVSOR User 3

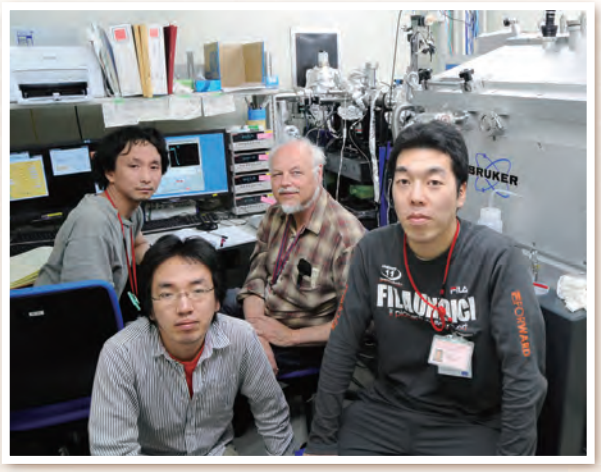

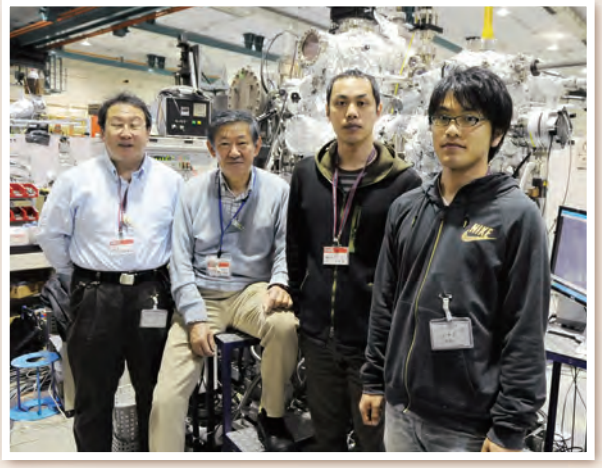

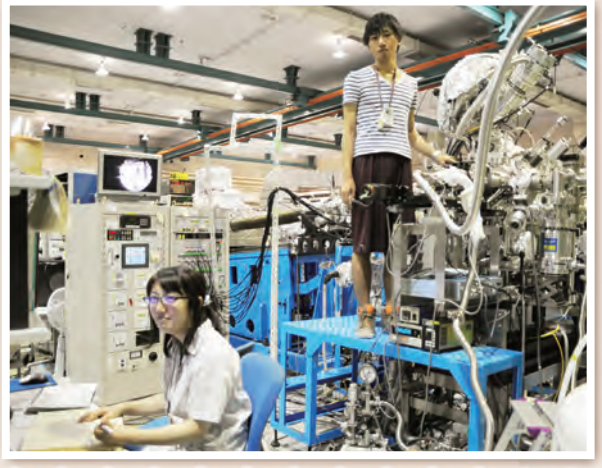

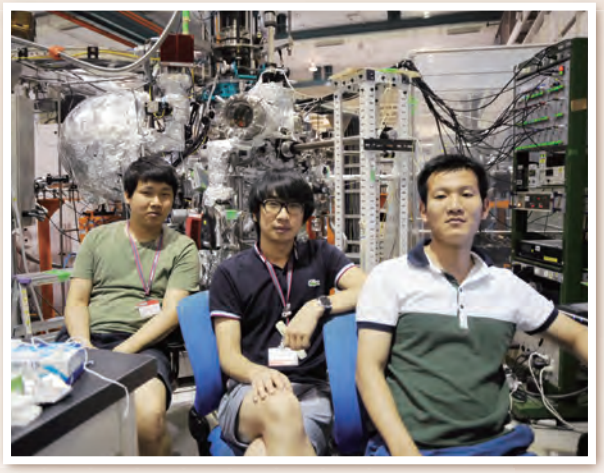

Ⅲ-3

Atoms and Molecules

BL3U

In-Situ Observation of Electrochemical Reaction by Soft X-Ray Absorption Spectroscopy with Potential Modulation Method

M. Nagasaka, H. Yuzawa, T. Horigome and N. Kosugi
Institute for Molecular Science, Myodaiji, Okazaki 444-8585, Japan

For understanding the electrochemical reaction, it is most important to investigate local structures of electrolytes including electric double layers at different potentials. Soft X-ray absorption spectroscopy (XAS) is an element specific method to study local electronic structures of solutions and interfaces. Recently, we developed a liquid cell for XAS in transmission mode [1], in which the thickness of the liquid layer is controllable between 20 and 2000 nm. In addition, we successfully measured XAS of electrolytes in electrochemical reaction by using a liquid cell with built-in electrodes [2]. From the Fe L-edge XAS spectra of aqueous iron sulfate solutions in electrochemical reaction, we revealed change in the valence of Fe ions at different potentials, where each XAS spectrum was measured at a constant potential and the scanning rate of the potential (0.08 mV/s) was quite slower than that in regular cyclic voltammetry (CV) (typically 100 mV/s). In this study, we have developed a potential modulation method to make possible in-situ XAS observation of electrochemical reaction at the same scanning rate of CV.

In the XAS measurement with a potential modulation method, the electrode potential is swept at a fixed photon energy, and soft X-ray absorption coefficients at different potentials are measured at the same time. After repeating the potential modulation at different photon energies, we can get XAS of electrolytes in electrochemical reaction at the same scanning rate of CV.

The experiments were performed at BL3U. XAS spectra of electrolytes were measured by using a liquid cell with built-in electrodes [2]. Figure 1 shows the Fe L-edge XAS spectra of aqueous iron sulfate solutions in electrochemical reaction at 100 mV/s. By increasing the potential from 0.0 to 1.0 V, the peak intensity of Fe(II) (708 eV) is decreased and that of Fe(III) (710 eV) is increased by the oxidation of Fe(II). By decreasing the potential from 1.0 to -0.4 V, the peak intensity of Fe(II) is increased, and that of Fe(III) is instead decreased by the reduction of Fe(III).

To obtain the fraction of Fe(II) and Fe(III) ions, the Fe L-edge XAS spectra at different potentials are fitted by superposition of the reference XAS spectra of Fe(II) and Fe(III) ions. Figure 2 shows fractions of Fe(II) and Fe(III) ions in electrochemical reaction at 100 mV/s. By increasing the potential, the fraction of Fe(III) is increased and that of Fe(II) is decreased. The Fe(II) ions are partially changed to the Fe(III) ions by the oxidation process. It is because a thick liquid layer is necessary for XAS of dilute Fe ions in transmission mode. As shown in the inset of Fig. 2, the XAS spectra includes both the solid-liquid interface that occurs the Fe redox reaction and the bulk electrolyte of Fe(II) that does not involve the electrochemical reaction. The mechanism of these Fe redox process will be discussed by correlating the XAS results with those at the different scanning rates.

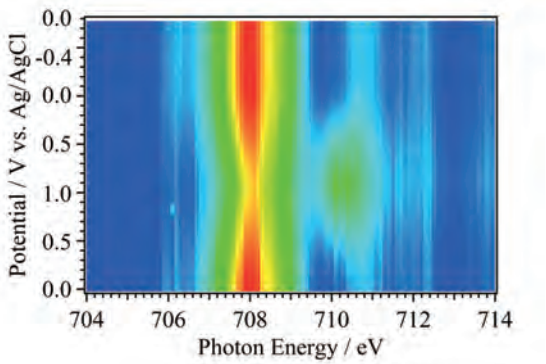

Fig. 1. Two dimensional plots, photon energy and potential (versus Ag/AgCl), of the Fe L-edge XAS spectra in electrochemical reaction of aqueous iron sulfate solutions at the scanning rate of 100 mV/s.

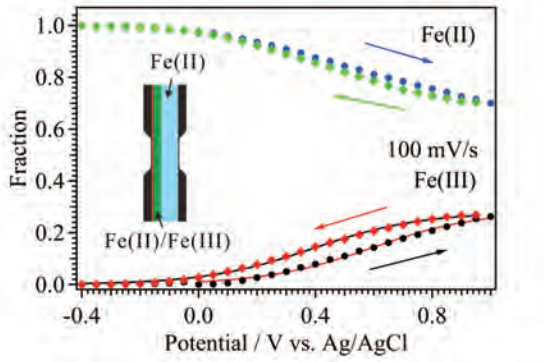

Fig. 2. Fractions of Fe(II) and Fe(III) ions as a function of potential (versus Ag/AgCl) in electrochemical reaction at 100 mV/s. The inset shows a partial oxidation model in a liquid cell.

[1] M. Nagasaka *et al.*, J. Electron Spectrosc. Relat. Phenom. **177** (2010) 130.
[2] M. Nagasaka *et al.*, J. Phys. Chem. C **117** (2013) 16343.

BL3U

Interaction of Pyridine with Water in Aqueous Solution Studied by Soft X-Ray Absorption Spectroscopy in C and N K-edges

M. Nagasaka, H. Yuzawa and N. Kosugi
Institute for Molecular Science, Myodaiji, Okazaki 444-8585, Japan

Pyridine is liquid and is soluble in water at any concentration. In aqueous pyridine solution, the formation of hydrogen bond (HB) between the N site of pyridine and the H site of water is proposed by the vibrational spectroscopy [1]. But the local structure of pyridine-water mixture is unknown. Soft X-ray absorption spectroscopy (XAS) is an element specific method applicable to the local structure study. In the present work, we have measured the C and N K-edge XAS of pyridine-water mixtures at different concentrations, and investigated the interaction of the C and N sites of pyridine with water in the binary solutions.

The experiments were performed at BL3U. XAS of liquid samples were measured by a transmitted-type liquid cell at 25 °C [2]. The liquid layer was sandwiched between two 100 nm-thick Si_3N_4 membranes. The thickness of the liquid layer is controllable between 20 and 2000 nm by adjusting the He backpressure.

Figure 1(a) shows the C K-edge XAS of pyridine gas and pyridine-water solution $(C_5H_5N)_X(H_2O)_{1-X}$. The transition C 1s → π* shows two peaks: First peak (C1) is derived from the *meta*- and *para*-C sites of pyridine. The second peak (C2) is the *ortho*-C sites. From gas to liquid pyridine (X=1.0), both the C1 and C2 peaks are shifted to the lower photon energy. Figure 1(b) shows the N K-edge XAS of pyridine gas and pyridine-water solutions. The N 1s → π* peak shows the higher energy shift from gas to liquid. These energy shifts are consistent with those of the pyridine clusters with an antiparallel structure [3], but are smaller than in the cluster case.

By increasing the molar fraction of water in pyridine-water solution, the XAS peaks are shifted as shown in Fig. 1. Table 1 shows the peak shifts of pyridine-water mixtures from that of liquid pyridine. The C1 peaks related to the *meta*- and *para*-C sites are not changed at different concentrations. The C2 peaks related to the *ortho*-C sites are slightly shifted to the higher photon energy by increasing the molar fraction of water. The N peaks are more evidently shifted to the higher photon energy. These energy shifts are reasonable, assuming that the energy shift arises from HB between the N site of pyridine and water in the pyridine-water binary solutions. The order of the magnitude of the peak energy shift (N > C2 > C1) is caused by weakening the influence of HB interaction of water at each site of pyridine with father from the N site of pyridine.

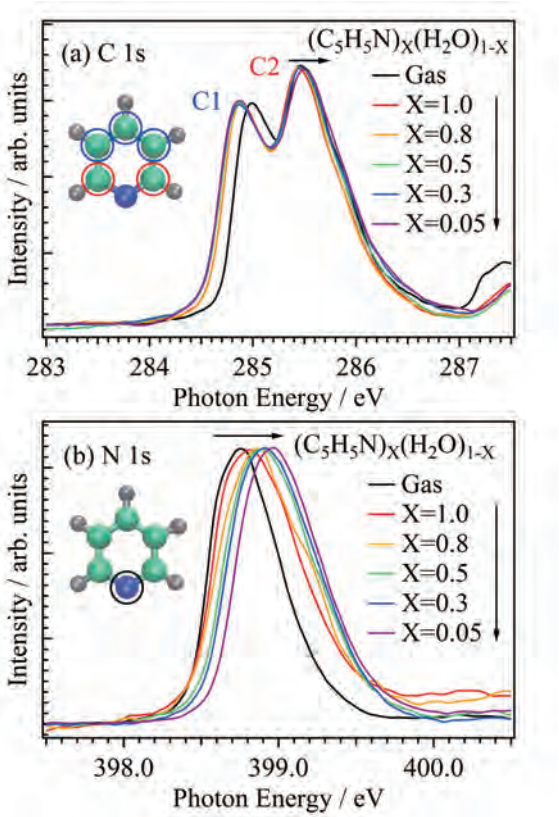

Fig. 1. XAS spectra of pyridine-water mixtures at different concentrations in (a) C and (b) N K-edges. The XAS spectra of pyridine gas are also shown. The peaks are shifted to the direction of arrows by increasing the molar fraction of water.

Table 1. Peak energy shifts (eV) of pyridine-water mixtures from liquid pyridine (X=1.0).

$(C_5H_5N)_X(H_2O)_{1-X}$	C1	C2	N
Gas	0.10	0.04	-0.08
X=1.0	–	–	–
X=0.8	0.00	0.01	0.04
X=0.5	-0.02	0.02	0.08
X=0.3	-0.02	0.02	0.10
X=0.05	-0.02	0.05	0.14

[1] S. Schlücker *et al.*, J. Phys. Chem. A **105** (2001) 9983.
[2] M. Nagasaka *et al.*, J. Electron Spectrosc. Relat. Phenom. **177** (2010) 130.
[3] I. L. Bradeanu *et al.*, J. Phys. Chem. A **112** (2008) 9192.

BL3U

Soft X-Ray Absorption Spectroscopic Study of Solid-Liquid Interface

H. Yuzawa, M. Nagasaka and N. Kosugi
Institute for Molecular Science, Okazaki 444-8585, Japan

Detailed understanding of the interface interaction is important to clarify physical and chemical phenomena such as molecular adsorptions, catalytic reactions and so on. However, the solid/liquid interface is difficult to measure because it involves two different condensed phases. We generally use particle (electron, ion etc.) or light (IR, X-ray etc.) probe to investigate geometric and electronic structures, but the former interacts too strong with both phases to observe the interface. The latter only gives average information of the interface and bulk, where the information of the interface (minor component) get covered up by that of the bulk [1]. Thus, new approaches are required to measure the solid/liquid interface.

We developed a transmission-type liquid XAS (X-ray Absorption Spectroscopy) cell with Si_3N_4 or SiC windows, which is able to control easily the thickness of the liquid thin layer (20-2000 nm), for the soft X-rays [2]. From the other point of view, this liquid cell contains solid/liquid interfaces and can strengthen the information of the interface for light probe by controlling the liquid thickness. Thus, we tried to detect the interaction of solid/liquid interface in the liquid XAS cell, whose surface is modified to objective structures.

The experiments were carried out in BL3U. Two Au (thickness: 20 nm) and Cr (5 nm) deposited Si_3N_4 (100 nm) membranes were used as liquid cell windows. The model surface in this study was prepared by the modification (chemisorption) of 1H, 1H, 2H, 2H -perfluorodecanethiol (F-thiol) monolayer on the gold surface (Fig. 1).

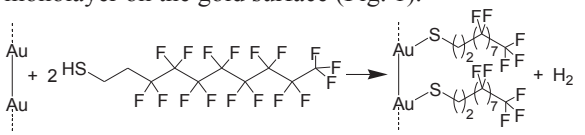

Fig. 1. Modification of gold surface by F-thiol monolayer.

Then, the cell was filled with liquid (water or benzene) and C K-edge XAS was measured at room temperature as shown in Fig. 2.

Figure 3 shows the C K-edge XAS spectra of the modified liquid cell filled with water (blue line) or benzene (red line). In both cases, three absorption peaks (> 290 eV), which correspond to the excitation from C 1s to σ* of F-thiol, were observed. It was confirmed that this system could detect the soft X-ray absorption of molecule at the solid/liquid interface. Nevertheless, the energy positions of each absorption peak were consistent regardless of liquid phase.

On the other hand, when the absorption peak (285.1 eV, 1s→π*) of benzene (green line) extracted from the red line was compared with that without the liquid cell modification of F-thiol (black line), the width of the absorption peak broadened. This would be because the electronic state of benzene molecule was influenced by the interactions between the F atom in F-thiol and the benzene molecule at the interface, e.g., -F···H- interaction [3] and -F···π interaction [4]. Thus, the trace of the interface interaction could be detected in the liquid side.

Through the above experiments, we can conclude that the transmission soft X-ray XAS approach has a potential to detect the interaction of solid/liquid interface.

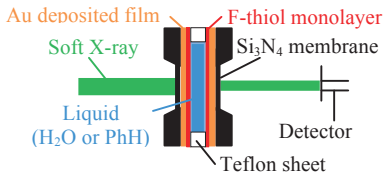

Fig. 2. Schematic (side view) of soft X-ray XAS measurement to detect the interaction at the solid/liquid interface.

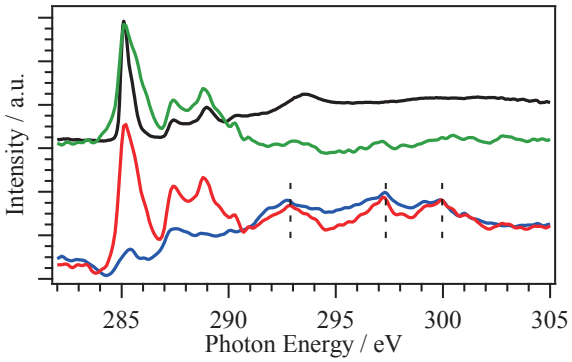

Fig. 3. C K-edge XAS spectra of the modified liquid cell filled with water (blue line) or benzene (red line) and that of the unmodified one filled with benzene (black line). Green line corresponds to the spectrum of the red line subtracted by that of the blue line to remove the influence of the absorption of F-thiol.

[1] F. Zaera, Chem. Rev. **112** (2012) 2920.
[2] M. Nagasaka *et al.*, J. Electron Spectrosc. Relat. Phenom. **177** (2010) 130.
[3] M. D. Prasanna *et al.*, Cryst. Eng. **3** (2000) 135.
[4] B. Brammer *et al.*, New J. Chem. **23** (1999) 965.

BL3U

Interaction of Acetonitrile with Water in Aqueous Solution Studied by Soft X-Ray Absorption Spectroscopy in C and N K-edges

M. Nagasaka, H. Yuzawa and N. Kosugi
Institute for Molecular Science, Myodaiji, Okazaki 444-8585, Japan

Acetonitrile is liquid and is soluble in water at any molar fraction. In aqueous acetonitrile solution, two models of the acetonitrile-water dimer were proposed [1]: One is a hydrogen bond structure between the N site of acetonitrile and the H site of water. The other is a dipole-bonded structure that water is parallel to the C≡N group of acetonitrile by the dipole interaction. Huang *et al.* measured the O K-edge X-ray absorption spectra (XAS) [2] and proposed that the dipole-bonded dimer is abundant compared to the hydrogen bond structure. However, the interaction has not yet been studied from the acetonitrile side. In this study, we have measured the C and N K-edge XAS of acetonitrile-water solutions at different concentrations, and revealed the interaction of the C≡N group of acetonitrile with water.

The experiments were performed at BL3U. XAS of liquid samples were measured by a transmitted-type liquid cell [3]. The liquid layer was sandwiched between two 100 nm-thick Si_3N_4 membranes. The thickness of the liquid layer is controllable between 20 and 2000 nm by adjusting the He backpressure.

Figure 1 shows the C and N K-edge XAS spectra of acetonitrile gas and acetonitrile-water solution $(CH_3CN)_X(H_2O)_{1-X}$. From gas to liquid acetonitrile (X=1.0), both the C 1s → C≡N π* and N 1s →C≡N π* peaks are shifted to the higher photon energy. It is because liquid acetonitrile shows the antiparallel structure between the C≡N groups of acetonitrile by the dipole interaction.

Table 1 shows the peak shifts of acetonitrile-water mixtures from that of liquid acetonitrile. The C peak is shifted to the higher photon energy by increasing the molar fraction of water. On the other hand, the N peak is shifted to the lower photon energy. The interaction of the C site of the C≡N group is increased by water, and that of the N site is slightly decreased. These results suggest that the acetonitrile-water solution may have the dipole-bonded structure, in which the oxygen site of water is close to the C site of the C≡N group of acetonitrile. It should be also noted that the peak width at X=0.05 is narrower than those at different molar fractions, suggesting that in dilute aqueous solutions acetonitrile molecules may be isolated by the dipole interaction with water molecules.

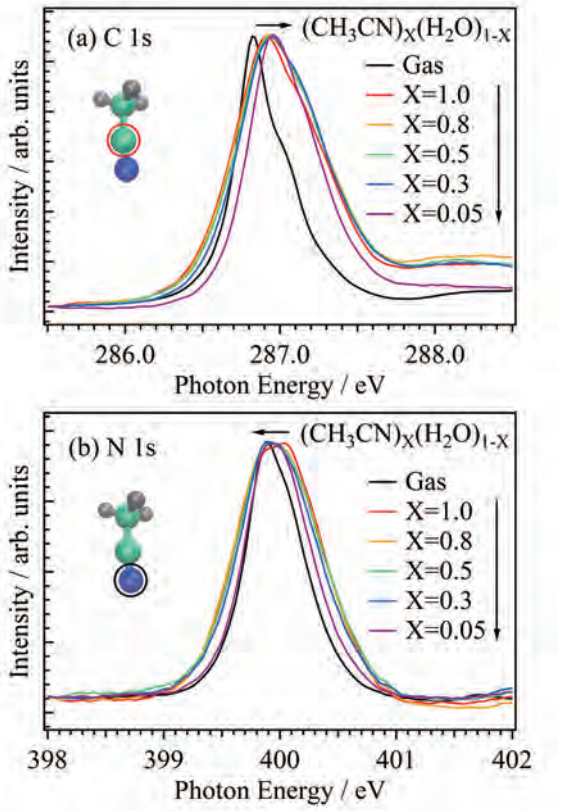

Fig. 1. XAS spectra of acetonitrile-water mixtures at different concentrations in (a) C and (b) N K-edges. The XAS spectra of acetonitrile gas are also shown. The peaks are shifted to the direction of arrows by increasing the molar fraction of water.

Table 1. Peak energy shifts (eV) of acetonitrile-water mixtures from liquid acetonitrile (X=1.0).

$(CH_3CN)_X(H_2O)_{1-X}$	C	N
Gas	-0.09	-0.09
X=1.0	–	–
X=0.8	0.02	-0.02
X=0.5	0.02	-0.02
X=0.3	0.02	-0.03
X=0.05	0.05	-0.03

[1] I. Bakó, T. Megyes and G. Pálinkás, Chem. Phys. **316** (2005) 235.
[2] N. Huang *et al.*, J. Chem. Phys. **135** (2011) 164509.
[3] M. Nagasaka *et al.*, J. Electron Spectrosc. Relat. Phenom. **177** (2010) 130.

BL3B, BL5B, BL7B

Absorption Measurement of Amino Acid Films Using a Novel *in situ* Vacuum Sublimation System

K. Ishiyama, Y. Tanigawa, S. Takenaka and K. Nakagawa
Graduate school of Human Development and Environment, Kobe University, Kobe 657-8501, Japan

It was suggested by Platzman [1] that the magnitude of radiation effect by high energy particle radiation is proportional to

$$\int_0^T \frac{df}{dE}\frac{dE}{E} ,$$

where, T the kinetic energy of particle, f the oscillator strength and df/dE is the oscillator strength distribution which is proportional to the absorption cross section σ. Since T is sometimes order of MeV, we need to measure $\sigma(E)$ for 5 eV<E<1 MeV. Synchrotron radiation is very powerful tool to measure such wide-energy-range absorption spectra.

One of difficulties to measure $\sigma(E)$ within such wide energy range is the large dynamic range of σ (E). For example, for alanine film, σ (E=17eV) =1.2x10^{-16} cm^2 and σ (E=250eV) =6.8x10^{-19} cm^2 ; the ratio is 5600. Thus in order to obtain the reliable spectrum, we must change the film thickness over 20 times. In order to do this, we developed a novel *in situ* sublimation system (Fig. 1). Substrate is made of Kapton film with very small heat capacity, which is helpful to prevent overheat. Wide area of substrate allows us to get the high sublimation yield.

Figure 2 shows an example of absorption spectrum of glutamine measured at BL-5B. First we measured with the grating 2 and the mirror 4 (G2M4) plus the aluminum filter. After that we changed the measurement system to G2M4 and added the thickness of the same glutamine film to get the spectrum designated by "G2M4". Repeating this procedure, we obtained four spectra shown in Fig. 2. Thickness of "G2M1" film was roughly estimated to be about 4.5 times of "G2M4+Al" film.

Connecting four spectra in Fig. 2, we determined the experimental data as shown in Fig. 3.

Using the *in situ* sublimation system, we will complete the measurement of 20 amino acid molecules, among which several spectra were already reported [2].

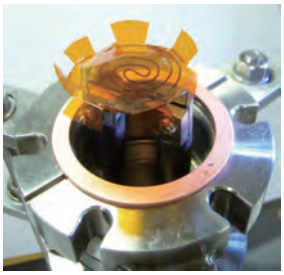

Fig. 1. A novel *in situ* sublimation system.

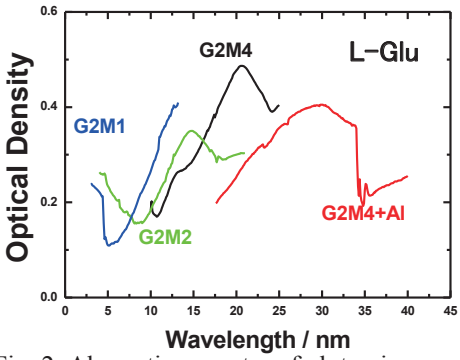

Fig. 2. Absorption spectra of glutamine measured at BL5B.

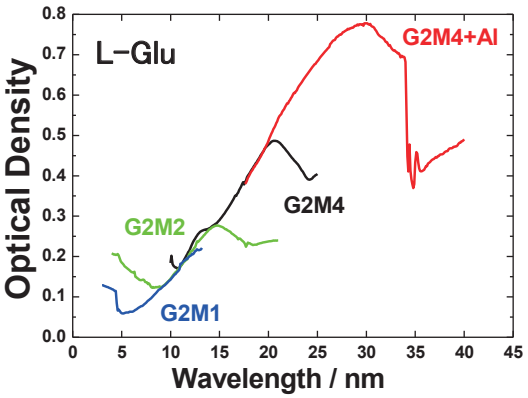

Fig. 3. Determined experimental data.

[1] R. L. Platzman, Vortex, **23** (1962) 372.
[2] M. Kamohara, Y. Izumi, M. Tanaka, K. Okamoto, M. Tanaka, F. Kaneko, Y. Kodama, T.Koketsu and K. Nakagawa, Rad. Phys. Chem. **77** (2008) 1153.

BL4B

Multi-Electron-Ion Coincidence Spectroscopy by Using a Magnetic Bottle Electron Spectrometer

I. Umekawa[1], Y. Shibata[1], K. Soejima[1], E. Shigemasa[2] and Y. Hikosaka[1]
[1] *Department of Environmental Science, Niigata University, Niigata 950-2181, Japan*
[2] *UVSOR Facility, Institute for Molecular Science, Okazaki 444-8585, Japan*

A doubly-charged molecular ion can be formed by double photoionization in which two electrons are released from the molecule by absorbing a photon with energy above the double ionization potential. Such molecular dication states are inherently dissociative due to the Coulomb repulsion between the two positive charges, though the lifetimes are different from the electron states and further from the vibrational levels. While the information of the lifetimes is important in simulations of atmosphere compositions [1], experimental determinations of the lifetimes depending on vibronic states are still limited even for simple molecules.

In this work, we have developed an electron-ion coincidence spectrometer, with an aim to investigate the stabilities of individual vibronic states in molecular dications. The coincidence spectrometer is based on a magnetic-bottle time-of-flight electron spectrometer [2], which schematic is shown in Fig. 1. Electrons produced by photoionization of sample molecules are collected by an inhomogeneous magnetic field over 4π solid angle, and their kinetic energies are determined from the times of flight to a micro channel plate detector. At 10 μs later than the incidence of the photoionization light pulse, pulsed high voltages are applied to the electrodes placed across the photoionization region, which extracts the ions staying in the ionization region toward the same detector.

Figure 2 shows a time-of-flight spectrum measured for CO_2 at a photon energy of 59.7 eV, where times-of-flight of electrons (ions) are observed before (after) 10 μs. In the spectrum, a weak peak for double-charged CO_2^{2+} ions can be seen, in addition to mono-cation peaks. The observation of the CO_2^{2+} ions is attributed to the formation of doubly-charged ion states with lifetimes in the order of μs or longer; otherwise, only the fragment ions should be observed due to dissociation before reaching the detector.

In order to investigate the doubly-charged ion states relevant to the metastable CO_2^{2+} ions, kinetic energies of the electron pairs observed in coincidence with the CO_2^{2+} ions are extracted. Figure 3 shows the energy correlations of the electron pairs. Two photoelectrons emitted on double photoionization shares the available energy which is the energy difference of the photon energy and the binding energy of a formed doubly-charge ion state. Thus, the formation of a doubly-charge ion state appears on the energy correlation map as a diagonal structure with a slope of -1. In practice, corresponding structures are discernible on the map in Fig. 3 around (faster electron energy) + (slower electron energy) = 20 eV. The binding energies of doubly-charge ion states relevant to the metastable CO_2^{2+} are determined to 40 eV, which confirms a previous measurement [3]. We plan further measurements, as detailed discussion needs higher statistics in the coincidence data.

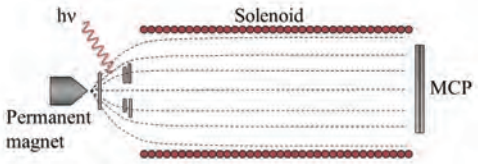

Fig. 1. Schematic of the electron-ion coincidence spectrometer.

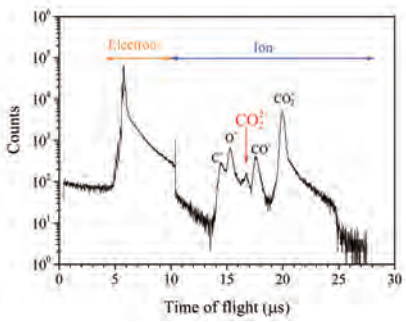

Fig. 2. Time-of-flight spectrum measured for CO_2 at a photon energy of 59.7 eV, where times-of-flight of electrons (ions) are observed before (after) 10 μs.

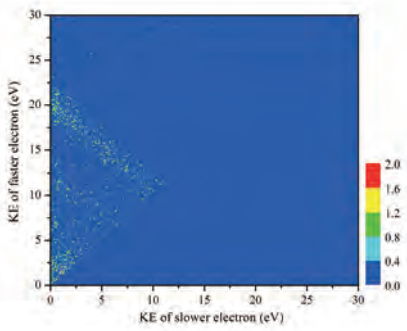

Fig. 3. Energy correlation between two photoelectron observed in coincidence with metastable CO_2^{2+} ions.

[1] R. Thissen *et al.*, Phys. Chem. Chem. Phys. **13** (2011) 18264.
[2] A. Matsuda *et al.*, Rev. Sci. Instrum. **82** (2011) 103105.
[3] A. E. Slattery *et al.*, J. Chem. Phys. **122** (2005) 084317.

BL6U

The Observation of Doppler Profile of Photoelectrons Emitted from Rydberg Oxygen Atom Following O 1s Inner-Shell Excitation of CO_2

T. Gejo[1], K. Myojin[1], T. Tajiri[1], K. Maekawa[1], K. Honma[1], H. Iwayama[2] and E. Shigemasa[2]
[1]*University of Hyogo, Ako-gun 678-1297, Japan*
[2]*UVSOR Facility, Institute for Molecular Science, Okazaki 444-8585, Japan*

Molecules following photo-excitation in the vicinity of inner-shell ionization thresholds provides interesting properties. For photon energies just above ionization threshold, an electron can escape from the ion as a slow photoelectron. The core-hole ion, however, immediately undergoes Auger decay, emitting a fast Auger electron. This leads to a drastic increase of the strength of the Coulomb interaction between the slow out-going photoelectron and the residual ion. When the slow electron lose sufficient kinetic energy by this retardation, it become recaptured by the molecular ion into a Rydberg state. The recapture of the photoelectron results in high-n Rydberg states in singly charged ion. After that, the ion undergoes fragmentation. Since the electron in Rydberg states are relatively stable, Rydberg atom can be generated after this ion fragmentation. This can be confirmed by photoelectron spectra in low kinetic energy region, since Rydberg atom may emit the electron by changing its ion core state.

We have investigated low energy photoelectron spectra of CO_2 in O 1s excited state region. Since two oxygen atom locate at ends of CO_2, one can expect high kinetic energy of Rydberg oxygen atom (O*). As a result, the photoelectron spectra due to O* is expected to show splitting by strong Doppler effect, which gives the information about dynamics of O* generation.

The experiment was performed on the soft X-ray undulator beamline BL6U at UVSOR. To record the electron kinetic energy spectra, we used a hemispherical electron energy analyzer (MBS1) equipped with a gas cell. The resolution of the electron analyzer was set to approximately 8 meV. The typical pressure in the main chamber housing the gas cell was about 1.0×10^{-3} Pa during the measurements. The polarization of the incident photon beam generated by the undulator is horizontal and the photoelectron analyzer can be rotated at horizontal or vertical position respect to this polarization. Energy calibration of the incident photon beam was carried out by recording the total ion yield spectrum of CO_2 in the vicinity of the O 1s ionization threshold.

Figure 1 shows the photoelectron spectra of CO_2 obtained at photoexcitation energies of 538.85, 539.50, 539.90, and 540.65 eV. The peaks clearly show the Doppler splittings, implying that O*s are generated to polarization direction. We have fitted the Doppler profiles with assuming on Gaussian kinetic energy distribution and one β parameter. The result of the fittings provides β ~ 1.2. These results show high preference for parallel direction, which is more than those expected from the β value obtained by the angular distribution of fragment ions, which is 0 ~ 1 at excitation energies around 1s ionization threshold [1]. Thus, these relatively high β values suggest that the absorption due to Σ ← Σ transition is more important role on the generation of O* fragments than Π ← Σ transition. This can be rationalized by that npσ type Rydberg transition is much suitable to generate these O*.

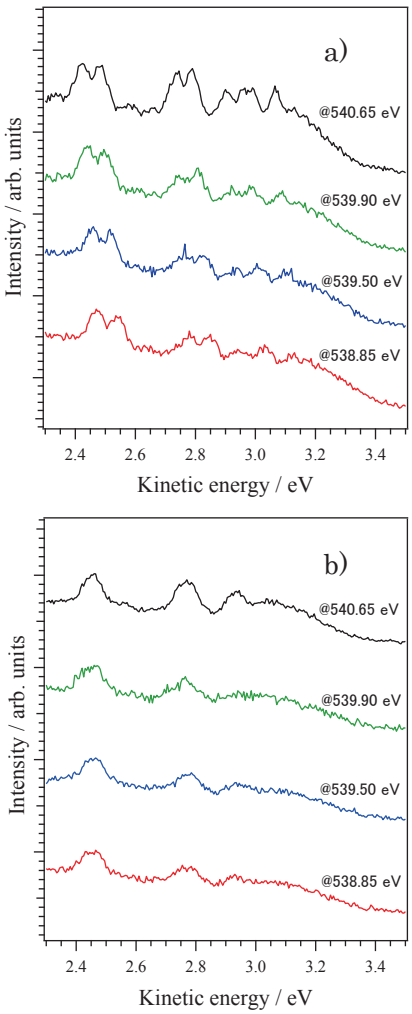

Fig. 1. Photoelectron spectra of Rydberg oxygen atom, following O 1s inner-shell excitation of CO_2 The electron analyzer set at a) horizontal and b) vertical position to polarization of SR, and the excitation energies are 538.85, 539.50, 539.90, and 540.65 eV .

[1] K. Okada *et al.,* Phys. Rev. A, **66** (2002) 032503.

BL6U

Formation of H_3^+ Fragment Following Auger Decay in Ethane

Y. Shibata[1], T. Shirota[2], K. Hoshina[2], H. Iwayama[3], E. Shigemasa[3] and Y. Hikosaka[1]
[1]*Department of Environmental Science, Niigata University, Niigata 950-2181 Japan*
[2] *Faculty of Pharmaceutical Sciences, Niigata University of Pharmacy and Applied Life Sciences, Niigata 956-8603 Japan*
[3]*UVSOR Facility, Institute for Molecular Science, Okazaki 444-8585 Japan*

Formation of H_3^+ fragment ion has been widely observed in the dissociations of organic molecular dications. The mechanism of the H_3^+ formation has absorbed special attention, in connection with rearrangements of the molecular structures due to rapid hydrogen migration [1, 2]. In this work, we have investigated the dication states relevant to the H_3^+ formation from C_2H_6 molecules, by using an Auger electron-ion coincidence method.

The experiment was performed at the undulator beamline BL6U, by using an Auger electron-ion coincidence spectrometer consisting of a double toroidal electron analyzer and a three-dimensional ion momentum spectrometer [3-5]. Auger electrons ejected at ~54.7º with respect to the electric vector of the incident light were sampled and analyzed in energy by the electron analyzer. According to the detection of each Auger electron, a pulsed electric field was applied to the interaction region, in order to extract the formed ions into an ion momentum spectrometer.

The top panel of Fig. 1 shows a time-of-flight spectrum of ions measured in coincidence with C1s Auger electrons emitted after inner-shell photoionization of C_2H_6 molecules. In this spectrum, fragment ion manifolds for the CH_n^+ and $C_2H_n^+$ sequences are observed around 1300 ns and 2000 ns, respectively. Below 500 ns, besides the H_2^+ peak, a weak peak assignable to H_3^+ is discernible. The bottom panel of Fig. 1 shows a two-dimensional map for the correlations between fragment ions detected in coincidence with an Auger electron. Here, an area covering coincidences between H_3^+ (vertical axis) and the counterpart ions (horizontal axis) is presented. On the two-dimensional map, clear structures for coincidences between the fragment ion pairs of H_3^++ $C_2H_3^+$ and H_3^++ $C_2H_4^+$ can be identified, while any structure for the pairs of H_3^++ CH_n^+, accompanying the C-C bond dissociation, is indiscernible.

Figure 2 shows a C 1s Auger spectrum filtered with the detection of the H_3^++$C_2H_3^+$ ion pair, compared with the total Auger spectrum. The total Auger spectrum exhibits only a broad band structure resulting from overlap of different dication states. One finds that the formation of the H_3^++$C_2H_3^+$ ion pair is associated with low-lying dication states in the binding energy range of 40-55 eV, and the dissociation of the states lying in this range result in the formation of H_3^+ fragment. The dication states with the electronic configuration of $1e_g^{-2}$ are known to lie in this binding energy range [6].

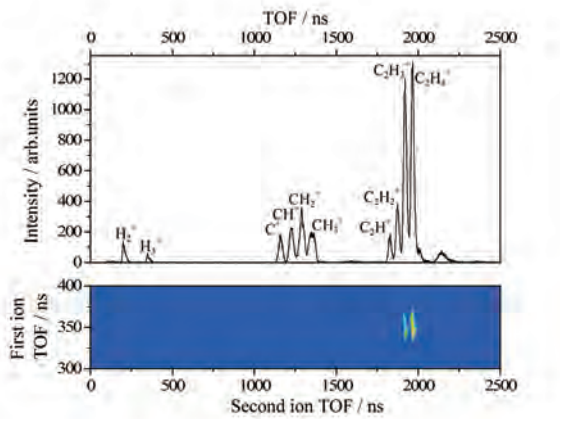

Fig. 1. (Top) Time-of-flight spectrum of ions and (Bottom) two-dimensional map for the correlations between fragment ions, both of which are measured in coincidence with C1s Auger electrons emitted after inner-shell photoionization of C_2H_6 molecules.

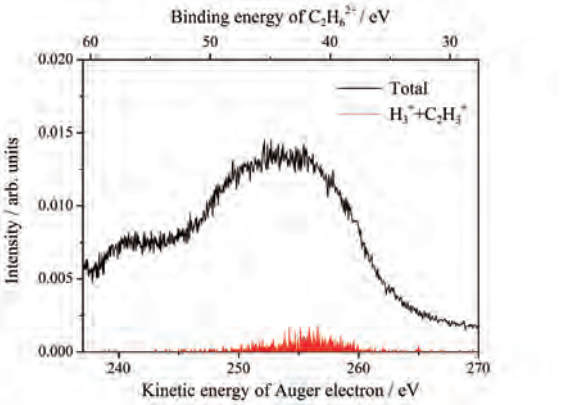

Fig. 2. C1s Auger spectrum of C_2H_6 (black), and coincidence Auger spectrum filtered with the formation of the H_3^++$C_2H_3^+$ ion pair (red).

[1] K. Hoshina *et al*., J. Chem. Phys. **134** (2011) 064324.
[2] K. Hoshina *et al*., J. Chem. Phys. **129** (2008) 104302.
[3] T. Kaneyasu *et al*., AIP Conf. Proc. **879** (2007) 1793.
[4] T. Kaneyasu *et al*., J. Electron Spectrosc. Relat. Phenom. **156-158** (2007) 279.
[5] Y. Hikosaka *et al*., submitted.
[6] R. R. Rye *et al*., J. Chem. Phys. **73** (1980) 4867.

BL6U

Study on Deexcitation Processes Following the Cl 2p Photoexcitation of CCl_4 and HCl Molecules Using Two-Dimensional Electron Spectroscopy

H. Iwayama[1], M. N. Piancastelli[2,3,4], D. W. Lindle[5] and E. Shigemasa[1]
[1]*UVSOR Facility, Institute for Molecular Science, Okazaki 444-8585, Japan*
[2]*CNRS, UMR 7614, LCPMR, F-75005, Paris, France*
[3]*Sorbonne Universités, UPMC Univ Paris 06, UMR 7614, LCPMR, F-75005, Paris, France*
[4]*Department of Physics and Astronomy, Uppsala University, PO Box 516, SE- 75120 Uppsala, Sweden*
[5]*Department of Chemistry, University of Nevada, Las Vegas, Nevada 89154-4003, USA*

A molecular inner-shell excitation to the lowest unoccupied anti-bonding orbital is generally followed by two competing processes: molecular dissociation and resonant Auger decay. In particular, for hydrogen halide molecules such as HBr [1] and HCl [2], it has been shown that the molecular dissociation can be faster than the Auger decay. This process is referred to as ultrafast dissociation [1,2]. In their resonant Auger spectra, sharp peaks at electron energies corresponding to the atomic Auger decays have been observed. Two-dimensional electron spectroscopy (2D-ES), in which electron energy spectra are recorded as a function of the photon energy, is one of the most powerful methods to explore the decay dynamics of inner-shell excited molecules. Here we report on the result for the 2D-ES following the Cl *2p* → $7a_1^*$ excitation for CCl_4 molecules. As a comparison, we have also measured a 2D map following the Cl *2p* → σ^* excitation for HCl molecules.

The experiment was performed on the soft X-ray beamline BL6U at UVSOR. The photon energy resolution E/ΔE was set to 2000. Kinetic energies of the emitted electrons were measured by a hemispherical electron energy analyzer (MBS-A1). The direction of the electric vector was set to be parallel to the axis of the electrostatic lens of the analyzer. The kinetic energy resolution of the analyzer was set to 120 meV. The 2D maps were obtained by taking spectra at a regular photon energy interval of 100 meV across the resonances.

Figure 1 shows the 2D maps for CCl_4 and HCl molecules measured in the Cl *2p* excitation region. We can find two sets of five prominent constant kinetic energy lines in the photon energy range from 200 to 204 eV in Fig. 1(b). The two sets correspond to the atomic Auger decays of the Cl $2p_{3/2}^{-1}$ and $2p_{1/2}^{-1}$ states [2]. For the Cl *2p* → σ^* excitation of HCl molecules, a large part of Auger decays occurs in the atomic chlorine after the complete dissociation.

Then we look at the 2D map following the Cl *2p* → $7a_1^*$ excitation for CCl_4 molecules. As in the case of HCl molecules, we can find two sets of prominent constant kinetic energy lines in Fig. 1(a). Their kinetic energies are the same as those of atomic Auger lines in Fig. 1(b). This means that the ultrafast dissociation process following the Cl *2p* → $7a_1^*$ excitation for CCl_4 molecules exists, where the C-Cl bond is broken before the Auger decay. This behavior can be explained by the fact that the $7a_1^*$ orbital of CCl_4 has a strong anti-bonding character which plays a similar role as in the case the σ* orbital in HCl. However, we can clearly see other constant kinetic energy lines in Fig. 1(a), which are not observed in Fig. 1(b). They are attributable to the Auger decays from molecular fragments. This fact strongly suggests that the atomic Auger decay is not predominant decay processes for CCl_4 molecules. The branching ratio of molecular versus atomic Auger decays depends on the mass of fragments. It is reasonable to consider that the dissociation time for the CCl_3 + $Cl^*(2p^{-1}3p^6nl)$ fragmentation following the Cl *2p* → $7a_1^*$ excitation in CCl_4 is much longer than that for the H + $Cl^*(2p^{-1}3p^6nl)$ following the Cl *2p* → σ^* excitation in HCl. This reasonably explains the present observation.

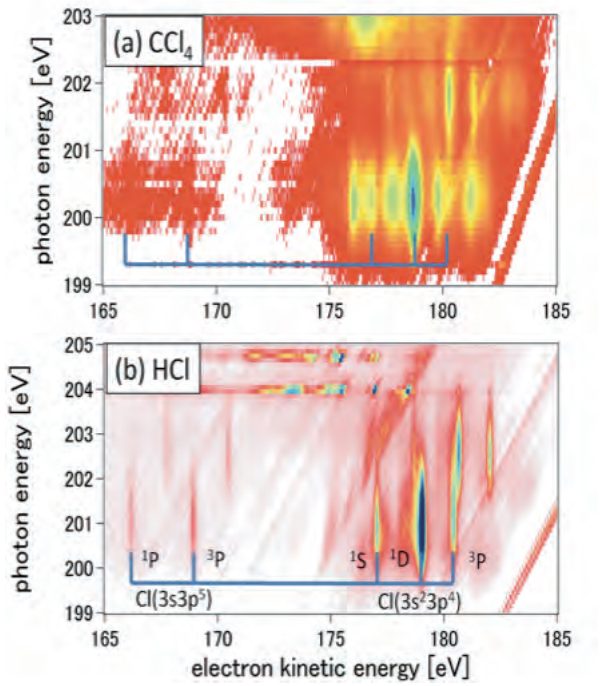

Fig. 1. 2D-PES for (a) CCl_4 and (b) HCl molecules measured in the Cl *2p* excitation region.

[1] P. Morin and I. Nenner Phys. Rev. Lett. **56** (1986) 1913.
[2] H. Aksela *et al*., Phys. Rev. A **41** (1990) 600.

BL6U

Decay Processes Following S 2p Photoexcitation of OCS Studied by High-Resolution Two-Dimensional Electron Spectroscopy

H. Iwayama[1], M. Simon[2] and E. Shigemasa[1]
[1]*UVSOR Facility, Institute for Molecular Science, Okazaki 444-8585, Japan*
[2] *LCPMR, Université Pierre et Marie Curie, 75231 Paris Cedex 05, France*

Molecular inner-shell photoabsorption spectra often exhibit rich structures below the ionization thresholds, which correspond to the excitations of an inner-shell electron into unoccupied valence or Rydberg orbitals. In the case of the molecules composed of light elements, the inner-shell excited states are mainly relaxed via Auger electron emission, and subsequently fragmentation follows in general. Thanks to the continuous works on high-resolution resonant Auger electron spectroscopy, it has been revealed that the nuclear motion of the molecular core-excited states is promoted in competition with the Auger decay.

In the previous report [1], angle-resolved two dimensional (2D) electron spectroscopy, where the resonant Auger-electron spectra are measured as a function of the photon energy, has been applied to the deexcitation processes in the S 2p excitation region of OCS with moderate energy resolution, and compared to the previous work [2]. Here we present the 2D maps following the S $2p_{3/2} \rightarrow \pi^*$ excitation with previously unprecedented resolution.

The 2D measurements were performed at BL6U. The undulator radiation was monochromatized by a variable included angle varied line-spacing plane grazing monochromator. Concerning the 2D electron spectroscopy, the monochromator bandwidth was set to ΔE_{Ph} ~20 meV at hν=165 eV. Kinetic energy of the emitted electrons was measured by a hemispherical electron energy analyzer (MBS-A1) placed at a right angle with respect to the incident photon beam direction. The direction of the electric vector was set to be either parallel (horizontal) or perpendicular (vertical) to the axis of the electrostatic lens of the analyzer. The energy resolution of the analyzer was set to ΔE_k ~15 meV.

Figure 1 shows the 2D maps of resonant Auger electron spectra following the S $2p_{3/2} \rightarrow \pi^*$ resonant excitation of OCS measured in horizontal (a) and vertical (b) directions. The diagonal lines in Fig. 1 are attributed to the valence photoelectron lines, which clearly show vibrational side bands indicating that the net energy resolution is far below 50 meV. The peak intensities for the valence photoelectrons in Fig. 1(a) are much stronger than those in Fig. 1(b), indicating that the β values for the valence shells are close to 2 in the vicinity of the S 2p ionization thresholds.

Clear island-like structures elongated in the vertical direction are detected both in Fig. 1(a) and Fig. 1(b) in the kinetic energy region from 144 to 148 eV. Three island-like structures with almost no dispersion between 146.5 and 148 eV have been assigned to three shake-up satellite states [2]. These states are detected mainly in the lower photon energy region and show almost isotropic angular distributions. For the island-like structures with no dispersion in the kinetic energy range from 144 to 146 eV, large differences between Fig. 1(a) and Fig. 1(b) are seen. To our knowledge, no assignments are given to these structures. In order to understand the origins of the structures, sophisticated theoretical calculations are highly desired.

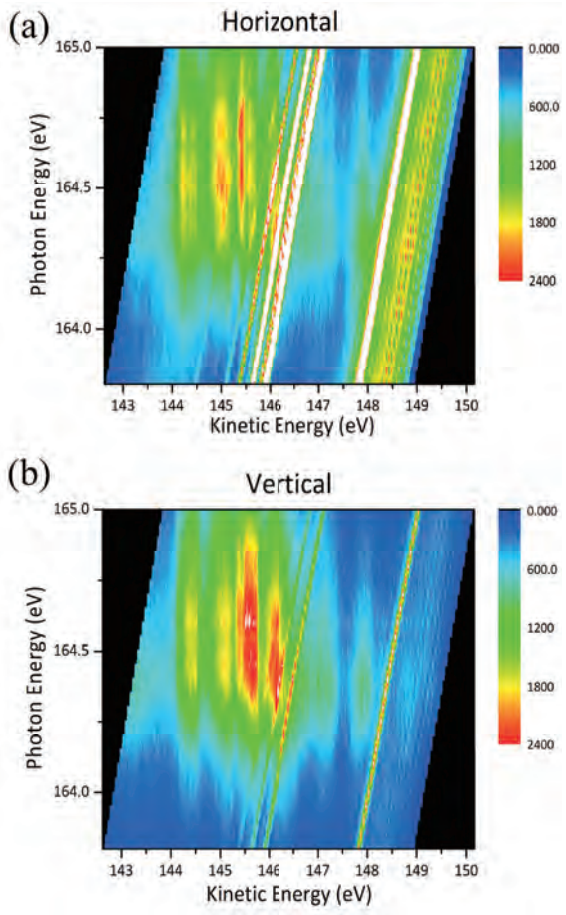

Fig. 1. 2D maps of resonant Auger electron spectra after the S $2p_{3/2} \rightarrow \pi^*$ excitation of OCS, measured at horizontal (a) and vertical (b) directions.

[1] L. Ishikawa, H. Iwayama and E. Shigemasa, UVSOR Activity Report **40** (2013) 61.
[2] S. Masuda, T. Hatsui and N. Kosugi, J. Electron Spectrosc. Rlat. Phenom. **137-140** (2004) 351.

BL6U

Fluorine K Resonant Auger Decays of *cis*-Hexafluorocyclobutane

T. Kaneda[1], S. Ishikawa[1], K. Okada[1], H. Iwayama[2,3] and E. Shigemasa[2,3]
[1]*Department of Chemistry, Hiroshima University, Higashi-Hiroshima 739-8526, Japan*
[2]*UVSOR Facility, Institute for Molecular Science, Okazaki 444-8585, Japan*
[3]*School of Physical Sciences, Graduate University for Advanced Studies (SOKENDAI), Okazaki 444-8585, Japan*

Inner-shell excited states of molecules relax into various molecular cationic states through Auger decays. The resultant cations are in general unstable and dissociate into fragment ions. Information on the correlation between the Auger-final states and the products provides us deeper insight into the fragmentation dynamics of the inner-shell excited molecules. We found in our previous study that the $C1s^{-1}\sigma_{CC}$* excited *cis*-1,1,2,2,3,4-hexafluorocyclobutane (*cis*-c-$C_4H_2F_6$) molecule decays mainly into the $\sigma_{CC}^{-1}v^{-1}\sigma_{CC}$* states, where v means a σ_{CC} or n_F outer-valence orbital, from which fragment ions such as CHF_2^+ and CF^+ are specifically formed [1]. This report is based on our successive experiments measured in the F 1s excitation region.

The experiments have been performed on the soft X-ray beamline BL6U. The experimental setup has been described in a previous paper [2]. The main chamber was equipped with a pair of a double toroidal electron analyzer (DTA) and an ion time-of-flight mass spectrometer. Synchrotron radiation was irradiated at right angles to the effusive beam of the gaseous *cis*-c-$C_4H_2F_6$ sample. The electrons traveling through the DTA tube were detected with a position sensitive detector (RoentDek, DLD40). The pass energy was set to 400 eV in this study. The electron spectra were acquired at the photon energies including typical resonant peaks as well as at the above-threshold energy of 707.5 eV. The photoelectron spectrum was measured at 684.0 eV for subtracting the contribution from valence ionization. The light intensity at each run was monitored downstream on the beamline. In addition, Auger-electron–photoion coincidence data were obtained at some photon energies.

Figure 1 shows a series of resonant Auger spectra plotted on the final-state energy scale, after subtracting the photoelectron components. The normal Auger spectrum measured under the same experimental conditions is also displayed at the top of Fig. 1 on the double ionization energy (DIP) scale. The DIP value for *cis*-c-$C_4H_2F_6$ is evaluated to be 694.4 eV. The spectra present a great contrast to those in the C 1s region [1]. The resonant Auger spectra resemble the normal Auger spectrum well, indicating that the spectator Auger transitions predominate in the F 1s region. We can assign the intense peak at around 50 eV to the transition to the $n_F^{-1}n_F^{-1}$ final states and at around 70 eV to that to the $F2s^{-1}n_F^{-1}$ states. We also found the peak shifts that change almost linearly with the photon energy. The spectator electron contributes to the screening in the 2-hole-1-electron final states, resulting in the peak shifts towards the higher kinetic energies.

The Auger-electron–photoion coincidence data exhibit that the molecular ion in the $F2s^{-1}n_F^{-1}\sigma^{*1}$ Auger-final states dissociates exclusively into the fragment ions without C–F bonds, namely, C^+/CH^+, $C_2H_2^+$ and F^+. Further analysis is needed to state conclusive results and is eagerly in progress now.

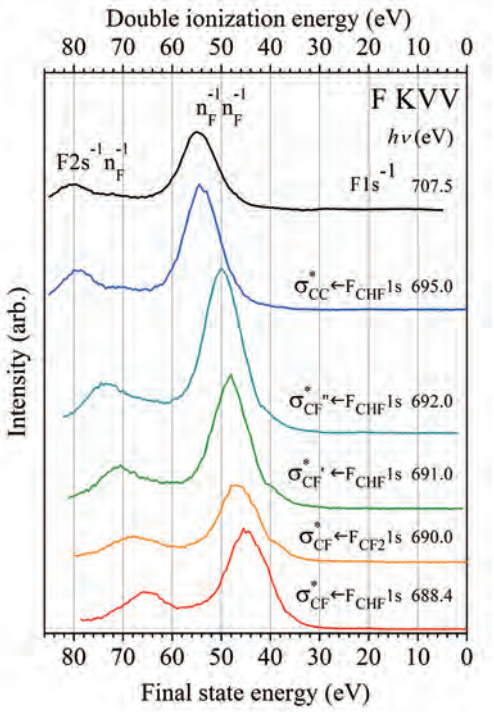

Fig. 1. Resonant Auger spectra of *cis*-c-$C_4H_2F_6$ acquired at a series of photon energies in the F 1s region. The normal Auger spectrum measured at 707.5 eV is also plotted at the top.

[1] S. Ishikawa, K. Okada, H. Iwayama, L. Ishikawa and E. Shigemasa, UVSOR Activity Report 2012 **40** (2013) 58.
[2] T. Kaneyasu, Y. Hikosaka and E. Shigemasa, J. Electron Spectrosc. Relat. Phenom. **156-158** (2007) 279.

BL6U

Stability of Auger Final Dicationic States Following Core-Ionization of N_2 Molecules Studied by an Auger-Electron–Ion Coincidence Method

H. Iwayama and E. Shigemasa
UVSOR Facility, Institute for Molecular Science, Okazaki 444-8585, Japan

Absorption of a soft x-ray photon creates a core hole in a molecule. The core hole state is quite unstable and usually decays via Auger-electron emission for light elements. The Auger decay process leads to various dicationic states with two valence holes. Although Auger final dicationic states are generally unstable, and often come apart into ionic fragments due to the Coulomb repulsion between the nuclear charges, metastable dications with lifetimes in microsecond range are known to exist, depending on the nature of their electronic states as shown in Fig. 1. Here we report on the stability of Auger final states following the 1s photoionization of N_2 molecules by using an Auger-electron–ion coincidence method.

The Auger-electron–ion coincidence measurements were carried out on the undulator beamline BL6U at UVSOR. The radiation from an undulator was monochromatized by a variable included angle varied line-spacing plane grazing monochromator. The electrons ejected at 54.7° with respect to the electric vector of the incident radiation were analyzed in energy by a double toroidal analyzer (DTA), while ions were extracted from the interaction region into a momentum spectrometer by a pulsed electric field according to the electron detection. Arrival positions on the detector and time-of-flights of ions were recorded for every event. The pass energy of the DTA was set to 200 eV for observing the Auger electrons. The energy resolution was about 1.9 eV. All signals from the detectors were recorded with an 8ch TDC board. The photon energy was set to 450eV.

Figure 2 (a) shows a coincidence map for N_2^{++} and N^+ production, in the binding energy region of the dicationic states with two holes in the outer valence orbitals. The vertical and horizontal axes correspond to the kinetic energy of ions and the binding energy of Auger electrons, respectively. Figures 2(b) and 2(c) show the total ion kinetic energy distribution and Auger electron spectrum, which are gained by projecting the counts on the map into the vertical and horizontal axes, respectively. Although the time-of-flights of the N_2^{++} and N^+ ions are the same due to the same mass-to-charge ratio, they can easily be distinguished from their kinetic energy differences, as seen in Figs. 2(a) and (b). The peak at 0 eV in Fig. 2(b) is relevant to the metastable N_2^{++} ions, while that centered at 6 eV is associated with the N^+ ions.

For (N^+, N^+) fragmentation processes, a strong correlation between Auger-electron binding energies and ion kinetic energies is detected in Fig. 2(a). The slope of -1, which is represented by the broken line, means that these fragmentation processes correlate to the same dissociation limit. According to the NIST Atomic Database, the corresponding dissociation limit is $N^+(^3P) + N^+(^3P)$.

It is seen in Fig. 2(a) that the Auger final states ranging from 50 to 54 eV lead to $N^+(^3P) + N^+(^3P)$. According to the theoretical work [1], these Auger final states are mainly attributed to the $1\pi_u^{-2}$ configuration. Since the $1\pi_u$ orbital has strong bonding character, it is reasonable that the $1\pi_u^{-2}$ dicationic states lead to the dissociation. It also turns out that the Auger final states ranging from 46 to 50 eV and from 54 to 56 eV result in the production of N_2^{++}. These Auger final states are mainly attributable to the $3\sigma_g^{-2}$ and $3\sigma_g^{-1}1\pi_u^{-1}$ configurations.

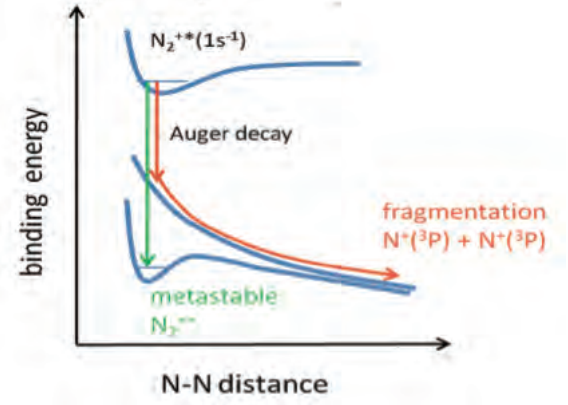

Fig. 1. A schematic representation of core ionization and subsequent decay processes in N_2.

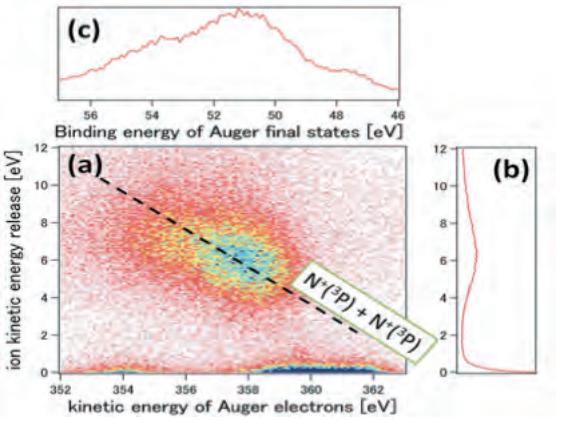

Fig. 2. (a) Auger-electron–ion coincidence map for N_2^{++} and N^+ production. (b) and (c) represent the total ion kinetic distribution and Auger electron spectrum plotted on a binding energy scale, respectively.

[1] H. Agren, J. Chem. Phys. **75** (1982) 1267.

BL6U

Decay Dynamics of Core-Excited HCl and H_2S

M. N. Piancastelli[1,2,3], D. W. Lindle[4], R. Guillemin[1,2], M. Simon[1,2], H. Iwayama[5] and E. Shigemasa[5]

[1]*CNRS, UMR 7614, Laboratoire de Chimie Physique-Matière et Rayonnement, F-75005, Paris, France*
[2]*Sorbonne Universités, UPMC Univ Paris 06, UMR 7614, Laboratoire de Chimie Physique-Matière et Rayonnement, F-75005, Paris, France*
[3]*Department of Physics and Astronomy, Uppsala University, PO Box 516, SE- 75120 Uppsala, Sweden*
[4]*Department of Chemistry, University of Nevada, Las Vegas, Nevada 89154-4003, USA*
[5]*UVSOR Facility, Institute for Molecular Science, Okazaki 444-8585, Japan*

We have obtained high-resolution resonant Auger spectra in two isolated systems, HCl and H_2S, following Cl 2p and S 2p core excitation respectively. The experimental results have been obtained as 2D maps, namely by taking decay spectra at many photon energy values spaced by 100 meV across the below-threshold resonance regions up to above threshold. The 2D maps allow one to follow in detail the evolution of the spectral features, in terms of relative intensity and dispersion law. We have already successfully applied the same method to another molecular system, namely CF_4 [1].

In Figs. 1 and 2 we show the 2D maps for HCl and H_2S. A wealth of spectral structures is present below threshold in both cases. The different dispersion law (linear versus nonlinear behavior) is indicative of spectral features related to molecular parent ions or to fragments, Cl^+ in HCl and HS^+ in H_2S. The interpretation of the spectral features is under way.

Together with the spectral assignment, another goal of the present experiments is to compare the data obtained at UVSOR with another data set at the moment under acquisition at the beam line GALAXIES [2], SOLEIL, France.

There we will obtain 2D maps for the same systems, but after 1s core excitation followed by radiative Kα decay. The intermediate state will be the same ($2p^{-1}$LUMO or $2p^{-1}$Rydberg), but prepared via two different pathways, so we will be able to detect subtle differences in the final states due to the different decay dynamics in the two cases. In particular, we have already demonstrated for HCl that during the lifetime of the Cl 1s→LUMO core-excited state some nuclear motion takes place, resulting in a stretch of the H-Cl chemical bond of about 0.1 A [3]. Therefore the internuclear distance in the Cl $2p^{-1}$LUMO core-excited state should be different if such state is reached by direct photoexcitation or by Cl 1s→LUMO excitation followed by Kα decay. We expect to locate the signature of such difference in the decay spectra.

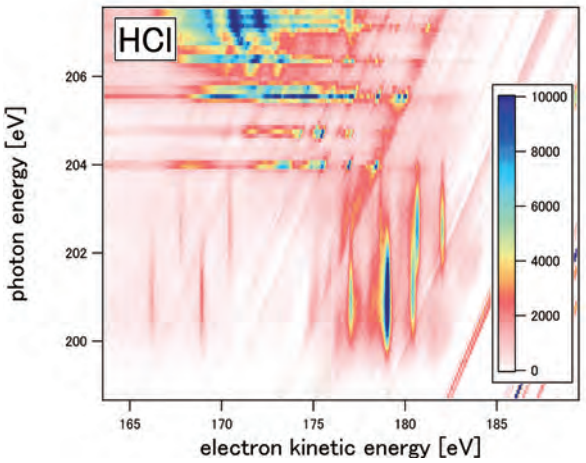

Fig. 1. 2D map for HCl around the Cl 2p threshold.

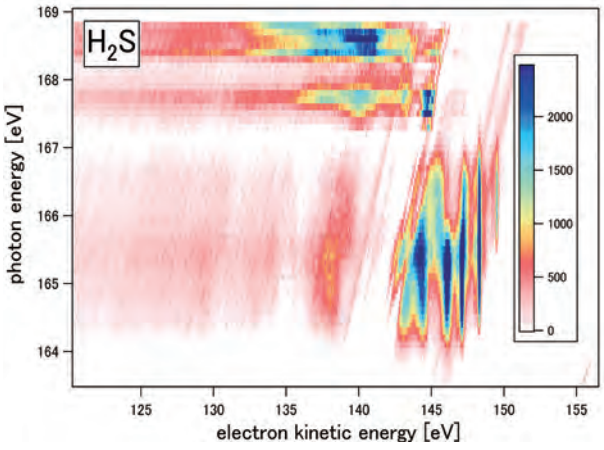

Fig. 2. 2D map for H_2S around the S 2p threshold.

[1] M. N. Piancastelli, R. Guillemin, M. Simon, H. Iwayama, and E. Shigemasa, J. Chem. Phys. **138** (2013) 23430.
[2] D. Céolin *et al.*, J. Electron Spectrosc. Relat. Phenom. **90** (2013) 188.
[3] M. Simon *et al.*, Phys. Rev. A **73** (2006) 020706.

BL6U

3d Hole Decay of the Isoelectronic Br and Kr^+ $3d^{-1}4s^24p^6$ Configurations

P. Lablanquie[1], H. Iwayama[2], K. Soejima[3] and E. Shigemasa[2]
[1]*LCPMR, Université Pierre et Marie Curie, 75231 Paris Cedex 05, France*
[2]*UVSOR Facility, Institute for Molecular Science, Okazaki 444-8585, Japan*
[3]*Department of Enviromental Science, Niigata University, Niigata 950-2181, Japan*

We compare here the Auger decay of a 3d hole in the same isoelectronic configuration $3d^{-1}4s^24p^6$ but in two different atoms. The aim is to test the influence of the nucleus charge Z. Namely we compare the decay of the Kr^+ $3d^{-1}4s^24p^6$ state (Z=36), created by photoionization of the Kr atom, with that of the Br $3d^{-1}4s^24p^6$ state (Z=35), created by ultra-fast dissociation of the HBr molecule upon 3d→σ* excitation [1].

The experiments were carried out on the soft X-ray beamline BL6U at UVSOR. The monochro- matized radiation was introduced into a gas cell filled with sample gas. Kinetic energies of the emitted electrons were measured by a hemispherical electron energy analyzer (MBS-A1) placed at a right angle relative to the photon beam direction. The axis of the electrostatic lens of the analyzer was set to be at the magic angle compared to the polarization direction of the incident light. The energy resolution of the analyzer was set to ~12 meV. The monochromator exit slit opening was set to 300 μm, which corresponds to a resolving power of ~1000.

Figure 1 displays a Kr^+ 3d Auger spectrum. It was obtained at 99 eV photon energy in order to avoid contamination by the decay of 3d satellite states. The main Auger lines are grouped in 3 zones, associated with the formation of the Kr^{2+} final states of $4s^14p^5$, $4s^24p^34d$ and $4s^04p^6$ configurations [2]. The Double Auger decay produces electrons of 0 to ~22 eV [3].

The ultra-fast dissociation of the HBr 3d→ σ* resonance is known to produce an excited atomic Br* $3d^{-1}4s^24p^6$ fragment [1] after the dissociation. In 2012 we showed that the equipment at UVSOR allows one to measure the Auger electron spectrum of the Br* fragment with an unprecedented resolution. Here, we extend this work to the complete Auger spectrum. Figure 2 (top red) displays the result directly comparable to the Kr^+ case of Fig. 1, which was obtained by combining the measurements on the $3d_{3/2}$ and $3d_{5/2}$ → σ* resonances. One observes a similar distribution for the Kr^{2+} and Br^+ final states of $4s^14p^5$ and $4s^04p^6$ configurations, but the structures of the 'satellite' states of a $4s^24p^34d$ configuration are richer in Br^+ than Kr^{++}, suggesting the sensitivity of the 4d orbital to the Z value of the core. Another marked difference is the energy region where double Auger decay contributes. From energetics reasons [4], it is expected to be wider in the Br case, producing electrons up to ~32 eV. The $4s^04p^6$ Br^+ states are thus predicted to decay further. Finally a measurement on the $3d_{5/2}$ → σ* resonance (Fig. 2, bottom) isolates the lines associated with the decays of the $3d_{5/2}$ hole, without the need of coincidence experiments used in the Kr^+ case [3].

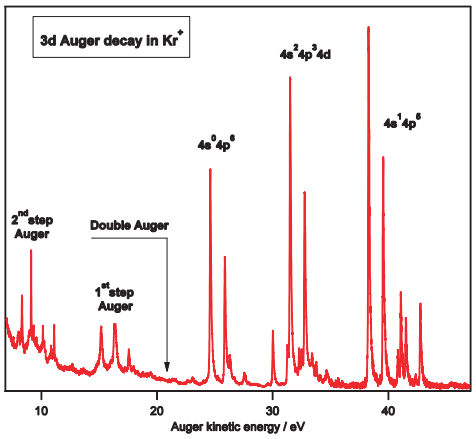

Fig. 1. Auger spectrum following the decays of a 3d hole in Kr^+ $3d^{-1}4s^24p^6$.

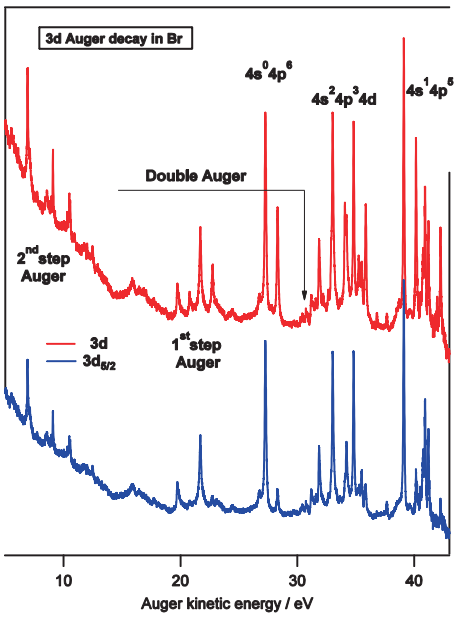

Fig. 2. Auger spectrum following the decays of a 3d hole in Br $3d^{-1}4s^24p^6$. Top (red) is directly comparable to the Kr case. Bottom (blue) was measured on the HBr $3d_{5/2}$ → σ* resonance and selects essentially the $3d_{5/2}$ hole decays.

[1] P. Morin and I. Nenner, PRL **56** (1986)1913.
[2] J. Jauhiainen *et al.*, J. Phys. B **28** (1995) 3831.
[3] J. Palaudoux *et al.*, PRA **82** (2010) 043419.
[4] http://physics.nist.gov/asd

BL8B

Ultraviolet Photoelectron Spectra of $Tm_2@C_{82}$ (III) and $Tm_2C_2@C_{82}$ (III)

T. Miyazaki[1], Y. Tokumoto[1], R. Sumii[2,3], H. Yagi[1], N. Izumi[4], H. Shinohara[4] and S. Hino[1]
[1]*Graduate School of Science and Engineering, Ehime University, Matsuyama 790-8577, Japan*
[2]*Institutes for Molecular Science, Okazaki, 444-858, Japan*
[3]*Research Center for Materials Science, Nagoya University, Nagoya 464-8602, Japan*
[4]*Graduate School of Science, Nagoya University, Nagoya 464-8602, Japan*

Fullerenes cages often encapsulated metal atom(s) and metal-carbide clusters, and entrapped metal atom(s) donate electrons to the cage, which induce the change in their electronic structure. As for mono-metal atom and multiple atoms encapsulated C_{82}, the oxidation state of encapsulated metal atom is either +2 or +3. We have been measuring the ultraviolet photoelectron spectra (UPS) of endohedral metallofullerenes and revealed their valence band electronic structure [1-3]. In the course of the investigation a following empirical rule has been established: the UPS in the upper binding energy region (E_b < 5 eV) were significantly different when either the cage structure or the amounts of transferred electrons is different. Recently, Tm atoms and Tm_2C_2 encapsulated C_{82} fullerenes, $Tm_2@C_{82}$ (III) and $Tm_2C_2@C_{82}$ (III), have been isolated. In this report, the UPS of $Tm_2@C_{82}$ (III) and $Tm_2C_2@C_{82}$ (III) are presented and are compared with those of other endohedral fullerenes.

The UPS were measured at BL8B of UVSOR facility of Institute for Molecular Science. The base pressure of the UPS measurement chamber was 4×10^{-8} Pa and the pressure during the measurement was about 6×10^{-8} Pa. The measured UPS were referenced against the Fermi level (E_F) of gold and were plotted as a function of binding energy relative to E_F. All UPS were normalized by the peak height of a structure appeared at around 5.5 eV.

The UPS of $Tm_2@C_{82}$ (III) and $Tm_2C_2@C_{82}$ (III) obtained with $h\nu$ = 20 ~ 60 eV incident photon energy. The UPS of two metal atoms encapsulated endohedral fullerenes $Y_2@C_{82}$-C_{3v}, $Er_2@C_{82}$-C_{3v} and $Tm_2@C_{82}$ (III) (M_2 group), and those of metal-carbide (M_2C_2) encapsulated metallofullerenes $Y_2C_2@C_{82}$-C_{3v}, $Er_2C_2@C_{82}$-C_{3v} and $Tm_2C_2@C_{82}$ (III) (M_2C_2 group) obtained by 40eV photon energy are shown in Fig. 1 for comparison. The UPS of the M_2 group are almost identical; the peaks of structures A – C appear at the same binding energy region with almost the same intensity. Resemblance of these UPS suggests that the electronic structure of the M_2 group is almost identical. Since the electronic configuration of $Er_2@C_{82}$ and $Y_2@C_{82}$ was determined to be $M_2^{6+}@C_{82}^{6-}$, the oxidation state of Tm atom in $Tm_2@C_{82}$ can be deduced to be +3. This finding is rather surprising since the oxidation state of Tm atom in $Tm@C_{82}$ is +2. The UPS of the M_2C_2 group are also identical, which suggests their analogous electronic structure. The UPS of groups M_2 and M_2C_2 show good correspondence among them; three structures A – C appear at more or less the same energy region. The comparison of the UPS of $Y_2@C_{82}$ (II) and $Y_2C_2@C_{82}$ (II) suggested that the electronic configuration of $Y_2C_2@C_{82}$ is $(YC)_2^{4+}@C_{82}^{4+}$.

Present findings of the oxidation state of entrapped Tm atom(s) are rather surprising. The oxidation state of Tm atom is easily changed when the number of entrapped atoms is changed. When Y atom(s) are entrapped in the C_{82} cage, the oxidation state of Y atom is +3, and it is independent on the number of entrapped atoms. The most stable oxidized form of a compromise to have the stable electronic states of the C_{82} cage and Tm atoms.

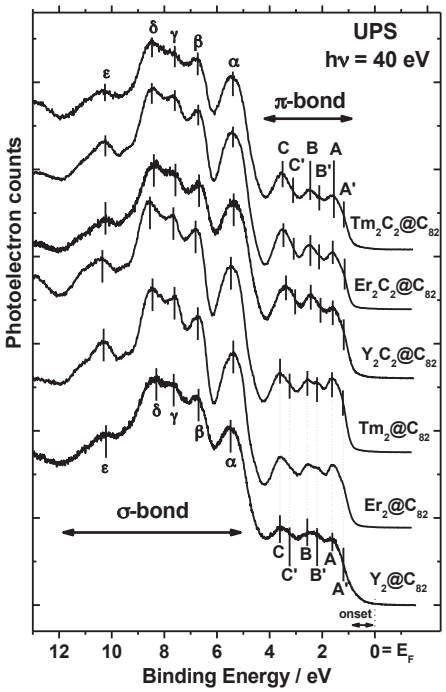

Fig. 1. UPS of $M_2@C_{82}$-C_{3v} and $M_2C_2@C_{82}$-C_{3v} (M=Y, Er, Tm) with $h\nu$ = 40 eV.

[1] S. Hino *et al.,* Bull. Chem. Soc. Jpn. **82**(2009) 963.
[2] T. Miyazaki *et al.,* Chem. Phys. **378** (2010) 11.
[3] T. Miyazaki *et al.,* Chem. Phys. **397** (2012) 87.

One year of at UVSOR

Ⅲ-4

Surface and Thin Films

Highlight

BL6U

Substituent-Induced Intermolecular Interaction in Organic Crystals Revealed by Precise Band-Dispersion Measurements

H. Yamane and N. Kosugi

Department of Photo-Molecular Science, Institute for Molecular Science, Okazaki 444-8585, Japan

Solid-state functionalities of organic molecules are governed not only by individual molecular properties but also by their intermolecular interactions. This concerted interplay dominates a key process of the electric conduction in functional molecular systems. In this work, we have investigated the intermolecular energy-*vs*-momentum $E(\boldsymbol{k})$ relation, originating from the molecular stacking periodicity, of sub-100-meV scale in metal phthalocyanine (MPc) crystalline films. The small $E(\boldsymbol{k})$ relation of MPc with different terminal groups and central metals are sensitive and essential to characterize the intermolecular interaction in terms of the intermolecular distance, the molecular conformation, and the orbital symmetry.

Figure 1 shows the emission angle (θ) dependence of the angle-resolved photoemission (ARPES) spectra and its intensity map for the flat-lying monolayer and crystalline films of ZnPc on Au(111) at 15 K. For the monolayer, the dispersive and non-dispersive peaks appear around the binding energy (E_b) of 0~0.32 eV and 0.74 eV, respectively. The parabolic dispersion at E_b = 0~0.32 eV is derived from the Shockley state (SS) of the Au(111) surface, which is modified by the complex interplay of molecule-substrate interactions. The non-dispersive peak at E_b = 0.74 eV is derived from the highest occupied molecular orbital (HOMO) of C 2p (π) character in ZnPc. The observed HOMO-peak intensity shows a sharp θ dependence with the maximum at θ = 34°. This is due to the reflection of the spatial electron distribution of HOMO. For the ZnPc crystalline film, the SS band of Au(111) is suppressed and the HOMO peak is stabilized as E_b ~ 1.3 eV. Since the ZnPc molecule deposited on Au(111) shows the Stranski-Krastanov growth, the quite weak substrate signal of E_F appears and is utilized for the energy calibration for the precise $E(\boldsymbol{k})$ measurement. The θ dependence of the HOMO-peak intensity in the ZnPc crystalline film is almost the same as that in the ZnPc monolayer; that is, the molecular orientation indicates the layer-by-layer growth in the crystalline domain and induces orbital delocalization. Indeed, the HOMO peak of the ZnPc crystalline film shows a small dispersive behavior with θ. Such a dispersive behavior is not observed in the monolayer film and is related to the delocalized band formation.

In order to investigate the $\boldsymbol{k}$ component along the π-π stacking direction ($\boldsymbol{k}_\perp$), we measured the normal emission ARPES as a function of the photon energy ($h\nu$) for crystalline films of various MPc (H_2Pc, MnPc, CoPc, ZnPc, and F_{16}ZnPc) on Au(111) at 15 K. From this systematic experiment, we revealed quite small but different $E(\boldsymbol{k}_\perp)$ relations. The transfer integral ($t_\perp$) of the C 2p band is found to be dependent on the intermolecular distance ($a_\perp$) with the 75±5 meV/Å relation (see, Fig. 2). Furthermore, we observed the different dispersion phase and periodicity, depending on the terminal group and central metal in MPc, which originate from the site-specific intermolecular interaction induced by substituents [1].

As described above, precise and systematic $E(\boldsymbol{k})$ studies provide deeper insights into the nature of the intermolecular interaction, which further represents the importance of the site specificity in the intermolecular interaction as a possible origin of unique molecular electronic and magnetic properties.

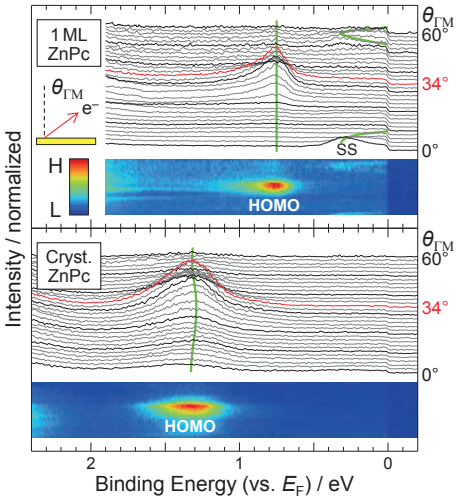

Fig. 1. The θ dependence of the ARPES spectra ($h\nu$ = 45 eV) and its intensity map for the monolayer and crystalline films of ZnPc on Au(111) at 15 K.

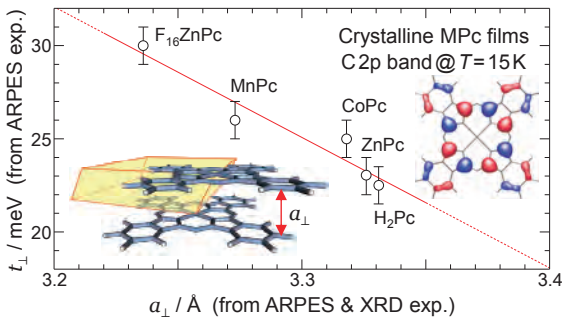

Fig. 2. The $t_\perp$-*vs*-$a_\perp$ relation for the C 2p band in MPc crystals at 15 K, with $t_\perp/a_\perp$ = 75 meV/Å line.

[1] H. Yamane and N. Kosugi, Phys. Rev. Lett. **111** (2013) 086602.

BL2A

Near-Edge X-Ray Absorption Fine Structure Spectroscopic Study of the Annealed Metal Oxide Thin Film

E. Kobayashi[1], K. K. Bando[2] and T. Okajima[1,3]
[1]*Kyushu Synchrotron Light Research Center, Tosu 841-0005, Japan*
[2]*National Institute of Advanced Industrial Science and Technology, Tsukuba 305-8565, Japan*
[3]*Research Center for Synchrotron light applications, Kyushu University, Kasuga 816-8580, Japan*

Metal oxide is an important material from a fundamental physical point of view and is widely used in the field. It is recognized that the surface structure and surface chemical states are important for applications because it can significantly affect the material characteristics. In this study, the annealing behavior of surface chemical states on Magnesium oxide (MgO) thin film was studied by using near-edge X-ray absorption fine structure (NEXAFS). MgO plays a prototype of metal oxides and is also a wide-gap insulator [1]. In addition, MgO is widely used in the field of catalytic, optical and electrical applications [2, 3].

Mg *K*-edge NEXAFS spectra of MgO thin film on Si(100) wafer (MgO/Si) were measured at the beamline 2A of the UVSOR in the Institute of Molecular Science. MgO thin films of about 10 nm in thickness were prepared by RF magnetron sputtering. The NEXAFS spectra were obtained using the total electron yield (TEY) mode and the partial fluorescence yield (PFY) mode at room temperature. The incident angle of the synchrotron radiation was 0° from the surface normal. The spectra were normalized to the incident photon flux, recorded as a photocurrent at a photon-flux monitor consisting of a gold-evaporated mesh.

The MgO/Si thin film was annealed at several temperatures with 373 K ~ 833 K of 10^{-5} ~ 10^{-6} Pa order in vacuum. After the annealing, the film was slow cooled in vacuum.

Figure 1 shows the Mg *K*-edge NEXAFS spectra of MgO/Si before and after annealing obtained from PFY mode. Three strong peaks are observed at around 1309.1 eV (A), 1314.7 eV (B) and 1316.9 eV (C), respectively. The spectral features are similar to the experimentally obtained for polycrystalline MgO [4]. However, the intensity ratio of peak A, peak B and peak C change gradually with a rise in annealing temperature. Similar changes were also observed in TEY spectrum.

According to first-principles density functional calculations, the intensity of peak C is stronger than peak B. It is considered that the carbonate and hydroxide on the thin film surface was decomposed and desorbed by heating, the crystallinity of the thin film was improved.

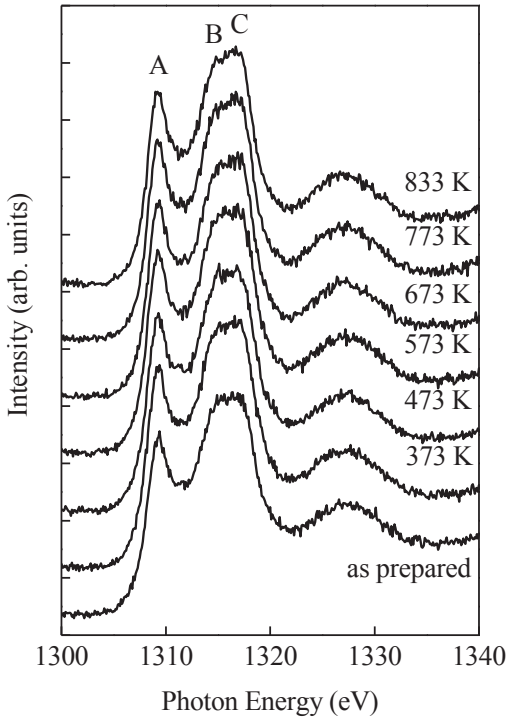

Fig. 1. Mg *K*-edge NEXAFS spectra of MgO/Si before and after annealing obtained from PFY mode.

[1] D. M. Roessler and W. C. Walker, Phys. Rev. **159** (1967) 733.
[2] E. A. Colbourn, Surf. Sci. Rep. **15** (1992) 281.
[3] G. H. Rosenblatt *et al.,* M. W. Rowe, G. P. Williams, Jr., R. T. Williams, and Y. Chen, Phys. Rev. B **39** (1989) 10309.
[4] P. Luches, S. D. Addato, S. Valeri, E. Groppo, C. Prestipino, C. Lamberti and F. Boscherini, Phys. Rev. B **69** (2004) 045412.

BL3U

In Situ Observation of Nickel-Borate Catalyst for Oxygen Evolution Reaction by Soft X-Ray Electrochemical XAFS

M. Yoshida[1], M. Nagasaka[2], T. Iida[1], T. Mineo[1], T. Yomogida[1], H. Yuzawa[2], N. Kosugi[2] and H. Kondoh[1]

[1]*Department of Chemistry, Keio University, Yokohama 223-8522, Japan*
[2]*Department of Photo-Molecular Science, Institute for Molecular Science, Okazaki 444-8585, Japan*

Electrochemical hydrogen production from water has attracted considerable attention due to the potential toward highly efficient energy conversion. This reaction consists of two half reactions of hydrogen and oxygen evolution. However, the efficiency of oxygen evolution reaction (OER) is insufficient for many electrode materials because of the high overpotentials. Recently, Bediako *et al*. reported that a nickel-borate thin film can function as an efficient electrocatalyst for OER and the activity was likely to be dependent on the concentration of potassium borate (KB_i) in electrolyte aqueous solution [1]. Therefore, in this study, the nickel-borate thin film was investigated by *in situ* O *K*-edge XAFS measurements under potential control conditions with changing the electrolyte aqueous solution.

The soft X-ray electrochemical XAFS measurements were performed with the transmission mode at BL3U of UVSOR, according to the previous works [2]. Au/Cr/SiC thin film substrates were used as working electrodes. A home-made electrochemical cell was used with a Pt mesh counter electrode and a Ag/AgCl (saturated KCl) reference electrode.

O *K*-edge XAFS spectra were taken for the electrodeposition reaction of nickel-borate thin film at 1.0 V vs. Ag/AgCl in a 0.1 M KB_i aqueous solution containing 0.4 mM $Ni(NO_3)_2$, as shown in Fig. 1. A peak associated with oxygen species was observed at ca. 528.5 eV and kept to grow for 90 min. Next, the electrolyte solution was changed to 0.5 M KB_i aqueous solution without nickel ions and the XAFS measurements were tested with changing the applied electrode potential (Fig. 2). The peak at ca. 528.5 eV disappeared at the lower potential (0.5 V) and regenerated at the higher potential (1.0 V) accompanying with the OER activity. In previous works of Ni *K*-edge XAFS [1], it is indicated that the nickel borate electrocatalyst forms μ–oxo/hydroxo nickel centers organized into higher-order domains of edge sharing NiO_6 octahedra at the higher potential. Thus, our present study demonstrated the presence of the NiO_6 octahedra domain by the direct observation of oxygen species in the nickel borate thin film. When the concentration of KB_i in electrolyte solution decreased, the XAFS peak was not observed even at 1.0 V accompanying with the decrease of the OER activity, which indicates that the formation of the NiO_6 octahedra domain was suppressed. Therefore, we found that the high activity of nickel borate thin film for OER is derived from the formation of the NiO_6 octahedra domain and related with the KB_i concentration in the electrolyte aqueous solution.

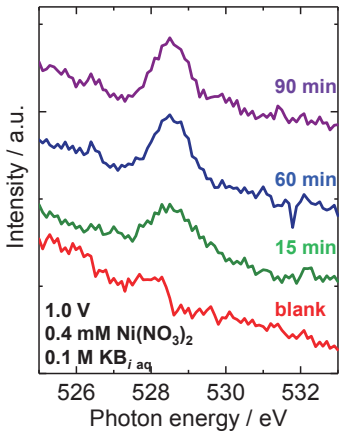

Fig. 1. Time course of *in situ* O *K*-edge XAFS spectra during electrodeposition reaction of nickel-borate thin film.

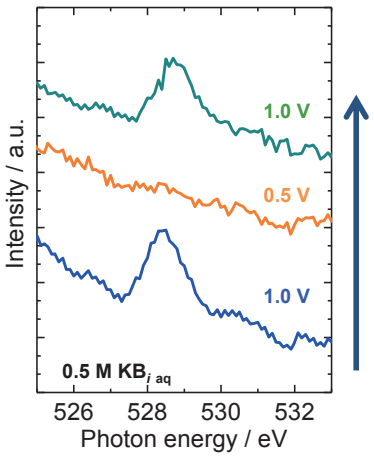

Fig. 2. *In situ* O *K*-edge XAFS spectra under electrochemical control in 0.5 M KB_i aqueous solution.

[1] D. K. Bediako *et al*., J. Am. Chem. Soc. **134** (2012) 6801., **135** (2013) 3662.
[2] M. Nagasaka *et al*., J. Electron. Spectrosc. Relat. Phenom. **177** (2010) 130., J. Phys. Chem. C **117** (2013) 16343.

BL3U

Polarized NEXAFS Study on Structure of Nitrogen Doped Rutile TiO_2(110)

Y. Monya[1], M. Yoshida[1], M. Nagasaka[2], H. Yamane[2], N. Kosugi[2] and H. Kondoh[1]
[1]*Graduate School of Science and Technology, Keio University, Yokohama 223-8522, Japan*
[2]*Institute for Molecular Science, Okazaki 444-8585, Japan*

Nitrogen doped TiO_2, which is one of most promising visible-light-response photocatalysts, has been extensively studied to understand the mechanism of its visible-light-response. Although many structural studies on nitrogen dopants in TiO_2 have been conducted with various techniques, neither doping site nor chemical state of the nitrogen dopant is known in detail. In this work, we measured polarized NEXAFS spectra for nitrogen doped rutile TiO_2(110) to elucidate its structure.

The samples were prepared by heating rutile TiO_2(110) substrates under NH_3 atmosphere at 1.0 Torr. Polarized NEXAFS measurements were performed at BL3U with using the partial electron yield method. The photon energies were calibrated by the energy of the first peak (530.6 eV) at O-K edge.

Figure 1 shows O-K edge NEXAFS spectra of rutile TiO_2(110) with different polarization directions. For example, NI [001] indicates that x-ray incidence angle is 90° from the surface parallel and its electric vector is lying along the [001] direction (see Fig. 2). In the grazing incidence (GI) geometry, the incidence angle was 30°. For the O-K edge spectra, we observe five peaks (*a*-*e*) and they are seen in the typical spectra of rutile TiO_2(110). Considering the previous assignments for these peaks [1, 2], peaks *a* and *b* can be attributed to excitations to unoccupied states: (Ti 3d + O 2pπ) and (Ti 3d + O 2pσ), respectively. Peaks *c*-*e* are assigned to (Ti 4sp + O 2p). In NI[001] spectrum, peak *b* exhibits different polarization dependence from the other peaks. It might be because part of peak *b* is associated with a surface oxygen species shown in Fig. 2. Considering its bonding direction, the excitation to an unoccupied state of (Ti 3d + O 2pσ) character for surface oxygen should be observed only in the [001] direction and particularly strong in NI[001]. Therefore, it can be said that the N doped rutile TiO_2(110) has a similar structure to pristine TiO_2 and the surface oxygen species bridging two Ti atoms remain after doping reactions. Figure 3 shows N-K edge NEXAFS spectra of the nitrogen dopants in the rutile TiO_2(110), where the incidence angle was 15° for GI and 90° for NI from the surface parallel. As a result, seven peaks (*a*'-*d*' and X, Y, Z) were observed. Peak *a*' and *b*' can be attributed to excitations to unoccupied states: (Ti 3d + N 2pπ) and (Ti 3d + N 2pσ), respectively. Peaks *c*' and *d*' are assigned to (Ti 4sp + N 2p). From these results, the doped N species are likely to occupy the lattice oxygen sites via substitution. It should be noted that peaks X, Y, Z appear exclusively in the N-K edge spectra. Based on the results of XPS, DFT calculations and a previous report [3], it is proposed that the nitrogen dopants are not only in the form of N but also in the form of NH. Thus, peaks X and Y can be attributed to excitations to NH-derived unoccupied states. Peak Z could be associated with an edge structure.

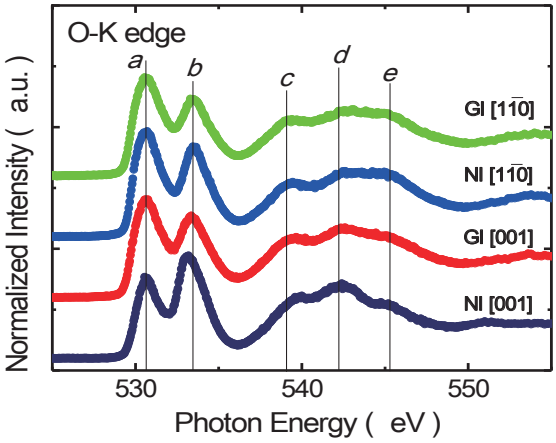

Fig. 1. O-K NEXAFS spectra of N doped rutile TiO_2(110).

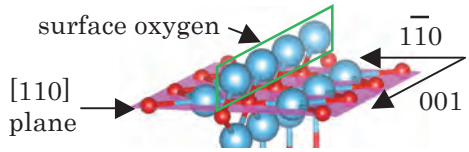

Fig. 2. Structure model for rutile TiO_2(110) surface.

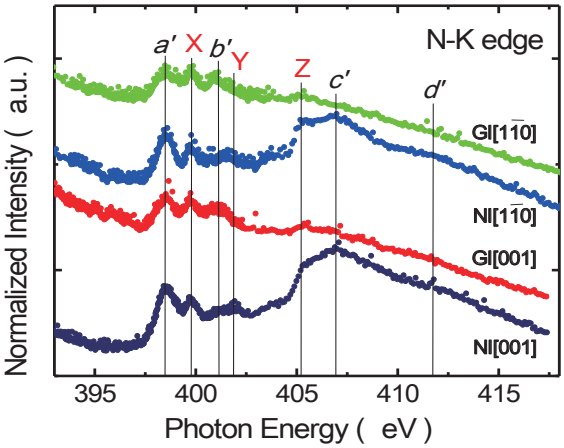

Fig. 3. N-K NEXAFS spectra of nitrogen dopants in rutile TiO_2(110) .

[1] J. G. Chen, Surf. Sci. Rep. **30** (1997) 1.
[2] E. Filatova *et al.*, Phys. Status Solidi B **246** (2009) No.7, 1454.
[3] Y. Kim *et al.*, J. Phys. Chem. C **115** (2011) 18618.

BL4B

Perpendicular Magnetic Anisotropy in Ultrathin Fe Film on MgO Studied by Angular-Dependent X-Ray Magnetic Circular Dichroism

J. Okabayashi[1], J. W. Koo[2], H. Sukegawa[2], S. Mitani[2], Y. Takagi[3] and T. Yokoyama[3]
[1]*Research Center for Spectrochemistry, The University of Tokyo, Tokyo 113-0033, Japan*
[2]*National Institute for Materials Science (NIMS), Tsukuba 305-0047, Japan*
[3]*Institute of Molecular Science, Okazaki 444-8585, Japan*

Perpendicular magnetization is one of the crucial issues in spintronics research field because it has benefits for thermal stability enhancement and the low current magnetization switching, which are very important for the development of spintronics devices. MgO-based magnetic tunnel junctions have been developed by exploiting the strong perpendicular magnetic anisotropy (PMA) at the interfaces between MgO and CoFeB transition metal alloys, measuring 2.1×10^5 J/m^3 [1], which is comparable to PMA in Co/Pt multilayers. As a fundamental understanding of PMA induced at the interface between ferromagnetic layer and MgO barrier layer, the electronic and magnetic structures of interfaces between ultrathin Fe layer and MgO have to be clarified explicitly [2]. It brings the understanding for the origin of FeCo alloys on MgO [3]. In order to investigate PMA energy (K), it is necessary to evaluate the orbital magnetic moments along parallel and perpendicular directions to the surface. Here, we report the anisotropic orbital moments of Fe/MgO by using angular dependent x-ray magnetic circular dichroism (XMCD).

Samples were grown by electron-beam evaporation methods on MgO substrates. The 0.7-nm-thick Fe layer was deposited on Cr buffer layer and MgO layer was also grown on thin Fe layer. Post annealing at 450 °C was performed to enhance PMA, which was estimated to be 1.4 MJ/m^3 by vibrating sample magnetometer (VSM) at room temperature [2]. Saturation magnetic field of 0.7 nm Fe layer on MgO was estimated to be 2 T. XMCD measurements were done at UVSOR BL-4B under the conditions of 5 K [4]. Circular polarization was evaluated to be 71%. A magnetic field of 5 T using superconducting magnet was applied along the incident polarized soft x-ray, which is enough to saturate the magnetization along magnetically hard axis direction. The total electron yield mode was adopted. Normal incidence (NI) and grazing incidence (GI) geometries were employed to deduce the anisotropic orbital magnetic moments.

Figure 1 shows Fe L-edge x-ray absorption spectra and XMCD. Clear metallic peaks in absorption spectra reveal no mixing with oxygen atoms. XMCD spectra in NI and GI setups reveal the difference in L_3 edges, suggesting that the large orbital moments are induced in NI geometry. Using orbital sum rules, 0.22 and 0.17 μ_B are estimated for NI and GI geometries, respectively. Considering the Bruno relationship; $K=(\xi/4)\Delta m_l$, where ξ is spin-orbit coupling, we obtain K=0.9 MJ/m^3, which is comparable to the results obtained by VSM. We note that VSM measurements at low temperature are difficult due to the diamagnetic contribution from MgO substrates. Therefore, element specific XMCD measurements become a unique technique for probing ultrathin magnetic layer on MgO.

Considering above results, the origin of PMA in Fe/MgO interface can be understood by the anisotronic orbital moments induced by spin-orbit interaction at the interface. Fe $3d_{z2}$ states are pushed up above the Fermi level through the hybridization with O $2p_z$ orbitals and large perpendicular orbital moments are induced. Therefore, we conclude that anisotropic orbital moments are the origin of large PMA in Fe/MgO interface.

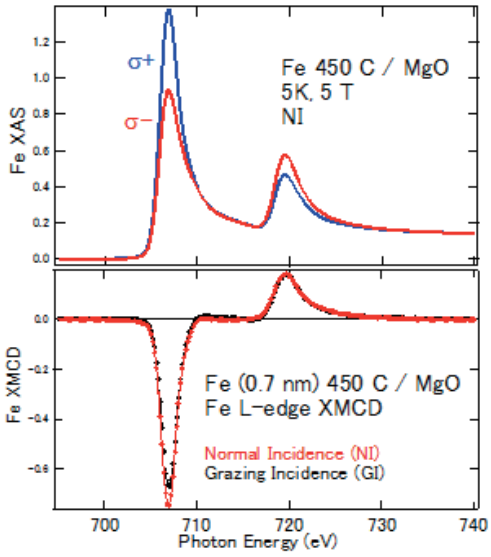

Fig. 1. X-ray absorption spectra of NI and XMCD of both NI and GI setups in Fe/MgO at 5 K and 5 T.

[1] S. Ikeda *et al.*, Nature Mater. **9** (2010) 721.
[2] J. W. Koo *et al.*, Appl. Phys. Lett. **103** (2013) 192401.
[3] J. Okabayashi *et al.*, Appl. Phys. Lett. **103** (2013) 102402.
[4] T. Yokoyama *et al.*, Int. Rev. Phys. Chem. **27** (2008) 449.

BL4B

XAS Study of Magnetic Atoms on Pb/Ge(111)

S. Hatta, N. Sakata, H. Okuyama and T. Aruga
Graduate School of Science, Kyoto University, Kyoto 606-8502, Japan

The Pb monolayer on Ge(111) has surface states exhibiting spin splitting due to the Rashba spin-orbit interaction [1, 2]. One of the spin-split surface states makes spin-polarized Fermi surfaces with the spin splitting of 200 meV. Our four-point-probe conductivity measurements of the monolayer demonstrated the metallic temperature dependence of the conductivity and the high conductivity of ~10 mS. Therefore the monolayer is actually suitable to study the role of the spin-orbit interaction and spin polarization of two-dimensional states in electron transport. Recently, the spin-orbit interaction is expected to have a significant effect in the coupling with conduction electrons and a local magnetic moment, resulting in the increase or decrease of the Kondo temperature [3, 4]. In order to address such a issue, we have investigated the magnetic properties of Co and Fe atoms adsorbed on the Pb monolayer.

We performed X-ray absorption spectroscopy (XAS) experiments at BL4B using the x-ray magnetic circular dichroism (XMCD) end station. The Ge(111) substrate was cleaned by cycles of annealing and Ar ion sputtering until a sharp c(2×8) low-energy electron diffraction (LEED) pattern was observed. The Pb deposition of ~3 ML was done from an alumina crucible heated by tungsten loops, followed by annealing at 550 K. Figure 1 shows the obtained (√3×√3)*R*30° LEED pattern of the Pb monolayer. A small amount of Co or Fe was evaporated by electron bombardment with a rate of ~0.005 ML/sec. Immediately after the deposition on the room temperature Pb/Ge(111) surface, the sample was transferred to the XMCD chamber and cooled down to 6 K.

Figures 2 show $L_{2,3}$-edge XAS spectra of Co (0.22 ML) on Pb/Ge(111) at ±1 T and the incidence angles of 0° and 55° from the surface normal. The broad feature of the adsorption peaks seemed to be unchanged from 0.07 to 0.22 ML. This indicates the significant interaction between the Co 3d and surface states. For XMCD, unexpectedly little signal was observed both at normal and grazing incidence, as shown in Fig. 2. It was same in the measurements with ±3T. This result shows that the magnetic moment of the adsorbed Co atoms is quenched. On the other hand, a XMCD signal was observed for Fe (0.17 ML) on Pb/Ge(111). The magnetic field and the incidence angle dependence of the XMCD signal was found. We are proceeding with further analysis of the magnetic moments of the adsorbed Fe atoms.

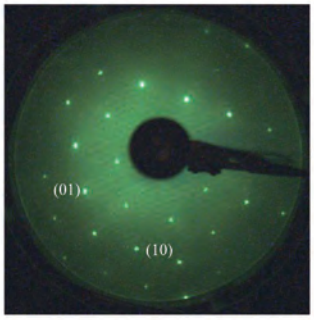

Fig. 1. A (√3×√3)R30° LEED pattern observed for the Pb monolayer on Ge(111) (E_p=90 eV).

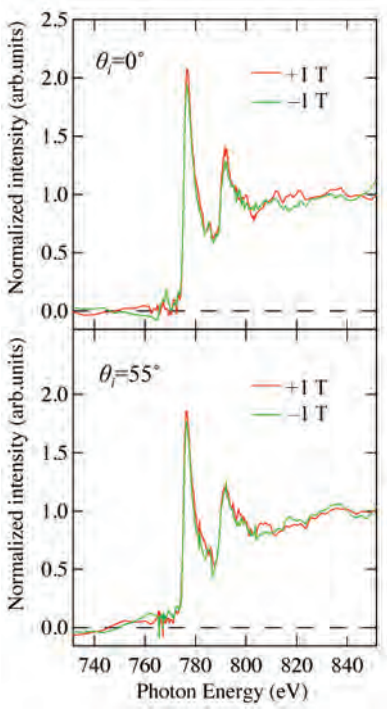

Fig. 2. $L_{2,3}$-edge XAS spectra of Co (0.22 ML) on the Pb/Ge(111) recorded at 6 K and ±1 T.

[1] K. Yaji *et al*., Nat. Comm. **1** (2010) 17.
[2] K. Yaji *et al*., Phys. Rev. B **86** (2012) 235317.
[3] M. Zarea, S. E. Ulloa and N. Sandler, Phys. Rev. Lett. **108** (2012) 046601.
[4] T. Yanagisawa, J. Phys. Soc. Jpn. **81** (2012) 094713.

BL4B

Study on Magnetic Properties of Metal-Coordinated Phthalocyanine Molecules Self-Assembled on Semiconductor Surface Reconstructions

T. Uchihashi and S. Yoshizawa
International Center for Materials Nanoarchitectonics (MANA), National Institute for Materials Science, Tsukuba 305-0044, Japan

Thin film complex molecules fabricated by thermal evaporation onto a metal surface have been extensively studies using X-ray absorption spectroscopy (XAS) and X-ray magnetic circular dichroism (XMCD) for the purpose of device applications [1]. In this work, we studied the magnetic properties of Co-Phthalocyanine (Pc) and MnPc self-assembled on the Si(111)-(√7×√3)-In surface reconstruction [referred to as (√7×√3)-In], which is made of monatomic indium layers on a clean silicon surface. Since the (√7×√3)-In surface exhibits superconducting phase transition at 3 K [2], interesting competition effects between superconductivity and magnetism are expected to occur in this system.

The experiment was performed in the ultrahigh vacuum XMCD system with a superconducting magnet, which was set at the UVSOR beam line BL4B in the Institute for Molecular Science. Figure 1 shows the LEED patters of the (√7×√3)-In surface before (left) and after (right) MnPc was evaporated to a monolayer level. High crystallinity was confirmed for both cases. Similar results were obtained for CoPc/(√7×√3)-In. XMCD spectra were determined from the difference between the XAS spectra taken at B = ±5 T.

For the CoPc/(√7×√3)-In sample, no XMCD signal was obtained. Since CoPc has a spin 1/2 at the Co atom in a free state, this spin must be quenched, for example, by charge transfer between the molecule and the substrate. In contrast, clear XMCD signals were obtained for the MnPc/(√7×√3)-In sample (see Fig. 2). This clearly indicates that spins in the Mn atom still survive when the molecule is adsorbed on this surface. These behaviors are similar to the ones observed for their adsorption on noble metal surfaces.

According to our recent experiments, superconducting energy gap is retained on the first and the second layers of CoPc on (√7×√3)-In. This is consistent with our observation that the spin of CoPc is quenched on absorption. On the other hand, the spins surviving in the MnPc molecule can suppress the superconductivity of the (√7×√3)-In surface. This will be further studied by combining the XMCD experiment, STM, and electron transport measurement.

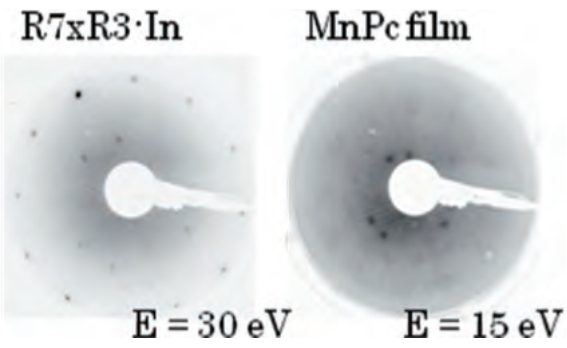

Fig. 1. LEED patterns of the CoPc/(√7×√3)-In sample.

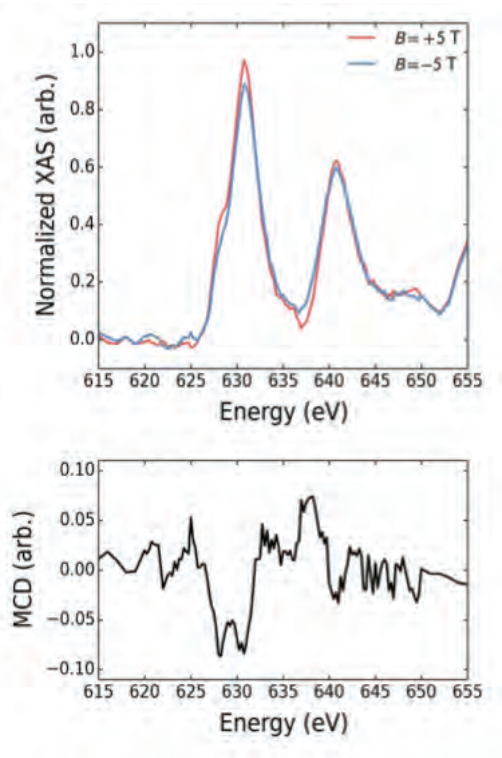

Fig. 2. XAS and XMCD spectra of the CoPc/(√7×√3)-In sample taken at the incident angle θ = 0 .

[1] Y. Takagi *et al.,* UVSOR ACTIVITY REPORT **38** (2011) 67.
[2] T. Uchihashi *et al,* Phys. Rev. Lett., **107** (2011) 207001.

BL4B

Magnetic Linear Dichroism Study of Non-Ferromagnetic Co on W(110)

H. Nakano[1], T. Nakagawa[2], K. Eguchi[1], N. Takagi[1] and T. Yokoyama[1]
[1]*Institute for Molecular Science, Okazaki 444-8585, Japan*
[2]*Department of Molecular and Material Sciences, Kyushu University, Kasuga 816-8580, Japan*

Metallic Co is known as a robust ferromagnetic material, irrespective of its crystal structures and pressure. Thus antiferromagnetic phase of Co has not been found so far both for bulk and thin films. However, the magnetism of Co single layer grown on refractory metals, W and Mo, has been a puzzling issue since no evidence of magnetic ordering has been found [1]. On the other hand, Fe, a typical ferromagnetic material at ambient conditions, shows variety of magnetic phases such as ferromagnetic, antiferromagnetic, spin density waves, depending on the crystal structure, lattice constant, and thickness. Here we report non parallel alignment of Co magnetic moment proved by x-ray magnetic linear dichroism (XMLD).

Experiments were done in a x-ray magnetic circular dichroims (XMCD) chamber with superconducting magnet (H ~ 6 T). Co was deposited on W(110), which was cleaned by repeated cycles of oxidation and high temperature flash upto 2200 K. The x-ray linear dichroism (XLD) was measured with the polarization of the light fixed and the azimuthal angle of the crystal rotated.

Figure 1(a) shows XMCD spectra taken on single layer Co grown on W(110) at T_s = 5 K and a magnetic field of 5 T. The spectra for the parallel and antiparallel alignment between the light helicity and the magnetic field are nearly identical, indicating the disappearance of the macroscopic spin moments. The zero spin magnetic moment obtained in XMCD has several scenarios. One is the non-parallel alignment of the spin moment such as antiferromagnetic structure so as to give the macroscopic zero moment, and another is the missing of the magnetic moment in Co due to the strong hybridization with W substrate.

Linear dichroism could be observed for non-parallel alignment of the magnetic moment owing to the asymmetry of the magnetic structure. Figure 1(b) shows XLD spectra taken between 5 K and 60 K, where the dichroic signal is shown as the difference between the light polarization (***E***) //[110] and ***E***//[001] directions. In Fig. 1(c) the XMLD intensity is largest at T_s = 5 K, and decreases with increasing the temperature. Above 20 K, the XMLD stays at the almost constant value, which comes from C_2 symmetry of Co/W(110) and the instrumental asymmetry. The temperature dependence of the XLD suggests an additional ordering below 20 K.

It is unlikely that the Co magnetic moment adjacent to W atoms vanishes due to the strong banding. Since the thickness dependence of Co magnetic moment (not shown) demonstrates a rapid increase above 1 ML Co thickness and recover to ~ 80% of bulk Co spin moment at 2 ML, which cannot be explained by the zero magnetic moment in the first Co layer.

In summary, we show for the first time that the monolayer Co on W(110) is not non-magnetic, but it exhibits the non-parallel alignment of the magnetic moment, which cancels with each other such as an antiferromagnetic structure.

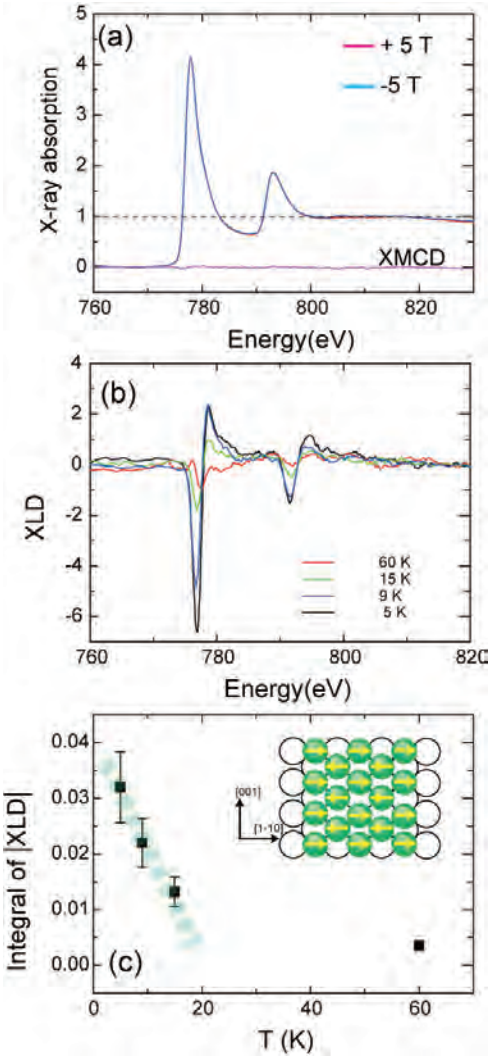

Fig. 1. (a) XAS and XMCD spectra for 0.6 ML Co on W(110) at T_s = 5 K. (b) Temperature dependent XLD spectra for 0.6 ML Co on W(110). (c) XMLD intensity as a function of temperature. The inset is a schematic drawing of the Co spin structure.

[1] G. Garreau, M. Farle, E. Beaurepaire and K. Baberschke, Phys. Rev. B **55** (1997) 330.

BL4B

Magnetic Property of Vanadyl Phthalocyanine on Ferromagnetic Iron Surface Studied by XMCD

K. Eguchi[1], Y. Takagi[1,2], T. Nakagawa[1,2] and T. Yokoyama[1,2]
[1] *The Graduate University for Advanced Studies (SOKENDAI), Okazaki 444-8585, Japan*
[2] *Institute for Molecular Science, Okazaki 444-8585, Japan*

It is important to understand the magnetic interactions between phthalocyanine compounds containing transition metals (TMPcs) and ferromagnetic surfaces for realizing molecular spintronics. Recently we have reported on the ferromagnetic coupling of central metal ions like manganese [1] and iron [2] with ferromagnetic Co films. In this study, we investigated the molecular orientation and magnetic properties of vanadyl phthalocyanine (VOPc) deposited on a ferromagnetic iron surface by using x-ray absorption spectroscopy (XAS) and x-ray magnetic circular dichroism (XMCD).

Sample preparation was carried out in an ultrahigh vacuum condition. First, a ferromagnetic iron film was prepared by the electron bombardment evaporation on a clean Cu(001) substrate at low temperature (T~110 K). The thickness of the iron film was confirmed by the reflection high-energy electron diffraction oscillations during the evaporation. Subsequently, purified VOPc was deposited on the iron film using a homemade Knudsen cell at 570 K. During the sublimation deposition, the substrate was kept at room temperature. The deposition rate estimated by a quartz crystal oscillator was 0.1 ML/min and the amount of deposition was 0.9 ML (1 ML = 0.5 molecule/nm^2). XAS and XMCD measurements were performed at 5 K by means of the total electron yield detection mode. In the XMCD measurement, the helicity of the circularly polarized x-rays was fixed positively while the magnetic field was reversed.

Figure 1(a) shows angle dependence of the linearly polarized N K-edge XAS of 0.9 ML VOPc deposited on the iron surface. The peaks labeled A, B and C are mainly attributed to transitions from N 1s to the π* molecular orbitals and the intensity of the π* peaks increases with increasing the x-ray incidence angle. This indicates that the framework of phthalocyanine is adsorbed with a flat orientation. In addition, the satellite peak S is observed due to strong interaction of the N atoms with the iron surface.

Figure 1(b) shows V L-edge and O K-edge circularly polarized XAS and XMCD spectra at the incident angle of 0° and 55°. Although the XMCD spectra or the magnetization curves for the iron film were not shown, we confirmed that the magnetization of the iron film is saturated at 5 T in both the 0° and 55° configurations. The XMCD signal is detected at the V L-edge, which means that the V spin in VOPc is maintained. Then, the XMCD signal shows a positive sign at the V L_3-edge, while it is negative at the Fe L_3-edge. This implies that the central vanadium ions are magnetized to the opposite direction to the magnetization of the iron film. In contrast to the previous cases of MnPc/Co and FePc/Co systems, the spins of the central vanadium ions are antiferromagnetically coupled with those of the iron atoms in the ferromagnetic iron film.

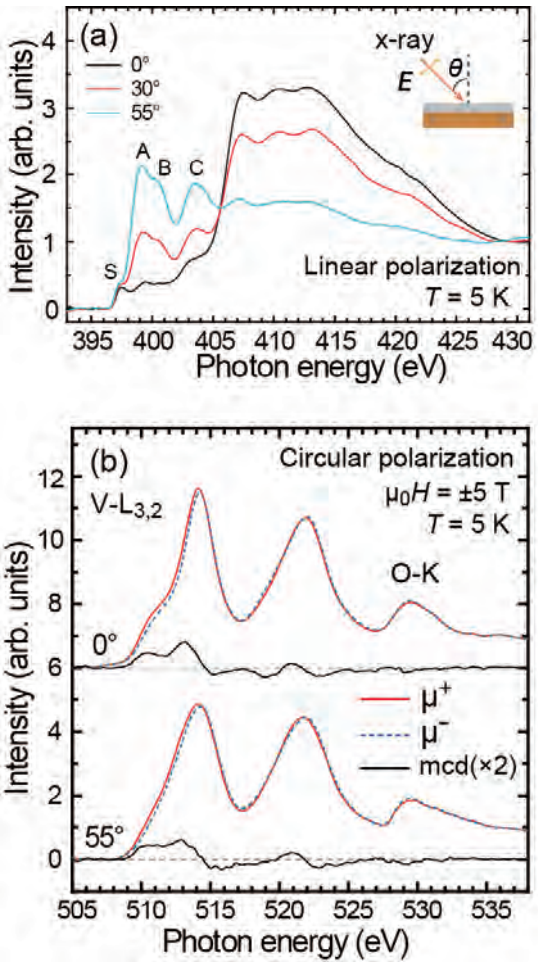

Fig. 1. (a) The linearly polarized N K-edge XAS intensities of 0.9 ML VOPc on Fe (3 ML)/Cu(001). (b) V L-edge and O K-edge XAS and XMCD spectra of 0.9 ML VOPc on Fe (3 ML)/Cu(001) taken at the incident angle of 0° and 55° from the surface normal at T=5 K and $\mu_0 H$=5 T.

[1] I. Yamamoto *et al.*, UVSOR ACTIVITY REPORT **37** (2010) 74.
[2] Y. Takagi *et al.*, UVSOR ACTIVITY REPORT **38** (2011) 74.

BL5U

Photoemission Study of $CaCu_3Ru_4O_{12}$

H. J. Im[1], M. Iwataki[1], M. Tsunekawa[2], T. Watanabe[1], M. Matsunami[3,4] and S. Kimura[3,4,5]

[1]*Department of Advanced Physics, Hirosaki University, Hirosaki 036-8224, Japan*
[2]*Faculty of Education, Shiga University, Hikone 522-8522, Japan*
[3]*UVSOR Facility, Institute for Molecular Science, Okazaki 444-8585, Japan.*
[4]*School of Physical Sciences, The Graduate University for Advanced Studies, Okazaki 444-8585, Japan.*
[5]*Graduate School of Frontier Biosciences, Osaka University, Suita, 565-0871, Japan.*

A-site ordered perovskite compounds of the stoichiometry of $AA'_3B_4O_{12}$ are formed by the substitution of three-fourths of A-site ions by A'-site ions in the typical ABO_3 structure. Particularly, $CaCu_3B_4O_{12}$ compounds (B: Ti^{4+}, Ru^{4+}, Mn^{4+}, Fe^{3+}) have been attracted much attention due to a variety of intriguing physical properties which come from the strong correlation effects. For instance, $CaCu_3Ti_4O_{12}$ (CCTO), which shows extremely high dielectric constant [1], is Mott-insulator which has turned out to be caused by the band shift and the band narrowing in angle-resolved photoemission studies [2, 3]. And $CaCu_3Ru_4O_{12}$ (CCRO) have extensively studied due to heavy-fermion like behaviors and non-Fermi liquid behaviors [4, 5].

Here, in order to understand the underlying physics of A-site ordered perovskites, we have performed photoemission measurements on CCRO at BL5U and compared it with the previous results of CCTO.

The polycrystalline sample has been synthesized by conventional solid state reaction technique using $CaCO_3$, CuO, and TiO_2. In order to decompose the calcium carbonate, stoichiometric mixtures were initially calcined at 700 °C for 12 h. The pressed pallets were annealed at 1050 °C for 24 h. Single phase has confirmed by X-ray diffraction pattern.

The photon energy of 90 eV was used in PES measurements. The clean sample surface was prepared by *in situ* cleaving in the ultra-high vacuum. The measurement temperature is 300 K.

Figure 1 shows the PES spectra of CCRO and CCTO in the valence band regime obtained by angle-integrated analyzer mode. We recognized the spectral shape of CCRO is similar with CCTO except for the Fermi level. The most intensive peaks are observed around 4 eV which come from the mainly Cu 3d states. Interestingly, the peak positions are almost same in CCRO and CCTO. It was already reported in CCTO that the Cu 3d peaks are shifted to higher binding energy due to strong correlation effects, indicating the localized character [2]. In 5 – 8 eV, the broad peak are mainly O 2p states. The hump around 2.5 eV are observed. Particularly, in CCRO the spectral weights are clearly observed near the Fermi-level where there are mainly Ru 4d-states in the band calculations, indicating the itinerant character.

We have reported that most Ti 3d states in CCTO are located in the unoccupied regime [2]. In contrast, Ru 4d states are expected to be exist in the occupied regime due to strong hybridization of broader Ru 4d states with Cu 3d and O 2p states in the band calculations. Therefore, we suggest that the differences of the spectral shape between CCTO and CCRO are attributed to the participation of Ru 4d states in the occupied regime.

For future work, it should be studied how the itinerant Ru 4d states and the localized Cu 3d states play a role in heavy-fermion behaviors and non-Fermi liquid behaviors.

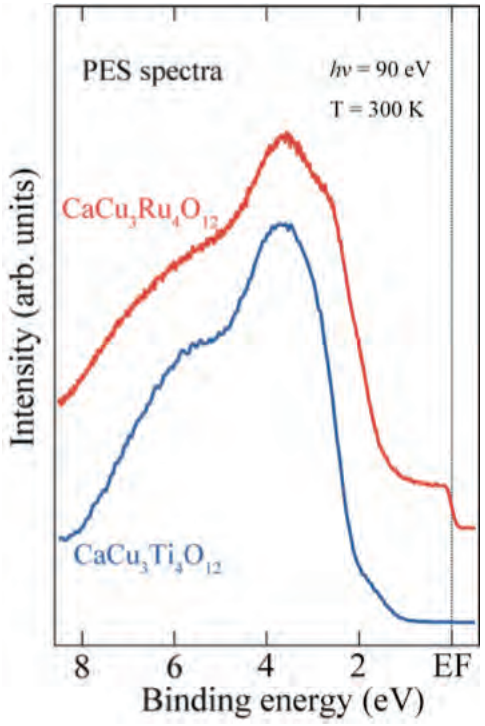

Fig. 1. Photoemission spectra of $CaCu_3Ru_4O_{12}$ and $CaCu_3Ti_4O_{12}$ in the valence band regime at room temperature, obtained at $h\nu$ = 90 eV.

[1] M. A. Subramanian *et al.*, J. Solid State Chem. **151** (2000) 323.
[2] H. J. Im *et al.*, Phy. Rev. B **88** (2013) 205133.
[3] H. J. Im *et al.*, UVSOR Activity Report **40** (2013) 100.
[4] W. Kobayashi *et al.*, J. Phys. Soc. Jpn. **73** (2004) 2373.
[5] A. Krimmel *et al.*, Phys. Rev. B **78** (2008) 165126.

BL5U

Soft X-Ray Photoemission Spectroscopy Study of $Fe_2P(0001)$ and $Ni_2P(0001)$

Y. Sugizaki[1], S. Ishida[1], T. Nakamura[1] and K. Edamoto[1,2]
[1]*Department of Chemistry, Rikkyo University, Tokyo 171-8501, Japan*
[2]*Research Center for Smart Molecules, Rikkyo University, Tokyo 171-8501, Japan*

The transition metal phosphides (TMPs) have attracted much attention because these materials show high catalytic activity for hydrodesulfurization (HDS) and hydrodenitrization (HDN)[1]. Of all TMPs, Ni_2P shows the highest catalytic activity for HDS, while that of Fe_2P is extremely low[1]. The difference is thought to originate from the difference in electric structure of surface metal atoms. The surface electronic structure of Ni_2P has been investigated by XPS, and it has been proposed that active Ni sites are stabilized through the bonding with segregated P atoms[2]. As for Fe_2P, very little information is available at present. To comprehend the origin of difference in catalytic activities, we investigated surface properties of $Ni_2P(0001)$ and $Fe_2P(0001)$ by using soft X-ray photoemission spectroscopy (SXPES).

The experiments were performed at BL-5U of UVSOR, Institute for Molecular Science. The photoelectrons were collected by an electron energy analyzer of hemispherical type (MBS A-1), using an angle-integrated mode (acceptance angle of ±20°). The Ni_2P and Fe_2P single-crystals were grown by Dr. S. Otani of National Institute for Materials Science. The samples were cut at an orientation of (0001) by spark erosion, and the surfaces were polished mechanically to a mirror finish. The clean surfaces were prepared by several cycles of Ar^+ ion sputtering and several temperature annealing (600 ~ 900 K).

Figure 1 shows the P2p core-level spectra of Ni_2P (a) and Fe_2P (b) measured at hν=170eV. The background drawn by a Shirley procedure has been subtracted from each raw data. For Ni_2P, major peaks ($2p_{3/2}$ and $2p_{1/2}$ levels) are observed at 129.6 and 130.4eV, respectively, together with shoulder peaks around 129.9 and 130.7eV. Both shoulder peaks disappear by slight sputtering, and thus the shoulders are associated with segregated P atoms. For Fe_2P, in addition to the major peaks at 129.3 and 130.1eV, several minor peaks are observed in the region between 129 and 128eV. These peaks disappear by slight sputtering, and thus these are associated with segregated P atoms. These results indicate that P segregation occurs by annealing for both $Ni_2P(0001)$ and $Fe_2P(0001)$.

Figure 2 shows valence band spectra of Ni_2P (a) and Fe_2P (b). The bands observed at 0-4.5eV for Ni_2P and at 0-4eV for Fe_2P are Ni3d-P3p hybrid band and Fe3d-P3p hybrid band, respectively. For Ni_2P, annealing the sputtered surface at 900K induces the shift of the whole band toward the higher binding energy side and the growth of a new peak at 3.4eV, which is induced by bonding between Ni and segregated P atoms. These result shows that the surface Ni atoms are stabilized due to a ligand effect. On the other hand, valence band spectra of Fe_2P shows little change by annealing the sputtered surface, indicating that the ligand effect is not effective on $Fe_2P(0001)$. These results suggest that the control of the electronic structure of active metal sites is important to improve the catalytic performance of TMPs.

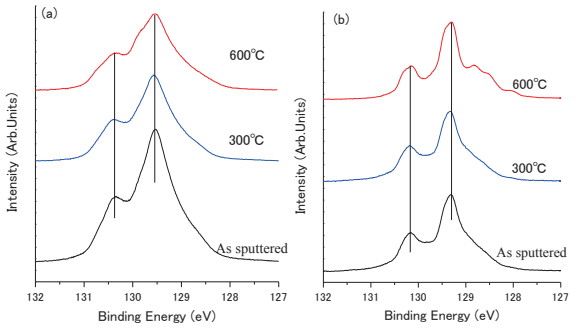

Fig. 1. P2p core-level spectra (hν=170eV) for (a) $Ni_2P(0001)$ and (b) $Fe_2P(0001)$.

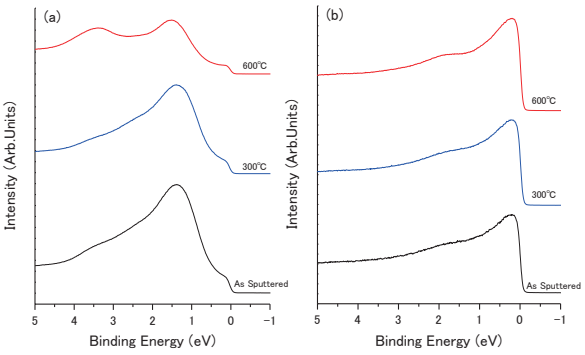

Fig. 2. Valence band spectra of Ni_2P (a) and Fe_2P (b). Ni_2P was measured at hν=60eV and Fe_2P was measured at hν=49eV.

[1] S. T. Oyama, J. Catal. **216** (2003) 343.
[2] K. Edamoto, *et al.,* Solid. Statate. Communication. **148** (2008) 135.
[3] Y. Sugizaki, *et al.,* Surf. Sci. **624** (2014) 21.

BL5U

Electronic Structure of a Magnetic Insulator / Topological Insulator Thin Film Heterostructure: MnSe / Bi_2Se_3

T. Hirahara[1], T. Kubo[1], T. Nakamura[1], T. Hajiri[2], M. Matsunami[2], S. Kimura[2] and S. Hasegawa[1]

[1]*Department of Physics, University of Tokyo, Tokyo 113-0033, Japan*

[2]*UVSOR Facility, Institute for Molecular Science, Okazaki 444-8585, Japan*

The metallic surface states of three-dimensional topological insulators are protected by time reversal symmetry (TRS). Although breaking TRS is generally detrimental to these states, it may also lead to exotic topological quantum effects, such as magnetic monopoles, quantized anomalous Hall effect, and giant magneto-optical effects. In terms of electronic structure, it has been predicted that the massless Dirac-cone (DC) surface states will undergo gap opening and become massive [1].

Up to now, most studies that have tried to break TRS in topological insulators have been performed with magnetic impurity doping in the bulk or at the surface [2]. Although this is a straightforward and simple strategy, various results have been reported that are in favor/unfavor of the TRS breaking in terms of gap-opening of the DC [3]. One study has even shown that a gap-opening is observed even when nonmagnetic impurities are incorporated [4]. Therefore, an alternative method to induce TRS breaking in topological insulators with well-defined structures is called for.

In the present study, we have fabricated a heterostructure of thin films of magnetic (MnSe) and topological insulators (Bi_2Se_3) and tried to see whether a gap opening can be observed in the DC. These two materials have nearly the same lattice constant and can be made into a heterostructure as confirmed with diffraction measurements. Although MnSe is an antiferromagnetic insulator, theoretical calculation predicts that a magnetic interaction at the interface is expected to induce a gap opening in the DC [5]. Figure 1 shows the band dispersion of a 10 quintuple layer (QL) Bi_2Se_3 film (a) and a heterostructure of 2.4 bilayer (BL) MnSe / 10 QL Bi_2Se_3 film (b). One can notice that the DC remains after MnSe deposition although its intensity has decreased drastically. Furthermore, the Dirac point has shifted towards the Fermi level, making the bulk insulating. The origin of this shift is unclear at the moment. Moreover, whether a gap has opened at the Dirac point is also not clear and needs higher resolution measurements.

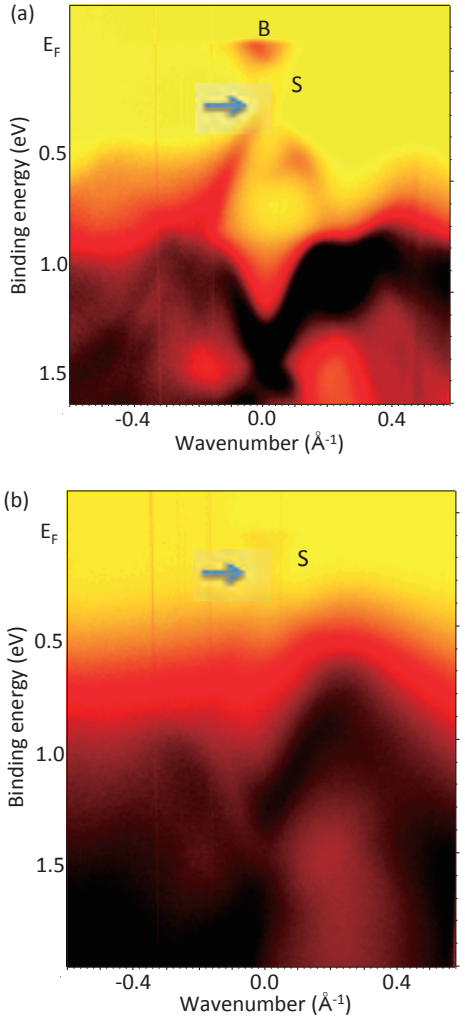

Fig. 1. Band dispersion of a 10 quintuple layer (QL) Bi_2Se_3 film, (a) and a heterostructure of 2.4 bilayer (BL) MnSe / 10 QL Bi_2Se_3 film, (b). S and B correspond to surface and bulk states and the arrows indicate the Dirac point.

[1] M. Z. Hasan and C. L. Kane, Rev. Mod. Phys. **82** (2010) 3045.
[2] S.-X. Xu *et al*., Nat. Phys. **8** (2012) 616.
[3] A. Varykhalv *et al*., Phys. Rev. X **2** (2012) 041017.
[4] T. Sato *et al*., Nature Physics **7** (2011840).
[5] S. V. Eremeev *et al*., Phys. Rev. B **88** (2012) 144430.

BL5U

Angle-Resolved Photoemission Study of $Ba_3Co_2O_6(CO_3)_{0.7}$

T. Hosokawa[1], T. Hajiri[1,2], T. Ito[1,3], M. Matsunami[2,4], S. Kimura[2,5], Y. Shimizu[6], Y. Kobayashi[6] and M. Ito[6]

[1]*Graduate School of Engineering, Nagoya University, Nagoya 464-0818, Japan*
[2]*UVSOR Facility, Institute for Molecular Science, Okazaki 444-8585, Japan*
[3]*Nagoya University Synchrotron Radiation Research Center, Nagoya University, Nagoya 464-8603, Japan*
[4]*School of Physical Sciences, The Graduate University for Advanced Studies (SOKENDAI), Okazaki 444-8585, Japan*
[5]*Graduate School of Frontier Biosciences and Physics Department, Osaka University, Osaka 565-0871, Japan*
[6]*Graduate School of Science, Nagoya University, Nagoya 464-8603, Japan*

Cobalt oxides have attracted attention due to their anomalous electronic/magnetic properties such as a large thermoelectric power. Recently it has been found that a quasi-one-dimensional cobaltate $Ba_3Co_2O_6(CO_3)_{0.7}$ shows a fairly large thermoelectric power comparable to one of Na0.75CoO2. In order to understand its physical properties, we have investigated the electronic structure of $Ba_3Co_2O_6(CO_3)_{0.7}$ by utilizing angle-resolved photoemission spectroscopy (ARPES).

ARPES measurements were performed at the beamline BL5U of UVSOR-III. Clean surfaces were obtained by *in situ* cleaving the samples in perpendicular to the *c* axis.

Figure 1 shows the ARPES image near the Fermi level (E_F) along the ΓA high-symmetry line measured at T = 20 K. We successfully obtain the clear dispersive features from 0.5 to 3 eV binding energy range. From the comparison with the Co 3p-3d resonant photoemission result of $Ba_3Co_2O_6(CO_3)_{0.7}$, the observed bands mainly consist of the Co 3d orbital character [3]. To show the symmetry of the electronic structure clearly, we have mapped out the intensity of ARPES spectra around 0.5 eV (valence band maximum) in the ΓA-ΓKM plane as indicated in Fig. 2. From the constant energy intensity map, we can find that the line-shape contrast along the AHL high-symmetry line. Furthermore, the intensity increases from the A to L point. It is expected that the one-dimensional atomic (molecular) chain form the plate-like electronic structure perpendicular to the one-dimensional conducting axis. Thus, the observed symmetry of the ARPES intensity ensures the appropriate sample setup along the quasi-one dimensional face-sharing CoO6 chains.

In contrast to the metallic/semimetallic properties on electronic conductivity along c axis, the valence band maximum seems to be located around 0.5 eV in Fig. 1. It should be noted that the ARPES spectra exhibit a low energy tail from 0.5 eV to EF around the A point, though the tail feature does not cross EF. To understand the origin of this discrepancy, more detailed ARPES measurements are intended.

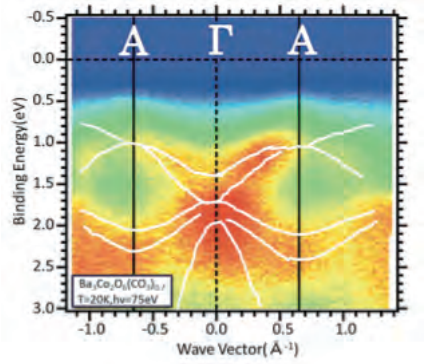

Fig. 1. ARPES image of $Ba_3Co_2O_6(CO_3)_{0.7}$ along the ΓA high-symmetry line measured at T=20K. White lines are guide for eyes to trace a main dispersive feature.

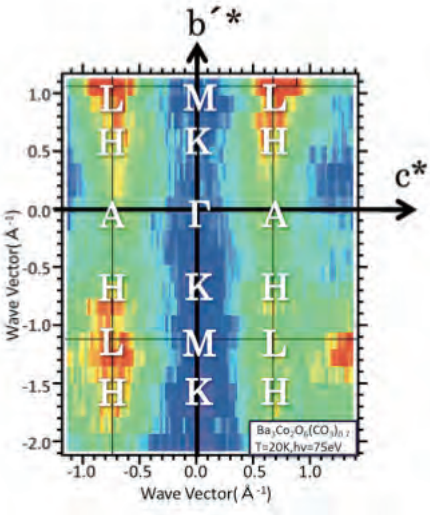

Fig. 2. The Valence Band Maximum (E_B=0.5eV) surface in the ΓA-ΓKM plane of $Ba_3Co_2O_6(CO_3)_{0.7}$ mapped by ARPES at T=20K.

[1]K. Iwasaki *et al.*, JOURNAL OF APPLIED PHYSICS **106** (2009) 034905.
[2]K. Igarashi *et al.*, Journal of Physics: Conference Series **400** (2012) 032024.
[3]K. Soda *et al.*, UVSOR Activity Report **37** (2010) 99.

BL5B

Photoinduced Changes of Amorphous Chalcogenide Thin Films Studied by Vacuum Ultraviolet Transmission Spectroscopy

K. Hayashi
Department of Electrical, Electronic and Computer Engineering, Gifu University, Gifu 501-1193, Japan

It is well-known that amorphous chalcogenide semiconductor materials show a variety of photoinduced effects [1-3] and are very expected as a potential material for optoelectronic devices because these materials are very sensitive to the light. For the device application, it is necessary to sufficiently understand the physical property of these materials. Although a large number of studies have been done on the photoinduced phenomena of these materials, little is known about the details of these mechanisms. These phenomena were studied by exciting outer core electrons with the irradiation of light with the energy corresponding to the optical bandgap or sub-bandgap. The interest has been attracted for the change of the optical properties in the energy region of the visible light. We are interesting for the changes of the optical properties in the higher energy region. To obtain a wide knowledge of the photoinduced phenomena, it is necessary to investigate to the photoinduced effects on wide energy region. Recently, we became able to measure directly the VUV transmission spectra of amorphous thin films [4]. In this paper we report on the study of the photoinduced changes of the as-deposited amorphous chalcogenide thin films before and after irradiation of the bandgap (BG) light by the VUV transmission spectroscopy.

Samples used for the measurement of the VUV transmission spectrum were amorphous chalcogenide (a-As_2Se_3 and a-As_2S_3) semiconductor thin films prepared onto aluminum thin films by conventional evaporation technique. Typical thickness of the samples and the aluminum films were around 180nm and 200nm respectively. The aluminum film was also used in order to eliminate the higher order light from the monochromator in the VUV region. The measurements were carried out at room temperature at the BL5B beam line of the UVSOR facility of the Institute for Molecular Science. And the spectrum was measured by using the silicon photodiode as a detector. A pinhole of 1.5mm in a diameter was inserted between the monochromator and sample to remove stray light. The intensity of the VUV light was monitored by measuring the TPEY of a gold mesh. The positions of the core levels for the samples were calibrated by referencing to the 2p core level absorption peak of the aluminum film.

Figure 1 shows the VUV transmission spectra of the 3d core levels of Se and As atoms in a-As_2Se_3 film before and after the irradiation of the BG light. As shown in the figure, the photoinduced changes are observed on the transmission spectra before and after the irradiation of the BG light.

Those changes might relate to the photoinduced defects created by the irradiation of the BG light. More detailed experiments are necessary to clarify the origin of the photoinduced changes of the VUV transmission spectra.

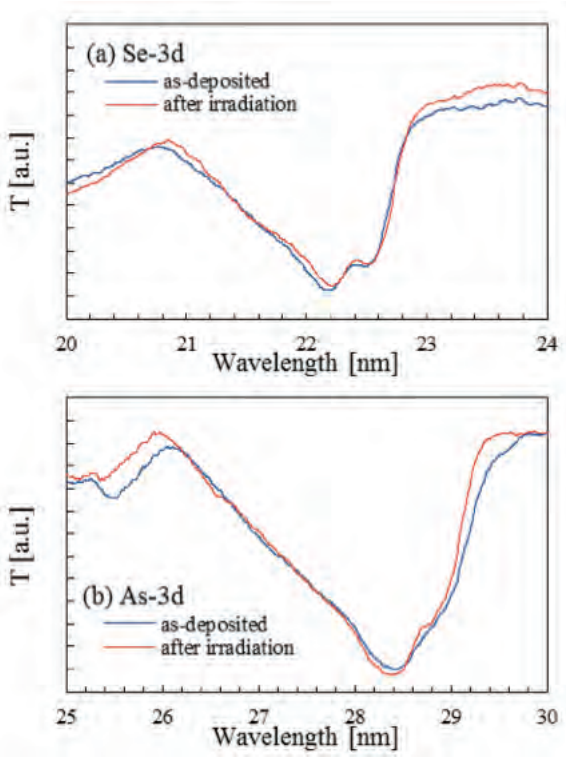

Fig. 1. VUV transmission spectra of (a) Se 3d and (b) As 3d core levels of as-deposited a-As2Se3 thin film before and after the irradiation of the BG light.

[1] K. Tanaka, Rev. Solid State Sci. **4** (1990) 641.
[2] K. Shimakawa, A.Kolobov and S. R. Elliott, Adv. Phys., **44** (1995) 475.
[3] K. Tanaka, Encyclopedia of Nanoscience and Nanotechnology, **7** (2004) 629.
[4] K. Hayashi, UVSOR Activity Report **34** (2007) 79.

BL6U

Hydrogen Interaction on MoS_2 Surface

S. W. Han[1,2], H. Yamane[3], N. Kosugi[3] and H. W. Yeom[1,2]

[1]*Center for Artificial Low Dimensional Electronic Systems, Institute for Basic Science (IBS), 77 Cheongam-Ro, Pohang 790-784, Korea*

[2]*Department of Physics, Pohang University of Science and Technology, 77 Cheongam-Ro, Pohang 790-784, Korea*

[3]*Institute for Molecular Science, Myodaiji, Okazaki 444-8585, Japan*

Recently, it has been reported that the hydrogenated MoS_2 induced a weak ferromagnetism persisting up to room temperature (RT) with the improved transport property [1]. It is important to understand the interaction between the H_2 molecule and the MoS_2 surface.

Angle-resolved photoemission (ARPES) experiments were performed at the undulator beamline BL6U of UVSOR-III in the Institute for Molecular Science. Natural and single crystalline MoS_2 samples were cleaved in UHV. The orientation of samples was confirmed by a hexagonal pattern in low-energy electron diffraction and the band structure from the ARPES data, which were collected at 140 K in the main chamber with a base pressure of 1×10^{-10} torr. The total energy and angular resolutions of the ARPES apparatus were better than 25 meV and 0.1°. The MoS_2 surface was exposed to the H_2 gas at RT by back filling the chamber with a pressure of 1×10^{-6} torr and postannealed in the preparation chamber.

Figure 1(a) shows the ARPES data of a cleaved MoS_2 surface along the Γ-K high-symmetry line of the hexagonal Brillouin zone. ARPES data were recorded with a photon energy of 100 eV and scaled by the maximum intensity. A valence band maximum (VBM) is located at the Γ-point with a binding energy of 0.34 eV. Below the VBM at Γ, there exists a strong band dispersing down (red rectangle) from the binding energy of 0.60 eV. This state is known to be a surface state, with the main contribution from the S $3p_z$ orbital on the top S layer above the Mo layer within a topmost layer of bulk MoS_2, while the VBM originates mainly from the Mo $4d_{z^2}$ orbital [2]. On the other hand, the top of the valence band dispersion at the K point (1.325 $Å^{-1}$, vertical dashed lines), stems from the mixed states of Mo $4d_{xy/x^2-y^2}$ and S $3p_{xy}$ orbitals and is located at a higher binding energy of 0.80 eV than that of VBM. This confirms the indirect bandgap of bulk MoS_2.

Figure 1(b) exhibits the band structure of MoS_2 surface after an exposure to hydrogen gas for 600 s, corresponding to 600 L (1 L = 10^{-6} Torr·s). Despite of the hydrogen exposure, band structure remains unchanged. Instead, the VBM slightly shifted toward Fermi energy (E_F) and it is located at 0.26 eV with a quite obvious band dispersion. The VBM further shifts to 0.20 eV in the case of a longer exposure of a new MoS_2 surface to the H_2 gas for 3600 s (3600 L) as shown in Fig. 1(c).

In contrast, after postannealing at 300 °C for 1 h [Fig. 1(d)], the VBM is located at the binding energy of 0.75 eV, which reversely shifted away from E_F.

In order to elucidate the hydrogenation, another MoS_2 sample was cleaved and annealed at 300 °C and then exposed to the H_2 gas for 1.5 h (5400 L). In Fig. 1(e), the VBM is obtained at a much higher binding energy of 1.24 eV with slightly broadened spectral features. Especially S p_z derived bands are enhanced at the higher binding energy side.

Figure 1(f) represents the shift of valence-band spectra, which were integrated from the ARPES data and normalized by the intensity of the first peak indicated by the (red) lines. Without a significant change of band structure, the H_2 exposure leads to shift the VBM toward E_F while the annealing shifts the VBM away from E_F.

These results suggest that the thermal annealing promotes the dissociation of H_2 molecules on the MoS_2 surface and then the atomic hydrogens are intercalated between van der Waals gaps.

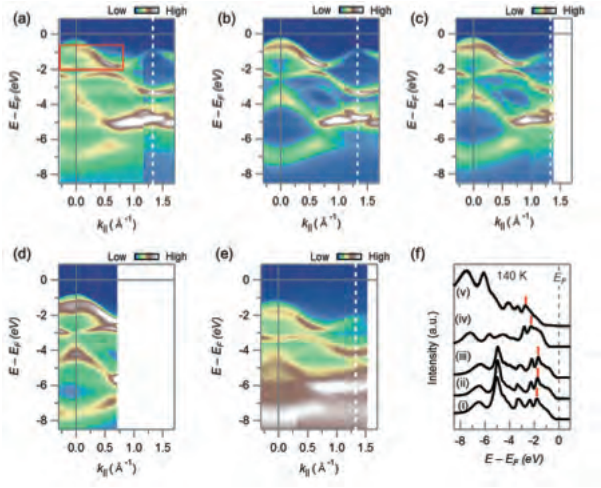

Fig. 1. ARPES intensity maps along the Γ-K direction of the Brillouin zone for three MoS_2 samples.

[1] S. W. Han *et al.*, Phys. Rev. Lett. **110** (2013) 247201.

[2] S. W. Han *et al.*, Phys. Rev. B. **86** (2012) 115105.

BL6U

Electronic Structure of Epitaxial, Metallic Germanium Nanofilms on Zirconium Diboride Thin Film Substrates – Identification of a New Form of Crystalline Germanium

R. Friedlein[1], H. Yamane[2], N. Kosugi[2] and Y. Yamada-Takamura[1]
[1]*School of Materials Science, Japan Advanced Institute of Science and Technology, Nomi 923-1292, Japan*
[2]*Dept. of Photo-Molecular Science, Institute for Molecular Science, Okazaki 444-8585, Japan*

While Si and Ge are right below C in the periodic table of elements, valence orbitals of Si and Ge atoms do not sp^2 hybridize as easily as for their smaller counterpart. However, considering that the experimental evidence for the existence of the largely sp^2-hybridized form of silicon called "epitaxial silicene" mounting [1-3], the verification of layered, hexagonal germanium structures with Dirac-cone like electronic signatures – in analogy to graphene and silicene conveniently coined "germanene" – would represent another important step towards novel two-dimensional nano-materials.

In this context, recently, in our home laboratory, we have succeeded in the preparation of nanofilms of germanium on the surface of $ZrB_2(0001)$ thin films grown on Ge(111) wafers. These epitaxial, single-crystalline-like Ge nanofilms are formed by surface segregation at elevated temperatures and oxidize upon exposure to air.

However, the native oxide can be removed by an annealing procedure under ultra-high vacuum conditions upon which again Ge nanofilms are formed. At BL6U, these films have then been studied *in situ* by angle-resolved valence band (ARPES) and core-level (XPS) photoelectron spectroscopy as well as by low-energy electron diffraction (LEED).

The measured electronic and structural properties of the films are consistent with a layered structure of hexagonal symmetry and a (1×1) in-plane lattice constant that is about 20 % smaller than that of bulk germanium in the diamond crystal structure.

Figure 1 shows the valence band structure along the $\bar{\Gamma}$-$\bar{K}$ direction of the (1×1) diboride Brillouin zone, as obtained at 15 K. A manifold of well-defined states with upwards curvature are observed. These states are likely thin film slab states that are related to the layered structure of the nanofilms. Some of these states cross the Fermi level indicating that the films are metallic. This behavior is expected for highly-strained germanium layers in which σ states are partially pushed above E_F [4].

At room temperature, the films are ($\sqrt{3}\times\sqrt{3}$)-reconstructed; on the other hand, below about 100 K, the films undergo a phase transition into a $3\sqrt{3}\times3\sqrt{3}$ structure. This phase transition is connected to a significant change in the low-energy band structure which may be associated with a charge-density wave ground state related to an electronic instability characteristic of low-dimensional systems. This may indicate that the interlayer coupling is weaker than anticipated.

At present, the results are compared with those of quantum-chemical calculations in order to understand both the structural and electronic properties.

This work was supported by the Joint Studies Program (No. 615, 2012~2013) of the Institute for Molecular Science.

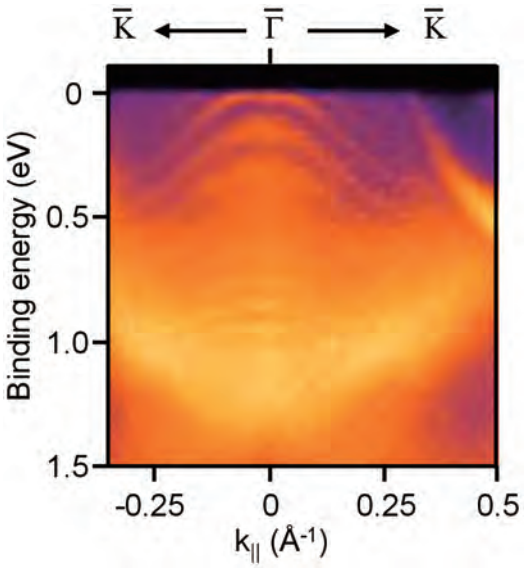

Fig. 1. ARPES spectrum of a Ge nanofilm on $ZrB_2(0001)$ thin films on Ge wafers, along the $\bar{\Gamma}$-$\bar{K}$ direction, with the sample held at 15 K. The photon energy of 43 eV was used.

[1] P. Vogt, P. De Padova, C. Quaresima, J. Avila, E. Frantzeskakis, M. C. Asensio, A. Resta, B. Ealet and G. Le Lay, Phys. Rev. Lett. **108** (2012) 155501.
[2] A. Fleurence, R. Friedlein, T. Ozaki, H. Kawai, Y. Wang and Y. Yamada-Takamura, Phys. Rev. Lett. **108** (2012) 245501.
[3] R. Friedlein, A. Fleurence, J. T. Sadowski and Y. Yamada-Takamura, Appl. Phys. Lett. **102** (2013) 221603.
[4] Y. Wang and Y. Ding, Solid State Commun. **155** (2013) 6.

BL6U

Formation of Interface State and Intermolecular Band Dispersion in Coronene/Au(111) Superstructure

H. Yamane and N. Kosugi
Department of Photo-Molecular Science, Institute for Molecular Science, Okazaki 444-8585, Japan

Study of organic/metal interfaces is essential to investigate electronic phenomena derived from the complex interplay between van der Waals interaction and exchange-correlation interaction. Previous studies on organic/metal energetics have been performed mainly for non-ordered or multi-domain systems due to experimental difficulties. In the present work, we applied the precise angle-resolved photoemission spectroscopy (ARPES) to the single-domain monolayer of coronene physisorbed on Au(111).

The present experiments were performed at BL6U. The cleanliness of the Au(111) surface was confirmed by the low-energy electron diffraction with a micro channel plate (MCP-LEED) and the Shockley surface state in ARPES, as obtained from the repeated cycles of the Ar^+ sputtering (I ~ 2 μA) and the subsequent annealing (T = 700 K). The total energy resolution in the present ARPES measurement was 16 meV.

Figure 1 shows (a) the LEED image and (b) the surface Brillouin zone (SBZ) of the coronene monolayer deposited on Au(111). The LEED image shows the (4×4) single-domain superstructure with respect to the Au(111) hexagonal surface lattice.

The energy-*vs*-momentum $E(\boldsymbol{k})$ map along the $\bar{\Gamma}$-$\bar{K}$ direction ($\boldsymbol{k}_{\Gamma K}$) of the clean Au(111) surface and the coronene/Au(111) interface, obtained from ARPES, is shown in Figs. 2(a) and 2(b), respectively. Upon the formation of the coronene/Au(111) superstructure, some new electronic states are observed. The free-electron-like dispersive bands are weakly appeared below the Fermi level E_F (E_b = 0~0.4 eV) and above the Au 5d band (E_b = 1.7~2.4 eV). The inflection point of the parabolic dispersions appears at the $\bar{\Gamma}$ point of the monolayer's SBZ ($\boldsymbol{k}_{\Gamma K}$ = 1.08 Å^{-1}). The parabolic dispersions at the low- and high-E_b side may originate from the Shockley- and Tamm-type interface states, respectively, both of which are induced by the surface potential due to the coronene superstructure. Here, the E_b position of the parabolic dispersions are almost the same for the original Shockley and Tamm surface states of the clean Au(111) surface. Therefore, the interface interaction between coronene and Au(111) is considered to be quite weak.

At E_b ~ 1.6 eV, a highest occupied molecular orbital (HOMO) peak is observed. The energy distribution curve at $\boldsymbol{k}_{\Gamma K}$ = 1.40 Å^{-1} shows a sharp HOMO line shape with the high-E_b satellite due to the hole- vibration coupling. This observation also suggests the weak physisorption between coronene and Au(111). Note that, the HOMO peak shows a quite weak but non-negligible dispersion of ~20 meV.

The in-plane band dispersion of molecular electronic states has been observed for strongly chemisorbed interfaces with larger dispersion of 0.2~0.3 eV due to the interfacial orbital hybridization [1, 2]. By considering the quite weak interaction between coronene and Au(111), the observed in-plane band dispersion is ascribed to the genuine intermolecular interaction in two-dimensional sheets of aromatic hydrocarbons.

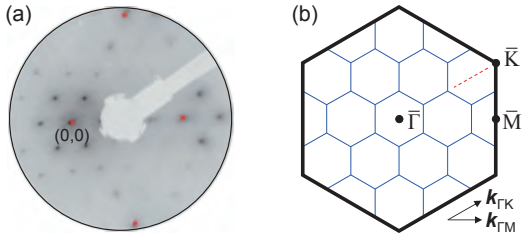

Fig. 1. (a) The MCP-LEED image of the coronene monolayer on Au(111) at 15 K, taken with the 70-eV incident electron beam. The red spot indicates the substrate's spot. (b) The surface Brillouin zone (SBZ) of the monolayer superstructure of coronene on Au(111). The black and blue solid lines indicate the substrate and monolayer SBZs, respectively. The red dashed line indicates the scan region of ARPES.

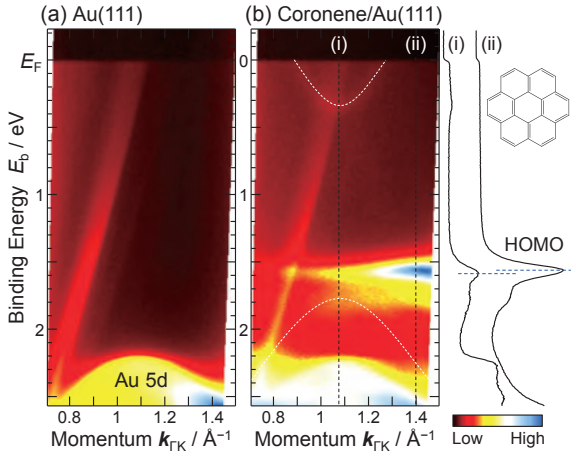

Fig. 2. The $E(\boldsymbol{k})$ map at T = 15 K around the 2nd $\bar{\Gamma}$ point in the monolayer's SBZ [cf. Fig. 1(b)]; (a) The clean Au(111) surface. (b) The coronene monolayer on Au(111) with the energy distribution curve at (i) $\boldsymbol{k}_{\Gamma K}$ = 1.08 Å^{-1} and (ii) $\boldsymbol{k}_{\Gamma K}$ = 1.40 Å^{-1}. The molecular structure of coronene is also shown.

[1] H. Yamane *et al.*, Phys. Rev. B **76** (2007) 165436.
[2] M. Wießner *et al.*, Nat. Commun. **4** (2013) 1514.

BL6U

Linearly-Dispersive Electronic States at the Interface of Organic Monolayers on Graphite

H. Yamane and N. Kosugi
Department of Photo-Molecular Science, Institute for Molecular Science, Okazaki 444-8585, Japan

Organic monolayers on solid surfaces show various electronic states and complex electronic phenomena, depending on electronic interactions at their interface. Some interfacial electronic phenomena, such as the charge transfer, have been applied to the control of interface energetics in functional molecular systems. In this work, by using angle-resolved photoemission spectroscopy (ARPES), we succeeded in observation of a linearly-dispersive electronic state at the interface of organic monolayers on graphite.

This work was performed at BL6U. The single-crystalline graphite [Gr(0001)] was obtained by the direct resistive heating of a 6H-SiC(0001) wafer at 1500°C [1], as confirmed by the low-energy electron diffraction (LEED) and the valence band dispersion. In order to obtain the well-ordered organic monolayer, the Gr(0001) substrate was heated at ~120°C during the deposition at 1~2 Å/min. The energy resolution in the present ARPES was 16 meV at 15 K.

Figure 1(a) shows the LEED image of the metal-free phthalocyanine (H_2Pc) monolayer on Gr(0001) at 15 K. The observed LEED image indicates the well-known multi-domain structure for Pc molecules on six-fold symmetric surfaces. The molecular unit cell of H_2Pc/Gr(0001) determined from LEED [Fig. 1(b)] agrees with the previous STM study [2]. Considering the symmetry of the molecular unit cell, we measured the azimuthal-angle-dependent ARPES.

Figure 1(c) shows the energy-*vs*-momentum $E(\boldsymbol{k})$ map and its energy- and momentum-distribution curves (EDC and MDC) for H_2Pc/Gr(0001) at 15 K along the $\boldsymbol{b}_1^*$ direction ($h\nu$ = 45 eV). The highest occupied molecular orbital (HOMO) peak appears at the binding energy (E_b) of 1.4 eV. In addition, as indicated by the dashed line in the $E(\boldsymbol{k})$ map and MDC, the linearly-dispersive feature appears weakly but undoubtedly at E_b = 0~2.2 eV, like Dirac cone. This is the interface-specific electronic state, which is observable for neither the clean Gr(0001) surface nor the thick multilayer film. In general, the Dirac cone in a honeycomb structure, such as graphene, is appeared not at the edge but at the corner of the Brillouin zone. In the present case, we found that the linearly-dispersive interface state appears at all azimuth directions. Therefore, the observed linearly-dispersive interface state could be due to the scattering from the Dirac band of the underlying Gr(0001) substrate.

In order to elucidate the origin of the linearly-dispersive interface state, we measured ARPES as functions of temperature, substrate, and molecule. We found that the linearly-dispersive interface state is getting weak at 300 K, and is not observable for the H_2Pc/Au(111) interface. These results suggest the importance of the electronic coupling between organic monolayers and Gr(0001). Furthermore, the linearly-dispersive interface state is observed also for other monolayers of pentacene, coronene, and C_{60} grown on highly oriented pyrolytic graphite (HOPG) with different dispersion parameters such as the Fermi momentum ($\boldsymbol{k}_F$) and the Fermi velocity (v_F). On the other hand, both $\boldsymbol{k}_F$ and v_F at the CoPc/HOPG interface are almost the same as those at the H_2Pc/HOPG interface, suggesting the importance of the molecular unit cell.

Judging from the present observations, the linearly-dispersive interface state is governed by both the size of the molecular unit cell and the electronic coupling at molecule/graphite interfaces. The Dirac band of the graphite surface could be scattered and modified by the intermolecular phonons of adsorbate's lattices as a result of the surface Umklapp process, which plays a crucial role in the charge/spin extraction in molecule-graphene hybrid systems.

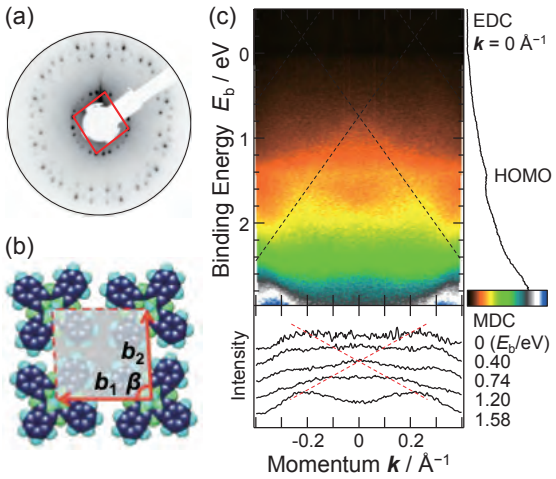

Fig. 1. (a) The LEED image of the H_2Pc monolayer on Gr(0001) at 15 K, taken with 20-eV incident electrons. (b) The molecular unit cell of H_2Pc/Gr(0001), where b_1 = 13.8 Å, b_2 = 13.1 Å, and β = 87.6° [2]. (c) The $E(\boldsymbol{k})$ map along the $\boldsymbol{b}_1^*$ direction with the energy- and momentum-distribution curves (EDC and MDC) of H_2Pc/Gr(0001) at 15 K ($h\nu$ = 45 eV).

[1] I. Forbeaux *et al.*, Phys. Rev. B **58** (1998) 16396, and references therein.
[2] K. Nilson *et al.*, J. Chem. Phys. **127** (2007) 114702.

BL7U

Low-Energy Angle-Resolved Photoemission Study on Ultrathin Bi Films II

T. Hirahara[1], T. Shirai[1], M. Matsunami[2], T. Hajiri[2], S. Kimura[2] and S. Hasegawa[1]
[1]*Department of Physics, University of Tokyo, Tokyo 113-0033, Japan*
[2]*UVSOR Facility, Institute for Molecular Science, Okazaki 444-8585, Japan*

Semimetal bismuth (Bi) is one of the most extensively studied elements in solid state physics because of its extreme physical properties, such as the highest resistivity and Hall coefficient of all metals. Bi has tiny hole and electron pockets at *T* and *L* points, respectively, [Fig.1(a) and 1(b)], and therefore the Fermi wavelength λ_F is very large (about 30 nm). Because of this large λ_F, the quantum size effect shows up in the properties of Bi films, and the oscillation of the film resistance with the film thickness *d* was reported [1]. Furthermore, it was predicted that when the lowest quantized subband of the electron pocket is raised to an energy higher than the highest hole subband, a band gap will develop [semimetal-to-semiconductor (SMSC) transition at *d*~30 nm, Fig. 1(c)][2]. However, although many angle-resolved photoemission (ARPES) measurements have been performed on ultrathin Bi films, none has actually been able to verify whether this SMSC transition occurs or not [6-9]. The main reason is that the cross section for the bulk bands depends dramatically on the photon energy and polarization.

Therefore in the present study, we have performed ARPES measurements on ultrathin Bi films by systematically changing the photon energy (7-40 eV) and polarization (*P*- and *S*- polarization). Figures 2(a) and (b) show the Fermi surface and band dispersion near the Fermi level (hν = 9.5eV) of a 25Å thick Bi(111) film measured with *S*-polarized photons. There is a circular structure at the Γ point. However when the polarization is switched to *P*-polarization ((c) and (d)), it becomes hexagonal. These features correspond to the bulk (B) and surface (S) states, respectively. This suggests that the bulk bands remain metallic and the SMSC transition does not occur. Further sophisticated study is needed to reach a definite conclusion.

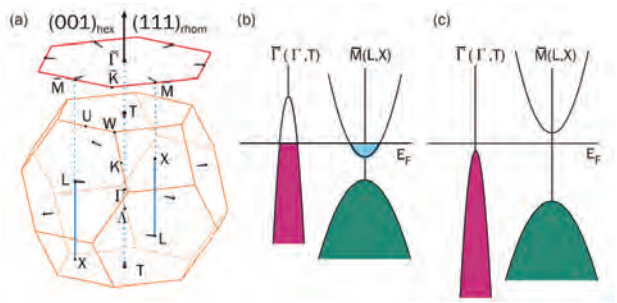

Fig. 1. (a) The Fermi surface of bulk Bi depicted in bulk (orange) and its projection to the surface (red) Brillouin zone. Electron (hole) pockets are filled with light blue (purple). (b), (c) Schematic drawing of the Bi bulk band projection near the Fermi level before (b) and after (c) the SMSC transition [2].

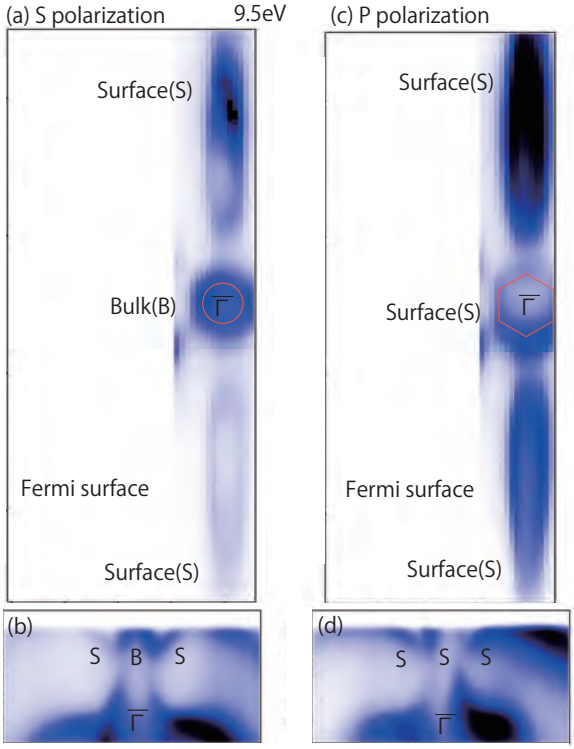

Fig. 2. The Fermi surface and band dispersion of a 25 Å thick Bi(111) film measured at hν=9.5eV with *S*- (a), (b) and *P*- (c), (d) polarized photons, respectively. S (B) represents surface (bulk) states.

[1] Yu. F. Ogrin *et al.,* JETP Lett. **3** (1966) 71.
[2] V. B. Sandomirskii, Sov. Phys. JETP **25** (1967) 101.
[3] T. Hirahara *et al.,* Phys Rev. Lett. **97** (2006) 146803; Phys. Rev. B **75** (2007) 035422; Phys. Rev. B **76** (2007) 153305; New Jour. Phys. **10** (2008) 083038.
[4] A. Takayama *et al.,* Phys. Rev. Lett. **106** (2011) 166401; Nano Lett. **12** (2012) 1766.
[5] H. Miyahara *et al.,* eJSSNT 10, 153 (2012); T. Okuda *et al.,* Rev. Sci. Inst. **82** (2011) 103302.

BL7B

Filterless Vacuum Ultraviolet Photoconductive Detector Based on YF_3 Thin Film Prepared by Pulsed Laser Deposition

M. Yanagihara[1], H. Ishikawa[1], T. Tsuji[1], H. Ohtake[2] and S. Ono[1]
[1] *Nagoya Institute of Technology, Gokiso-cho, Showa-ku, Nagoya 466-8555, Japan*
[2] *Aisin Seiki Co.,Ltd., 2-1 Asahi-machi, Kariya 448-8650, Japan*

Due to potential applications such as monitoring for industrial processes and gas sensing, considerable attention has been focused on the development of vacuum ultraviolet (VUV) detectors. Currently, the study of photoconductive detectors using diamond, nitride, and oxide are demonstrated. However, these devices response deep-UV (DUV) range not only VUV range because of limitation by the band gap. Fluorides are relatively wide band gap in contrast to these materials[1, 2]. Here, we report on the development of VUV photoconductive detector, which has no sensitivity in DUV region without any filters, by utilizing the YF_3 thin films.

YF_3 thin film was grown by pulsed laser deposition (PLD) on the quartz glass substrate. YF_3 ceramic target was irradiated with the femtosecond laser pulses (wavelength: 790 nm, laser fluence: 13.5 J/cm^2). Growth was carried out 3 h under high vacuum condition (2×10^{-4} Pa). The substrate heating temperature was controlled at 670 K. Figure 1 is scanning electron microscope (SEM) images of YbF_3 thin film. A sub-micron-sized particulates make up the majority of the deposition layer. The thickness of the thin film was about 170 nm.

To evaluate these thin films as photoconductive detectors, a pair of interdigitated aluminum electrodes was fabricated onto the thin film by vacuum deposition. The patterned area of interdigitated electrodes was 5×4 mm^2. Both the gap between the electrodes and the width of the electrodes were 0.2 mm. In addition, we covered them with YF_3 thin film to prevent photoelectron emission from electrodes. Figure 2 shows I-V characteristic measured in the dark (unirradiation) and under illumination of VUV light from deuterium lamp (irradiation). The dark current was below 1 pA. The current value increased 3-digit before and after VUV illumination at an applied bias of 300 V.

To evaluate the spectral responsivity of the detector using YbF_3 thin film, a bias voltage of 200 V was applied to a pair of interdigitated electrodes. Photocurrent was measured at each wavelength of irradiative light from 100 to 300 nm. Figure 3 shows the results of the spectral responsivity evaluation combined with the transmission of the sample. It turned out that this detector responded only to VUV wavelengths shorter than 170-nm wavelength. The 170-nm wavelength corresponds to band gap of YbF_3. Consequently, these results indicated that we developed a VUV photoconductive detector.

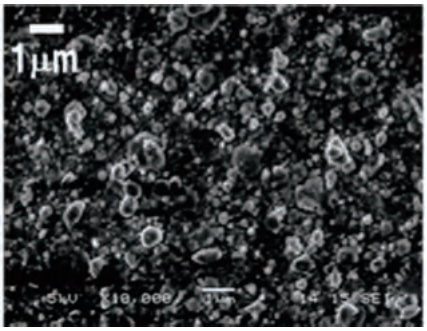

Fig. 1. SEM images of the surface and section of YbF_3 thin films.

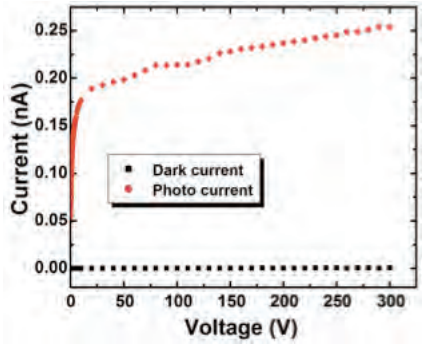

Fig. 2. I-V characteristic of YF_3 thin film.

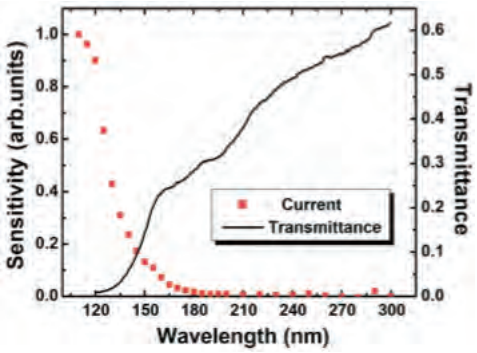

Fig. 3. Transmission spectrum and spectral response of the detector.

[1] M. Ieda, T. Ishimaru, S. Ono, K. Yamanoi, M. Cadatal, T. Shimizu, N. Sarukura, K. Fukuda, T. Suyama, Y. Yokota, T. Yanagida and A. Yoshikawa, Jpn. J. Appl. Phys. **51** (2012) 022603.
[2] T. Ishimaru, M. Ieda, S. Ono, Y. Yokota, T. Yanagida and A. Yoshikawa, Thin Solid Films, **534** (2013) 12-14.

BL8B

ARUPS Study of Molecular Orientation of Pentacene Thin Film on SAM-Covered SiO_2

K. K. Okudaira, N. Kanayama and N. Ueno
Association of Graduate Schools of Science and Technology, Chiba Univererity, Chiba 263-8522, Japan

Field effect transistors (FETs) based on organic semiconducting materials have made rapid progress in recent years. Pentacene (Pn) is one of the best candidates for use in fabricating thin film transistors because of their high field effect charge mobility. A more efficient device is expected if all the molecules are packed orderly with the conducting channels in correct alignment relative to the electrodes. The self-assembled monolayers (SAMs) provide a systematic way to modify surface properties such as wetting and polarity of a substrate, which, in turn, may affect the orientation of a film deposited on top of it.

In this work we used methyl and phenyl group terminated SAMs for substrate and examined the molecular orientation of pentacene thin films crystals thermally deposited on these SAM surfaces by angle-resolved ultraviolet photoelectron spectroscopy (ARUPS) measurements. To obtain the quantitative analysis on the molecular orientation; we compare observed take-off angle dependence of π band and calculated ones by the independent-atomic-center (IAC)/MO approximation.

ARUPS measurements were performed at the beam line BL8B2 of the UVSOR storage ring at the Institute for Molecular Science. The take-off angle (α) dependencies of photoelectron spectra were measured at incident angle of photon (θ) = 45^{O} with the photon energy (hν) of 28 eV. We use octadecyltrichlorosilane (OTS) and trichloro(phenetyl)silane (phenyl) as coupling agent for SAM. The SAMs were prepared by dipping SiO_2 substrate at room temperatures. Pentacene thin film was deposited on these SAMs.

We observed take-off angle (α) dependence of HOMO peak in UPS of pentacene thin film (thickness of about 2.0 nm on OTS-SAM and 1.5nm on phenyl-SAM).

In Fig. 1 (a) the α dependences of Pn(2.0nm)/OTS-SAM have a sharp maximum at α=50°, while α dependences of Pn(1.5nm)/phenyl-SAM show two maxima at α=50° and 20°, which are different from those of Pn(2.0nm)/OTS-SAM. From the comparison with calculated results it is found that on the OTS-SAM pentacene molecules have stand-up orientation, while on the phenyl-SAM, pentacene molecules have not only stand-up orientation but also lie-flat orientation. This difference of film structure is responsible for the interaction between substrate surface and molecules since the surface energy of OTS-SAM is smaller than that of phenyl-SAM.[1]

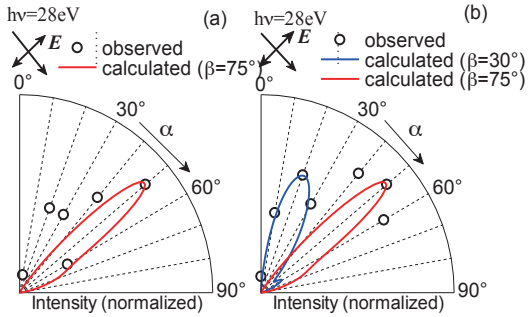

Fig. 1. Take-off angle (α) dependences of photoelectron intensities of HOMO peak of Pn(2.0nm)/OTS-SAM (a) and Pn(1.5nm/ phenyl-SAM (b). (——) and (——) : calculated α-dependence for inclination angle (β) = 75 ° and 30°.

[1] D. Janssen, *et al*., Thin. Solid. Films **515** (2006) 1433.

BL8B

Photoelectric Emission from Au on Zinc-Phthalocyanine Film

S. Tanaka[1], T. Otani[2] and I. Hiromitsu[2]

[1] *Department of Electric and Electronic Engineering, Faculty of Science and Engineering, Kinki University, Higashiosaka 577-8502, Japan*

[2] *Department of Physics and Materials Science, Graduate School of Science and Engineering, Shimane University, Matsue 690-8504, Japan*

In general, the work function of thin films of metals and the ionization potential of organic thin films are no less than 4 eV. It is therefore expected that light energy of less than 4 eV cannot generate photoelectric emission from the surfaces of metal or organic films. However, we observed photoelectric emission from Ag on a zinc-phthalocyanine (ZnPc) layer at a photon energy of 3.4 eV. [1, 2] The threshold energy for this photoelectric emission is much smaller than the work function of Ag. Although the mechanism of this anomalous photoelectric emission is not clear, the previous results suggest that the vacuum level shift at the Ag/ZnPc interface play a key role. To investigate the mechanism of the anomalous photoelectric emission, we studied the photoelectric emission from Au on ZnPc film under UV-visible light irradiation.

The ZnPc was purchased from Kanto Chemical and sublimed three times for purification. ZnPc thin films were fabricated by vacuum deposition on a polycrystalline Ag substrate. The pressure used during the deposition was in the range of 10^{-5} Pa. Au was used as the metal layer on the ZnPc film. The thicknesses of the ZnPc and Au were measured using a quartz microbalance. A white light source (a Xe lamp with an air mass 1.5 filter, HAL-320, Asahi Spectra Co. Ltd.) was used as UV-visible region light source. The UV-visible light was introduced to the measurement chamber through a glass viewport that cut off the light with wavelength shorter than approximately 320 nm. The power of the white light on the sample surface was 100 ±10 mW/cm^2.

First, we fabricated the ZnPc thin film with the thickness of 10 nm. Under the white light irradiation, no photoelectric emission was observed from the ZnPc film as expected. The ionization potential of ZnPc film was estimated to be 5.0 eV by photoelectron spectroscopy using synchrotron radiation ($h\nu$ = 39.6 eV) (Fig. 1). On the other hand, in the case of the Au (0.2 nm)/ZnPc sample, we observed weak but obvious photoelectric emission under the white light irradiation. This is surprising since both of the work function of Au and the ionization potential of ZnPc are much larger than the highest energy of white light. Interestingly, no photoelectric emission under the white light irradiation was observed from the Au (1.0 nm)/ZnPc sample. In the case of Ag, the photoelectric emission under the white light irradiation was observed even at the Ag thickness of 20 nm.

Figure 1 shows the variation in the photoelectron spectrum of the ZnPc thin film (10 nm) during the incremental deposition of Au. The secondary cutoff was shifted toward higher kinetic energy by deposition of 1.0 nm Au. The HOMO peak of ZnPc (indicated by the bars in Fig. 1) showed a similar variation to that of the secondary electron cutoff. Vacuum level shift at metal/organic interfaces has been reported in many systems, and is attributed to the formation of an interfacial dipole layer. The direction and magnitude of interfacial dipole is affected by the work function of metal. Au has larger work function than Ag. Basically, the large work function of Au increases the threshold energy for the photoelectric emission. Indeed, the magnitude of the anomalous photoelectric emission on the Au/ZnPc surface under the white light irradiation was weaker than that on the Ag/ZnPc surface. However, the very small amount of Au on ZnPc surface caused the anomalous photoelectric emission. Further studies are needed to understand the role of Au and Ag in the anomalous photoelectric emission.

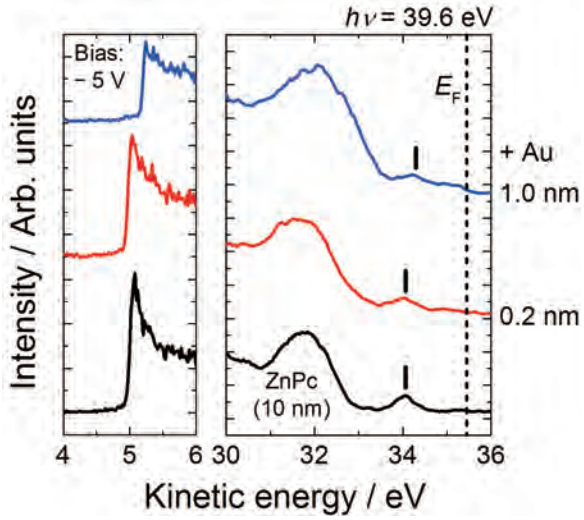

Fig. 1. Variation of the photoelectron spectra of the ZnPc film under incremental Au deposition (0.2, 1.0 nm). Left panel: Secondary electron cutoff region. The sample was biased at –5.0 V during the measurements. Right panel: Around the Fermi level. No bias voltage was applied to the sample.

[1] S. Tanaka *et al.*, UVSOR Activity Report **40** (2013) 144.
[2] S. Tanaka *et al.*, submitted.

BL8B

Electronic Structures of Organic Donor-Acceptor Interfaces of a Squaraine Dye and C_{60}

Y. Nakayama[1], K. R. Koswattage[2], Y. Ozawa[1], N. Ohashi[3] and H. Ishii[1,2]
[1]*Graduate School of Advanced Integration Science, Chiba University, Chiba 263-8522, Japan*
[2]*Center for Frontier Science, Chiba University, Chiba 263-8522, Japan*
[3]*School of Engineering, Tohoku University, Sendai 980-8579, Japan*

Squaraine dyes are recently attracting growing interest as promising donor materials for organic solar cell application owing to their efficient far red - near IR absorption [1, 2]. Kido *et al.* reported that blends of fullerenes with a member of the squaraine family, 2,4-bis[4-(N,N-di-isobutylamino)-2,6-dihydroxyphenyl] squaraine (SQ; see Fig. 1 inset), exhibited excellent solar cell efficiency [3]. In the present study, we investigated these organic donor-acceptor interfaces of SQ and C60 fullerene by means of ultraviolet photoelectron spectroscopy (UPS).

SQ and C_{60} were successively deposited onto indium-tin oxide (ITO) substrate precleaned by ultrasonication followed by UV/O_3 treatment. UPS measurement was conducted at BL8B of UVSOR.

Firstly, we determined the ionization energy (I_s) of SQ accurately. In this experiment, the excitation photon energy was carefully calibrated to be 29.76 eV by using the Fermi edge position of the second-order light. This allows one to decide the absolute value of the work function (WF) of the sample from the secondary electron cut-off (SECO) position. Figure 1 shows a UPS spectrum of a SQ film (5 nm-thick) plotted with respect to the vacuum level. Accordingly I_s value of SQ is settled to be 5.15 eV.

Figure 2 shows evolution of the UPS spectra of the C_{60}-on-SQ and its reverse interfaces. For the former, stacking of C_{60} lifted the vacuum level up as shown in Fig. 2(a), and the highest occupied molecular orbitals (HOMO) of both SQ and C_{60} also shifted to the low binding energy (BE) side (Fig. 2(b)). In contrast, for the reverse interface (Fig. 2(c,d)), WF decreased on coverage of SQ over C_{60}. The SQ HOMO exhibited the similar behavior to WF, while the C_{60} HOMO stuck to its original position.

According to the UPS results, the energy level diagrams of the C_{60}-on-SQ and SQ-on-C_{60} interfaces can be drawn as shown in Fig. 3. Here the energy gap width of C_{60} is assumed to be 2.3 eV [4]. The joint upward shift observed in the former system should be attributed to a band bending across the interface. Meanwhile, the downward shift of the vacuum level E_{vac} and SQ-HOMO apart from C_{60} may be caused by orientation polarization of the SQ molecules [5].

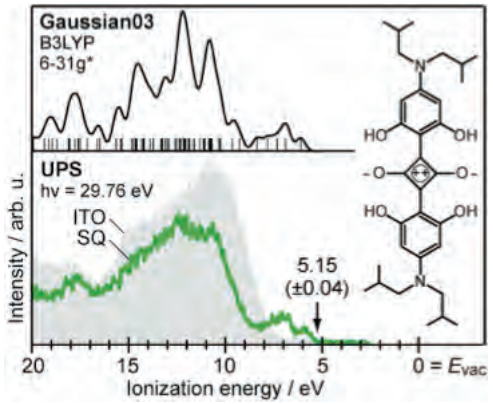

Fig. 1. UPS spectra of SQ film (5 nm) on ITO. A simulated density-of-states curve derived from the density functional theory calculation is also shown for reference. (Inset) The chemical structure of SQ.

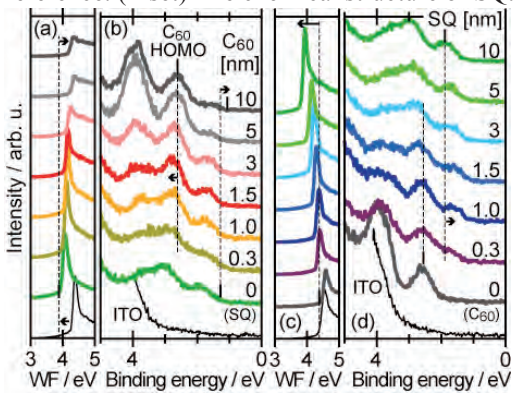

Fig. 2. Series of UPS spectra of (a,b) C_{60}-on-SQ and (c,d) SQ-on-C_{60} interfaces.

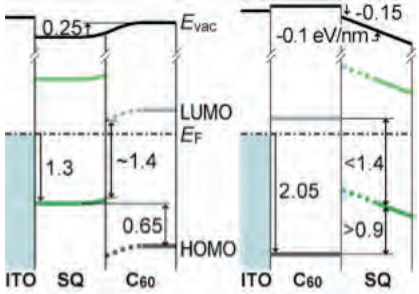

Fig. 3. Energy level diagrams of the (left) C_{60}-on-SQ and (right) SQ-on-C_{60} interfaces (units: eV).

[1] K. Y. Law, Chem. Rev. **93** (1993) 449.
[2] G. Wei *et al.*, ACS Nano **6** (2012) 972.
[3] G. Chen *et al.*, Adv. Mater. **24** (2012) 2768; Appl. Phys. Lett. **101** (2012) 083904.
[4] R. W. Lof *et al.*, Phys. Rev. Lett. **68** (1992) 3924.
[5] Y. Nakayama *et al.*, Org. Electron. **13** (2012) 2850.

BL8B

Efficiency of HATCN as a Hole Injection Layer in a Practical System

A . Yoneyama[1], K. R. Koswattage[2], Y. Nakayama[1,3] and H. Ishii[1,2,3]
[1] *Faculty of Engineering, Chiba University, Chiba 263-8522, Japan*
[2] *Center for Frontier Science, Chiba University, Chiba 263-8522, Japan*
[3] *Graduate School of Advanced Integration Science, Chiba University, Chiba 263-8522, Japan*

HATCN(dipyrazino[2,3-f:2',3'-h]quinoxaline-2,6, 7, 10,11-hexacarbonitrile) is knwon as a strong accepter and actually has been reported to play a role of a hole injection layer in real devices [1]. Niederhausen et al clearly proved that this molecular layer actually lifted the highest occupied molecular orbital (HOMO) energies of ad-layers of several organic materials up toward the Fermi level of the metal substrate [2]. In this study, we examined how efficient the HATCN interlayer play a role of a hole injector in a more practical system ; that is HATCN on indium-tin oxide (ITO) substrates.

Clean ITO substrates were prepared through ultrasonication in acetone followed by UV/O_3 treatment. The work function of the ITO substrates was 4.3 - 4.4 eV. One-nanometer thick HATCN was then deposited at the evaporation rate of 0.1 nm/sec onto an ITO substrate to prepare a 'passivated ITO' substrate, which increased the work function of the substrate to 4.9 eV. C_{60} was successively deposited onto the passivated and pristine (w/o HATCN) ITO substrates in a step-by-step manner up to 10 nm thick. All UPS spectra shown below were taken with the photon energy of 22 eV at BL-8B in UVSOR.

Figure 1 shows the evolutions of the UPS spectra in the secondary electron cut-off (SECO) region. On the pristine ITO the C_{60} overlayer induced almost no vacuum level shift as seen in Fig. 1(a). Meanwhile, on the passivated ITO, one can find a downward vacuum level shift by 0.1eV as shown in Fig. 1(b) .

Evolution of the valence band UPS spectra on growth of the C_{60} overlayers is shown in Fig. 2. As each abscissa axis are taken with respect to the Fermi level, the onset binding energy of the HOMO peak corresponds to the hole injection barrier (HIB) from the electrode into C_{60}. On the pristine ITO, the HOMO peak stayed at a constant energy position independent of the C_{60} thickness (Fig. 2(a)). The HIB is estimated to be around 1.95eV for this case. On the other hand, as observed in Fig. 2(b), the HOMO peak of C_{60} appeared at a smaller binding energy position on the HATCN interlayer; it emerged at the binding energy of 2.20 eV in the peak position, while it shifted further closer to the Fermi level by 0.15eV on growth to 2 nm or thicker. Accordingly, the HIB of C_{60} on HATCN is determined to be 1.58eV from the HOMO position the 0.4 nm-thick overlayer, while the HOMO onset lifts up by 0.07 eV in the bulk region.

Figure 3 shows the energy level diagrams based on the values extracted from SECO/valence spectra and a literature [3]. C_{60} on passivated ITO exhibited a 0.3eV lower HIB compared with the pristine ITO case. Also, in the passivated ITO case, band-bending in the in the C_{60} layer was observed toward the C_{60}/HATCN interface, supposedly there are electric dipoles at the interface.

In summary, comparison of the UPS spectra between C_{60}/HATCN/ITO and C_{60}/ITO has revealed that insertion of the HATCN layer results in a 0.3eV lower HIB from ITO to C_{60}. This supports that hole injection becomes advantageous by a HATCN interlayer in practical organic opto-electronic devices.

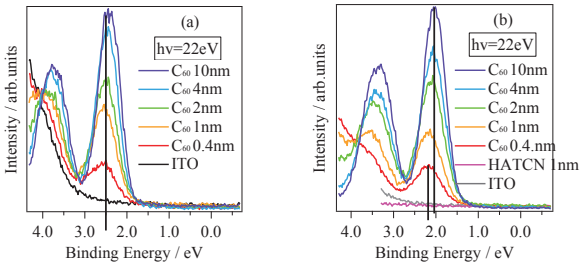

Fig. 1. UPS spectra in the SECO region of the C_{60} overlayers on (a) pristine and (b) passivated ITO.

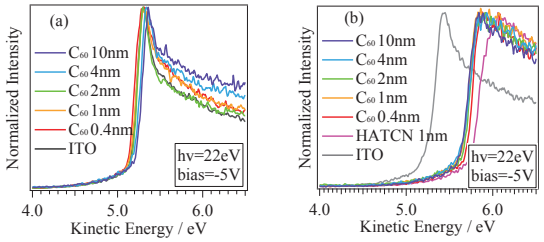

Fig. 2. UPS valence spectra of C_{60} deposited onto the (a) pristine and (b)

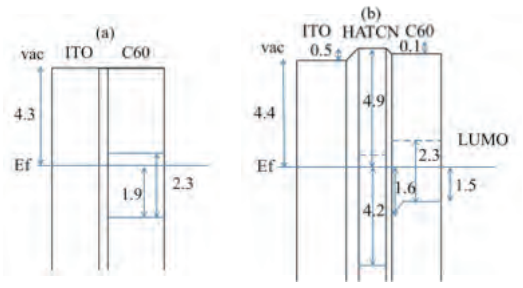

Fig. 3. Schematic energy level diagram for the deposition of C_{60} on (a) pristine ITO and (b) passivated ITO. The value of the band gap of C_{60} is take from Ref.3.

[1] S. M. Park, Y. H. Kim, Y. Yi, H. Y. Oh and J. W. Kim, Appl. Phys. Lett. **97** (2010) 063308.
[2] J. Niederhausen *et al.*, Phys. Rev. B **84** (2011) 165302.
[3] R. W. Lof, *et al.*, Phys. Rev. Lett. **68** (1992) 3924.

BL8B

HATCN on ITO: Work Function Variation and Influence of Air Exposure

K. R. Koswattage[1], A. Yoneyama[2], Y. Nakayama[2] and H. Ishii[1,2]
[1]*Center for Frontier Science, Chiba University, Chiba, Japan*
[2]*Graduate School of Advanced Integration Science, Chiba University, Chiba, Japan*,

HATCN (Hexaazatriphenylene-Hexanitrile) is used as an interlayer to increase the work function of metal electrodes for the application of organic electronics.

In this work, we mainly examined impact of air exposure on the valance electronic structure of HATCN prepared under UHV condition in order to evaluate its ionization potential (IP) because contradictory values are found in literatures and such discrepancy is likely to arise from variations in the experimental conditions. e.g. vacuum condition[1-3].

In this work, UPS measurements were done at BL8B, UVSOR. The excitation photon energy was carefully calibrated by using the Fermi edge energies of the first and second order light. ITO was cleaned by sequential ultra-sonication in acetone. The work function of the ITO substrate was determined to be 4.6 eV. Then, HATCN was subsequently deposited on the ITO, and a set of UPS measurements were performed at each step of the thickness.

Figure 1(a) shows the thickness-dependent UPS spectra of HATCN on ITO at the photon energy of 30 eV, and the top spectrum (dotted) of the Fig. 1(a) shows a calculated spectrum of HATCN using Gaussian. After about 1 nm, HOMO peak of HATCN can be distinguished from the O-2p feature of ITO and for the thickest film IP value of HATCN is estimated to be 9.1 eV. Kang *et al*. [3] performed similar works to investigate interface and molecular level alignment of HATCN on ITO and their results were almost consistent with our present findings. In Fig. 1(b), the work function change is plotted as a function of film thickness considering the energy position of the secondary energy cutoff (SECO; at -5 V sample bias). It is clear from the Fig. 1(b) that the work function can be controlled by HATCN.

To clarify the reason for the contradictory IP values of HATCN have been reported previously, we exposed this 10 nm-thick HATCN bulk film to the air in the dark for 12 h. The UPS measurements were subsequently performed and the results are shown in the Fig. 2. Figure 2(a) shows the HOMO region spectra before and after air exposure. The photon energy was set at 45 eV. Two additional features can be observed in the HOMO-LUMO gap region after air exposure. Considering the features separately, on-sets of them can be estimated as IP= 7.4 eV and 6.4 eV, while the original onset was IP = 9.1 eV. The value of 7.4 eV is consistent with the reported IP (7.5) by PYS [1] where the value might correspond to this gap states due to experimental condition of PYS. Further, it was observed that the SECO value changed to the low kinetic energy side after the air exposure as shown in Fig. 2(b). Such changes should be essential to consider the application of HATCN for practical devices.

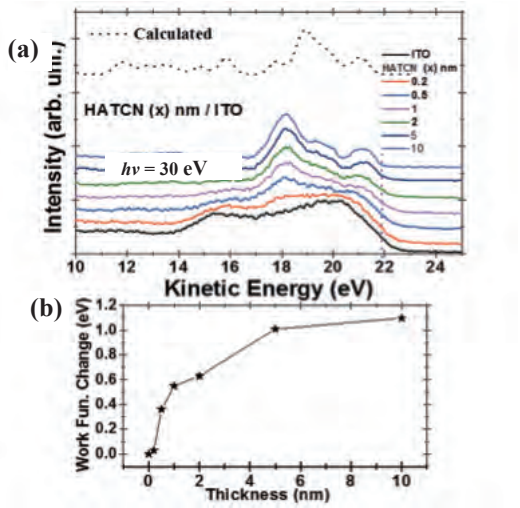

Fig. 1. (a) Thickness-dependent UPS of HATCN on ITO & simulated spectrum (top-dotted line). (b) Work function change of ITO as the function of HATCN thickness.

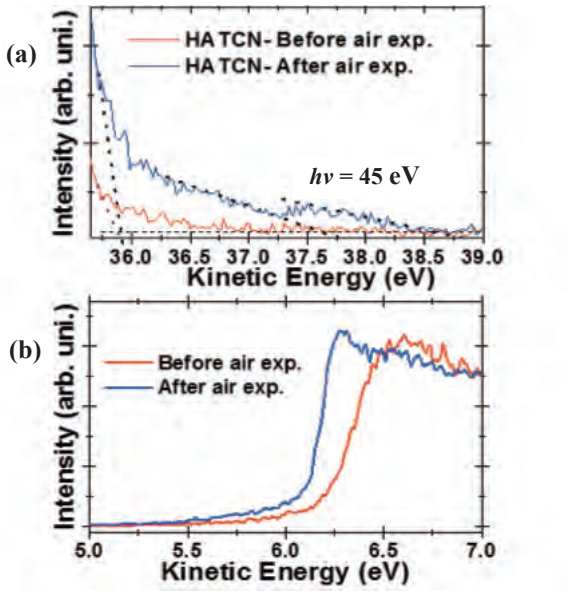

Fig. 2. UPS spectra of (a) HOMO and (b) SECO region before and after air exposure, respectively.

[1] T. Chiba *et al*., Org. Electron. **12** (2011) 710.
[2] Y. K. Kim *et al*., Appl. Phys. Lett. **94** (2009) 06330.
[3] H. Kang *et al*., J. Korean Phys. Soc. **59** (2011) 3205.

BL8B

Structural Requirements for the Charge-Transfer State Formation through Surface-Induced Aromatic Stabilization

T. Hosokai[1], K. Yonezawa[2], K. Kato[2], R. Makino[2], K. R. Koswattage[2], N. Ueno[2] and S. Kera[2]
[1]*Department of Materials Science and Technology, Iwate University, Morioka 020-8551, Japan*
[2]*Graduate School of Advanced Integration Science, Chiba 263-8522, Japan*

Recently Heimel *et al.* and we found a new phenomenon occurred at π-conjugated organic molecules/noble metal interfaces, i.e., surface-induced aromatic stabilization (SIAS), and succeeded to explain a mechanism leading to a formation of charge-transfer (CT) states at the interfaces [1]. However, there still remain questions on the condition inducing SIAS. Here, we investigated a role of chemical structure on the SIAS by employing three kinds of polycyclic aromatic molecules, diindenoperylene (DIP: $C_{32}H_{16}$), perylene ($C_{20}H_{12}$) and picene ($C_{22}H_{14}$), and angle-resolved ultraviolet photoelectron spectroscopy (UPS).

Figures 1(a) ~ 1(c) show the UPS results of DIP-monolayer (ML) on highly oriented pyrolytic graphite (HOPG), Ag(111) and Cu(111), perylene-ML on those substrates, and picene-ML and multlayer on Cu(111), respectively. All the measurements were performed at 295 K with the geometry illustrated in Fig. 1(d). The DIP (and perylene)/HOPG systems and the picene multilayer were measured for the reference of electronic structure at their physisorption, respectively. A lying-flat orientation was confirmed for all the monolayer systems by angular-dependence of photoelectron intensities (not shown). It is clear in Fig. 1(a) that DIP on Ag(111) and Cu(111) shows gap states (bold arrows), while other molecules do not (see Figs. 1(b) and 1(c)). As we discussed for DIP/Ag(poly) and Cu(poly) systems [2], the observed gap states for the DIP/Ag(111) and Cu(111) systems are attributed to CT states through SIAS due to electron transfers to the lowest unoccupied molecular orbital (LUMO) of the DIP monolayer from the substrates.

According to Ref. [1], the formation of CT states through SIAS requires a formation of *resonance state* of the adsorbate molecules; the resonance state brought by a site-specific substrate-molecule interaction reduces the LUMO binding energy, and results in the CT. As shown in Figs. 2(a) and 2(b), the DIP could have such a state, while its mother molecule, perylene, does not because, otherwise, two radicals remain at the center. However, as seen in Fig. 2(c) picene can also be drawn the entire resonance structure, although no CT state is observed in UPS (Fig. 1(c)). To ensure this, further experiments together with a theoretical calculation are strongly required.

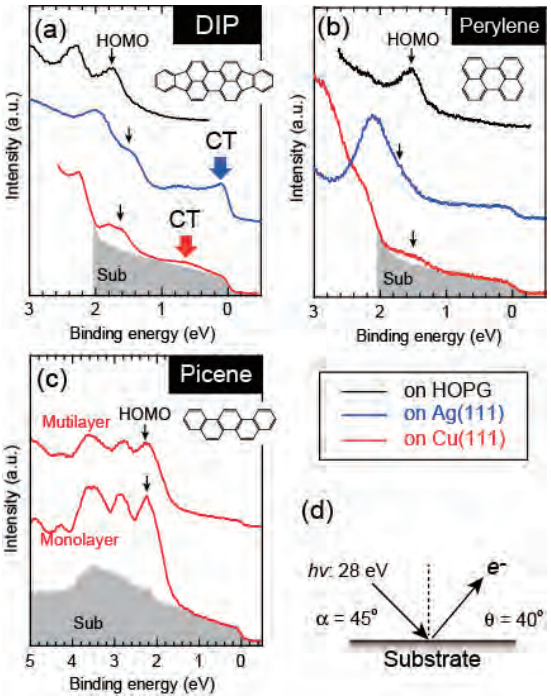

Fig. 1. Valence band structure of DIP-ML (a), perylene-ML (b), and picene-ML and -multilayer (c). Their chemical structure is depicted in each graph. The thin black arrows indicate the position of the highest-occupied molecular orbitals (HOMO). (d) The schematic at bottom right-hand side is the measurement geometry.

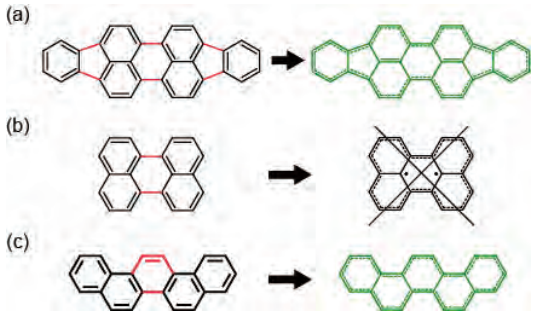

Fig. 2. A sketch of a resonance structure of DIP (a), perylene (b), and picene (c). All the molecules are connected with benzene and/or naphthalene rings (left, black lines).

[1] G. Heimel, *et al.*, Nature Chem. **5** (2013) 187.
[2] T. Hosokai, *et al.*, MRS proceedings, 1647 (2014) mrsf13-1647-gg01-03.

Ⅲ-5

Life, Earth and Planetary Sciences

BL2A

Mo L_{III}-Edge XANES Study of Active Mo Species on H-GaAlMFI Catalysts for Methane Dehydroaromatization

H. Aritani[1], T. Sugawara[1], N. Naijo[1], S. Mogi[1], Y. Takayama[1] and A. Nakahira[2]
[1]*Department of Life Science & Green Chemistry, Saitama Institute of Technology, Fukaya 369-0293 Japan*
[2]*Graduate School of Engineering, Osaka Prefecture University, Sakai 599-8531 Japan*

MoO_3-modified H-MFI (Mo/H-MFI) is a typical catalyst for methane dehydroaromatization, which is an important reaction for direct GTL (Gas to Liquid) processes. Many workers revealed that MoO_3-modified H-MFI zeolite (SiO_2/Al_2O_3=28-40) shows catalytically high activity for MTB (Methane to Benzene) reaction, which is so-called methane dehydroaromatization. The unique activity is based on strong acidity and sieving effects onto MFI zeolite support. During the reaction, MoO_x species must be reduced and carbonized to form carbide-like species (MoC_xO_y). But catalytic deactivation is brought about at the same tome by carbon contamination on MFI. Because the deactivation strongly depend on the strong acidity on H-MFI, an improvement of surface property onto H-MFI is called for. In our recent study, Ga-containing H-MFI (GaAl-MFI) supports have been synthesized hydrothermally,[1] and Mo-modified GaAl-MFI catalysts have been applied to employ the methane dehydroaromatization. By partially substitution of Ga ions onto H-MFI framework (Ga/Al=50-100), the strong acidity is slightly suppressed. The effect of Ga ion onto H-MFI, highly active and durable catalysts can be expected. In the present report, Mo L_{III}-edge XANES study is applied to characterize the Ga incorporation or surface modification onto Mo/H-MFI to evaluate the active Mo species after the MTB reaction.

Catalysts were prepared by impregnation of H-GaAlMFI support with $MoO_2(acac)_2$–$CHCl_3$ solution, and followed by drying overnight and calcination at 773 K for 3 h. The amount of MoO_3-loading is 5.0 wt% in this study. H-GaAlMFI supports were synthesized hydrothermally at 413 K for a week, and followed by ion-exchanging with NH_4Cl and calcination at 873 K. The catalytic activity of methane dehydroaromatization was evaluated by means of fixed bed flow reaction, as described in a separate paper [2]. The Ga-incorporated catalyst samples are denoted as Mo/GaMFI*n*, in which *n*=Si/Al_2 atomic ratios. The Ga-modified ones (in extraframework) are denorted as Mo/Ga/MFI*n*. Mo L_{III}-edge XANES spectra were measured in BL2A of UVSOR-IMS in a total-electron yield mode using InSb double-crystal monochromator. Photon energy was calibrated by using Mo metal-foil at Mo L_{III}-edge, and normalized XANES spectra and their second derivatives are presented. REX-2000 (Rigaku) software was used by normalization of each XANES spectrum.

Figure 1 shows the Ga-incorporated or modified Mo/MFI28 (upper). By Ga modification, edge energy of XANES becomes lower, suggesting the promotion of Mo reduction to form Mo_2C species. In case of Mo/MFI56 catalysts (Fig. 1, lower), similar feature of the results can be shown. But Mo/GaMFI in Mo/Ga=50-100 catalysts only enhance the catalytic MTB activity by Ga incorpotration. It is likely the modified Mo species are only present on MFI extraframework, and thus, Ga incorporation brings about the both inhibition of acidity and reduction of Mo species. Ga modification gives similar effect only for Mo species on MFI, but the acid site is poisoned. Thus the catalytic activity becomes lower.

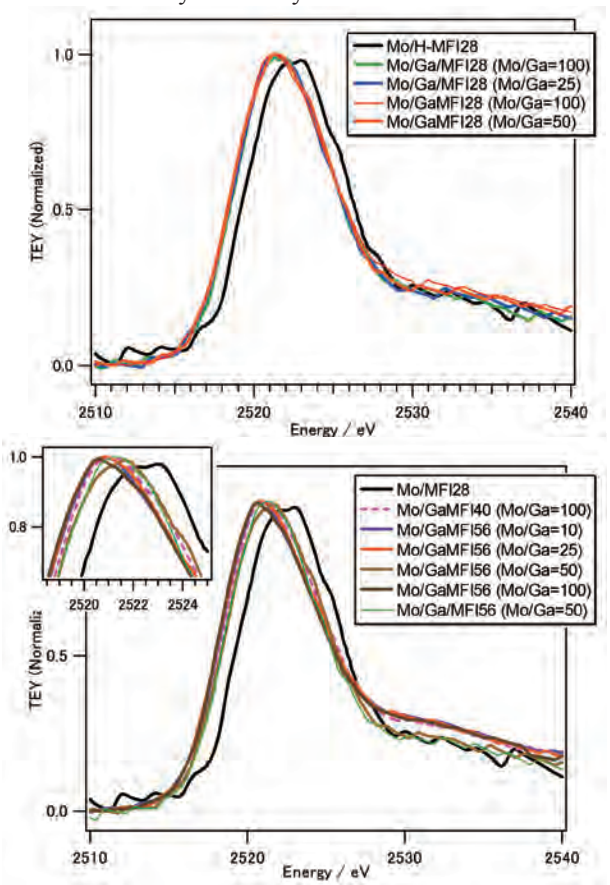

Fig. 1. Mo L_{III}-edge XANES of Ga- incorporated or modified Mo/MFI28 (upper) and Mo/MFI56 (lower) catalysts after MTB reaction at 1023 K.

[1] K. Nagashima, S. Nakamura, K. Okada, A. Nakahira and H. Aritani, Bull. Chem. Soc. Jpn., **82** (2009) 1203.
[2] H. Aritani, H. Shibasaki, H. Orihara and A. Nakahira, J. Environm. Sci. **21** (2009) 736.

BL4U

Uptake of Dexamethasone into Human Skin Investigated by Soft X-Ray Spectromicroscopy

R. Flesch[1], T. Ohigashi[2], S. Küchler[3], K. Yamamoto[1], S. Ahlberg[4], F. Rancan[4], A. Vogt[4], U. Blume-Peytavi[4], P. Schrade[5], S. Bachmann[5], M. Schäfer-Korting[3], N. Kosugi[2] and E. Rühl[1]

[1]*Physical Chemistry, Freie Universität Berlin, Takustr. 3, 14195 Berlin, Germany*
[2]*UVSOR Facility, Institute for Molecular Science, Okazaki 444-8585, Japan*
[3]*Institut für Pharmazie, Freie Universität Berlin, 14195 Berlin, Germany*
[4]*Charité Universitätsmedizin, 10117 Berlin, Germany*
[5]*Abteilung für Elektronenmikroskopie at CVK, 13353 Berlin, Germany*

The uptake of drugs, such as dexamethasone, topically applied onto human skin is investigated by soft X-ray spectromicroscopy. Dexamethasone is a widely used for the treatment of inflammatory skin diseases such as atopic dermatitis. It is aimed to study the depth profile of dexamethasone, so that specific information on the uptake process is derived. Dexamethasone was dissolved in ethanol and this 0.5% solution was applied onto the skin sample for 4 h. Subsequently, the sample was fixed and sliced into 300 nm thick sections.

The experiments were performed at the BL4U beamline at UVSOR III using a scanning X-ray microscope (STXM) [1]. Chemical selectivity is obtained from excitation at the O 1s-edge (525-560 eV). Figure 1 shows a comparison of the O 1s-absoption of fixed human skin and dexamethasone. Both spectra are similar in shape, showing an intense O 1s→ π* resonance dominating the pre-edge regime. This resonance occurs at slightly lower energy in dexamethasone (E=530.5 eV) than in skin (E=532.2 eV), providing chemical selectivity for probing the drug uptake into skin.

Figure 2 shows a comparison of a skin sample exposed to dexamethasone probed by optical microscopy and soft X-ray microscopy. Figure 2(a) clearly shows the layered structure of the stratum corneum, the outermost skin layer, probed by optical microscopy. It is followed by the viable epidermis and the dermis. Figure 2(b) shows for the same section of the skin sample the spatial distribution of absorption, which is obtained from a difference image in X-ray absorption measured at 528 eV (pre-edge regime) and on the O 1s→π*-transition (530.5 eV) of dexamethasone (cf. Fig. 1) providing chemical selectivity. The spatially resolved results indicate that highest absorption contrast is found in the stratum corneum, as indicated by red color. In contrast, lower concentration is observed in the viable epidermis and no change in absorption contrast occurs in the dermis. It is also evident that the cells nuclei in the viable epidermis (circular structures in Fig. 2(a)) do not show any evidence for drug uptake.

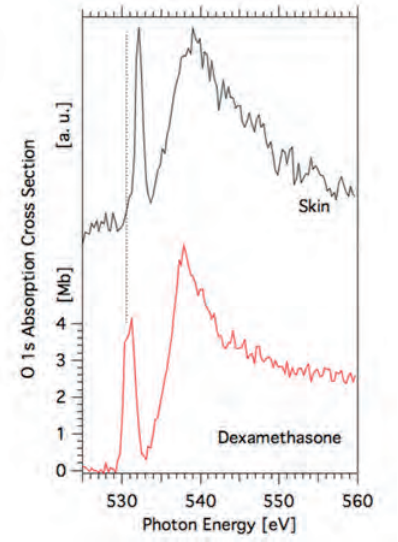

Fig. 1. O 1s excitation of fixed human skin (black curve) and dexamethasone (red curve).

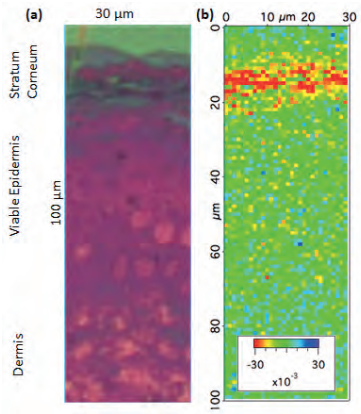

Fig. 2. (a) optical microscopy image of human skin; (b) spatial distribution of dexamethasone in the same skin section, as shown in (a). See text for further details.

[1] T. Ohigashi, H. Arai, T. Araki, N. Kondo, E. Shigemasa, A. Ito, N. Kosugi and M. Katoh, J. Phys. Conf. Ser. **463** (2013) 012006.

BL4U

Nanoscale Analysis of Microbe-Mineral Interface in Bioleaching Process by STXM Technique

S. Mitsunobu[1], S. Ming[1], H. Makita[2] and T. Ohigashi[3]
[1]*Institute for Environmental Sciences, University of Shizuoka, Shizuoka 422-8526, Japan*
[2]*Japan Agency for Marine-Earth Science and Technology (JAMSTEC), Yokosuka 237-0061, Japan*
[3]*UVSOR Facility, Institute for Molecular Science, Okazaki 444-8585, Japan*

Some kind of microbe can dissolve and leach "solid mineral" to obtain life energy from the solid phase. This biotic leaching rate of minerals is much fast compared with its abiotic leaching rate [1]. Accordingly, the bacterial mineral leaching is recently used as a save-cost and save-energy technique for extracting metals (eg., Cu, Ni, Zn) from sulfide ores such as pyrite [2]. Previous papers imply that the microbes would produce some powerful extracellular substances to promote dissolution of the minerals effectively. On the other hand, the leaching of sulfide minerals leads to the formation of acid mine drainage. It is also important subject to understand the bioleaching process from a viewpoint of environmental sciences. However, little is known about the interfacial process at mineral-bacteria interface leading to the degradation of metal sulfides, because the interface is microscopic region and it is difficult to analyze it directly.

Here, we have tried to analyze the extracellular substances in bacteria-mineral interface in pyrite (FeS_2) bioleaching with a high spatial resolution by scanning transmission X-ray microscopy (STXM) installed at UVSOR BL4U, where is the first STXM beamline in Japanese synchrotron facilities. In this study, powdered natural pyrite (Navajún mine, Spain) and *Acidithiobacillus ferrooxidans* (JCM 7812 and ATCC 23270) were used for the sulfide mineral and leaching bacteria, respectively. The acidophilic, iron(II)-oxidizing bacteria *A. ferrooxidans* is one of the most important mesophiles for the extraction of metals from sulfidic ores by the bioleaching [1-2]. Samples for the STXM analysis were collected after 30 days incubation. The sample was dropped on Si_3N_4 membrane and air-dried at RT.

Figure 1 shows STXM images of *A. ferrooxidans* cells accreted on the pyrite particle for oxygen (O) and nitrogen (N). Characterization of extracellular matter in the bacteria-mineral interface was performed by near edge X-ray absorption fine structure (NEXAFS) at the O K-edge (Fig. 2). Features around the absorption edge and post-edge of lipid, DNA, sugar, and protein clearly varied. Spectral features of *A. ferrooxidans* cell are mostly similar to those of alginate and albumin representative for sugar and protein, respectively. Thus, O NEXAFS results indicate that *A. ferrooxidans* forms the extracellular substances on the pyrite surface containing the sugar such as polysaccharide addition to the protein, which was also supported by N NEXAFS and lectin-staining results (data not shown). The biogenic polysaccharides often form a strong complex with Fe ion under wide pH region [3-4]. Thus, our findings imply that *A. ferrooxidans* could produce the polysaccharides to accelerate the dissolution of pyrite and/or mediate contact between the cell and pyrite surface.

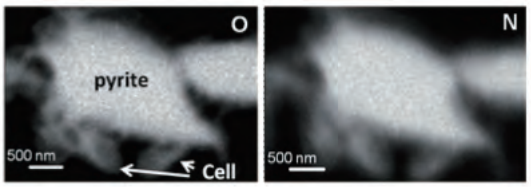

Fig. 1. STXM-derived elemental maps for oxygen (550 eV) and nitrogen (410 eV) of cells and surrounding pyrite particles.

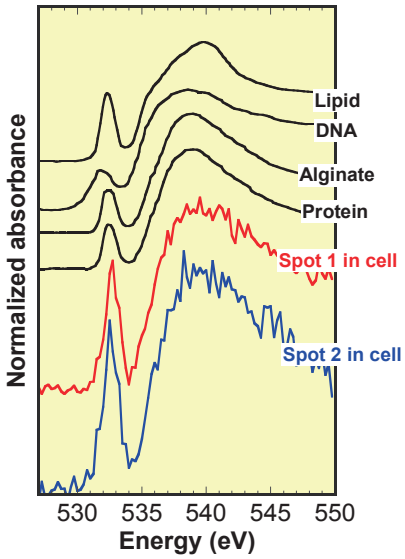

Fig. 2. STXM-based oxygen 1s NEXAFS spectra of standards and samples. Standards contain bovine serum albumin (protein), alginate (acidic polysaccharide), *E. coli* DNA and 1,2-dipalmitoyl-sn-glycero-3-phospho ethanolamine (lipid).

[1] H. Tributsch, Hydrometallurgy **59** (2001) 177.
[2] W. Sand *et al.*, Appl. Environ. Microbiol. **58** (1992) 85.
[3] C. Chan *et al.*, Geochim. Cosmochim. Acta **73** (2009) 3807.
[4] S. Mitsunobu *et al.*, Environ. Sci. Technol. **46** (2012) 3304.

BL4U

Observation of DNA and Protein Distributions in Mammalian Cell Nuclei Using STXM

T. Ohigashi[1,2], A. Ito[1,3], K. Shinohara[3,4], S. Tone[5], M. Kado[4], Y. Inagaki[1], Y. F. Wang[1] and N. Kosugi[1,2]

[1]*UVSOR Facility, Institute for Molecular Science, Okazaki 444-8585, Japan*
[2]*The Graduate University for Advanced Studies (SOKENDAI), Okazaki 444-8585, Japan*
[3]*Tokai University, Hiratsuka 259-1292, Japan*
[4]*Japan Atomic Energy Agency, Kizugawa 619-0215, Japan*
[5]*Kawasaki Medical School, Kurashiki 701-0192, Japan*

To observe the structure of biological samples, an electron microscope and a fluorescence microscope are extensively used. However, the former requires specimen in vacuum and the latter has relatively lower spatial resolution. Moreover, the electron microscope usually requires several preparation processes for the samples, such as fixing, slicing and staining. On the other hand, a soft X-ray microscopy is applicable to relatively thick specimen even under hydrated condition at high resolution, and is expected to be complementary to these two types of microscopes. A scanning transmission X-ray microscope (STXM) must be a powerful tool for this purpose [1]. The STXM has high spatial resolution, high transmittance and lower radiation damage than the electron beam. Especially, chemical analysis combined with near edge X-ray absorption fine structure (NEXAFS) enables us to obtain 2-dimensional chemical information of the sample [2]. In this study, nuclei of cultured human cells were observed with the STXM installed on UVSOR BL4U to image the distributions of DNA and protein separately.

NEXAFS spectra of the DNA and histone, a nuclear protein, were measured by the STXM as reference data. Their suspensions were dropped onto 100 nm-thick silicon nitride membranes and were dried in the air. Their NEXAFS spectra around nitrogen 1s are shown in Fig. 1. In these spectra, a remarkable feature to discriminate the DNA from the protein is seen on a peak at 400.8 eV as nitrogen 1s→π* resonance arising from C=N double bonds in the DNA.

Human A549 cells derived from lung cancer were cultured directly on the silicon nitride membrane, fixed with glutaraldehyde, and dried in the air. The sample was placed in the STXM chamber, which was then evacuated and was filled by helium to 30 mbar. The 51 X-ray transmission images (an energy stack) were acquired with changing the X-ray energies from 399 to 404 eV. The dwell time and the scanning pitch of the specimen were 5 ms and 0.2 μm step, respectively. The reference spectra of the DNA and the histone in Fig. 1 were fitted to the energy stack by using aXis2000 software [3] and their distributions are shown in Fig. 2. Figures 2 (a) and (b) show distributions of the DNA and the histone (protein), respectively. Figure 2 (c) shows the distribution of constant profile with no spectral feature, suggesting that in the nucleolus molecules other than the DNA and/or the histone (protein) are densely accumulated. The results show that the DNA was distributed over the nucleus, while the histone was poorly distributed in the nucleolus. Considering that RNA is rich in the nucleolus, the RNA may be present with less protein in the nucleolus.

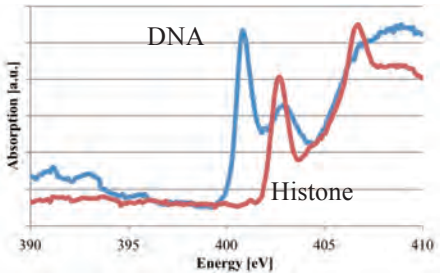

Fig. 1. X-ray absorption spectra of the DNA and the histone (protein) around nitrogen 1s resonance.

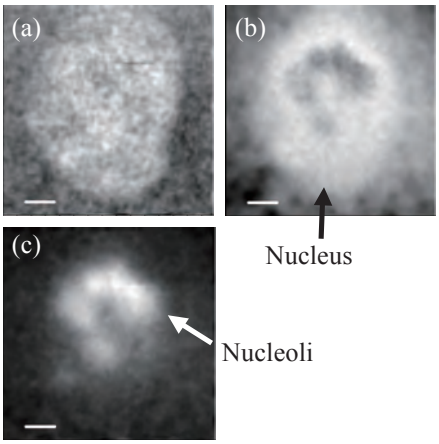

Fig. 2. Distributions of the DNA (a), the histone (protein) (b) and constant (c) in the cell. Bright color shows high density. Scale bars are 2 μm.

[1] J. Kirz *et al*., Nucl. Instr. and Meth. B **87** (1994) 92-27.
[2] T. Ohigashi *et al*., J. Phys. Conf. Ser. **463** (2013) 012006.
[3] http://unicorn.mcmaster.ca/aXis2000.html

BL4U

Nitrogen- and Oxygen-XANES Spectral Analysis of Mineral Olivine and Organic Material from Meteorite: Preliminary Measurements for Implementation Planning of a Synchrotron Cosmochemistry Research Base at UVSOR BL4U

H. Yabuta

Department of Earth and Space Science, Osaka University, Osaka 560-0043, Japan

The PI has eight years of experiences of a scanning transmission x-ray microscope (STXM) operations and analyses in cosmo- and geochemistry [e.g., 1-3]. Making great use of her experiences, she is planning to construct a synchrotron cosmochemistry research base at BL4U, UVSOR, under cooperation with a beamline manager. Because of the first use of the STXM (Bruker) built at BL4U, UVSOR, this year, the initial purpose of this study was to acquire the operation of the STXM and to confirm the reproducibility of the STXM measurements of organic materials from meteorites. However, unfortunately, it was impossible to measure Carbon K-edge XANES spectra, due to a bad condition of the STXM stage motions and contamination of the mirror. This report summarizes the preliminary result of Nitrogen and Oxygen K-edge XANES.

As samples, mineral olivine (magnesium iron silicate) and acid-insoluble organic solids (IOM) isolated from carbonaceous meteorite Asuka 881458 were used. Thin sections (100 nm thickness) of the individual samples were prepared by a focused ion beam (FIB) - scanning electron microscope (SEM). FIB sections of olivine Nos. 1 and 2 were prepared before and after that of IOM was prepared, respectively. Nitrogen- and Oxygen-X-ray absorption near edge structure (XANES) spectra of the FIB sections were acquired using a scanning transmission x-ray microscope (STXM) at the BL 4U, UVSOR.

Nitrogen- and Oxygen-XANES spectra of olivine (Nos. 1 and 2) and IOM are shown in Fig. 1. O-XANES spectrum of meteorite Asuka (A) 881458 IOM exhibits a peak of organic carbonyl group (C=O) at 532 eV. This peak was not identified from the O-XANES spectra of olivine samples 1 and 2, demonstrating that the previous sample did not contaminate the latter sample during the FIB procedures. Likewise, N-XANES spectrum of meteorite Asuka (A) 881458 IOM exhibits absorption peaks of organic imine (C=N), nitrile (C≡N), and amide (NHx(C=O)C) groups at 399, 400, 402 eV, respectively, while those of olivine samples 1 and 2 do not.

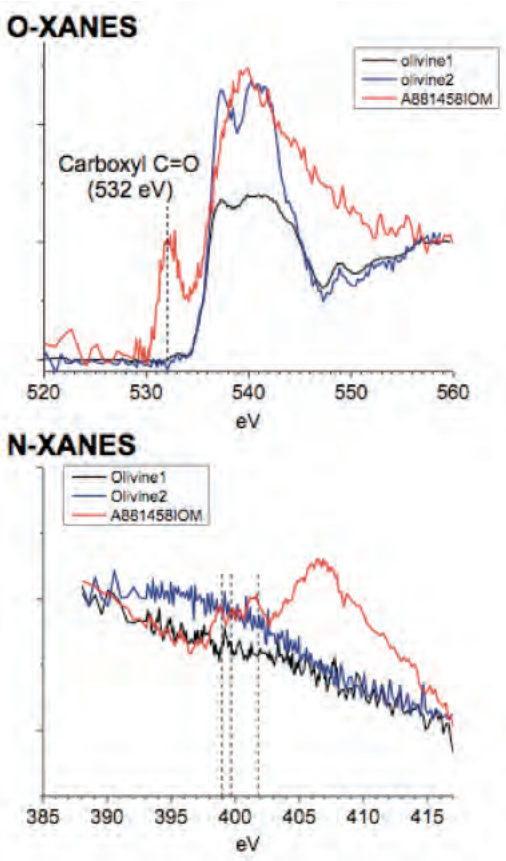

Fig. 1. N- and O-XANES spectra of mineral olivine samples Nos. 1 (black) and 2 (blue) and acid-insoluble organic solids isolated from carbonaceous meteorite Asuka (A) 881458 (red).

[1] S. A. Sandford *et al.,* Science **314** (2006) 1720-1724.
[2] G. D. Cody *et al.,* Meteoritics & Planetary Science **43** (2008) 353 – 365.
[3] H. Yabuta *et al.,* The 44th Lunar and Planetary Science Conference. Abstract (2013) #2335.

BL4U

Organelle-Spectra of a Leydig Cell in Cultural Fluid

T. Ejima[1], R. Hirose[1], M. Ishino[2], M. Kado[2], M. Aoyama[3], K. Yasuda[3] and T. Tamotsu[3]
[1]*IMRAM, Tohoku University, Sendai 980-8577, Japan*
[2]*Japan Atomic Energy Agency, Kizugawa 619-0215, Japan*
[3]*Dept. of Biological Sciences, Fac. of Science, Nara Women's University, Nara 630-8263, Japan*

To investigate suitable wavelength for observing organelles in a bio-cell with fluid in Water-window wavelength region, contrast of each organelle in a bio-cell to fluid or the other organelles will be determined by absorption spectra of each component. For this purpose, soft X-ray absorption images of Leydig cells in cultural fluid were observed controlling the thickness of the fluid. Spectra of both organelles and fluid will be obtained from the images that irradiate wavelength was changed.

At first, Leydig cells of mouse testes cultured and fixed on a SiN membrane were preserved in the cultural fluid during the X-ray observation. Thickness of the cultural fluid was controlled by a SU8 film deposited around the membrane. The membrane with the bio-cells was placed in a holder and the holder was set to the stage under He atmosphere to avoid leak of the fluid during the observation. The observation was made at 2.9～3.1nm (395～430eV) wavelength region under the conditions that the step width was 300nm, exposure time, 5 msec/pixel, and wavelength resolution λ/Δλ, 5000.

Organelle structures in a cell and spectra corresponding to the structures were obtained applying PCA and Cluster analyses to the observation results [1]. Figure 1 (a) shows an eigen-image that shows maximum value of the contribution ratio obtained from the PCA analysis. The eigen-image represents that several large organelles exist in the star-shaped bio-cell and many dot-structures are around the large organelles.

According to Cluster analysis, these organelles are categorized by the degree of similarity as the map represented in Fig. 1 (b). In the map, blue area represents the culture fluid and the other areas, a bio-cell and organelles in the cell.

Figure 1 (c) shows that the absorption spectrum that corresponds to the yellow area of Fig. 1(b). In the spectrum, there is a sharp peak at 400eV and a broad peak with a shoulder structure at 405 eV. In addition, small structures exist at 398 eV, 402 eV, and 404 eV. The sharp peak at 400 eV and the broad one at 405 eV should be originated from the π* and σ* structures, respectively, of C-N bonds in the organelles [2]. Small and shoulder structures will be satellite structures of C-N bonds and the details of the origin need further investigation.

Small organelles such as dot structures in Fig. 1(a) are recognized in the eigen-images, but the spectra of the small orgranelles are not clearly separated from the other organelles. The experimental conditions and image-analysis techniques will be improved.

This work was supported by JSPS KAKENHI Grant Numbers 23241038 and by Nanotechnology Platform Program (S-13-MS-1002) of MEXT, Japan.

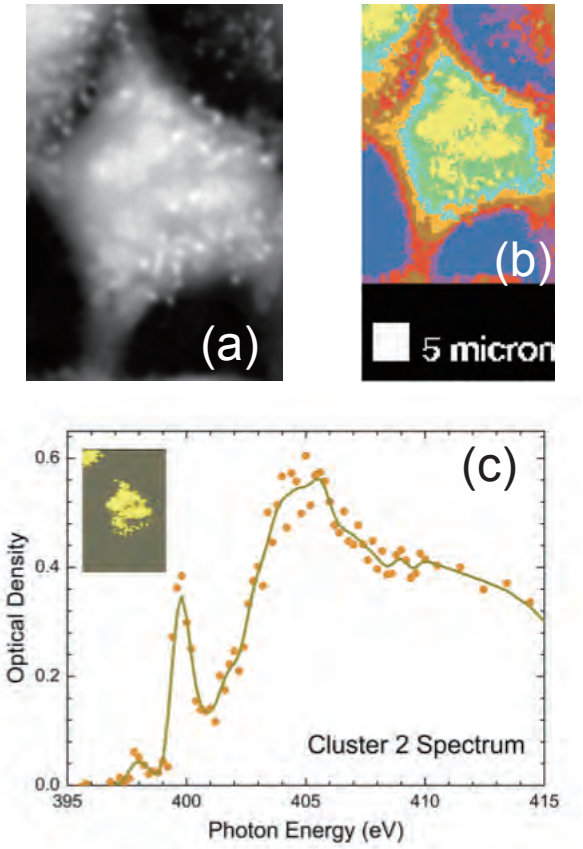

Fig. 1. (a) Optical density image of a Leydig cell. (b) Clusters obtained from cluster analysis on the basis of the results of PCA analysis. (c) Optical density spectrum of the yellow area represented in (b) (inset).

[1] M. Lerotic, C. Jacobsen, J. B and Gillow, A. J. Francis, S. Wirick, S. Vogt and J. Maser, J. Elec. Spectro. Rel. Phenom. **144-147** (2005) 1137-1143.
[2] Y. Zubavichus, A. Shaporenko, V. Korolkov, M. Grunze and M. Zharnikov, J. Phys. Chem. B **112** (2008) 13711-13716.

Ⅳ

List of Publications

List of Publications

K. Fukui, R. Ikematsu, Y. Imoto, M. Kitaura, K. Nakagawa, T. Ejima, E. Nakamura, M. Sakai, M. Hasumotoe and S. Kimura, **"Design and Performance of a New VIS_VUV Photoluminescence Beamline at UVSOR-III",** J. Sync. Rad. **21** (2014).

Q. Ge, H. C. Xu, X. P. Shen, M. Xia, B. P. Xie, F. Chen, Y. Zhang, R. Kato, T. Tsumuraya, T. Miyazaki, M. Matsunami, S. Kimura and D. L. Feng, **"Angle-Resolved Photoemission Study of the Electronic Structure of the Quantum Spin Liquid $EtMe_3Sb[Pd(dmit)_2]_2$",** Phys. Rev. B **89** (2014) 075105.

Y. Hikosaka, M. Sawa, K. Soejima and E. Shigemasa **"A High-Resolution Magnetic Bottle Electron Spectrometer and Its Application to a Photoelectron_Auger Electron Coincidence Measurement of the $L_{2,3}VV$ Auger Decay in CS_2",** J. Electron Spectrosc. Rel. Phenom. **192** (2014) 69.

H. J. Im, M. Tsunekawa, T. Sakurada, M. Iwataki, K. Kawata, T. Watanabe, K. Takegahara, H. Miyazaki, M. Matsunami, T. Hajiri and S. Kimura, **"Strong Correlation Effects in the A-Site Ordered Perovskite $CaCu_3Ti_4O_{12}$ Revealed by Angle-Resolved Photoemission Spectroscopy",** Phys. Rev. B **88** (2013) 205133.

T. Inushima, Y. Ota and H. Shiomi, **"Evolution of the Impurity Band to Diamond-Like Valence Bands in Boron Doped Diamond",** J. Phys. Soc. Jpn. **83** (2014) 024715.

R. Ishikawa, R. Kano, T. Bando, Y. Suematsu, S. Ishikawa, M. Kubo, N. Narukage, H. Hara, S. Tsuneta, H. Watanabe, K. Ichimoto, K. Aoki and K. Miyagawa, **"Birefringence of Magnesium Fluoride in the Vacuum Ultraviolet and Application to a Half-Waveplate",** Applied Optics **52** (2013) 8205.

T. Kawai, S. Nagata and T. Hirai, **"Comparison of Luminescence Properties of CsI Crystals Activated with Ag^-, Au^-, and Tl^+ Ions at Room Temperature",** Jpan. J. Appl. Phys. **52** (2013) 082401.

B. Kim, P. Kim, W. Jung, Y. Kim, Y. Koh, W. Kyung, J. Park, M. Matsunami, S. Kimura, J. S. Kim, J. H. Han and C. Kim, **"Microscopic Mechanism for Asymmetric Charge Distribution in Rashba-Type Surface States and the Origin of the Energy Splitting Scale",** Phys. Rev. B **88** (2013) 205408.

M. Kitaura, S. Watanabe, K. Ogasarawa, A. Ohnishi and M. Sasaki, **"Comparative Study of Auger-Free Luminescence of Rb_2ZnCl_4 Crystals between Experiment and Calculation",** Phys. Status Solidi C **10** (2013) 993.

M. Kitaura, A. Sato, K. Kamada, A. Ohnishi and M. Sasaki, **"Phosphorescence of Ce-Doped $Gd_3Al_2Ga_3O_{12}$ Crystals Studied Using Luminescence Spectroscopy",** J. Appl. Phys. **115** (2014) 083517.

S. Kuwano-Nakatani, Y. H. Han, T. Takahashi and T. Awano **"Broadband Spectroscopy of Nanoporous-Gold Promoter",** Advanced Electromagnetics **2** (2013) 5.

M. Matsunami, T. Hajiri, H. Miyazaki, M. Kosaka and S. Kimura, **"Strongly Hybridized Electronic Structure of $YbAl_2$: An Angle-Resolved Photoemission Study"**, Phys. Rev. B **87** (2013) 165141.

B. H. Min, J. B. Hong, J. H. Yun, T. Iizuka, S. Kimura, Y. Bang and Y. S. Kwon, **"Optical Properties of the Iron-Based Superconductor LiFeAs Single Crystal",** New J. Phys. **15** (2013) 073029.

T. Miyazaki, Y. Tokumoto, R. Sumii, H. Yagi, N. Izumi, H. Shinohara and S. Hino, **"Photoelectron**

Spectra of Thulium Atoms Encapsulated C_{82} Fullerene, $Tm_2@C_{82}$ (III) and $Tm_2C_2@C_{82}$ (III)", Chem. Phys. **431_432** (2014) 47.

H. Murata, T. Taniguchi, S. Hishita, T. Yamamoto, F. Oba and I. Tanaka , **"Local Environment of Silicon in Cubic Boron Nitride",** J. Appl. Phys. **114** (2013) 233502.

M. Nagasaka, H. Yuzawa, T. Horigome, A. P. Hitchcock and N. Kosugi, **"Electrochemical Reaction of Aqueous Iron Sulfate Solutions Studied by Fe L-Edge Soft X-Ray Absorption Spectroscopy",** J. Phys. Chem. C **117** (2013) 16343.

S. Nagata, T. Kawai and T. Hirai, **"Energy Transfer from CsI Host Lattice to Ag^- Centers in CsI:Ag^- Crystals",** Optical Materials **35** (2013) 1257.

H. Nishino, M. Hosaka, M. Katoh and Y. Inoue **"Photoreaction of *rac*-Leucine in Ice by Circularly Polarized Synchrotron Radiation: Temperature-Induced Mechanism Switching from Norrish Type II to Deamination",** Chem. Eur. J. **19** (2013) 13929.

T. Ohigashi, H. Arai, T. Araki, N. Kondo, E. Shigemasa, A. Ito, N. Kosugi and M. Katoh **"Construction of the Scanning Transmission X-Ray Microscope Beamline at UVSOR",** J. Phys.: Conference Series **463** (2013) 012006.

M. N. Piancastelli, R. Guillemin, M. Simon, H. Iwayama and E. Shigemasa, **"Ultrafast Dynamics in C 1*s* Core-Excited CF_4 Revealed by Two-Dimensional Resonant Auger Spectroscopy",** J. Chem. Phys. **138** (2013) 234305.

A. Ruammaitree, H. Nakahara, K. Akimoto, K. Soda and Y. Saito, **"Determination of Non-Uniform Graphene Thickness on SiC (0001) by X-Ray Diffraction",** Appl. Surface Sci. **282** (2013) 297.

T. Saito, K. Ozaki, K. Fukui, H. Iwai, K. Yamamoto, H. Miyake and K. Hiramatsu, **"Vacuum Ultraviolet Ellipsometer Using Inclined Detector as Analyzer to Measure Stokes Parameters and Optical Constants — With Results for AlN Optical Constants",** Thin Solid Films, Available online 12 March 2014.

T. Sato, Y. Tanaka, K. Nakayama, S. Souma, T. Takahashi, S. Sasaki, Z. Ren, A. A. Taskin, K. Segawa and Y. Ando, **"Fermiology of the Strongly Spin-Orbit Coupled Superconductor $Sn_{1-x}In_xTe$: Implications for Topological Superconductor",** Phys. Rev. Lett. **110** (2013) 206804.

A. Satoh, M. Kitaura, K. Kamada, A. Ohnishi, M. Sasaki and K. Hara, **"Time-Resolved Photoluminescence Spectroscopy of Ce:$Gd_3Al_2Ga_3O_{12}$ Crystals",** Jpn. J. Appl. Phys. **53** (2014) 05FK01.

E. Shigemasa, M. Nagasono, H. Iwayama, J. R. Harries and L. Ishikawa (Okihara), **"Resonance-Enhanced Three-Photon Single Ionization of Ne by Ultrashort Extreme-Ultraviolet Pulses",** J. Phys. B:At Mol. Opt. Phys. **46** (2013) 164020.

S. B. Singh, Y. F. Wang, Y. C. Shao, H. Y. Lai, S. H. Hsieh, M. V. Limaye, C. H. Chuang, H. C. Hsueh, H. Wang, J. W. Chiou, H. M. Tsai, C. W. Pao, C. H. Chen, H. J. Lin, J. F. Lee, C. T. Wu, J. J. Wu, W. F. Pong, T. Ohigashi, N. Kosugi, J. Wang, J. Zhou, T. Regier and T. K. Sham, **"Observation of the Origin of d^0 Magnetism in ZnO Nanostructures Using X-Ray-Based Microscopic and Spectroscopic Techniques"**, Nanoscale **6** (2014) 9166.

S. Suga, K. Sakamoto, T. Okuda, K. Miyamoto, K. Kuroda, A. Sekiyama, J. Yamaguchi, H. Fujiwara, A. Irizawa, T. Ito, S. Kimura, T. Balashov, W. Wulfhekel, S. Yeo, F. Iga and S. Imada, **"Spin-Polarized Angle-Resolved Photoelectron Spectroscopy of the So-Predicted Kondo Topological Insulator SmB_6",** J. Phys. Soc. Jpn. **83** (2014) 014705.

Y. Sugizaki, S. Ishida, Y. Kakefuda, K. Edamoto, M. Matsunami, T. Hajiri and S. Kimura, **"Soft X-Ray Photoelectron Spectroscopy Study of $Fe_2P(0001)$",** Surf. Sci. **624** (2014) 21.

S. Tanaka, M. Matsunami and S. Kimura, **"An Investigation of Electron-Phonon Coupling Via Phonon Dispersion Measurements in Graphite Using Angle-Resolved Photoelectron Spectroscopy ",** Nature Sci. Rep. **3** (2013) 03031.

Y. Tanaka, T. Shoman, K. Nakayama, S. Souma, T. Sato, T. Takahashi, M. Novak, K. Segawa and Y. Ando, **"Two Types of Dirac-Cone Surface States on the (111) Surface of the Topological Crystalline Insulator SnTe",** Phys. Rev. B **88** (2013) 235126.

J. Yamaguchi, A. Sekiyama, M. Y. Kimura, H. Sugiyama, Y. Tomida, G. Funabashi, S. Komori, T. Balashov, W. Wulfhekel, T. Ito, S. Kimura, A. Higashiya, K. Tamasaku, M. Yabashi, T. Ishikawa, S. Yeo, S. I. Lee, F. Iga, T. Takabatake and S. Suga, **"Different Evolution of the Intrinsic Gap in Strongly Correlated SmB_6 in Contrast to YbB_{12}",** New J. Phys. **15** (2013) 043042.

H. Yamane and N. Kosugi, **"Substituent-Induced Intermolecular Interaction in Organic Crystals Revealed by Precise Band-Dispersion Measurements",** Phys. Rev. Lett. **111** (2013) 086602.

〔in Japanese〕

K. Nakagawa, **"Toward the Completion of Measurement of Absorption Spectra of 20 Amino Acids and 5 Bases of Nuclear Acids Over Wide Energy Range"**, Rad. Chem. **97** (2014) 29.

The 30th anniversary of UVSOR

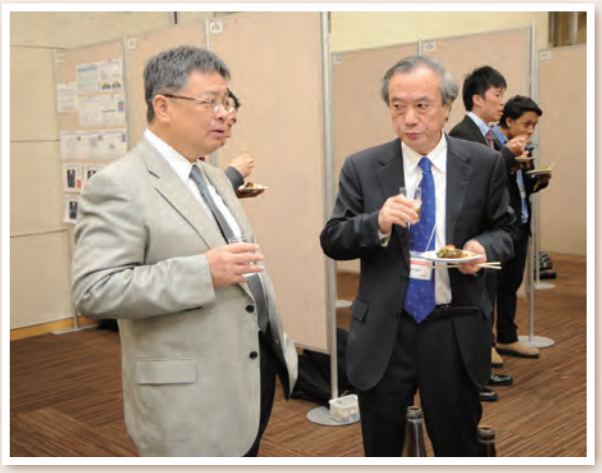

V

Workshops

UVSOR 30th Anniversary

Date : December 6, 2013
Place: Okazaki Conference Center, Okazaki, Japan

13:00 - 13:50 Facility Tour

14:00 - 15:10 Memorial Lecture

Iwao Ohmine
(IMS Director-General)
Yoshiaki Ando
(Section chief of the Basic and Generic Research Division of MEXT)
Masahiro Kato
(Director of UVSOR)
Nobuhiro Kosugi
(IMS Deputy Director General)

15:20 - 17:20 Special Lecture

Youichi Murakami
(Chairman of JSSRR, Director of Photon Factor)
Ingolf Lindau
(Professor Emeritus at Stanford University and Lund University)
Tetsuya Ishikawa
(Director of RIKEN SPring-8 Center)

UVSOR Symposium 2013

Date : December 7, 2013
Place : Okazaki Conference Center, Okazaki, Japan

09:00 - 09:05 Opening Remarks
M. Kato (UVSOR)

<Session 1, Chair : **T. Ito**>
09:05 - 09:25 Status of UVSOR-III
M. Kato (UVSOR)
09:25 - 09:40 Status of Electron Source Development in UVSOR
T. Konomi (UVSOR)
09:40 - 09:55 Spin-, Orbital-, and Momentum-Resolved Photoemission Microspectroscopy Beamline
S. Kimura (UVSOR)
09:55 - 10:25 Measuring the Photoelectron Spectra of Fullerenes for 20 Years
S. Hino (Ehime Univ.)

<Session 2, Chair : **M. Matsunami**>
10:55 - 11:25 Angle-Resolved Photoelectron Spectroscopy for Graphite with Low Photon Energy
S. Tanaka (Osaka Univ.)
11:25 - 11:40 High-Resolution ARPES Study on Related Material of Topological Crystalline Insulator SnTe
Y. Tanaka (Tohoku Univ.)

12:00 - 14:30 Poster Session and Lunch

<Session 3, Chair : **M. Kato**>
14:30 - 14:55 Comprehensive Study of Photo-Excited States of Solids by VUV Luminescence Spectroscopy
M. Kitaura (Yamagata Univ.)
14:55 - 15:20 Development of the Photoelectron Spectroscopy Beamline Suited for Organic Molecular Solids: Bl2b Reconstruction
S. Kera (Chiba Univ.)
15:20 - 15:35 Overview of Chromospheric Lyman-Alpha SpectroPolarimeter (CLASP) and Evaluations of its Optical Components with UVSOR BL7B
N. Narukage (NAOJ)
15:35 - 15:50 Ultraviolet Photoelectron Spectra of Multiple Atoms Encapsulated Fullerenes
T. Miyazaki (Ehime Univ.)

<Session 4, Chair : **E. Shigemasa**>
16:10 - 16:40 Electronic Structure of Organic Films & Interfaces Studied with Synchrotron Radiation

H. Yamane (UVSOR)

16:40 - 16:55 Preliminary Results of Spectromicroscopy of Biological Specimens Using Scanning Transmission Soft X-Ray Microscope (STXM)
A. Ito (Tokai Univ.)

16:55 - 17:10 The Study on Nickel-Borate Oxygen Evolution Catalyst by Electrochemical Soft X-Ray Absorption Spectroscopy
M. Yoshida (Keio Univ.)

17:10 - 17:25 Investigation of Magnetization of Co Ultrathin Films on W(110) by XMCD/XMLD
H. Nakano (Kyoto Univ.)

17:25 - 17:40 Closing Remarks and Discussion
K. Soda (Nagoya Univ.)

<Poster Session>

P01 Synchrotron ARPES Study on Three-Dimensional Superconducting-Gap Structure of $Ba(Fe_{1-x}Co_x)_2As_2$
T. Hajiri (Nagoya Univ.)

P02 Magnetic Property of Vanadyl Phthalocyanine on Ferromagentic Iron Surface
K. Eguchi (SOKENDAI)

P03 In-situ Observation of Electrochemical Reaction of Aqueous Iron Sulfate Solution by Soft X-Ray Absorption Spectroscopy
M. Nagasaka (IMS)

P04 Effect of Mechanochemical Coating on the Electrochemical Property of Li-Excess Mn-Based Layered Positive Electrode Materials
K. Takada (Kansai Univ.)

P05 Conversion from the Ag^+ to Ag^- Centers in Electrolytically-Colored NaCl:Ag^+ Crystals
T. Kawai (Osaka Prefecture Univ.)

P06 In-situ Observation of Cyanopyrazine Hydration on TiO_2 by Soft X-ray Absorption Spectroscopy
H. Yuzawa (IMS)

P07 Optical Spectroscopy of Rare-Earth Doped $Y_3Al_5O_{12}$(RE=Ce,Eu,Tb,Pr) Single Crystals
D. Susuki (Gifu Univ.)

P08 Site-Specific Fragmentation of the C K-Shell Excited cis-Hexafluorocyclobutane Molecule Probed by the Auger Electron–Photoion Coincidence Method
S. Ishikawa (Hiroshima Univ.)

P09 Valence Band Electronic Structure of $Mg_xZn_{1-x}O$ Synthesized under High Pressure
K. Takahama (Nagoya Univ.)

P10 Emission and Excitation Spectrum of a-CN_x
D. Itoh (Univ. of Fukui)

P11 Mass Resolved Velocity Map Imaging of Doubly Charged Photofragments from C_{60}
H. Katayanagi (IMS)

P12 Multi-Electron-Ion Coincidence Spectroscopic Study of Stability of Molecular

Dications
I. Umekawa (Niigata Univ.)

P13 Transient Phenomena of Charge-Up Effects in X-Ray Probe Spectroscopy
K. Okada (Waseda Univ.)

P14 Development of Spectroscopic Ellipsometry for UV-VUV Region
Y. Kubo (Univ. of Fukui)

P15 Angle-Resolved Photoemission Spectroscopy of C_{60} Single Crystal Films
H. Masuda (Tokyo Institute of Technology)

P16 Interface Electronic Structures of Various n-Type Organic Overlayers Stacked onto the NPB Films Modeling Donor-Acceptor Heterojunctions in Organic Light Emitting Diodes
Y. Nakayama (Chiba Univ.)

P17 Measurement of Emittance in Aichi Synchrotron Radiation Center
R. Kawakami (Nagoya Univ.)

P18 Low-Photon-Energy Polarization-Dependent Angle-Resolved Photoemission Study on Quasi-One Dimensional Organic Conductor $(TMTSF)_2SbF_6$
M. Mitamura (Nagoya Univ.)

P19 Optical Spectra and Electronic Structure of $SrCeO_3$ Crystals
H.Numata (Yamagata Univ.)

P20 X-Ray Absorption of Trace Elements by Fluorescence Yield with Silicon-Drift Detector
H. Murata (NIMS)

P21 Electronic Structure of Heusler-Type $Fe_2V_{1+x}Al_{1-x}$ Thermoelectric Materials Studied by Angle-Resolved Photoemission Spectroscopy
K. Ando (Nagoya Institute of Technology)

P22 The Effect of the Microwave Irradiation on ZnO
K. Yoshida (Kyoto Univ.)

P23 Characterization of Photoinduced Phenomena in Amorphous Chalcogenide Semiconductors by Vacuum Ultraviolet Absorption Spectroscopy
K. Hayashi (Gifu Univ.)

P24 Effect of Nb Doping on the Thermoelectric Properties of ZrNiSn Half-Heusler Compounds
K. Hattori (Nagoya Institute of Technology)

P25 Formation of Metastable Carbon Dioxide Dications Studied with Electron-Ion Coincidence Spectroscopy
Y. Shibata (Niigata Univ.)

P26 Study on the Interface State Formed by Surface-Induced Aromatic Stabilization
K. Kato (Chiba Univ.)

P27 Auger-Free Luminescence Spectra and Decay Curves of A_2ZnCl_4 (A = K, Rb, Cs) Crystals
T. Sasaki (Yamagata Univ.)

P28 Measurement of Temoral Response of Transmission-Type Spin-Polarized Photocathodes
T. Inagaki (Nagoya Univ.)

P29 Development of Transmission-Type Polarized Electron Source for Inverse Photoemission Spectroscopy
Y. Kajiura (Nagoya Univ.)

UVSOR Mini-Workshop
Accelerator Technologies for Small Synchrotron Light Sources

Date : March 27-28, 2014
Place: UVSOR 304, Okazaki, Japan

March 27th (Thur)

13:30 - 13:35	Opening Remarks **M. Katoh** (UVSOR)
13:35 - 14:00	Present Status of UVSOR Accelerators **J. Yamazaki** (UVSOR)
14:00 - 14:30	Present Status of Aichi-SR Accelerators **A. Mano** (Nagoya Univ.)
14:30 - 15:00	The Trouble History of The SAGA Light Source **Y. Iwasaki**（SAGA-LS）
15:00 - 15:30	Water Leakage Troubles, Orbit Instability at Saga-LS **T. Kaneyasu** (Saga-LS)
15:30 - 16:00	Present Status of Accelerator of Ritsumeikan U. SR Center **Y. Yamamoto** (Ritsumeikan Univ.)
16:15 -	Other Topics From the Facilities Control System and LOCO at Aichi-SR **T. Takano** (Nagoya Univ.) Beam Loss Monitor Using Optical Fiber at UVSOR **K. Hayashi** (UVSOR) Signal Generator Trouble at UVSOR **K. Hayashi** (UVSOR)

March 28th (Fri)

09:30 - 10:30	UVSOR Facility Tour
13:00 - 14:00	Aichi-SR Facility Tour

IMS Workshop on Advanced Spectroscopy of Correlated Materials (ASCM 13)

Date : August 2 - 4, 2013
Place: Okazaki Conference Center, Okazaki, Japan

August 2nd (Fri)

17:00 - 20:00 Registration
18:00 - 20:00 Welcome Reception

August 3rd (Sat)

<Session 1. Heavy Fermion System, Chairperson : **M. Matsunami**>

10:10 - 10:35 Global K-Space Perspective of Temperature-Dependent U 5f-States in URu_2Si_2
J. Denlinger (Lawrence Berkeley National Laboratory)

10:35 - 11:00 Soft X-Ray ARPES Study of Uranium Compounds
S. Fujimori (Japan Atomic Energy Agency)

11:00 - 11:25 Optical Study of Archetypical Valence-Fluctuating Eu Systems
J. Sichelschmidt (MPI Chemische Physik Fester Stoffe)

11:25 - 11:50 Low-Energy Optics of Uranium-Based Heavy Fermions: Drude Response of Slow and Fast Electrons
M. Scheffler (Univ. Stuttgart)

11:50 - 13:00 Group Photo and Lunch

<Session 2. Molecular Solids and Novel Technical Aspects including New Synchrotron Beamlines, Chairperson : **G.R. Sunye**>

13:00 - 13:25 Time-Resolved ARPES of Graphite Using Femtosecond Pulsed Light in the Deep-to-Extreme UV Region
Y. Ishida (Univ. Tokyo)

13:25 - 13:45 Electron-Phonon Coupling Investigation Via Phonon Dispersion Measurement in Graphite by Angle-Resolved Photoelectron Spectroscopy
S. Tanaka (Osaka Univ.)

13:45 - 14:05 Angle-Resolved Photoemission Study of Quasi-One-Dimensional Organic Conductor
T. Ito (Nagoya Univ)

14:05 - 14:20 Coffee Break

14:20 - 14:45 Angle Resolved Photoemission Spectroscopy of Two Dimensional Organic Metal
T. Kiss (Osaka Univ.)

14:45 - 15:15 SOR-ARPES Studies on Pi-Electronic Interaction in Organic Films and Interfaces
H. Yamane (IMS)

15:30 - 16:30 UVSOR Site Tour
16:30 - 18:30 Check-in and Free Time
18:45 - 21:00 Open-air Banquet at IMS

August 4th (Sun)

<Session 3. Rare-Earth and Transition Metal Oxides, Chairperson **H. Miyazaki**>

09-00 - 09:25 Observation of Laser-Induced Magnetization Precession in Ferromagnetic EuO
T. Makino (Univ. Fukui)

09:25 - 09:50 Investigating the Spin-Polarized Metal-Insulator Transition in Carrier Doped $Eu_{1-x}Gd_xO$ Thin Films and Heterostructures by ARPES
K. Shen (Cornel Univ.)

09:50 - 10:15 Quantum Confinement of Strongly Correlated Electrons in Oxide Artificial Structures
K. Yoshimatsu (Tokyo Institute of Technology)

10:15 - 10:40 Coffee Break

<Session 4. Topological Insulator, Chairperson **S. Kimura**>

10:40 - 11:05 Theoretical Proposal of Topological Insulator for a Kondo Insulator SmB_6
T. Takimoto (Hanyang Univ.)

11:05 - 11:30 Topological Phase Transitions in Ultrathin Films
T. Hirahara (Univ. Tokyo)

11:30 - 11:55 Spin-and Angle-Resolved Photoemission as a Direct Probe of Spin Textures in Topological Insulators
A. Kimura (Hiroshima Univ.)

11:55 - 12:20 Local Orbital Angular Momentum and Circular Dichroism ARPES
C. Kim (Yonsei Univ.)

12:20 - 12:30 Closing Remarks
S. Kimura (Osaka Univ.)

Institute for Molecular Science
National Institutes of Natural Sciences
Okazaki 444-8585,Japan

Tel : +81-564-55-7402
Fax : +81-564-54-7079
http://www.uvsor.ims.ac.jp

ISSN 0911-5730